The chiral phase transition in the bare parameter space of staggered lattice QCD

Dissertation
zur Erlangung des Doktorgrades
der Naturwissenschaften

vorgelegt beim Fachbereich Physik
der Johann Wolfgang Goethe-Universität
in Frankfurt am Main

von
Alfredo D'Ambrosio
aus Cosenza, Italien

Frankfurt am Main 2023
D30

vom Fachbereich Physik der
Johann Wolfgang Goethe-Universität als Dissertation angenommen.

Dekan: Prof. Dr. Roger Erb

Gutachter: Prof. Dr. Owe Philipsen
Dr. Olaf Kaczmarek

Datum der Disputation:

Table of contents

Abstract

The core of this work is represented by the investigation of the chiral phase transition, using Monte Carlo simulations and unimproved staggered fermions, both in the weak and strong coupling regimes of Quantum Chromodynamics. Based on recent results from Monte Carlo simulations, both using unimproved staggered fermions and Wilson fermions, the chiral phase transition in the continuum and chiral limit shows compatibility with a second-order phase transition for $N_f \in [2:7]$, at zero baryon chemical potential. This achievement relies on the analytic continuation of N_f to non-integer values on the lattice, which allows to make use of extrapolation techniques to the chiral limit, where simulations are not possible. Furthermore, these results provide a resolution to the ambiguous scenario for $N_f = 2$ in the chiral limt. The first part of this thesis is devoted to the investigation of the chiral phase transition when a non-zero imaginary baryon chemical potential is involved, whose value corresponds to the 81% of the Roberge-Weiss one, $\mu = i\pi T/3$. Using the same extrapolation techniques aforementioned, the order of the chiral phase transition in the continuum and chiral limit shows compatibility with a second-order phase transition for $N_f \in [2:6]$, highlighting a lack of dependence of the order of the chiral phase transition on the imaginary baryon chemical potential value. The second part of this thesis is about the study of the extension of the first-order chiral region in the strong coupling regime, at zero baryon chemical potential. Using Monte Carlo techniques, this can be done by investigating the Z_2 boundary on a coarse lattice, whose temporal extent reads $N_\tau = 2$, and simulations are realised for $N_f = \{4, 8\}$. The results in the weak coupling regime show, for $N_\tau = \{8, 6, 4\}$ and fixed N_f value, an inflating first-order chiral region. As in the strong coupling limit a second-order chiral phase transition is expected, the first-order chiral region has to shrink as the strong coupling regime is approached, resulting in a non-monotonic behaviour of the Z_2 boundary. For $N_f = 8$, a critical mass on the Z_2 boundary has been obtained, confirming the expected non-monotonic behaviour. For $N_f = 4$ the results do not provide a unique conclusion: Either a Z_2 boundary at extremely low bare quark mass or a second-order chiral phase transition in the $O(2)$ universality class in the chiral limit can take place. In addition to the two main topics, the performances of the second-order minimum norm integrator (2MN) and the fourth-order minimum norm integrator (4MN) have been compared, after implementing the 4MN one in the CL^{2}QCD code used to realise our simulations. The 2MN integrator had already been implemented in the code since the first version was released. The two integrators belong to the class of symplectic integrators and represent an essential component of the RHMC algorithm, involved in our investigation. This step is extremely important, in order to guarantee the best quality when collecting data from simulations, and the results of the comparison suggested to favor the 2MN integrator, for both the topics.

Deutsche Zusammenfassung

Thermische Quantenfeldtheorie stellt ein lebendiges Forschungsfeld dar, welches sich der sorgfältigen Analyse der phänomenologischen Details widmet, die die frühesten Stadien der Entwicklung des Universums charakterisierten und die sich noch heute in der Komplexität der Zusammensetzung von Himmelsobjekten aüßern, wie zum Beispiel in den inneren Teilen von Neutronensternen, sowie in den Produkten von Schwerionenkollisionen in geeigneten Collidern. Nach dem Urknall begann das Universum und seine Bestandteile sich in Raum und Zeit zu expandieren und extreme Zustände zu durchlaufen, die sich bis heute auf die kosmologischen Strukturen auswirken. Die Entstehung und der Fortschritt der Elementarteilchen, ihre Aggregation in zusammengesetzten Teilchen und schrittweise in makroskopischen Objekten, die sich zu Planeten, Sterne, Galaxien und Galaxienhaufen entwickelten, waren Gegenstand vieler philosophischer Theorien und, insbesondere im letzten Jahrhundert, physikalischer und mathematischer Untersuchungen, die zur Formulierung verschiedener Modelle führten. Die Rekonstruktion der ersten Sekunde der Existenz des Universums ist seit Jahren eine herausfordernde Aufgabe: Die vier grundlegenden Wechselwirkungen begannen sich voneinander aufzuspalten in dem Zeitintervall nach dem Urknall zwischen 10^{-43} s and 10^{-35} s – der sogenannten *kosmologische Inflation*, in der sich die Gravitation von den restlichen drei Kräften abspaltet. Um 10^{-35} s konnte die starke Wechselwirkung unterschieden werden und näherungsweise nach 10^{-10} s begannen die elektromagnetischen und schwachen Wechselwirkungen ihre Aufspaltung. Die Untersuchungen von Teilchen, ihrer Entstehung und Evolution führen zur Aufteilung der Zeitachse der Evolution in verschiedene Sektoren, *Epochen* genannt. In den letzten sechzig Jahren wurden erhebliche Anstrengungen unternommen, um die Hauptmerkmale der grundlegenden Wechselwirkungen zu sammeln und zu katalogisieren: Das Standardmodell (SM) der Elementarteilchenphysik erklärt die Existenz der Teilchen, ihre Eigenschaften und die Art der Wechselwirkungen, denen sie ausgesetzt sind, in Bezug auf die starken, schwachen und elektromagnetischen Wechselwirkungen. Das SM wurde ständig aktualisiert, um die neuesten Forschungsergebnisse einzubeziehen. Das Gebiet der Quantenchromodynamik (QCD) wird in dieser Dissertation erforscht. Quarks und Gluonen stellen die wesentlichen Bausteine der QCD dar, die die Theorie der starken Wechselwirkungen darstellt. Quarks gehören zur Familie der Leptonen: Da sie Teilchen mit einem halbzahligen Spin sind, werden sie als Fermionen bezeichnet und interagieren anhand der drei fundamentalen Wechselwirkungen, die im SM dargestellt sind. Die Hauptmerkmale, die Quarks im Rahmen von Teilchen unterscheiden, bestehen unter anderem in dem Flavour Freiheitsgrad und der Farbladung. Ersteres garantiert die Existenz von sechs Arten von Quarks, nämlich die Up-, Down-, Strange-, Charme-, Bottom- und Top-Quarks, während die Farbladung mit der starken Wechselwirkung verbunden ist, die drei verschiedene Arten von Ladungen definiert, nämlich die roten, blauen und grünen Farben. Quarks sind massereiche Teilchen, bei denen die Up-, Down- und Strange-Quark normalerweise in der *Familie der leichten Quarks* enthalten sind und eine elektrische Bruchladung

tragen, die es den Quarks auch ermöglicht, über elektromagnetische Wechselwirkungen zu interagieren. Darüber hinaus interagieren sie auch über schwache Wechselwirkung. Gluonen stellen die Eichbosonen dar, die die starke Wechselwirkung vermitteln. Gluonen sind masselose Teilchen, die selbst Farbladung tragen und daher auch mit anderen Gluonen wechselwirken. Darüber hinaus tragen sie als Bosonen einen ganzzahligen Spin. Die Entwicklung der QCD als unabhängige Theorie war stark mit dem technologischen Fortschritt in den Jahren vieler Collider-Anlagen verbunden. In den sechziger Jahren wurden Baryon und Mesonen nach der Identifizierung und Klassifizierung der Eigenschaften neuer Resonanzen mittels Darstellungen der unitären SU(3)-Symmetriegruppe als zusammengesetzte Teilchen klassifiziert, deren Bestandteile Quarks sind, nämlich gebundene Zustände von Quarks. Die Bestätigung des vermuteten Spektrums der Teilchen, abhängig von den betrachteten SU(3)-Darstellungen, kam zustande, als neue Experimente in den oben genannten Laboratorien produziert wurden, die eine Verbesserung der Energie der Beschleuniger und Collider lieferten. In den siebziger Jahren wurde Farbeladung in der Theorie als eine exakte SU(3)-Symmetrie eingeführt, nach Studien über Elektron-Positron-Kollisionen aus experimenteller und theoretischer Sicht, Gleichzeitig veränderte eine wichtige Entdeckung die Perspektive bezüglich der phänomenologischen Aspekte starker Wechselwirkungen: Die *asymptotische Freiheit*. Letzteres ist das Hauptergebnis der Farbladung, die auch von Gluonen getragen wird, und die wichtigsten Folgen dieses Phänomens bestehen in einer Variation der Werte der Kopplungskonstante, wenn starke Wechselwirkung bei verschiedenen Energien stattfindet: Für höhere Energien verhäl sich der gebundene Zustand von Quarks und Gluonen wie ein System quasi-freier Teilchen; das Gegenteil gilt für niedrigere Energiewerte. Unter Berücksichtigung der QCD-Energieskala Λ_{QCD}, die von der Anzahl der Quarks-Flavours und dem verwendeten Renormierungsschema abhängt, kann für Energiewerte, die größer sind als Λ_{QCD}, ein perturbativer Ansatz verwendet werden, um die Phänomenologie von QCD zu beschreiben; während für Werte, die niedriger als Λ_{QCD} sind, ein nicht-perturbativer Ansatz notwendig ist. Ein grundlegendes Werkzeug zur Untersuchung nicht-perturbativer Effekte in QCD ist die Gitterdiskretisierung der Raumzeit, die 1974 von Kenneth Wilson konzipiert wurde. Diese basiert auf der Möglichkeit, die Lagrange-Funktion und die Wirkung eines spezifischen Systems auf einem euklidischen Raum-Zeitgitter zu formulieren, bestehend aus Gitterstellen und Gitterverbindungen, wo auch die Fermions- und Gluonenfelder richtig neu definiert werden. Das Gitter stellt ein nicht-perturbatives Regularisierungsschema dar, in dem QCD untersucht werden kann, abhängig von einem spezifischen Gitterabstand a. Der Kontinuumslimes wird durch Extrapolation auf einen verschwindenden Gitterabstands ermittelt, wobei physikalische Größen ohne Gitterabhängigkeit gewonnen werden sollen. Die Idee erwies sich in vielen Bereichen als erfolgreich und bot die Möglichkeit, Phänomene wie das Brechen der chiralen Symmetrie, das Confinement und im Allgemeinen Phasenübergänge in QCD im Detail zu untersuchen. Eine detaillierte Einführung in Gitter-QCD und Diskretisierungstechniken wird im ersten Kapitel dieser Dissertation gegeben. Ein weiterer interessanter Punkt ist die Einführung von Temperatur und Dichte in die Theorie. Zum Beispiel erfordert die Anwendung von QCD auf die in den ersten Zeilen dieser Zusammenfassung genannten Systeme einen thermodynamischen Ansatz und die Einführung der Grundlagen der statistischen Mechanik in die Theorie. Thermische Quantenchromodynamik stellt eine Kombination von QCD und Thermodynamik dar und beruht auf der Pfadintegralformulierung in der euklidischen Raumzeit. Die Beschreibung von QCD-Systemen in Abhängigkeit von Temperatur und Dichte (durch nicht verschwindender chemische Potentiale) führt zur Formulierung des *QCD-Phasendiagramms*, wo verschiedene Regionen, entsprechend verschiedenen Eigenschaften der nuklearen und

subnuklearen Materie, in Abhängigkeit von den Werten der beiden, neu eingeführten, thermodynamischen Parametern der Theorie studiert werden. Die Trennung zwischen solchen Regionen ist von besonderem Interesse, da sie mit QCD-Phasenübergängen zusammenfallen können. Das QCD-Phasendiagramm hängt von der Anzahl der Quarks-Flavours und der untersuchten Kopplungsstärke ab. Diese sogenannte Regimes unterscheiden sich durch die verschiedenen Werten der Gitter-Eichkopplung $\beta(a)$, die von dem Gitterabstand abhängt: Im Rahmen der starken Wechselwirkung definieren niedrigere Werte von $\beta(a)$ das starke Kopplungsregime von QCD, wobei $\beta(a) = 0$ den starken Kopplungslimes bezeichnet, während größere Werte von $\beta(a)$ das schwache Kopplungsregime von QCD kennzeichnen. In den letzten vierzig Jahren wurde viel Fokus auf die Untersuchung des chiralen Phasenübergang gelegt, der den Dreh- und Angelpunkt für diese Arbeit darstellt. Dabei wurden verschiedene Parameter, wie der Anzahl der Quark-Flavours und der *bare Quarkmassen*, berücksichtigt. Der Columbia-Plot bietet eine Darstellung des chiralen Phasenübergangs für $N_f = 2 + 1$, wobei sich der Wert "2" auf die entartete Masse der beiden leichtesten Quarks, den Up- und Down-Quarks, bezieht, während der Wert "1" sich auf die Masse des Strange-Quark bezieht. Die wichtigsten Merkmale des Columbia-Plots bestehen in verschiedenen Regionen, die einem chiralen Phasenübergang erster Ordnung oder einem Crossover entsprechen. Die verschiedenen Regionen werden für nicht verschwindender bare Quarkmassen durch Z_2 kritische Grenzen in der 3d Insing Universalitätsklasse getrennt. Die Art des chiralen Phasenübergangs wird seit den achtziger Jahren diskutiert: 1984 erhielten R. D. Pisarski und F. Wilczek bei der Untersuchung des chiralen Limes einen chiralen Phasenübergang erster Ordnung für $N_f \geq 3$, während das Szenario für $N_f = 2$ komplizierter war. Das Ergebnis war entweder ein chiraler Phasenübergang erster oder zweiter Ordnung, abhängig von der Realisierung der $U(1)_A$ Symmetrie. Betrachtet man die Ecke leichter Quarkmassen im Columbia-Plot und die chirale Region erster Ordnung, die sich hier ausdehnt: Wenn ein Phasenübergang zweiter Ordnung im chiralen Limes $N_f = 2$ stattfindet, dann ist für $m_{ud} = 0$ bei endlichem m_s ein trikritischer Punkt zu identifizieren. Im Columbia-Plot übersetzt sich dies in zwei möglichen Szenarien, mit unterschiedlichen Erweiterungen der chiralen Region erster Ordnung in der Nähe von $m_{ud} = 0$. Eine nützliche Technik zur Lösung dieser schwierigen Situation für $N_f = 2$ wurde in 2021 von F. Cuteri, O. Philipsen und A. Sciarra vorgeschlagen, die darin besteht, die Anzahl der Quark-Flavours N_f als Skalierungsparameter anstelle von m_s zu verwenden, um die trikritische Skalierung zu untersuchen. Dies erforderte, dass N_f analytisch von ganzzahligen zu nicht ganzzahligen Werten auf dem Gitter fortgesetzt wurde. Die Ergebnis dieser Untersuchung ist kompatibel mit einem chiralen Phasenübergang zweiter Ordnung für $N_f \in [2 : 7]$ im chiralen Limes und Kontinuumslimes. Dies löst die Mehrdeutigkeit für $N_f = 2$ definitiv. Der Columbia-Plot repräsentiert die Ordnung des chiralen Phasenübergangs nur im Fall der verschwindender Dichte. Lattice QCD Simulationen hat unter einem anderen herausfordernden Problem gelitten, dem *sign problem*: Wenn ein chemisches Potenzial in die QCD-Wirkung einbezogen wird, führt die Art, wie es zu den Feldern koppelt, zu einem negativen Zeichen der Determinante des Dirac-Operators, was die Untersuchung mittels numerischer Simulationen bedeutungslos macht. Eine Möglichkeit, dieses Problem zu umgehen, liegt in der analytischen Fortsetzung des chemischen Potenzials zu imaginären Werten, die es ermöglicht, Simulationen durchzuführen und den Columbia-Plot entsprechend zu erweitern. Die Verteilungsfunktion von QCD, $\mathcal{Z}_{\mathrm{QCD}}$, wenn auch ein imaginäres chemisches Potential enthalten ist, hat zwei Symmetrien: Die Ladungsparitätssymmetrie und die Roberge-Weiss-Symmetrie, die eher ein Periodizitätsmerkmal ist, das in $\mathcal{Z}_{QCD}$ auftritt. Der Columbia-Plot kann in einer dreidimensionalen Version um eine dritte Achse, $-(\mu/T)^2$

erweitert werden, die den Columbia-Plot bei $-(\mu/T)^2 = 0$ mit der Roberge-Weiss-Ebene bei $-(\mu/T)^2 = -(\pi/3)^2$ verbindet, was der ersten Periode $\mathcal{Z}_{\mathrm{QCD}}$ entspricht. Fokussiert auf die Fläche zwischen dem Columbia-Plot und der Roberge-Weiss-Ebene, werden für $N_\tau = 4$ die chiralen Phasenübergänge erster Ordnung vergrößert, was zu einer Schrumpfung der Ausdehnung des crossover-Bereichs führt. Die Untersuchung der Ausdehnung der chiralen Region erster Ordnung beim Übergang vom schwachen zum starken Kopplungsregime kann unter Berücksichtigung der gitterzeitlichen Ausdehnung durchgeführt werden: Wenn die Abhängigkeit von N_τ vom Gitterabstand a und die Abhängigkeit der laufende QCD-Kopplung $g(a)$ von a bestimmt ist, kann das starke Kopplungsregime bei Simulationen mit $N_\tau = 2$ untersucht werden, was die gröbste mögliche Wahl darstellt. In den letzten vierzig Jahren wurden die Grenzen und das Regime der starken Kopplung mit verschiedenen Techniken, die mit Monte-Carlo-Methoden und effektiven Modellen zusammenhängen, gründlich untersucht. Die Ergebnisse der chiralen Grenze und der verschwindender Dichte sind mit einem chiralen Phasenübergang zweiter Ordnung in der Universalitätsklasse $O(2)$ kompatibel. Das Ziel dieser Arbeit besteht darin, zwei verschiedene physikalische Rahmenbedingungen zu untersuchen:

- Die Erweiterung der chiralen Region erster Ordnung in der Nähe der Ecke leichter Quarkmassen des dreidimensionalen Columbia-Plots, wenn man ein chemisches Potenzial betrachtet, das ungefähr den 80% des Wertes der Roberge-Weiss-Ebene entspricht. Die Ergebnisse werden mit denen verglichen, die in der zuvor erwähnten Arbeit bei verschwindender Dichte erhalten wurden;

- Die Verlängerung des chiralen Phasenübergangs erster Ordnung beim Übergang vom schwachen zum starken Kopplungsregime bei verschwindendem chemischem Potential.

Eine vollständige Diskussion über das QCD-Phasendiagramm, den Columbia-Plot und seine Erweiterung sowie die beiden verschiedenen Regime der starken Kopplung werden im zweiten Kapitel dieser Dissertation detailliert dargestellt. Die Physik auf dem Gitter kann mit Hilfe von Monte-Carlo-Methoden untersucht werden, die einige spezifische Merkmale erfordern, die direkt mit statistischen mechanischen Methoden verbunden sind. Die Arbeit in dieser Dissertation basiert auf Monte-Carlo-Simulationen, bei denen unimproved staggered Fermionen verwendet werden. Daher wurden Simulationen mit dem Rational Hybrid Monte Carlo Algorithmus (RHMC) durchgeführt. Letzterer besteht aus einer Reihe von Algorithmen, die es erlauben, eine Reihe von Markov-Ketten zu erzeugen, an deren Ende einige Observablen gemessen werden, wie zum Beispiel das chirale Kondensat, das der Ordnungsparameter für den chiralen Phasenübergang ist. Innerhalb des RHMC-Algorithmus sind der Heat Bath-Algorithmus, der Molecular Dynamics-Algorithmus und der Metropolis-Algorithmus enthalten, die benötigt werden, um die Pseudofermionsfelder, die Eichfelder und die konjugierten Eichfelder über die Markov-Kettenproduktion zu aktualisieren. Für beide Projekte besteht die numerische Strategie in der Festlegung einer Reihe von Parametern, einschließlich der Anzahl der Flavour, der nackten Quarkmassen, der räumlichen und zeitlichen Gitterausdehnungen und der Eichkopplung am Gitter, und im zweiten Projekt auch nicht verschwindendem imaginäres chemisches Baryonpotential. Simulationen werden mit Hilfe des CL^{2}QCD-Codes erstellt, welcher in C++ geschrieben ist, und die erzeugten Daten werden mit Python-Skripten analysiert. Die Ergebnisse bezüglich des chiralen Kondensats werden als Histogramme erhalten und anhand der standardisierten Momente der Theorie der kontinuierlichen Wahrscheinlichkeitsverteilungen, der Jackknife-Methode und der Ferrenberg-Swendsen-reweighting analysiert. Am Ende wird ein Datensatz von kritischen Massen, die zur

Z_2 Grenze gehören, durch finite-size Skalierung für verschiedene zeitliche Ausdehnungen des Gitters berechnet; diese Analyse wird für verschiedene Kombinationen von Gitterparametern durchgeführt. Die Methodik und die numerische Strategie werden im dritten Kapitel dieser Arbeit diskutiert. Das letzte Kapitel beschäftigt sich mit der Darstellung der Ergebnisse der beiden verschiedenen Projekte. Vor der Diskussion der Hauptresultate wird ein weiterer, numerischer Aspekt der Arbeit vorgestellt, das die Familie der symplektische Integratoren betrifft, die am CL^{2}QCD-Code beteiligt sind, insbesondere die Integratoren zweiter Ordnung (2MN) und vierter Ordnung der Mindestnorm (4MN). Ersterer wurde seit der Veröffentlichung der ersten Version in CL^{2}QCD implementiert, während letzteres im ersten Teil meiner PhD implementiert wurde. Das Ziel der Implementierung bestand darin, die Leistungen der beiden verschiedenen Integratoren in unserem Code zu analysieren und zu entscheiden, welcher für die Untersuchung der beiden Hauptprojekte einbezogen werden soll. Nach einer detaillierten Studie war der 4MN-Integrator weniger attraktiv als der 2MN-Integrator, vor allem, weil er im Vergleich zum 2MN-Integrator extrem rechenzeitaufwändig war. Das erste Projekt zur Untersuchung der Region zwischen dem Columbia-Plot und der Roberge-Weiss-Ebene wurde unter Verwendung der zuvor eingeführten Methodik und durch Extrapolationen an die chirale Grenze entwickelt, wo Simulationen nicht möglich sind. Die trikritische Skalierung der Z_2-Grenze, abhängig von mehreren Parametern, wird anhand geeigneter Funktionen untersucht und die erzielten Ergebnisse bestätigen die Inflation der chiralen Region erster Ordnung für $N_\tau = 4$ und im Allgemeinen ein ähnlicher Trend in Richtung der chiralen Grenze wie für das Szenario verschwindender Dichte. Tatsächlich bieten die Schlussfolgerungen zu diesen Projekten Kompatibilität mit dem Vorhandensein eines trikritischen Punktes im chiralen Limes auf einem endlichen Gitter, was einen chiralen Phasenübergang zweiter Ordnung im Kontinuumslimes und chiralen Limes für $N_f \in [2:6]$ impliziert. Es ist erwähnenswert, dass dieses Projekt dank einer gemeinsamen Arbeit mit meinen Kollegen Reinhold Kaiser, der auch Mitglied der Gruppe von Professor Owe Philipsen ist, abgeschlossen wurde. Das zweite Projekt über die Untersuchung im starken Kopplungsregime bei verschwindender Dichte wurde autonom entwickelt und stützt sich auch auf die bereits vorgestellte numerische Strategie und Methodik. Simulationen wurden für $N_\tau = 4$ durchgeführt und das erwartete Verhalten aus der Literatur besteht in einem Schrumpfen der chiralen Region erster Ordnung im Vergleich zu den Ergebnissen für größere zeitliche Ausdehnungen des Gitters. Dies bedeutet, dass ein nicht-monotones Verhalten der Z_2-Grenze erkannt werden soll, nämlich eine Änderung der Steigung mit einem globalen Maximum zwischen $N_\tau = 4$ und $N_\tau = 2$. Die Untersuchung wurde für zwei, verschiedene Anzahlen von Quark-Flavours durchgeführt, $N_f = 4$ und $N_f = 8$ und stellte sich als herausfordernd dar, da die Erweiterung der chiralen Region erster Ordnung auf die Quark-Massenregion in der Nähe des chiralen Limes begrenzt ist. Für $N_f = 8$ war es möglich, eine kritische Masse an der Z_2-Grenze zu lokalisieren, während das Szenario für $N_f = 4$ keine eindeutige Lösung lieferte: Die Kombination aus zeitaufwändigen Simulationen, niedrigen Quark-Massen und dem starken Einfluss der erzeugten finite-size Effekte begrenzte die Menge der kumulierten Statistik, welche wiederum zu wenigen erhaltenen kritischen Massen führte. Dies wiederum schränkt die Anwendung der Finite-Size-Scaling ein. Infolgedessen wird das Szenario für $N_f = 4$ und $N_\tau = 2$ mit gleicher Wahrscheinlichkeit einen chiralen Phasenübergang zweiter Ordnung im chiralen Limes in der Universalitätsklasse $O(2)$ oder eine kritische Masse der kritischen Z_2 Linie haben, die deutlich niedrig und nahe der chiralen Grenze ist. Die im Rahmen dieser Arbeit durchgeführten Simulationen wurden am Goethe-HLR-Cluster, am HCP-Cluster VIRGO des GSI und am ehemaligen L-CSC-Cluster des GSI durchgeführt.

Introduction

The vibrant research activity in the nuclear and subnuclear physics field during the last century has produced, over the decades, fundamental discoveries to describe and understand many of the phenomenological aspects of the physics beyond the quotidinity of physical events. In concert with the theoretical features, a significant evolution in the experimental equipment needed to investigate physical processes has been observed, leading to the characterisation and cataloguing of atomic and subatomic particles, based on interaction and symmetry arguments. Specifically, during the first part of the Sixties a series of new particles, or resonances, were discovered through experimental observations and, subsequently, described through a symmetry scheme in 1961 by Y. Ne'eman [1] and in 1962 by M. Gell-Mann [2]. The symmetry group involved was the SU(3) group, whose elements are 3×3 unitary matrices, with determinant 1, and allowed to depict the properties of the discovered resonances by means of its representations. In 1964, M. Gell-Mann [3] and G. Zweig [4] presented the basis for the *quark model*, conceiving hadrons as composite particles, understood as bound states of quarks and anti-quarks. The subsequent characterisation of quarks led, eventually, to the definition of some specific properties. Quarks are massive particles, which carry a fractional spin, and thus they belong to the fermion family. They realise electric interaction, as they carry a non-zero, fractional electric charge and, due to a non-zero color charge which is well described by the SU(3) symmetry group, quarks interact by means of strong interaction, mediated by gluons. Gluons were observed in laboratory in 1979, thanks to many collaborations and are massless particles belonging to the family of gauge bosons. In particular, gluons also carry a color charge, which allows for gluon-gluon interactions to take place. The discovery of color at the beginning of the Seventies as degree of freedom for quarks and gluons was possible thanks to a series of experiments, realised at SLAC, and a detailed theoretical analysis about cross-sections in election-positron collisions. Despite quarks and gluons carry a non-zero color charge, mesons and baryons represent, in the frame of color, singlet states, as they are characterised by a zero net color charge. Another property related to quarks is *flavour*, which allows to distinguish between six different kind of quarks and corresponding anti-quarks, which form three different groups based on the electro-weak symmetry group SU(2): Up and down quarks represent the family of light quarks, then strange and charme quarks, where the former is usually also considered as a light quark, and top and bottom quarks, which are the most massive ones and, in particular, the top quark was observed from experiments in 1995 at Fermilab. The main turning point in the frame of the progress of Quantum Chromodynamics coincides with the discovery of the asymptotic freedom in 1973 by D. J. Gross and F. Wilczek [5] and H. D. Politzer [6], which allowed to better understand the mechanisms connected to strong interaction, defining the confinement and deconfinement regimes based on the value of the coupling constant. Said Λ_{QCD} the tipical QCD scale, for energy higher than Λ_{QCD} the bound states of quarks are to be considered as systems of quasi-free particles and, vice-versa, for energies lower

than Λ_{QCD} confinement is observed. The investigation of the properties of the former scenario required a non-perturbative approach to be involved which could count on a new powerful tool as from 1974 [7], the *lattice*, where the action and the Lagrange equation of the physical system of interest can be redefined by means of a discretisation processes. Thus, phenomena as the chiral symmetry, which represents the core of this dissertation, together with the spontaneous chiral symmetry breaking, have been and keep on being largely investigated, based on specific strategies related to the developement of lattice Quantum Chromodynamics. Moreover, considering physical systems where temperature and density play a non-negligible role, Quantum Chromodynamics can be *enhanced* by introducing these *new parameters* in the theory, together with some of the specifics of statistical mechanics and thermodynamics. Indeed, thermal QCD represents the perfect combination of QCD and thermodynamics and the results obtained during the last sixty years from its investigations have been eventually collected in the so called *QCD phase diagram*, where different regions represent different states of the nuclear matter, as temperature and density are varied. Particularly interesting are the borders of the different regions, where proper phase transitions can take place. Focusing on the chiral symmetry, it is well known that different mechanisms contribute to its breaking, which can either be a spontaneous or explicit phenomenon. Most of all, the former characterises the chiral limit, where chiral phase transition has been investigated for a long time. In 1984 a first indication about its order in the chiral limit for $N_f = 2$ and $N_f \geq 3$ was given [8], which confirmed for the latter a first-order chiral phase transition whereas for the former two scenarios were possible, depending on the realisation of the $U_A(1)$ anomalous symmetry: Either a first and a second-order chiral phase transition could take place. This scenario was depicted at the beginning of the Nineties in the *Columbia plot*, for $N_f = 2+1$, where the value \2" refers to the degenerate mass of the up and down quarks whereas the value \1" refers to the mass of the strange quark. It is worth to say already at this stage that the Columbia plot is not a phase diagram: Indeed, it just collects the order of the chiral phase transition when the values of the masses of the quarks involved is varied, for $1 \leq N_f \leq 3$. In the Columbia plot, a first-order chiral region occupies the area of the two light-mass $(m_{ud}, m_s \longrightarrow 0)$ and heavy-mass $(m_{ud}, m_s \longrightarrow \infty)$ corners, with a crossover region in the middle-mass region. The boundary between a first-order region and the cossover one is defined by a Z_2 line of critical masses, which represents a second-order line in the 3d Ising universality class. Until 2021, the extension of the first-order chiral region towards $N_f = 2$ was subject to the constraint deriving from the aforementioned ambiguity: In case of a second-order phase transition, the Z_2 boundary delimiting the first-order chiral region in the light-mass corner has to scale towards the chiral limit ($m_{ud} = 0$) according to a tricritical scaling. Then, the first-order region collapses and a tricritical point appears for a specific m_s value. The latter represents the meeting point between a first-order triple line [1] and a second-order line. In a work from 2021 by F. Cuteri, O. Philipsen and A. Sciarra [9] the analytic continuation of the number of flavours N_f from integer to non-integer values for numerical purposes was proposed and successfully applied to investigate the tricritical scaling of the Z_2 boundary on the extended Columbia plot, for $N_\tau = \{4, 6, 8\}$. The results showed compatibility with a second-order chiral phase transition in the chiral limit and continuum limit for $N_f \in [2 : 7]$, thus resolving the puzzling scenario of $N_f = 2$. The inclusion in the theory of a non-zero chemical potential represents a challenging point, due to the sign problem which renders simulations not possible. One way to avoid it consists in producing the analytic continuation to imaginary values of

[1] A first-order triple line characterises the chiral limit of a first-order region and highlights the presence of a three phase coexistence.

chemical potentials on the lattice, which results in a periodicity of the partition function, known as Roberge-Weiss periodicity. The latter allows to extend the Columbia plot in a three-dimensional version including a third axis beyond the m_{ud} and m_s ones, namely the $(\mu/T)^2$ axis: Along this axis, positive values correspond to real chemical potentials whereas negative values are referred to imaginary chemical potentials. The Columbia plot corresponds to the $(\mu/T)^2 = 0$ plane and the Roberge-Weiss plane corresponds to the $(\mu/T)^2 = -(\pi/3)^2$ one. On a $N_\tau = 4$ lattice, the extension of the first-order chiral region and the crossover region from the Columbia plot to the Roberge-Weiss plane shows compatibility with inflation for the two first-order chiral regions, which corresponds to a shriking of the Crossover region, as the Roberge-Weiss plane is approached [2]. Another interesting topic concerning the study of the QCD phase diagram and the extension of the first-order chiral region consists in the investigation of the critical Z_2 boundary when approaching the strong coupling regime, for a fixed N_f value. From the theoretical point of view, the two regimes are differentiated by the values assumed by the gauge coupling parameter, $\beta = 2N_c/g^2$, where larger values of β correspond to lower values of g, and thus to a weak coupling regime, whereas the opposite scenario coincides with the strong coupling regime, where the limit of $\beta \longrightarrow 0$ coincides with the strong coupling limit. On the lattice, both the regimes can be investigated at different values of $\beta(a)$, which now depends on the lattice cutoff through $g(a)$. During the last forty years many techniques have been developed to gather information in the strong coupling regime and limit, making use of Monte Carlo simulations and mean field approximation techniques. The results for zero baryon chemical potential showed compatibility with a second-order chiral phase transition in the chiral limit and strong coupling limit. [3]
The first Chapter of this dissertation is entirely dedicated to the introduction to Quantum Chromodynamics and the way it can be regularised on the lattice. Also, the chiral symmetry and the features of the lattice will be discussed, with the possible discretisation techniques and their advantages and disadvantages when realising the continuum limit. Temperature and chemical potential will be included in the theory and discussed as well, thus introducing the thermal QCD. In the second Chapter, the main results which led to the definition of the QCD phase diagram the way we know it today will be recapitulated, both in the weak and strong coupling regimes, with the different methodology used. The Columbia plot will be discussed in details, when also the extension by means of a non-zero chemical potential is provided, leading to the three-dimensional Columbia plot. The two main projects which build up this dissertation will be introduced at the end of the Chapter:

- The first project is devoted to the analysis of the extenion of the first-order chiral region in the light-mass corner of the three-dimensional Columbia plot as a non-zero imaginary baryon chemical potential is introduced in the theory, as a natural continuation of the work presented in [9]. Indeed, the methodology and techniques involved in the realisation of this project are the same ones used in [9], but the region of interest corresponds to the plane $\mu_i = 0.81\pi T/3$, namely coincinding with the area of the three-dimensional Columbia plot with imaginary baryon chemical potential approximatively equal to the 80% of the Roberge-Weiss one;

- The second project consists of the investigation of the extension of the first-order chiral region in the strong coupling regime at zero chemical potential, constraining

[2] In this dissertation we will not deal with the Roberge-Weiss plan investigation, thus we just consider the region between the Columbia plot and the Roberge-Weiss plane.

[3] All these topics will be discussed in details in this dissertation.

the Z_2 boundary for $N_f = 4$ and $N_f = 8$. This analysis is done using $N_\tau = 2$ as lattice temporal extent, and the results will be compared to the extension of the first-order region for $N_\tau = \{4, 6, 8\}$, as well as to the already existing works in literature.

Simulations in this thesis work, performed to the aim of analysing the chiral phase transition, have been produced by means of Monte Carlo techniques, which allowed to measure the observables of interest, in particular the chiral consendate. The latter represents the (approximate) order parameter [4]. A series of Markov chains are produced using unimproved staggered fermions and the Rational Hybrid Monte Carlo algorithm (RHMC), which includes the Heat Bath, Metropolis and Molecular Dynamics algorithms, and the study of the chiral condensate is performed by means of the multi-Histogram method, using the standardised moments of a continuous probability distribution to analyse the distribution of the chiral condensate. The latter allow to locate the $\beta(a)$ value for which the phase transition takes place on the lattice, using the third standardised moment (skewness), whereas the order of the phase transition is obtained using the fourth stardardised moment (kurtosis). Moreover, using the finite-size scaling it is possible to obtain the critical mass belonging to the Z_2 critical boundary for each N_f value for which simulations have been performed. These details, together with an introduction to the software and code used to perform simulations and analysis will be discussed in Chapter 3. The last part of this dissertation is devoted to report the results obtained for both the investigations aforementioned. But before diving in this section, a preliminary investigation has been produced and it is about comparing the performances of two integrators, which are necessary when realising the Molecular Dynamics steps. In the code we use to perform simulations, the second-order minimum norm integrator (2MN), which belongs to the family of symplectic integrators, has been implemented since the first version released. Besides this integrator, the fourth-order minimum norm one has been implemented by the author of this work and its performances have been compared to the ones of the 2MN integrator, in order to establish which one was more suitable to be involved during the realisation of the two projects. A scrupulous analysis led to the choice on the 2MN integrator. At this point, the results about the project focused on the non-zero imaginary baryon chemical potential will be discussed and compared to the ones in [9]: for $N_\tau = 4$, a larger first-order chiral region is detected, whereas the opposite applies for $N_\tau = 6$ and $N_\tau = 8$. At any chance, the behaviour shown by the Z_2 bundaries at different lattice temporal extents is compatible with a tricritical scaling when extrapolating to the chiral limit, which provides interesting results to the chiral limit for $N_f \in [2 : 6]$. The last part of Chapter 4 contains the results of the investigation in the strong coupling regime. This project has proven to be challenging, due to the extemely reduced extension of the first-order chiral region, resulting the dominance of finite-size effects when small lattice spacings are involved. Furthermore, simulations turned out to be extremely time-consuming for some sets of parameters. Although these features limited the data collection process, the total amount is still enough to elaborate some conclusions, resulting in the identification of a critical mass on the Z_2 critical line for $N_f = 8$ and a rather more complicated scenario for $N_f = 4$: In this particular case, the finite-size scaling does not allow to distiguish between a Z_2 and a $O(2)$ scaling. At any chance, the investigation in the strong coupling regime does not provide information on the continuum limit, as simulations are performed on the the coarsest possible lattice.

[4] The reason why we mention here the adjective *approximate* will be clear in the dedicated Chapter.

Chapter 1

Lattice QCD

This Chapter provides a brief introduction to Lattice Quantum Chromodynamics, recalling some preparatory definitions and tools necessary to go through the rest of this work. First, we start by recapitulating the fundamentals of the QCD Lagrange equation and action in the continuum limit and their regularisation process on the lattice will be discussed. The gauge and fermion actions on the lattice are introduced and a deepening about the fermion staggered formulation in provided in Appendix A. The realisation of the continuum limit will be presented, which, unavoidably, includes the challenging *fermion doubling*. Other important topics to be introduced are the realisation of the gauge invariance on the lattice and, with particular importance, the chiral symmetry in Quantumm Chromodynamics, both in the continuum and lattice formulations, as it will represent the core of this thesis. The final sections of this Chapter will be dedicated to the introduction to Thermal Quantum Chromodynamics, including temperature and chemical potential in the theory, both in the continuum and lattice formulations. Most of the introductory theory in this Chapter can be found on common textbooks as [10], [11], [12] and [13], with some remarks based on [14]. Most of the deepenings are inspired to the precious and meticulous Ph. D.thesis of Dr. Alessandro Sciarra [15], which represented for the author of this work a pedagogical introduction to this interesting topic.

1.1 The Lagrange equation of the continuum QCD

The Lagrange equation of Quantum Chromodynamics in the continuum formulation for N_f number of quark flavours reads

$$\mathcal{L}_{QCD} = \sum_{f}^{N_f} \{\bar{\psi}_f(x)[\gamma_\mu(\partial^\mu + igA_\mu(x)) + M_f]\psi_f(x)\} - \frac{1}{4}\mathcal{F}_{\mu\nu}\mathcal{F}^{\mu\nu}, \tag{1.1}$$

where the dependence on the fermion fields is fully expressed in the first block, contained within curly brackets, whereas the second term depends on the gauge fields only. The fermion fields $\psi(x)$ and $\bar{\psi}(x) = \psi(x)^\dagger\gamma^0$ [1], contain the degrees of freedom associated with quarks and antiquarks: For a generic number of quark flavours, they can be represented a triplets of Dirac 4-spinor fields in the three-dimensional color space, based on the $SU(3)$ color group

$$\psi(x) = \begin{pmatrix} \psi_r(x) \\ \psi_g(x) \\ \psi_b(x) \end{pmatrix}, \qquad \bar{\psi}(x) = \begin{pmatrix} \bar{\psi}_r(x) \\ \bar{\psi}_g(x) \\ \bar{\psi}_b(x) \end{pmatrix}, \tag{1.2}$$

[1] The matrix γ_0 is the first of the four Dirac matrices in the Minkowski spacetime

where the indices r, g, b refer, respectively, to the three labels used for the color degrees of freedom, *red*, *green* and *blue*. Making use of indices, the objects in (1.2) can be rewritten in a more compact form,

$$\psi(x)^f_{\alpha,a}, \qquad\qquad \psi(x)^f_{\beta,b}, \tag{1.3}$$

where $\alpha, \beta = \{1, 2, 3, 4\}$ are the Dirac indices, $a, b = \{r, g, b\}$ are the color indices and f is the index referred to the number of quark flavours. The gluon degrees of freedom are contained in the gauge fields $A_\mu(x)$ [2]: The gluons, differently from the photons in QED, carry their own color charge and, consequently, they realise interactions with other gluons as well as with fermions, through the strong interaction. As already done for the fermion fields, the gauge fields can be expressed in a more compact formulation by making use of indices of indices: For a fixed Lorentz index value, the gluonic fields can be represented by 3×3 hermitian and traceless matrices as

$$A_\mu(x)_{ab},$$

where a, b are again the color indices. As we will see in the next section, the gauge fields are strictly related to the field strength tensor $\mathcal{F}_{\mu\nu}(x)$ contained in pure the gauge contribution to the Lagrange equation in equation (1.1). Indeed, this can be made explicit by

$$\mathcal{F}_{\mu\nu}{}^a(x) = \partial_\mu A^a_\nu(x) - \partial_\nu A^a_\mu(x) + g f_{abc} A^b_\mu(x) A^c_\nu(x), \tag{1.4}$$

where a, b, c are related to the color indices whereas f_{abc} are the structure constant of the SU(3) color group.

1.2 The continuum QCD action

The QCD action for one-flavour fermions in the Minkowski space is given, similarly to the Lagrange equation, as the sum of a fermion contribution and a pure gauge one,

$$\begin{aligned} S_{QCD} = S_F[\psi, \bar{\psi}, A] + S_G[A] = \int d^4x\, \bar{\psi}(x)[i\gamma_\mu \partial^\mu - M - g\gamma_\mu A^\mu(x)]\psi(x) + \\ - \frac{1}{4} \int d^4x\, \mathrm{Tr}[F_{\mu\nu}(x) F^{\mu\nu}(x)], \end{aligned} \tag{1.5}$$

where the trace in the pure gauge term is understood over the color space. In order to translate this action from the Minkowski to the Euclidean spacetime, two operations are needed:

- The Wick rotation [16], applied to the time components of the four-vector x and to the component $A_4(x)$ of the gauge fields,

$$x^0 \longrightarrow -ix_4, \qquad\qquad A^0(x) \longrightarrow iA_4(x),$$

- The replacement of the four Dirac γ matrices with the set of four Euclidean γ^E matrices

$$\gamma^E_4 = \gamma^0, \qquad\qquad \gamma^E_i = -i\gamma^i.$$

[2] The $\mu = \{1, 2, 3, 4\}$ index which comes with the definition of the gauge fields is the Lorentz index.

where the latter satisfy to the commutation relation

$$\{\gamma_\mu^E, \gamma_\nu^E\} = 2\delta_{\mu\nu}.$$

Following this prescription, the Euclidean QCD action can be obtained as

$$S_{QCD}^E[\psi, \bar{\psi}, A] = \int d^4x\ \bar{\psi}(x)[\gamma_\mu^E(\partial_\mu + igA_\mu(x)) + M]\psi(x) - \frac{1}{4}\int d^4x\ \mathrm{tr}[F_{\mu\nu}(x)F^{\mu\nu}(x)], \tag{1.6}$$

and, as easily verifiable, it is related to the action in equation (1.5) through the relation

$$S_F^E[\psi, \bar{\psi}] = -iS_F[\psi, \bar{\psi}].$$

In the next sections, the two contributions to the QCD action will be discussed, providing a starting point for the lattice discretisation methods.

1.2.1 The fermionic action

The first contribution to the action in (1.6) to be analysed is the fermion one. Taking into account equations (1.3) and (1.1), the dependence on the different degrees of freedom is made explicit through the indices [3]

$$S_F[\psi, \bar{\psi}, A] = \int d^4x\ \bar{\psi}(x)_{\alpha a}[(\gamma_\mu)_{\alpha\beta}(\delta_{ab}\partial_\mu + igA_\mu(x)_{ab}) + M\delta_{\alpha\beta}\delta_{ab}]\psi(x)_{\beta b}. \tag{1.7}$$

As one can observe, the fermion action of QCD shares the same structure of the QED one, when one-flavour fermions are considered: Thus, assuming the special unitary $SU(3)_c$ [4] as gauge group, the gauge invariance can be investigated for QCD the same way it is done for QED. We start by assuming $\Omega(x)$ and $\Omega^\dagger(x)$ to be matrices of the $SU(3)_c$ group, namely they are unitary 3×3 matrices, which satisfy to $\Omega^\dagger(x) = \Omega^{-1}(x)$, and such that $\det(\Omega(x)) = 1$. The application of elements of the $SU(3)_c$ to the fermion spinors $\psi(x)$ and $\bar{\psi}(x)$ provides a rotation of such objects, which transform as

$$\begin{aligned} \psi(x) &\longrightarrow \psi^{'}(x) = \Omega(x)\psi(x) = [1 + i\theta_a(x)T_a]\psi_a(x), \\ \bar{\psi}(x) &\longrightarrow \bar{\psi}^{'}(x) = \bar{\psi}^{'}(x)\Omega^\dagger(x) = \bar{\psi}_a(x)[1 - i\theta_a(x)T_a], \end{aligned} \tag{1.8}$$

where $\theta^a(x)$ are the eight, real parameters of the $SU(3)_c$ group, whereas T_a are the eight generators of the $SU(3)_c$ group, with $a = \{1, \cdots, 8\}$. The latter are represented by 3×3 complex, hermitian matrices which obey to the algebra

$$[T_a, T_b] = if_{abc}T_c, \tag{1.9}$$

and they are related to the eight Gell-Mann matrices λ_a through

$$T_a = \frac{\lambda_a}{2}. \tag{1.10}$$

In equation (1.9), f_{abc} are again the structure constants of the $SU(3)_c$ group introduced at the end of the previous section. The action in (1.7) also depends on the gauge fields $A_\mu(x)$: Then, in order to make equation (1.7) fully invariant under $SU(3)_c$ transformations, it is

[3] Since we are working in the Euclidean formulation, the label E has not been included but is implicity considered.

[4] Here, the c label is used just to stress that rotations are applied to the three-dimensional color space.

crucial to understand how the gauge fields transform under such rotations. Using (1.8) inside (1.7), the necessary condition to realise the invariance is provided by the constraint

$$D_\mu(x) = \partial_\mu + igA_\mu(x) = \partial_\mu + \Omega(x)^\dagger(\partial_\mu\Omega(x)) + ig\Omega(x)^\dagger A_\mu^{'}(x)\Omega(x), \tag{1.11}$$

where $D_\mu(x)$ goes under the name of *covariant derivative*. From this requirement, it comes straighforward for the gauge fields $A_\mu(x)$ to transform as

$$A_\mu(x) \longrightarrow A_\mu^{'}(x) = \Omega(x)A_\mu(x)\Omega(x)^\dagger + i(\partial_\mu\Omega(x))\Omega(x)^\dagger, \tag{1.12}$$

where $A_\mu^{'}(x)$ is still a hermitian, traceless matrix.

1.2.2 The gauge action

Besides the fermionic contribution to the action, also the pure gauge one

$$S_G[A] = \frac{1}{4}\int d^4x\ \mathrm{Tr}[\mathcal{F}_{\mu\nu}(x)\mathcal{F}^{\mu\nu}(x)], \tag{1.13}$$

is investigated. As already well known, the gauge fields carry color indices: This means they can be expressed as a combination of the Gell-Mann matrices

$$A_\mu(x) = \sum_a \lambda^a A_\mu^a(x). \tag{1.14}$$

Since these fields are the same ones appearing in the covariant derivative D_μ in equation (1.11), it is then possible to express the field strength tensor $\mathcal{F}_{\mu\nu}(x)$ as a function of the covariant derivative by means of the commutator

$$\mathcal{F}_{\mu\nu}(x) = -i[D_\mu(x), D_\nu(x)],$$

which, after some algebra, can be shown to correspond to the definition in (1.4). Under $SU(3)_c$ transformations, this object becomes

$$\mathcal{F}_{\mu\nu}(x) = \sum_a \lambda^a \mathcal{F}_{\mu\nu}{}^a(x) \longrightarrow \mathcal{F}_{\mu\nu}^{'}(x) = \Omega(x)\mathcal{F}_{\mu\nu}(x)\Omega^\dagger(x),$$

which realises the gauge invariance thanks to the presence of the trace over the color space in $S_G[A]$,

$$S_G[A^{'}] = \frac{1}{4}\int d^4x\ \mathrm{Tr}[\Omega\mathcal{F}_{\mu\nu}(x)\mathcal{F}^{\mu\nu}(x)\Omega^\dagger] = \frac{1}{4}\int d^4x\ \mathrm{Tr}[\mathcal{F}_{\mu\nu}(x)\mathcal{F}^{\mu\nu}(x)] = S_G[A].$$

This is a good point to recall how the coupling parameter g is introduced inside the action. If one ignores the structure of $S_G[A]$, then the latter could be built up by means of $\mathcal{F}_{\mu\nu}(x)$: Indeed, since the way it transforms under $SU(3)_c$ guarantees an easy realisation of the gauge invariance, one could assume as a good candidatate for the gauge action the following one

$$S_G[A] = \frac{1}{4g^2}\int d^4x\ \mathrm{Tr}[\mathcal{F}_{\mu\nu}(x)\mathcal{F}^{\mu\nu}(x)],$$

where the g factor appearing to the denominator in front of the integral permits the introduction of the gauge coupling. In fact, it can be absorbed in the definition of the gauge fields by rescaling them,

$$\frac{1}{g}A_\mu(x) \longrightarrow A_\mu(x),$$

which results in a redefinition of the covariant derivative as

$$D_\mu \longrightarrow \partial_\mu + igA_\mu(x).$$

Clearly, the factor g is undestood now as the gauge coupling, which accounts for the interacting term between the gluonic and fermionic fields in the action. It is worth to remark that the dependence of $\mathcal{F}_{\mu\nu}(x)$ on the gauge field is not linear, since a quadratic term appears: This is the responsible for the mixing of the color degrees of freedom, resulting in the gluons self-interactions, which is, in turn, the responsible for the color confinement.

1.3 Lattice discretization

The investigation of the theory of strong interaction led to the conclusion that a non-Abelian theory was needed in order to describe such phenomena. Although the discovery of the asymptotic freedom [5; 6] allowed to have a more complete view of the perturbative phenomenology of Quantum Chromodynamics, the nonperturbative effects that rose up at long distances were more complicated to be handled: The perturbative theory only gave interesting results at short distances, but could not be used to draw conclusion at longer ones. A big step towards the analysis of nonperturbative effects in QCD arrived once a discretised gauge theory in a discretised spacetime was proposed, laying the first stone of Lattice Quantum Chromodynamics by K. G. Wilson in 1974 [7]. An interesting work by K. G. Wilson from 2005 [17] retraced the initial stages that led to the realisation of the Lattice Gauge Theory, necessary to understand the main ideas behind this revolutionary introduction. Discretization, as a process, involves both the fermionic and gluonic fields, provided the introduction of the lattice spacing (or lattice cutoff) a, and, after a suitable redefinition of the fields, a discretized S_{QCD} on the lattice can be formulated. The inverse to this process consists in performing the continuum limit, starting from the discretised action on the lattice, and is less trivial to be achieved: A naive realisation of the latter could result in errors, since the aim of this limit is to recover the original, continuum action that was used as a starting point. In the next sections we will show how equations (1.7) and (1.13) can be discretised, starting from the discretised verison of the fermionic and gauge fields on the lattice. At the end, we will show how the correct continuum QCD action can be obtain once the continuum limit is realised for both the object.

1.3.1 The fermionic action on the lattice

The action of non-interacting Dirac fermions in the Minkowski space is a useful starting point to understand how the discretisation of the fermion fields on the lattice is realised. This is given as

$$S_F[\psi,\bar{\psi}] = \int d^4x\ \bar{\psi}(x)(i\gamma^\mu\partial_\mu - M)\psi(x), \tag{1.15}$$

which can be rewritten by making explicit the Dirac indices $\alpha,\beta = \{1,2,3,4\}$, as

$$\begin{aligned} S_F[\psi,\bar{\psi}] &= \sum_{\alpha,\beta}\int d^4x\ d^4y\ \bar{\psi}_\alpha(x)K_{\alpha\beta}(x,y)\psi_\beta(y) \\ &= \sum_{\alpha,\beta}\int d^4x\ d^4y\ \bar{\psi}_\alpha(x)(i\gamma^\mu\partial_\mu - M)_{\alpha\beta}\delta^{(4)}(x-y)\psi_\beta(y), \end{aligned} \tag{1.16}$$

where γ^μ are again the four Dirac gamma matrices satisfying to anticommutation relation

$$\{\gamma^\mu, \gamma^\nu\} = 2g^{\mu\nu}.$$

Before proceeding, we recall that realising the field quantisation means to promote the fermion fields $\psi(x)$ and $\bar{\psi}(x)$ to the operators $\Psi(x)$, $\bar{\Psi}(x) = \Psi^\dagger(x)\gamma^0$, which satisfy to the equal time anticommutation relation

$$\{\Psi_\alpha(\mathbf{x}, t), \Psi^\dagger_\beta(\mathbf{y}, t)\} = \delta_{\alpha\beta}\delta^{(3)}(\mathbf{x} - \mathbf{y}),$$

where α, β are again the Dirac indices. The matrix term $K_{\alpha\beta}(x, y)$ between the two fermionic fields in (1.16) reads

$$K_{\alpha\beta}(x, y) = (i\gamma^\mu\partial_\mu - M)_{\alpha\beta}\delta^{(4)}(x - y), \tag{1.17}$$

and it is connected to the fermion propagator[5] through the expectation value over the ground state $|\Omega\rangle$ of the considered physical system,

$$iK^{-1}_{\alpha\beta}(x, y) = \langle\Omega|\mathbf{T}(\Psi_\alpha(x)\Psi_\beta(y))|\Omega\rangle. \tag{1.18}$$

In the latter, the operator $\mathbf{T}$ represents the time-ordering operation performed over the fermion field operators. Recalling that the fields $\psi(x)$ and $\bar{\psi}(x)$ obey to the Grassmann algebra, the path integral representation of (1.18) can be obtained,

$$iK^{-1}_{\alpha\beta}(x, y) = \frac{\int D\bar{\psi}D\psi\ \psi_\alpha(x)\bar{\psi}_\beta(x)e^{iS_F[\psi,\bar{\psi}]}}{\int D\bar{\psi}D\psi\ e^{iS_F[\psi,\bar{\psi}]}}, \tag{1.19}$$

where the integration measure $D\bar{\psi}D\psi$ is defined as

$$D\bar{\psi}D\psi = \prod_{\alpha,x} d\bar{\psi}_\alpha(x) \prod_{\beta,y} d\psi_\beta(y). \tag{1.20}$$

Now, a good point to introduce the lattice formalism has been reached. Moving from the Minkowski to the Euclidean spacetime again, the fermionic action (1.15) becomes

$$S^E_F[\psi, \bar{\psi}] = \int d^4x\ \bar{\psi}(x)(\gamma^E_\mu\partial_\mu + M)\psi(x). \tag{1.21}$$

In the process of discretisation, a generic four-vector in the continuum euclidean spacetime is replaced by a discretised one $n = (n_0, n_1, n_2, n_3)$, where the n_0 corresponds to the time component, whereas $n_{i,i=1,2,3}$ refers to the space components. The lattice is characterised by a set of *lattice sites*, as in figure (1.1), which correspond to points in the four-dimensional discretised spacetime, identified by a quadruplet n. Each of this points lays at a distance a from the first neighbors, which goes under the name of *lattice spacing*, or *lattice cutoff*. Given this brief introduction to the lattice structure, the measure in equation (1.22) can be discretised,

$$\prod_{\alpha,x} d\psi_\alpha(n) \prod_{\beta,y} d\psi_\beta(y) \longrightarrow \prod_{\alpha,n} d\bar{\psi}_\alpha(na) \prod_{\beta,m} d\psi_\beta(ma), \tag{1.22}$$

where the continuum variables x, y have been replaced by the discretised ones na, ma, being n and m the number of lattice sites along the two different directions. In general,

[5] This is the fermion two-point function.

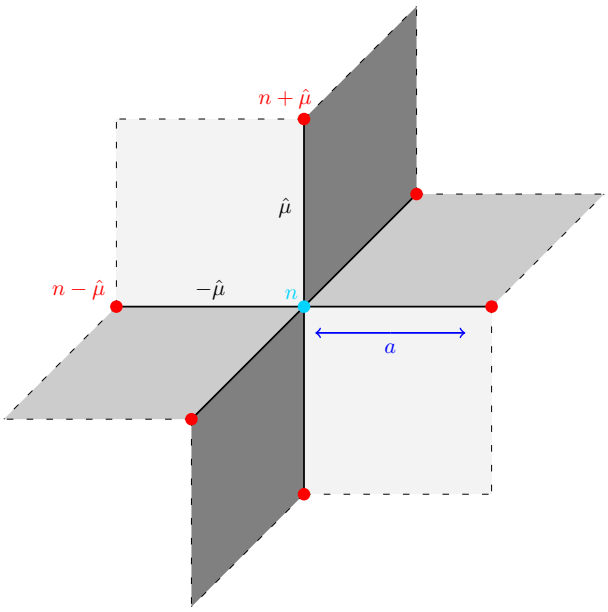

Figure 1.1: *Three dimensional representation of a lattice site in blue, identified by the quadruplet* $n = (n_0, n_1, n_2, n_3)$*, connected to the first neighbors in red, identified by the quaduplets* $n \pm \mu$*, along the different* $\hat{\mu}$ *directions.*

the objects evaluated on the lattice are adimensional objects: This means that a further step must be done when translating the dimensional quantities of the real world to the discretised one. The idea is to redefine the quantities inside equation (1.15) by taking into account their dimensions in mass units and, since the dimension of the lattice spacing a corresponds to the inverse of a mass[6], then on the lattice one observes that

$$\begin{aligned} M &= \frac{1}{a}\hat{M}, \\ \bar{\psi}_\alpha(x) &= \frac{1}{a^{3/2}}\hat{\bar{\psi}}_\alpha(n), \\ \psi_\alpha(x) &= \frac{1}{a^{3/2}}\hat{\psi}_\alpha(n), \\ \partial_\mu\psi_\alpha(x) &= \frac{1}{a^{5/2}}\hat{\partial}_\mu\hat{\psi}_\alpha(n), \end{aligned} \tag{1.23}$$

where the terms which come with the *hat* represent the adimensional ones on the lattice. The last one in the list can be made explicit through the symmetric discretisation as

$$\hat{\partial}_\mu\hat{\psi}_\alpha(n) = \frac{1}{2}[\hat{\psi}_\alpha(n+\hat{\mu}) - \hat{\psi}_\alpha(n-\hat{\mu})]. \tag{1.24}$$

Here, the quantity $\hat{\mu}$ represents a direction on the lattice: Starting from a lattice site n, the four-vector $(n \pm \hat{\mu})$ identifies the first neighbours, as in figure (1.1). In the discretised Euclidean spacetime the integration over the four-dimensional spacetime will be replaced by a summation over the n sites

$$\int d^4x \longrightarrow a^4 \sum_n,$$

[6]This is true in mass units.

and, finally, the discretised version of the fermion action in equation (1.15) becomes

$$\begin{aligned} S_F^{\text{latt}}[\hat{\psi},\bar{\hat{\psi}}] &= \sum_{n,m}\sum_{\alpha,\beta}\bar{\hat{\psi}}(n)K_{\alpha\beta}(n,m)\hat{\psi}(m) \\ &= \sum_{n,m}\sum_{\alpha,\beta}\sum_{\mu}\bar{\hat{\psi}}(n)\left[\frac{1}{2}(\gamma_\mu)_{\alpha\beta}\left[\delta_{m,n+\hat{\mu}}-\delta_{m,n-\hat{\mu}}\right]+\hat{M}\delta_{mn}\delta_{\alpha\beta}\right]\hat{\psi}(m), \end{aligned} \tag{1.25}$$

where the sum over μ is unterstood over the different directions on the lattice [7]. Using equation (1.22), the matrix $K_{\alpha\beta}(n,m)$ from equation (1.25) can be linked to the fermionic propagator on the lattice the same way it was done in equation (1.19), in the continuum formulation. Using the path integral representation on the lattice, one can find

$$\langle\hat{\Psi}_\alpha(n)\bar{\hat{\Psi}}_\beta(m)\rangle = \frac{\int D\bar{\hat{\psi}}D\hat{\psi}\ \hat{\psi}_\alpha(n)\bar{\hat{\psi}}_\beta(m)e^{-S_F}}{\int D\bar{\hat{\psi}}D\hat{\psi}\ e^{-S_F}} \tag{1.26}$$

and, after some algebra, it can be shown that

$$\langle\hat{\Psi}_\alpha(n)\bar{\hat{\Psi}}_\beta(m)\rangle = K^{-1}_{\alpha\beta}(n,m). \tag{1.27}$$

One can further act on the fermion propagator by making it explicit in the lattice momentum space. From the theory, we know that the δ function in momentum space can be obtained as

$$\delta_{nm} = \int_{-\pi}^{\pi}\frac{d^4\hat{k}}{(2\pi)^4}\ e^{i\hat{k}(n-m)}. \tag{1.28}$$

For ease of convenience, two quantities $K_{\alpha\rho}(n,l)$ and $K^{-1}_{\rho\beta}(l,m)$ can be defined in the momemtum space,

$$K_{\alpha\rho}(n,l) = \int_{-\pi}^{\pi}\frac{d^4\hat{k}}{(2\pi)^4}\tilde{K}_{\alpha\rho}(\hat{k})e^{i\hat{k}(n-l)}, \tag{1.29}$$

$$K^{-1}_{\rho\beta}(l,m) = \int_{-\pi}^{\pi}\frac{d^4\hat{k}}{(2\pi)^4}\tilde{H}_{\rho\beta}(\hat{k})e^{i\hat{k}(l-m)}, \tag{1.30}$$

and, starting from the following relation in the lattice coordinate space

$$\sum_{\rho,l}K_{\alpha\rho}(n,l)K^{-1}_{\rho\beta}(l,m) = \delta_{\alpha\beta}\delta_{nm}, \tag{1.31}$$

it can be shown that, making use of equations (1.28), (1.29) and (1.30), the following identity holds in the momentum space,

$$\sum_{\rho}\tilde{K}_{\alpha\rho}(\hat{k})\tilde{H}_{\rho\beta}(\hat{k}) = \delta_{\alpha\beta}. \tag{1.32}$$

The result in equation (1.32) can be used as a starting point to derive the explicit form of the fermion propagator: Indeed, from equation (1.32) it is enough to invert the quantity $\tilde{K}_{\alpha\rho}(\hat{k})$ in order to obtain the operator $\tilde{H}_{\rho\beta}(\hat{k})$. Taking into account equation (1.25) and using

$$\tilde{K}_{\alpha\rho}(\hat{k}) = \sum_{n-m}K_{\alpha\rho}(n,m)e^{i\hat{k}(n-m)}, \tag{1.33}$$

[7] This index must not be confused with the index in the γ_μ matrices, which counts the Dirac matrices

it can be shown, after some algebra that

$$\langle \hat{\Psi}_\alpha(n)\bar{\hat{\Psi}}_\beta(m)\rangle = \int_{-\pi}^{\pi} \frac{d^4\hat{k}}{(2\pi)^4} \frac{[-i\sum_\mu \gamma_\mu \sin(\hat{k}_\mu) + \hat{M}]_{\alpha\beta}}{\sum_\mu \sin^2(\hat{k}_\mu) + \hat{M}^2}. \tag{1.34}$$

So far we have obtained the the discretised fermion action in (1.25) and the fermion propagator in the lattice momentum space in (1.34). The next step consists in checking whether the original action in the continuum formulation can be obtained once the continuum limit is applied to the aforementioned quantities, which basically consists in performing the limit $a \longrightarrow 0$. We will deeply investigate this topic in the next sections, with a short focus on the most difficult tasks hidden behind this procedure.

1.3.2 The continuum limit of the fermion action

The realisation of the continuum limit appears to be a naive operation. Indeed, given the results in equations (1.25) and (1.34), the only thing to be demonstrated is that the corresponding results in the continuum limit can be recovered once the limit $a \longrightarrow 0$ is performed, namely as the lattice cutoff vanishes. Starting from the action (1.25), this can be done by making explicit the dependence of the fermion fields on the lattice spacing a,

$$\hat{\psi}_\alpha(n) = a^{3/2}\psi_\alpha(an), \qquad \hat{\psi}_\alpha(n \pm \hat{\mu}) = a^{3/2}\psi_\alpha(an \pm a\hat{\mu}). \tag{1.35}$$

A Taylor expansion can be done for the second term in equation (1.35), for small enough lattice spacings a, along the different $\hat{\mu}$ directions

$$a^{3/2}\psi_\alpha(an \pm a\hat{\mu}) = a^{3/2}\big[\psi_\alpha(na) + a\partial_{\hat{\mu}}\psi_\alpha(na) + \mathcal{O}(a^2)\big],$$

where the derivative $\partial_{\hat{\mu}}$ is understood as a directional derivative. These results, included in equation (1.25), allow to express the action as an explicit function of the lattice spacing, and it can be shown that, after performing the continuum limit, the fermionic action of non-interacting fermions in the continuum formulation is recovered

$$\lim_{a\longrightarrow 0} S_F^{\text{latt}}[\psi,\bar{\psi}] = S_F[\psi,\bar{\psi}].$$

Using the same strategy of above, one can attempt to recover the fermionic propagator in the continuum formulation, from the discretised one. We can start from the correlation function

$$\langle \psi_\alpha(x)\bar{\psi}_\beta(y)\rangle = \lim_{a\longrightarrow 0} \frac{1}{a^3} G_{\alpha\beta}\Big(\frac{x}{a}, \frac{y}{a}, aM\Big),$$

where the fraction $1/a^3$ comes out once we make explicit the dependence of the fermionic fields and the integration measure on the lattice spacing a. Consider $G_{\alpha\beta}(n,m,\hat{M}) = K^{-1}_{\alpha\beta}(n,m)$ and taking into account equation (1.34), after some algebra the continuum limit of (1.34) can be obtained,

$$\langle \psi_\alpha(x)\bar{\psi}_\beta(y)\rangle = \lim_{a\longrightarrow 0} \int_{-\frac{\pi}{a}}^{\frac{\pi}{a}} \frac{d^4p}{(2\pi)^4} \frac{[-i\sum_\mu \frac{\sin(p_\mu a)}{a} + M]_{\alpha\beta}}{\sum_\mu \frac{\sin^2(p_\mu a)}{a^2} + M^2} e^{ip(x-y)}. \tag{1.36}$$

At first glance, making use of the limit

$$\lim_{a\longrightarrow 0} \frac{\sin(p_\mu a)}{a} = p_\mu \tag{1.37}$$

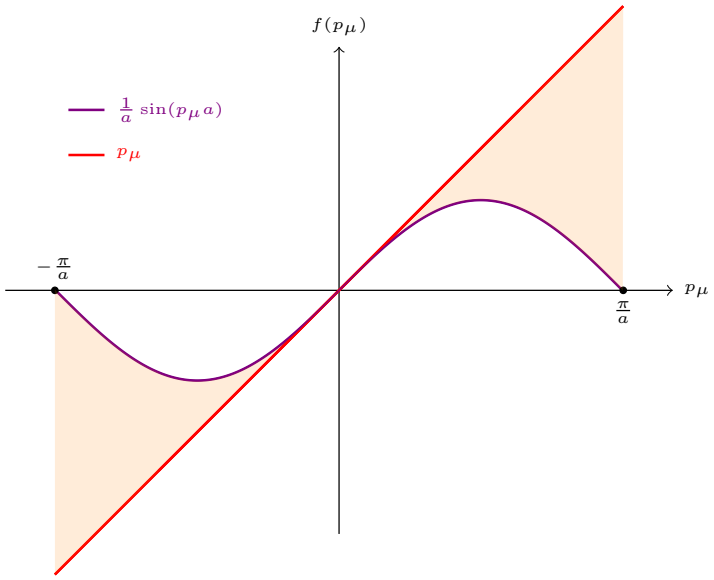

Figure 1.2: *Plot of the sinusodial term inside equation* (1.36) *(violet), as a function of the moment* p_μ *in the Brillouin zone contained in the range* $[-\pi/a, \pi/a]$*, and the linear function* $f(p_\mu) = p_\mu$ *(red).*

in equation (1.36) could sound correct. In reality, this operation results quite dangerous: In fact, as can be seen in figure (1.2), the approximation of the sinusoidal functions in equation (1.36) with the result of the limit (1.37) is only possible in the proximity of the origin of the axis, and, moving towards the boundaries of the integration area, the two functions become more and more distant. Then, another strategy must be involved, in order to avoid gross errors.

Before continuing, it is worth to focus on the number of poles of the fermionic porpagator on the lattice (1.34). In the continuum limit, considering massless fermions, the propagator presents one pole for $p_\mu = 0$, which corresponds to a single fermion, described by the Dirac operator in the fermionic action. Moving to the discretised momentum space and considering again a massless fermion scenario, equation (1.36) becomes

$$\langle \psi_\alpha(x)\bar{\psi}_\beta(y)\rangle = \lim_{a\longrightarrow 0}\int_{-\frac{\pi}{a}}^{\frac{\pi}{a}} \frac{d^4p}{(2\pi)^4}\frac{[-i\sum_\mu \frac{\sin(p_\mu a)}{a}]_{\alpha\beta}}{\sum_\mu \frac{\sin^2(p_\mu a)}{a^2}} e^{ip(x-y)}. \tag{1.38}$$

Comparing the integrand in equation (1.38) to the plot in figure (1.2), one observes that $a^{-1}\sin(p_\mu a)$ vanishes for $p_\mu = \{0, \pi/a, -\pi/a\}$, namely it vanishes at the borders of the Brillouin zone. If we consider the four dimensional spacetime, it can be shown after solving the integral in equation (1.36) that the overall number of poles is sixteen: Of these poles, one corresponds to the expected $p_\mu = 0$ whereas the other fifteen are produced as the sinusoidal function vanishes at the boundaries. But what are the consequences of such result in the continuum limit?

For $a \longrightarrow 0$, the continuum propagator receives contribution from sixteen different fermion-like excitations, corresponding to sixteen different fermions described by the Dirac

operator. This result has been obtained considering as a starting point the fermionic action in equation (1.15), where the Dirac operator describes one, single fermion. The process of multiplication of the number of fermions in the continuum limit is called *doubling* and the excess fermions at issue are called *doublers*. The origin of such phenomenon has been deeply investigated and is directly connected to the use of a symmetric discretisation for the derivative in equation (1.24), which spans over a lattice distance of $2a$ rather than just a. At all events, using a non-symemtric discretised derivative would bring, as aftermath, to a non-renormalizable lattice gauge theory, which is a major problem: Making reference to the Nielsen-Ninomiya *no-go* theorem [18], it is not possible to have a doublers-free theory which simultaneously guarantees chiral symmetry, locality and invariance under translation.

Another interesting point is the conservation of the axial current. From the studies of [19], Bell and Jackiw [20] for continuum QED at the end of the Sixties, it was demonstrated that the axial current was not conserved[8]. But, using a regularised theory on the lattice implies the conservation of the axial current, for any lattice cutoff a. In their work from 1981 [21], L. K. Karsten and J. Smith stated that the extra fermions which raise up when using the naive method to discretise the fermion action presents axial charges such that the axial anomaly corresponding to the $p_\mu = 0$ pole is cancelled in the continuum limit: This means that doubling can be understood as a compensation phenomenon. A detaild analysis of the topic is provided in Chapter 4 of [10]. This represents a new starting point in the way to obtain a correct discretisation of the fermionic action on the lattice. In the next sections we will focus on the Wilson and staggered fermion formulations.

1.3.3 Wilson fermions

A first strategy which leads to doublers cancelation was finalised in 1975 by K. G. Wilson [22], which basically consisted in adding a second derivative-like term inside the action in equation (1.25). In order to preserve the physics from any unwanted contamination, the new term has to vanish both for $p_\mu = 0$ and in the continuum limit. The Wilson fermion action reads

$$S_F^W[\bar{\hat{\psi}}, \hat{\psi}] = S_F^{\text{latt.}}[\bar{\hat{\psi}}, \hat{\psi}] - \frac{r}{2} \sum_n \bar{\hat{\psi}}(n) \hat{\Box} \hat{\psi}(n), \tag{1.39}$$

where r is a real parameter known as *Wilson parameter*, whereas the operator $\hat{\Box}$,

$$\hat{\Box}\hat{\psi}(n) = \sum_\mu \left[\hat{\psi}(n + \hat{\mu}) + \hat{\psi}(n - \hat{\mu}) - 2\hat{\psi}(n) \right],$$

is the discretised version of the d'Alembert operator, corresponding to the extension of the Laplace operator to four dimensions. Making this object explicit in equation (1.39), one obtains

$$\begin{aligned} S_F^W[\bar{\hat{\psi}}, \hat{\psi}] = & \sum_n \left\{ \frac{1}{2} \sum_\mu \left[\bar{\hat{\psi}}(n) \gamma_\mu \left(\hat{\psi}(n + \hat{\mu}) - \hat{\psi}(n - \hat{\mu}) \right) \right] + \bar{\hat{\psi}}(n) \hat{M} \hat{\psi}(n) \right\} + \\ & - \sum_n \sum_\mu \; r \left\{ \frac{1}{2} \bar{\hat{\psi}}(n) \hat{\psi}(n + \hat{\mu}) + \bar{\hat{\psi}}(n) \hat{\psi}(n - \hat{\mu}) - \bar{\hat{\psi}}(n) \hat{\psi}(n) \right\} \\ & = \sum_{n,m} \bar{\hat{\psi}}_\alpha(n) K^W_{\alpha\beta}(n, m) \hat{\psi}_\beta(m) \end{aligned} \tag{1.40}$$

[8] The scientific world refers to this phenomenon as *the axial anomaly*.

where the matrix $K^W_{\alpha\beta}(n,m)$ reads

$$K^W_{\alpha\beta}(n,m) = -\frac{1}{2}\sum_\mu \left[(r-\gamma_\mu)_{\alpha\beta}\delta_{m,n+\hat{\mu}} + (r+\gamma_\mu)_{\alpha\beta}\delta_{m,n-\hat{\mu}}\right] + \left(\hat{M}+4r\right)\delta_{nm}\delta_{\alpha\beta}. \quad (1.41)$$

At this point, taking into account the transformations in equation (1.23) for $\hat{\psi}(n)$ and $\hat{\bar{\psi}}(n)$ and considering that $\hat{\Box} = a^2\,\Box$, it is easy to show that the new term [9], which acts as a mass-like term inside the action, will vanish as the continuum limit is approached, since it is linear in a and, therefore, the correct continuum action is recovered. In order to check what happens when the continuum limit is applied the fermionic propagator, the same prescription as in the previous sections can be used. The result one obtains after some algebra is

$$\langle\psi_\alpha(x)\bar{\psi}_\beta(y)\rangle = \lim_{a\longrightarrow 0}\int_{-\frac{\pi}{a}}^{\frac{\pi}{a}} \frac{d^4p}{(2\pi)^4}\frac{[-i\gamma_\mu\tilde{p_\mu}+M(p)]_{\alpha\beta}}{\sum_\mu \tilde{p_\mu}^2 + M(p)^2}e^{ip(x-y)}, \quad (1.42)$$

with

$$\tilde{p_\mu} = \frac{1}{a}\sin(p_\mu a), \qquad M(p) = M + \frac{2r}{a}\sum_\mu \sin^2\left(\frac{a}{2}p_\mu\right). \quad (1.43)$$

At this stage, some conclusions can be drawn. From equation (1.43), when investigating the momentum region in the proximity of the origin of the axis in figure (1.2) where the pole at $p_\mu = 0$ takes place, one observes that that $M(p) \longrightarrow M$ for vanishing a. On the contrary, in the proximity of the borders of the Brillouin zone at $p_\mu = \pm\pi/a$, the Wilson term diverges for $a \longrightarrow 0$, thus resulting in heavier doublers, which decouple from the theory. Hence, the theory described after adding the Wilson term to the action is a doubler-free one.

Nevertheless, one must be careful about the symmetries: Indeed, in the chiral limit when $M \longrightarrow 0$, one obtains that $M(p) \neq 0$. This translates in the explicit breaking of chiral symmetry even for massless fermions, which results in big aftermaths. For instance, when performing simulations in the proximity of the chiral limit, a fine-tuning of the $\hat{M}$ has to be involved, in order to understand which values it assumes as the chiral limit is approached. For a more detailed discussion about the discrete symmetry of when Wilson fermions are involved we refer to Chapter 5 of [11].

1.3.4 Staggered fermions

The cancellation of the doubling problem when using the Wilson formulation led to the explicit breaking of the chiral symmetry, due to the nature of the Wilson term in the action. In this section, another approach will be discussed, which has the merit of restoring the chiral symmetry in the chiral limit through a recombination of the fermionic degrees of freedom on the lattice. This formulation goes under the name of *staggered formulation* and the fundamental idea behind it was introduced in 1975 by J. Kogut and L. Susskind [23]: It consists in reducing the extension of the Brillouin zone in figure (1.2), where it is clear that the extra poles at the boundaries produce the unwanted doubling. This can be done through a redefinition of the fermion fields, whose effect resides in the distribution of the fermionic degrees of freedom over a lattice, whose lattice spacing reads $2a$. In

[9] We can refer to this term as Wilson term.

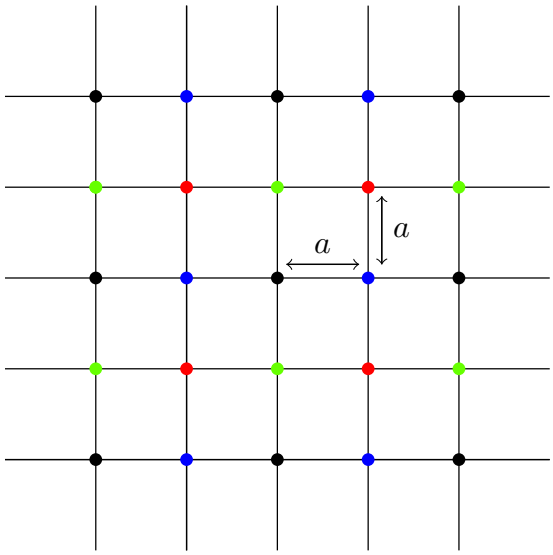

Figure 1.3: *Two dimensional lattice with four fermonic degrees of freedom distributed on different lattice sites, distinguished by four different colours. The distance between two identical degrees of freedom equals twice the lattice spacing a.*

general, on a d-dimensional lattice the number of total sites reads 2^d and the fermionic fields come with $2^{d/2}$ components. Supposing the lattice to consist of a series of different hypercubes, the extension of the Brillouin zone can be reduced by a factor $1/2$ and the different degrees of freedom can be distributed on the different sites. This can be easily seen when moving to a two-dimensional lattice, as in figure (1.3), where identical degrees of freedom are located on sites at a distance $2a$. From the theoretical point of view, this can be done by suitably changing the fermion fields variables on the lattice: Staggered transformations are defined as

$$\begin{aligned} \hat{\psi}(n) &= T(n)\chi(n), \\ \hat{\bar{\psi}}(n) &= \bar{\chi}(n)T^{\dagger}(n), \end{aligned} \tag{1.44}$$

where in a generic d dimensional space the $T(n)$ and $T^{\dagger}(n)$ operators are $2^{d/2} \times 2^{d/2}$ matrices which take the form

$$T(n) = \gamma_1^{n_1}\gamma_2^{n_2}\cdots\gamma_d^{n_d}, \tag{1.45}$$

being $\{n_1, n_2, \cdots n_d\}$ the labels of the d dimensional lattice sites. The *hat* above the $\chi(n)$, $\bar{\chi}(n)$ fields has been avoided for ease of notation, but, clearly, the fields belong to the lattice, thus being adimensional. The operators in equation (1.45) satisfy to the identity

$$T^{\dagger}(n)\gamma_\mu T(n \pm \hat{\mu}) = \eta_\mu(n)\mathbb{1}, \tag{1.46}$$

which can be easily proven by taking into account the commutation relations between the γ matrices. The objects $\eta_\mu(n)$ are complex numbers which act like a multiplicative phase to the identity matrix, and, depending on the Dirac index μ, the values they assume are

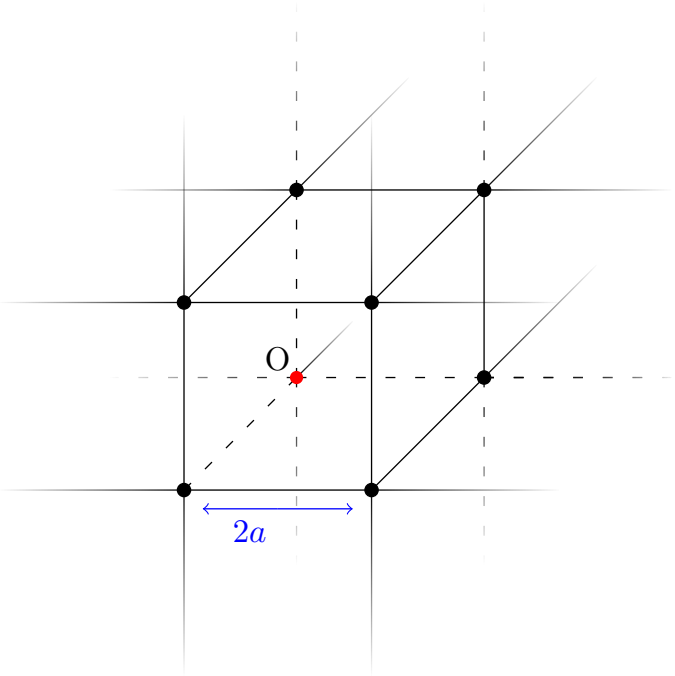

Figure 1.4: *Three dimensional representation of a lattice hypercube, whose origin falls in the site labelled with O.*

$$\begin{cases} \eta_1(n) = 1, \\ \eta_\mu(n) = (-1)^{\sum_{\nu<\mu}}, \qquad \text{for} \quad \mu \neq 1. \end{cases} \tag{1.47}$$

We now recall the discretised fermion action we derived in equation (1.25),

$$S_F^{\text{latt.}}[\psi, \bar{\psi}] = \frac{1}{2} \sum_{\mu,n} \left[\hat{\bar{\psi}}(n) \gamma_\mu \hat{\psi}(n + \hat{\mu}) - \hat{\bar{\psi}}(n) \gamma_\mu \hat{\psi}(n - \hat{\mu}) \right] + \hat{M} \sum_n \hat{\bar{\psi}}(n) \hat{\psi}(n).$$

After the application of the transformations in equation (1.44), the action becomes diagonal in the Dirac space,

$$\begin{aligned} S_F^{\text{latt.}}[\psi, \bar{\psi}] = \frac{1}{2} \sum_{\mu,n} \Big[& \bar{\chi}_\alpha(n) T^\dagger_{\alpha\beta}(n) (\gamma_\mu)_{\beta\gamma} T(n + \hat{\mu})_{\gamma\rho} \, \chi(n + \hat{\mu})_\rho + \\ & - \bar{\chi}_\alpha(n) T^\dagger_{\alpha\beta}(n) (\gamma_\mu)_{\beta\gamma} T(n - \hat{\mu})_{\gamma\rho} \, \chi(n - \hat{\mu})_\rho \Big] + \\ & + \hat{M} \sum_n \bar{\chi}_\alpha(n) T^\dagger_{\alpha\beta}(n) T_{\beta\gamma}(n) \, \chi_\gamma(n), \end{aligned} \tag{1.48}$$

where the Dirac indices have been made explicit and a sum over the same indices is understood. Making use of equation (1.46), the action finally becomes

$$\begin{aligned} S_F^{\text{latt.}}[\psi,\bar{\psi}] =& \frac{1}{2}\sum_{\mu,n}\Big[\eta_\mu(n)\bar{\chi}_\alpha(n)\chi(n+\hat{\mu})_\rho\delta_{\alpha\rho} - \eta_\mu(n)\bar{\chi}_\alpha(n)\chi(n-\hat{\mu})_\rho\delta_{\alpha\rho}\Big] + \\ &+ \hat{M}\sum_n \delta_{\alpha\rho}\bar{\chi}_\alpha(n)\chi(n)_\rho. \end{aligned} \tag{1.49}$$

Since the *remnant* of the γ_μ matrices is represented by the phases η_μ, the two indices α, ρ are not to be undestood as effective Dirac indices, and, in principle, the sum over these indices can run from 1 to a generic integer l. Without loss of generality, we can set $\alpha, \rho = 1$ and the complete staggered action will be

$$S_F^{\text{stagg.}}[\psi,\bar{\psi}] = \frac{1}{2}\sum_{\mu,n}\eta_\mu(n)\Big[\bar{\chi}(n)\chi(n+\hat{\mu}) - \bar{\chi}(n)\chi(n-\hat{\mu})\Big] + \hat{M}\sum_n \bar{\chi}(n)\chi(n), \tag{1.50}$$

which describes a lattice theory with only one degree of freedom per lattice site n, since the $\bar{\chi}(n)$ and $\chi(n)$ fields do not carry Dirac indices but only color indices. Making use of the symmetric derivative on the lattice, as introduced in equation (1.24), we finally obtain

$$S_F^{\text{stagg.}}[\psi,\bar{\psi}] = \sum_{\mu,n}\Big[\eta_\mu(n)\bar{\chi}(n)\hat{\partial}_\mu\chi(n)\Big] + \hat{M}\sum_n \bar{\chi}(n)\chi(n). \tag{1.51}$$

The overall results of this application consist in the reduction of the total number of degrees of freedom by a factor 1/4 in a four-dimensional spacetime. When the continuum limit is performed, the fermionic action reads

$$\lim_{a\longrightarrow 0} S_F^{\text{stagg.}}[\hat{\psi},\hat{\bar{\psi}}] = \sum_{\alpha,\beta}\sum_f \int d^4x\ \bar{\psi}^f_\alpha(x)(\gamma_\mu\partial_\mu + M)_{\alpha\beta}\psi^f_\beta(x), \tag{1.52}$$

where α, β are the four Dirac indices whereas the index f refers to the *tastes* of the fermions in the continuum [10]. The four, degenerate fermion fields described by (1.52) are obtained through the linear combination of the sixteen degrees of freedom on the sixteen lattice sites which belong to a hypercube. Thus, the coordinates of $\psi^f_\alpha(x)$ in the continuum limit trace back to a single hypercube on the lattice. In order to show that the limit in equation (1.52) holds, one has to deal with the hypercube geometry on the lattice and the actual lattice spacing used. This will be discussed in more detail in Appendix A to this work, where also the fermionic two-point function will be briefly discussed, when staggered formulation is used.

As in the previous subsection, it is worth to focus again on the fate of the chiral symmetry in the chiral limit, when staggered fermions are used in the fermion action. Analogously to what happened for the Wilson formulation, also in this case a term which explicitly breaks the chiral symmetry comes out, as shown in equation (A.12) in Appendix A. Nevertheless, it can be shown that a $U(1) \times U(1)$ remnant of the chiral symmetry survives when the staggered formulation is involved, as the chiral limit is performed. As a consequence, this allows to extrapolate results in the chiral limit from simulations without necessity of a fine tuning on the values that the mass term M can assume.

[10] The tastes are the degrees of freedom associated with the doublers when the continuum limit is performed.

1.3.5 Gauge fields and gauge invariance on the lattice

In section 1.2.1 we obtained the discretisation of the fermion action on the lattice, starting from the one in the continuum formulation in (1.15), and we saw it describes a one-flavoured, non-interacting system of Dirac fermions. So far, the gauge fields have not been considered: At this point, it becomes necessary to deal with them on the lattice, both to describe the pure gauge theory and the strong interaction in QCD. Let's consider the continuum QCD action in the Euclidean formulation in equation (1.6), which is reported here for ease of convenience,

$$S^E_{\mathrm{QCD}}[\psi,\bar{\psi},A] = \int d^4x\ \bar{\psi}(x)[\gamma^E_\mu(\partial_\mu + iA_\mu(x)) + M]\psi(x) - \int d^4x\ \mathrm{tr}[F_{\mu\nu}(x)F^{\mu\nu}(x)],$$

and, for the fermionic contribution, suppose to have a system of non-interacting fermions on the lattice, whose action, making use of the Wilson discretisation, reads

$$\begin{aligned} S^W_F[\psi,\bar{\psi}] = -\frac{1}{2}\sum_n\sum_\mu \Big[\bar{\hat{\psi}}(n)(r-\gamma_\mu)\hat{\psi}(n+\hat{\mu}) + \bar{\hat{\psi}}(n+\hat{\mu})(r+\gamma_\mu)\hat{\psi}(n)\Big] + \\ + (\hat{M}+4r)\sum_n \bar{\hat{\psi}}(n)\hat{\psi}(n). \end{aligned} \tag{1.53}$$

Differently from the assumption made in the previous sections, we now consider the fermionic fields $\hat{\psi}(n)$ and $\bar{\hat{\psi}}(n)$ to be N-dimensional vectors in the color space. In this way, these fields can be represented as

$$\hat{\psi}^a(n) = \begin{bmatrix} \psi_1(n) \\ \psi_2(n) \\ \vdots \\ \psi_N \end{bmatrix}, \qquad \bar{\hat{\psi}}^a(n) = \Big[\bar{\hat{\psi}}_1(n), \bar{\hat{\psi}}_2(n), \cdots, \bar{\hat{\psi}}_N\Big], \tag{1.54}$$

with the a index running from 1 to N. From now on, the *hat* on the fermionic fields will be understood. By performing rotations of the fermionic fields under global $SU(N)$ transformations Ω,

$$\begin{aligned} \psi(n) &\longrightarrow \psi^{'}(n) = \Omega\ \psi(n), \\ \bar{\psi}(n) &\longrightarrow \bar{\psi}^{'}(n) = \bar{\psi}(n)\ \Omega^\dagger, \end{aligned}$$

equation (1.53) is essentially left invariant. At this stage, the matrices Ω and Ω^{-1} do not depend on the lattice site where the fermionic fields were defined: This is the reason why we refer to this invariance as global $SU(N)$ invariance. At any chance, it is important to also explore how this invariance can be realised when the $SU(N)$ elements become also dependent on n, namely when local transformations are performed on the fermionic fields. In this regard, we can focus on (1.53) and observe that, introducing the n-dependent $G(n)$ elements of the $SU(N)$ group, the local invariance is guaranteed for the mass-like term

$$\bar{\psi}(n)\psi(n) \longrightarrow \bar{\psi}^{'}(n)\psi^{'}(n) = \bar{\psi}(n)\ \Omega^\dagger(n)\ \Omega(n)\ \psi(n) = \bar{\psi}(n)\psi(n),$$

whereas it does not apply to the term which originated from the symmetric derivative

$$\bar{\psi}(n)\psi(n+\hat{\mu}) \longrightarrow \bar{\psi}^{'}(n)\psi^{'}(n+\hat{\mu}) = \bar{\psi}(n)\ \Omega^\dagger(n)\ \Omega(n+\hat{\mu})\ \psi(n+\hat{\mu}),$$

since the transformations take place at different lattice sites. One way to realise the invariance also for the latter consists in introducing a new field $U_\mu(n)$ which is located on

the lattice *links* bewtween different lattice sites, where μ represents the direction on the lattice along which it is defined. The presence of this new object must guarantee

$$\bar{\psi}(n)U_\mu(n)\psi(n+\hat{\mu}) \longrightarrow \bar{\psi}^{'}(n)U^{'}_\mu(n)\psi^{'}(n+\hat{\mu}) = \bar{\psi}(n)\ \Omega^\dagger(n)U^{'}_\mu(n)\Omega(n+\hat{\mu})\ \ \psi(n+\hat{\mu}),$$

such that, under Ω rotations, one obtains

$$\begin{aligned} U_\mu(n) &\longrightarrow U^{'}_\mu(n) = \Omega(n)U_\mu(n)\Omega^\dagger(n+\hat{\mu}), \\ U^\dagger_\mu(n) &\longrightarrow U^{'\,\dagger}_\mu(n) = \Omega(n+\hat{\mu})U_\mu(n)\Omega^\dagger(n+\hat{\mu}). \end{aligned}$$

This strategy would make (1.53) fully invariant under local $SU(N)$ transformations. The $U_\mu(n)$ field can be introduced in the theory as element of the $SU(N)$ group,

$$U_\mu(n) = e^{i\phi_\mu(n)}, \tag{1.55}$$

where the matrix given in the exponent are elements of the Lie algebra of the $SU(N)$ group. Equation (1.53) can be rewritten as

$$\begin{aligned} S^W_F[\psi,\bar{\psi}] = -\frac{1}{2}\sum_n\sum_\mu \Big[\bar{\hat{\psi}}(n)(r-\gamma_\mu)U_\mu(n)\hat{\psi}(n+\hat{\mu}) + \bar{\hat{\psi}}(n+\hat{\mu})(r+\gamma_\mu)U^\dagger_\mu(n)\hat{\psi}(n)\Big] + \\ + (\hat{M}+4r)\sum_n \bar{\hat{\psi}}(n)\hat{\psi}(n), \end{aligned} \tag{1.56}$$

which is now invariant under $SU(N)$ transformations, namely it is gauge invariant. The object in equation (1.55) is the equivalent of the *Schwinger line integral* in the continuum formulation

$$U(x,y) = \mathbf{P}\Big[e^{ig\int d_{x_\mu}A_\mu(x)}\Big],$$

which is necessary to realise the gauge invariance of the QCD action, where the label $\mathbf{P}$ here refers to the path ordering in the path integral formulation. Now, one can proceed to the three dimensional color space: The theory presented so far is valid in this scenario, assuming the transformations to belong to the $SU(3)$ gauge group. Since in the continuum limit the fermionic action we need to recover is the following

$$S_F[\psi,\bar{\psi},A] = \int d^4x\ \bar{\psi}(x)[\gamma_\mu(\partial_\mu + igA_\mu(x)) + M]\psi(x), \tag{1.57}$$

the field in (1.55) must depend on the gauge fields $A_\mu(n)$. To this aim, we can define

$$\phi_\mu(n) = agA_\mu(n), \tag{1.58}$$

where a is the lattice cutoff, and, for small values of a, the field $U_\mu(n)$ can be expanded in series as

$$U_\mu(n) = \mathbb{1} + iagA_\mu(n) + \mathcal{O}(a^2). \tag{1.59}$$

At this point, we make use of the latter inside equation (1.56) and, recalling the dimensional fields and the explicit dependence on the cutoff a, it can be shown that the correct continuum limit is achieved,

$$\lim_{a\longrightarrow 0} S^W_F[\psi,\bar{\psi},A] = \int d^4x\ \bar{\psi}(x)\Big[\gamma_\mu\Big(\partial_\mu + igt^A A^A_\mu(x)\Big) + M\Big]\psi(x), \tag{1.60}$$

where the label A is the color index, with a sum over it understood, since it has been made use of equation (1.14).

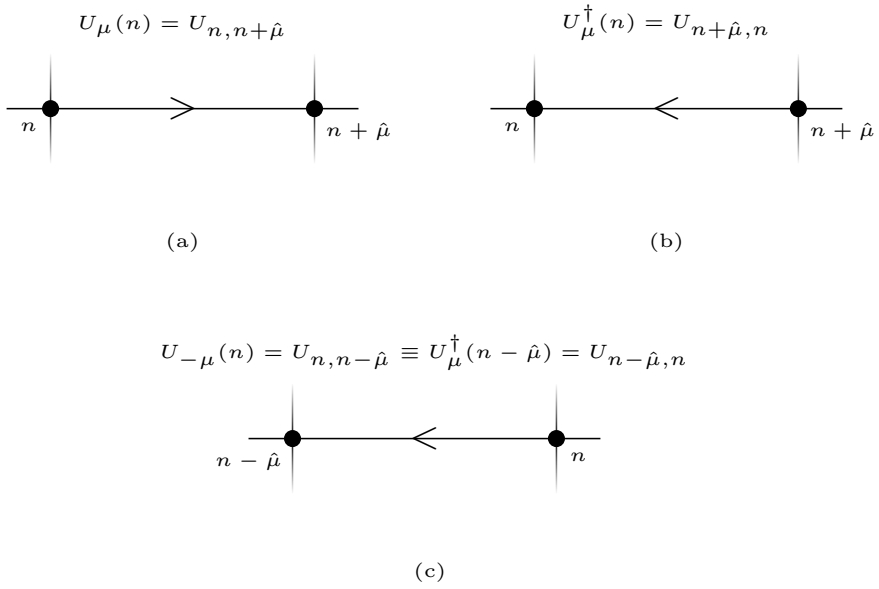

Figure 1.5: *Graphic representation of the gauge links on a two dimensional lattice of spacing a. The naming of the fields depends on the position of the two sites which are connected.*

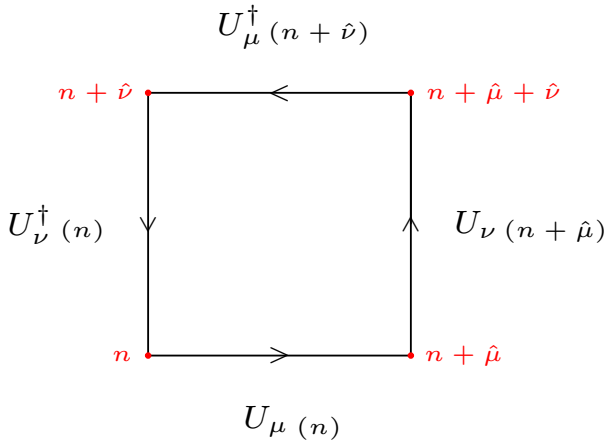

Figure 1.6: *Closed loop on a 2D lattice, corresponding to the plaquette in* (1.62).

1.3.6 The gauge action on the lattice

The last piece of the QCD action to be discretised on the lattice is the pure gauge one, which we report here once more,

$$\int d^4x \ \mathrm{tr}[F_{\mu\nu}(x)F^{\mu\nu}(x)]. \tag{1.61}$$

The idea to keep in mind is strictly connected to what has been said in section 1.3.5, since we want to build up a discretised gluonic action which is invariant under $SU(3)$ gauge transformations and, furthermore, we need it to only depend on the link variables in (1.55). The easiest possible choice which satisfies to the two requirements falls in a lattice loop generated by the multiplication of four link variables,

$$U_{\mu\nu}(n) = U_\mu(n)U_\nu(n+\hat{\mu})U^\dagger(n+\hat{\nu})U^\dagger_\nu(n), \tag{1.62}$$

which goes under the name *plaquette*. From the representation given in figure (1.5) it is easy to map the plaquette on a squared loop on the lattice, where the $\hat{\mu}$ direction is understood as the orizontal one whereas the $\hat{\nu}$ direction refers to the vertical one. Using equations (1.55) and (1.58) in equation (1.62), the plaquette can be made explicitly dependent on the gauge fields $A_\mu(n)$ as follows

$$U_{\mu\nu}(n) = e^{igaA_\mu(n)}e^{igaA_\nu(n+\hat{\mu})}e^{-igaA_\mu(n+\nu)}e^{-igaA_\nu(n)}. \tag{1.63}$$

Although this object may seem easy to handle, it is important to remark that, being QCD a non-abelian gauge theory, the correct ordering of the fields in the exponents is fundamental, since they do not satisfy to commutation. As a result, when working with (1.63), the Baker-Campbell-Hausdorff formula must be involved,

$$\exp(A)\exp(B) = \exp\Big(A + B + \frac{1}{2}[A,B] + \frac{1}{12}\{[A,[A,B]] + [B,[B,A]]\}\Big),$$

being A and B generic operators. Making use of the latter and performing a suitable Taylor expansion when considering a sufficiently small lattice spacing, the plaquette can be redefined: This result becomes the starting point to define the discretised gauge action on the lattice. Indeed, taking the real part of the trace over the color space of the plaquette, the gauge action on the lattice reads

$$\begin{aligned}
\mathrm{Re}(U_{\mu\nu}(n)) &= \mathrm{Re}\Big\{\mathrm{Tr_c}\Big[\mathbb{1} - \frac{1}{2}g^2a^4F_{\mu\nu}(n)F_{\mu\nu}(n) + \mathcal{O}(a^5)\Big]\Big\} \\
&\approx N_c - \frac{1}{2}g^2a^4\mathrm{Tr_c}\Big[F_{\mu\nu}(n)F_{\mu\nu}(n)\Big] \\
&= N_c\Big\{1 - \frac{g^2}{2N_c}\mathrm{Tr_c}\Big[F_{\mu\nu}(n)F_{\mu\nu}(n)\Big]\Big\},
\end{aligned} \tag{1.64}$$

and it can be to shown that, in order to obtain in the continuum limit the action in equation (1.61), the correct lattice gauge action must be

$$S_G^{\mathrm{latt.}}[A] = \frac{2N_c}{g^2}\sum_n\sum_{\mu<\nu}\Big[1 - \frac{1}{N_c}\,\mathrm{Re}(\mathrm{Tr_c}U_{\mu\nu}(n))\Big]. \tag{1.65}$$

The factor which multiplies the two summations is $\beta = (2N_c)/g^2$ and goes under the name of *lattice gauge coupling*. As it depends on the running coupling g, it provides information on the *intensity* of the strong interaction, in the frame of weak and strong

coupling regimes. [11] Both the regimes will be presented in detail in the next Chapter.

As a conclusion to this section, it is worth to say some words on the integration measure. Computing quantities as, for instance, correlation functions in the path integral formulation involves integration measures on the fermionic fields and gauge fields. The latter, in QCD, also carry color degrees of freedom and, in particular, the integration measure DU depends on the eight parameters of the $SU(3)$ group through $A_\mu(x)$. This feature results in more quantum fluctuations introduced in the theory, which can undermine the validity of the gauge invariance. In general, when performing a $SU(3)$ group integration, the Haar measure reads

$$DU = \prod_w J(\alpha_w)(d\alpha_w), \qquad\qquad d\alpha_w = \prod_{A=1}^{8} d\alpha_w^A, \tag{1.66}$$

where α_w corresponds to the eight group parameters of the $SU(3)$ group on which the w^{th} gauge coupling depends and the Jacobian $J(\alpha_w)$ can be computed by means of gauge invariance arguments. For a detailed discussion about this topic and how to treat the integration measure DU we refer, in particular, to [11].

1.4 The chiral symmetry

The chiral symmetry is for sure one of the most important topics concerning Quantum Chromodynamics. The process of explicit and spontaneous breaking, as well as restoring of this symmetry has big implication in the standard model of particles and is a fundamental part of the thermodynamics of QCD, thanks to the analysis of the phase transition associated with this phenomenology. In this section we will recall the fundamentals of the chiral symmetry in continuum QCD and we will mostly refer to chapter 7 of [11].

1.4.1 Chiral symmetry in continuum QCD

Suppose to have, for ease of notation, the Lagrange equation of a system of fermions with one single flavour in the Euclidean spacetime

$$\mathcal{L}[\psi, \bar{\psi}, A] = \bar{\psi}(x)\Big[\gamma_\mu\Big(\partial_\mu + igA_\mu(x)\Big) + M\Big]\psi(x), \tag{1.67}$$

and suppose to transform the fermionic fields under $U(1)$ global rotations as

$$\begin{aligned} \psi(x) &\longrightarrow \psi^{'}(x) = e^{i\alpha\gamma_5}\psi(x), \\ \bar{\psi}(x) &\longrightarrow \bar{\psi}^{'}(x) = \bar{\psi}(x)e^{i\alpha\gamma_5}, \end{aligned} \tag{1.68}$$

where α is a real constant parameter whereas γ_5 is the fifth Dirac matrix. The rotations in (1.68) act on the *chiral space* and leave, in the massless fermions limit, the Lagrange

[11] From now on, in order to make explicit the dependence on the lattice cutoff, we will refer to the running coupling as g_0, whereas g will be used for the continuum theory one.

equation (1.67) completely unaffected

$$\begin{aligned}\mathcal{L}'[\psi,\bar{\psi},A] &= \bar{\psi}'(x)\Big[\gamma_\mu\Big(\partial_\mu + igA_\mu(x)\Big)\Big]\psi'(x)\\ &= \bar{\psi}(x)e^{i\alpha\gamma_5}\Big[\gamma_\mu\Big(\partial_\mu + igA_\mu(x)\Big)\Big]e^{i\alpha\gamma_5}\psi(x)\\ &= \bar{\psi}(x)e^{i\alpha\gamma_5}\gamma_\mu\Big(\mathbb{1} + i\alpha\gamma_5\Big)\Big(\partial_\mu + igA_\mu(x)\Big)\psi(x)\\ &= \bar{\psi}(x)e^{i\alpha\gamma_5}\Big(\mathbb{1} - i\alpha\gamma_5\Big)\gamma_\mu\Big(\partial_\mu + igA_\mu(x)\Big)\psi(x)\\ &= \bar{\psi}(x)e^{i\alpha\gamma_5}e^{-i\alpha\gamma_5}\gamma_\mu\Big(\partial_\mu + igA_\mu(x)\Big)\psi(x) = \mathcal{L}[\psi,\bar{\psi},A],\end{aligned} \tag{1.69}$$

where the commutation relations between the γ matrices have been used. This does not apply when the fermion masses are restored: Indeed, the effect (1.68) on the new term consists in the explicit breaking of the chiral symmetry,

$$\bar{\psi}(x)M\psi(x) \longrightarrow \bar{\psi}'(x)M\psi'(x) = e^{i2\alpha\gamma_5}\bar{\psi}(x)\psi(x). \tag{1.70}$$

Going back to the massless fermions case, the effects of the chiral symmetry can also be highlighted though a split in the Lagrange equation equation (1.67). Defining two projection operators,

$$\begin{aligned}P_R &= \frac{\mathbb{1}+\gamma_5}{2},\\ P_L &= \frac{\mathbb{1}-\gamma_5}{2},\end{aligned} \tag{1.71}$$

where L refers to *left-handed* and R to *right-handed*, the fermionic fields can be defined as combination,

$$\psi(x) = \psi_R(x) + \psi_L(x), \qquad\qquad \bar{\psi}(x) = \bar{\psi}_L(x) + \bar{\psi}_R(x),$$

where $\psi_{R,L}(x) = P_{R,L}\psi(x)$ and $\bar{\psi}_{R,L}(x) = \bar{\psi}(x)P_{L,R}$, since in $\bar{\psi}(x) = \psi^\dagger(x)\gamma_0$. Using these definitions in the Lagrange equation of massless fermions, one obtains

$$\begin{aligned}\mathcal{L}[\psi,\bar{\psi},A] &= \Big(\bar{\psi}_L(x) + \bar{\psi}_R(x)\Big)\Big(\partial_\mu + igA_\mu(x)\Big)\Big(\psi_R(x) + \psi_L(x)\Big)\\ &= \bar{\psi}_R(x)(\partial_\mu + igA_\mu)\psi_R(x) + \bar{\psi}_L(x)(\partial_\mu + igA_\mu)\psi_L(x),\end{aligned} \tag{1.72}$$

and observe that the contributions coming from the mixed terms vanish. Considering $\gamma_\mu(\partial_\mu + igA_\mu(x)) = D$, this can be easily shown as follow:

$$\begin{aligned}\bar{\psi}(x)_R D\,\psi_L(x) &= \bar{\psi}(x)\Big(\frac{\mathbb{1}-\gamma_5}{2}\Big)D\Big(\frac{\mathbb{1}-\gamma_5}{2}\Big)\psi(x)\\ &= \frac{1}{4}\Big[\bar{\psi}(x)D\psi(x) - \bar{\psi}(x)\gamma_5 D\psi(x) +\\ &\quad - \bar{\psi}(x)D\gamma_5\psi(x) + \bar{\psi}(x)\gamma_5 D\gamma_5\psi(x)\Big]\\ &= \frac{1}{4}\Big[\bar{\psi}(x)D\psi(x) - \bar{\psi}(x)\gamma_5 D\psi(x) +\\ &\quad + \bar{\psi}(x)D\gamma_5\psi(x) - \bar{\psi}(x)D\psi(x)\Big] = 0,\end{aligned} \tag{1.73}$$

and the analogue applies to the other term. Restoring the mass term in the Lagrange equation and using the left and right-handed fields and, observing that $P_L P_R = P_R P_L = 0$, one obtains

$$\Big(\bar{\psi}_R(x) + \bar{\psi}_L(x)\Big)M\Big(\psi_R(x) + \psi_L(x)\Big) = M\Big[\bar{\psi}_L(x)\psi_R(x) + \bar{\psi}_R(x)\psi_L(x)\Big]. \tag{1.74}$$

From equation (1.73) we see that the chiral symmetry is realised when

$$\{\gamma_5, D\} = 0, \tag{1.75}$$

and, since the chiral symmetry is only valid in the massless fermions case, we refer to the limit $M \longrightarrow 0$ as to the *chiral limit*.

This discussion can now be extended to the N_f flavours case by simply considering the fermionic fields as N_f dimensional vectors of spinors in the flavour space and the mass term as a $N_f \times N_f$ diagonal matrix M in the flavour space. The list of the possible transformations that one can apply in the flavour space are the following

- Vector transformations

$$\psi(x) \longrightarrow \psi^{'}(x) = e^{i\alpha T_i}\psi(x), \qquad \bar{\psi}(x) \longrightarrow \bar{\psi(x)}^{'} = \bar{\psi}(x)e^{-i\alpha T_i}, \tag{1.76}$$

$$\psi(x) \longrightarrow \psi^{'}(x) = e^{i\alpha \mathbb{1}}\psi(x), \qquad \bar{\psi}(x) \longrightarrow \bar{\psi(x)}^{'} = \bar{\psi}(x)e^{-i\alpha \mathbb{1}}, \tag{1.77}$$

- Axial vector or chiral transformations

$$\psi(x) \longrightarrow \psi^{'}(x) = e^{i\alpha\gamma_5 T_i}\psi(x), \qquad \bar{\psi}(x) \longrightarrow \bar{\psi(x)}^{'} = \bar{\psi}(x)e^{i\alpha\gamma_5 T_i}, \tag{1.78}$$

$$\psi(x) \longrightarrow \psi^{'}(x) = e^{i\alpha\gamma_5 \mathbb{1}}\psi(x), \qquad \bar{\psi}(x) \longrightarrow \bar{\psi(x)}^{'} = \bar{\psi}(x)e^{i\alpha\gamma_5 \mathbb{1}}, \tag{1.79}$$

where $T_{i,i=1,2,\cdots,Nf^2-1}$ are the generators of the $SU(N_f)$ group and $\mathbb{1} \equiv \mathbb{1}_{N_f \times N_f}$. The chiral symmetry in the chiral limit is realised for N_f flavours as

$$SU(N_f)_L \times SU(N_f)_R \times U(1)_V \times U(1)_A, \tag{1.80}$$

where A refers to axial $U(1)$ symmetry, V to the vectorial one and, as for the one flavour case, L and R are the left and right-handed $SU(N_f)$ symmetries, provided again the split in the Lagrange equation. Recalling the results from [19] and [20], the axial current was shown not to be conserved, which corresponds to an explicit breaking of the $U(1)_A$ symmetry from equation (1.79), which reduces the complete chiral symmetry to

$$SU(N_f)_L \times SU(N_f)_R \times U(1)_V.$$

Furthermore, if the system of massless fermions is promoted to a system of N_f degenerate fermions in the flavour space, the mass matrix will read $M = \mathrm{diag}(m, m, \cdots, m)$, and the total symmetry will reduce to

$$SU(N_f)_V \times U(1)_V,$$

since the $SU(N_f)_R \times SU(N_f)_L$ symmetry reduces to the $SU(N_f)_V$ one, due to the explicit breaking of the symmetry given by transformations in equation (1.78). The $SU(N_f)_V$ symmetry corresponds to the *isospin symmetry* generalised to N_f flavours, and is realised since also in the degenerate mass scenario the transformations (1.76) guarantee a symmetry of the Lagrange equation. For $N_f = 2$ this can be easily shown by taking into account the first Pauli matrix σ_1 and apply the transformations (1.76) to the mass term in equation (1.67). At any chance, for $N_f = 2$ the latter can be considered a good symmetry: Indeed, the masses for the up and down quarks, namely the *light* quarks, up-to-date with the latest results presented by the Particle Data Group [24], are

$$m_u = 2.16^{0.49}_{-0.26}\mathrm{MeV}, \qquad m_d = 4.67^{0.48}_{-0.17}, \mathrm{MeV},$$

which show a really light explicit breaking of the chiral symmetry, being these masses much close to each other. This is particulary eye-catching if $m_{u,d}$ are compared to the masses of the other quarks. The last step is to consider a system of non-degenerate N_f fermions: In this scenario, the matrix M will still be diagonal, but every entry will assume a different value. As a result, the total chiral symmetry reduces to

$$U_V(1) \times U_V(1) \times \cdots \times U_V(1),$$

which is a chain of N_f transformations of the type of equation (1.77), which guarantees the conservation of the baryonic number.

So far, we have investigated the phenomenology which leads to the explicit breaking of the chiral symmetry, but there is more to say about. Since the explicit breaking of the chiral symmetry for $N_f = 2$ is light, one would expect to find traces of the symmetry in the standard model of particles, and, in particular, a degeneracy between protons and neutrons and their partner with negative parity. From [24] we know their masses to be

$$m_P = 938.27208816(29)\ \text{MeV}, \qquad m_N = 939.56542052(54)\text{MeV},$$

but for the resonance $m_{N(1/2)^-} = 1535$ MeV [24], which results in a difference in mass of approximatively 600 MeV. This suggests that another mechanism must be taken into account, a besides the explicit breaking of the chiral symmetry. Between 1960 and 1961, Y. Nambu [25] and J. Goldstone [26] laid the basis for the known Goldstone model, which explains the phenomenology of the spontaneous breaking of continuum symmetries of the Lagrange equation. Assuming to have a Lagrange equation $\mathcal{L}$ invariant under some symmetry transformations, two possible scenarios can be realised concerning a given energy level of the system described:

- If the energy level is non-degenerate, then the corresponding eigenstate is invariant under the same symmetry transformations of $\mathcal{L}$ and it is unique;
- If the energy level is degenerate, then the corresponding eigenstates are not unique but they are linearly related through the same symmetry transformations which make $\mathcal{L}$ invariant.

Assuming to have the second realisation, and assuming to work with the vacuum state of the theory, if one eigenstate is selected among the possible degenerate ones, such state will not satisfy to the original symmetry of the Lagrange equation. This process takes the name of *spontaneous symmetry breaking* and allows to characterise the vacuum state by means of a quantity which does not vanish and does not satisfy to the symmetry of the Lagrange equation. Concerning the chiral symmetry in QCD, this object is the *chiral condensate*

$$\langle \bar{\psi}(x)\psi(x) \rangle, \tag{1.81}$$

which behaves as a mass-like term and does not satisfy to the invariance under chiral transformations. This can be used as order parameter to investigate the chiral phase transitions in QCD as will be widely shown in the next Chapters: Indeed, in the chiral limit, one observes that

$$\begin{aligned} \langle \bar{\psi}(x)\psi(x) \rangle = 0 &\longrightarrow \text{chirally broken phase}, \\ \langle \bar{\psi}(x)\psi(x) \rangle \neq 0 &\longrightarrow \text{ symmetric phase}. \end{aligned}$$

For a more detailed discussion about the Goldston Model we refer to Chapter 18 of [14].

1.4.2 Chiral symmetry on the lattice

After the introduction to the chiral symmetry in the continuum formulation of QCD, it is necessary to go through the steps to realise it correctly on the lattice as well. As it has been pointed out in sections (1.3.2), (1.3.3) and (1.3.4), the no-go theorem provides some important prescription which act as guidelines in evaluating the properties of a discretised action. We have seen that the Wilson and staggered fermion actions both break explicitly the chiral symmetry in different ways, even in the chiral limit, due to the additional terms inside the actions that survive as $\hat{M} \longrightarrow 0$, and this can be understood as the *duty* to be paid in order to get rid of the doublers in the continuum limit. In a discretised formulation, one could say that the lattice version of the condition in equation (1.75) is not satisfied by both the discretisations we have presented. For more details about different fermionic discretisation connected to the chiral symmetry realisation on the lattice we refer to the literature. Also, the chiral condensate in equation (1.81) must be defined on the lattice in order to use it in simulations, when the chiral phase transition must be analysed. In the following of this work we will show some useful techniques to this aim.

1.5 The continumm limit of QCD

In the last sections we have seen how regularising a gauge theory on the lattice can be difficult a diffult task. The definiton of fields and QCD action on the lattice does not guarantee, a priori, to recover the correct continuum limit actions if a set of precautions is not involved. At any chance, in many cases, the dependence of the physical objects on the lattice spacing a is not explicitly given: In this situation, obtaining a continuum gauge theory from its discretised version requires to deal with the critical points of the theory. An example comes from the two-points function for free scalar fields on the lattice,

$$\langle \hat{\phi}(n)\hat{\phi}(m)\rangle = \int_{-\pi}^{\pi} \frac{d^4\hat{k}}{(2\pi)^4} \frac{e^{i\hat{k}\cdot(n-m)}}{4\sum_\mu \sin^2(\hat{k_\mu}/2) + \hat{M}^2},$$

whose associated correlation length on the lattice is inversely proportional to the lattice mass $\hat{M}$. Recalling the physical dimension of the latter, $\hat{M} = aM$, the lattice correlation length reads

$$\hat{\xi} = \frac{1}{aM}, \tag{1.82}$$

which diverges as the continuum limit is performed,

$$\lim_{a\longrightarrow 0} \hat{\xi} = \infty.$$

The divergence of the lattice correlation length is connected to the presence of a critical point of the theory, where the continuum limit is realised. Thus, a parameter can be used to *control* the lattice correlation function as the lattice spacing vanishes. This represents a fundamental idea for gauge theories: Given a specific parameter on which a lattice regularised theory depends, if the physical system described does not show critical points for any value of the parameter, then no continuum gauge theory can actually be described. Considering Quantum Chromodynamics, the realisation of the continuum limit can be done by means of the lattice running coupling, g_0, on which the lattice correlation length depends. Let's assume to have a specific, critical value of the running coupling, $g_0^{\text{crit}} = g_0'$,

where the theory exhibits criticality. Based on the previous discussion, the presence of the g_0' point suggests that the continuum limit can be realised as

$$\lim_{g_0 \longrightarrow g_0'} \hat{\xi}(g_0) = \infty.$$

To further investigate this aspect, suppose to have a generic observable $\mathbb{O}$, whose dimension in mass units reads $d_{\mathbb{O}}$,

$$\mathbb{O}(g_0, a) = \Big(\frac{1}{a}\Big)^{d_{\mathbb{O}}} \hat{\mathbb{O}}(g_0), \tag{1.83}$$

where $\hat{\mathbb{O}}(g_0)$ represents the observable on the lattice and, in the continuum limit, this quantity is expected to stay finite and realise the corresponding physical one, $\mathbb{O}_{\text{phys.}}$. Since divergences are to be avoided, the parameter $g_0 = g_0(a)$ must be tuned to g_0' as a is varied: According to the previous statement, this requirement guarantees to obtain the physical quantity in the continuum limit,

$$\lim_{a \longrightarrow 0} \mathbb{O}(g_0(a), a) = \mathbb{O}_{\text{phys.}},$$

and, if the dependence of $\hat{\mathbb{O}}(g_0(a))$ on $g_0(a)$ is known for sufficiently small a, then $g_0(a)$ can be approximated as a function of $\mathbb{O}_{\text{phys.}}$. The last statement can be translated as follow: Tuning $g_0(a)$ as a is varied allows to the quantity $\mathbb{O}(g_0(a), a)$ to be independent on a. Recalling the renormalization group theory, the previous statement ensures the quantity $\mathbb{O}(g_0(a), a)$ to satisfy to the renormalization group equation,

$$\Big[a\frac{\partial}{\partial a} - \beta(g_0)\frac{\partial}{\partial g_0}\Big]\mathbb{O}(g_0(a), a) = 0, \tag{1.84}$$

which allows to describe the scaling of $g_0(a)$ with respect to a. In (1.84), the quantity $\beta(g_0)$ is the *Callan-Symanzik β-function*, which reads

$$\beta(g_0) = -\beta_0 g_0^3 - \beta_1 g_0^5 + \mathcal{O}(g_0^7) = -a\frac{\partial g_0}{\partial a}, \tag{1.85}$$

where β_0 and β_1 are coefficients which depend on the number of flavours and colors[12],

$$\beta_0 = \frac{1}{16\pi^2}\Big(11 - \frac{2}{3}N_f\Big), \qquad \beta_1 = \frac{1}{(16\pi^2)^2}\Big(102 - \frac{38}{3}N_f\Big), \tag{1.86}$$

but they do not depend on the chosen renormalisation scheme. After some algebra, the differential equation in (1.85) can be solved, resulting in

$$a(g_0) = \frac{1}{\Lambda_L} R(g_0), \tag{1.87}$$

where Λ_L represents a mass scale, which can be used when quantities are measured, whereas $R(g_0)$ reads

$$R(g_0) = (\beta_0 g_0^2)^{-\beta_1/2\beta_0} \exp\Big\{-\frac{1}{2\beta_0 g_0^2}\Big\}. \tag{1.88}$$

Taking into account equations (1.85), (1.86) and (1.87), it can be shown that a varies *accordingly* to g_0: Said in different words, smaller values of g_0 correspond to smaller

[12] Here, the number of colors has been set to $N_c = 3$.

values of a, and, vice versa, larger values of g_0 to coarser lattices. As a consequence, considering equation (1.87), the critical value $g_0^{'}$ for vanishing lattice spacing $a \longrightarrow 0$ is obtained as

$$g_0(a) \longrightarrow g_0^{'} = 0.$$

Finally, using the results from (1.87) and (1.88) in equation (1.83), the following holds

$$\lim_{g_0 \longrightarrow 0} \frac{\mathbb{O}(g_0)}{R(g_0)^{d_{\mathbb{O}}}} = \text{const.}, \tag{1.89}$$

for g_0 values in the proximity of the critical one. [13]

The idea that the ratio (1.89) is constant as the parameter g_0 tends to the critical allows to perform simulations in the continuum limit: Indeed, the ratio in (1.89) can be directly measured and, as long as it stays constant, it will not depend on the lattice spacing through the lattice gauge coupling. Thus, this guarantees simulations to be realised in the continuum limit.

1.6 Thermal Lattice QCD

The introduction of temperature and chemical potential as parameters inside quantum field theory allows to investigate the thermodynamics of the described physical system. Thermal Quantum Chromodynamics represents a fundamental tool to enhance the knowledge about the earliest stages of the expansion of the Universe, in particular the ones contained in the time interval which goes from the quark epoc to the hadron phase, from 10^{-12} s to 1 s after the Big Bang, approximatively. Also, astonomical object like, the neutron stars represent a natural application field for thermal QCD, due to the elevated temperature and densities which characterise the inner layers of such objects, as well as the results of heavy-ion collisions. In this section we will briefly go through the necessary steps to involve temperature and chemical potential in the Lagrange equation of Quantum Chromodynamics. For a more detailed analysis of this topic, we refer, in particular, to [13].

1.6.1 The temperature

The introduction of temperature in a field theory comes with the definition of the partition function of a physical system in the path integral formalism. Suppose to have a bosonic system described by the Hamiltonian density $\mathcal{H} = \mathcal{H}(\hat{\pi}(\mathbf{x}, t), \hat{\phi}(\mathbf{x}, t))$, where $\hat{\phi}(\mathbf{x}, t)$ represents the bosonic field operator and $\hat{\pi}(\mathbf{x}, t)$ the bosonic conjugate field operator, both at time t. From the field quantisation, we recall the orthogonality conditions satisfied by the field operators

$$\langle \phi | \psi \rangle = \exp\Big\{ \int d^3x \; \pi(\mathbf{x}, \phi(\mathbf{x}) \Big\},$$

$$\int d\phi(\mathbf{x}) |\phi\rangle\langle\phi| = 1, \qquad \langle \phi_a | \phi_b \rangle = \delta(\phi_a(\mathbf{x}) - \phi_b(\mathbf{x})),$$

$$\int \frac{d\pi(\mathbf{x})}{2\pi} |\pi\rangle\langle\pi| = 1, \qquad \langle \pi_a | \pi_b \rangle = \delta(\pi_a(\mathbf{x}) - \pi_b(\mathbf{x})),$$

[13] Quantities which exhibit such behaviour are said to show *asymptotic scaling*.

where $\phi(\mathbf{x})$ and $\pi(\mathbf{x})$ are the eigenfunctions at $t = 0$ of the field operators, when applied to the eigenstates $|\phi\rangle$, $|\pi\rangle$. Suppose to evolve the system from the initial state $|\phi_a\rangle$ to a final state, coinciding to the initial one, after a time interval $t = t_f$. Also, suppose to compute the associated transition amplitude. Given the Hamiltonian operator

$$\hat{H}(t) = \int d^3x \; \mathcal{H}(\hat{\pi}(\mathbf{x}, t), \hat{\phi}(\mathbf{x}, t)),$$

and the separation of the time interval $(0, t_f)$ in N subintervals Δt, the evolution is performed as follow,

$$\langle\phi_a| \exp\Big(i\hat{H}(t)t_{\mathrm{f}}\Big)|\phi_a\rangle = \lim_{N\longrightarrow\infty} \langle\phi_a| \exp\Big(i\hat{H}(t)\Delta t_1\Big) \; \exp\Big(i\hat{H}(t)\Delta t_2\Big) \cdots \exp\Big(i\hat{H}(t)\Delta t_N\Big)|\phi_a\rangle.$$

Making use of the orthogonality relations above, it is possible to show that the latter becomes

$$\begin{aligned}
\langle\phi_a| \exp\Big(i\hat{H}(t)t_{\mathrm{f}}\Big)|\phi_a\rangle = \lim_{N\longrightarrow\infty} \int \prod_{i=1}^{N} \frac{d\pi(\mathbf{x})}{2\pi} d\phi_i(\mathbf{x}) \delta(\phi_a(\mathbf{x}) - \phi_1(\mathbf{x})) \times \\
\times \exp\Big\{ i \sum_{l=1}^{N} \Delta_t \int d^3x \Big[\pi_l \frac{\phi_{l+1} - \phi_l}{\Delta_t} - \mathcal{H}(\phi(\mathbf{x}, t)\pi(\mathbf{x}, t)) \Big] \Big\}, \\
= \int \mathcal{D}\pi \int_{\phi_{(\mathbf{x},\mathbf{0})}=\phi_a(\mathbf{x})}^{\phi_{(\mathbf{x},t_{\mathrm{f}})}=\phi_a(\mathbf{x})} \mathcal{D}\phi \; \exp\Big\{ i \int_0^{t_{\mathrm{f}}} dt \int d^3x \Big(\pi(\mathbf{x},\mathbf{t}\partial_t\phi(\mathbf{x}, t)) + \\
- \mathcal{H}(\phi(\mathbf{x}, t)\pi(\mathbf{x}, t)) \Big) \Big\}
\end{aligned}$$

where it has been used that $\phi_{N+1} \equiv \phi_a$ and that the functional integration measures, when $\Delta t \longrightarrow 0$, become

$$\lim_{N\longrightarrow\infty} \int \prod_{i=1}^{N} \frac{d\pi(\mathbf{x})}{2\pi} = \int \mathcal{D}\pi, \qquad\qquad \lim_{N\longrightarrow\infty} \prod_{i=1}^{N} d\phi_i(\mathbf{x}) = \int \mathcal{D}\phi.$$

At this point, from statistical mechanics, one recalls the partition function of a canonical ensemble,

$$\mathcal{Z} = \mathrm{Tr}\Big[e^{-\beta\hat{H}}\Big],$$

with $\beta = 1/(K_B T)$. After some algebra, using the relations found for the transition amplitude above, the partition function can be defined as

$$\mathcal{Z} = \int d\phi \langle\phi|e^{-\beta\hat{H}}|\phi\rangle = \int \mathcal{D}\pi \int \mathcal{D}\phi \exp\Big[\int_0^{\beta} d\tau \int d^3x \; (i\pi\partial_\tau\phi - \mathcal{H}) \Big],$$

where the Wick rotation on the temporal variable has been performed, by means of the analytic continuation to imaginary time $t \longrightarrow it = \tau$. Furthermore, the integration over the $\hat{\phi}$ fields is understood as periodic in the imaginary time direction and the object inside the integral corresponds to the Lagrange equation density in the Euclidean spacetime formalism. One can now observe that the temperature has naturally been introduced through the partition function of the physical system: Indeed, β is directly linked to the imaginary time variable, since it comes as an extreme of integration along the τ direction. This procedure can be applied to more complicated and specific systems, also including fermions. Since our intention was to just visualise how the temperature is included in the

formalism, then we move straightforwardly to the QCD partition function without go in other details, which can be found on different textbooks, in particular we refer to [10; 13].

Based on this brief introduction and avoiding to go through the intermediate steps, it can be shown that the partition function of Quantum Chromodynamics in the Euclidean spacetime reads

$$\mathcal{Z}[T,V,M,g] = \int \mathcal{D}A \int \mathcal{D}\bar{\psi}\mathcal{D}\psi \exp\Big\{ - S_{QCD}[\psi,\bar{\psi},A]\Big\}, \tag{1.90}$$

where the integration over the gauge fields is periodic whereas the one over the fermionic fields is antiperiodic. The QCD action in the exponent is given as the sum of the fermionic and gluonic contributions,

$$\begin{aligned} S_F[\psi,\bar{\psi},A] &= \int_0^{1/T} dx_4 \int_V d^3x \sum_{f=1}^{N_f} \Big[\ \bar{\psi}^f(x)\Big(\gamma_\mu\partial_\mu + igt_A\gamma_\mu A^A_\mu(x) + M^f\Big)\psi^f(x)\Big], \\ S_G[A] &= \frac{1}{4}\int_0^{1/T} dx_4 \int_V d^3x\ \mathcal{F}^A_{\mu\nu}(x)\mathcal{F}^{\mu\nu}_A(x), \end{aligned} \tag{1.91}$$

where the spatial integration is restricted to a box of volume V and $K_B = 1$. This allows to directly connect the continuum limit to the discretised QCD on the lattice. Indeed, simulations are performed along discretised directions in the four-dimensional lattice space, with finite extensions defined as

$$L_x = L_y = L_z = aN_\sigma, \qquad\qquad \beta = 1/T = aN_\tau, \tag{1.92}$$

with N_σ and N_τ labelling, respectively, the number of sites along the spatial and temporal directions. Simulations on the lattice are only possible if the lattice temporal and spatial extents are finite. In the limit of $T \longrightarrow 0$, for instance, the temporal direction would ideally extent up to $\beta = 1/T = \infty$, which would inhibit simulations to be performed, and this explains why simulations are always performed at *finite temperature* on the lattice. In case N_σ is *sufficiently large* to make the theory lightly sensitive to the space boundaries, then using $N_\tau > N_\sigma$ realises the insensitivity of theory also to the boundary along the temporal direction. When this parameter setup is used, simulations are said to be performed at *zero temperature*, even though $T \neq 0$ always during simulations. Simulating for $N_\tau < N_\sigma$ means to generically simulate at finite temperature. But how can one allow for variations of temperature on the lattice?

Suppose to consider again the relations in (1.92). One observes that:

- Discontinuous variations of T are realised as N_τ is varied;
- Continuous variations of T are realised as the lattice spacing a varies continuously.

The second option can be performed if we consider again equation (1.65) and focus on the lattice gauge coupling. This quantity, on the lattice, clearly depends on the lattice spacing through the running coupling,

$$\beta(a) = \frac{2N_c}{g^2(a)}, \tag{1.93}$$

and, from the considerations made by solving the Callan-Symanzik equation in the previous section, we know that $g(a)$ varies accordingly to a. This allows to conclude that,

varying the values of the lattice gauge coupling corresponds to a variation in temperature as N_τ is fixed, since this results in a variation of $g(a)$ and, in turns, of a itself. This provides the possibility to investigate, for instance, the critical temperature at which a specific phase transition takes place on the lattice as different β values are used in simulation. These values can also be translated in the critical temperature at which the phase transition takes place in the continuum limit, based on the called *scale setting*: Depending on the physical system, there are several techniques that have been tuned during the last forty years, and the main ones can be consulted in Chapter 3 of [11].

1.6.2 The chemical potential for baryon number

The introduction of chemical potential in theory allows to study physical situations where a net baryonic density is to be taken into account, which is what we refer to as *non-zero density*. In general, the baryon number B is directly linked to the number of quarks N_q and antiquarks $N_{\bar{q}}$ through

$$B = \frac{1}{3}N = \frac{1}{3}(N_q - N_{\bar{q}}).$$

The partition function in equation (3.1) describes a system of gluons and quarks with a net zero fermionic density, namely the number of quarks and antiquarks coincides, without unbalance. Anyway, such discrepancy must be considered as soon as physical systems as ultra-dense environments, as well as the products of heavy ion collisions, are investigated. In this subsection we will mainly refer to [27], [28] and to Chapter 12 of [11]. In statistical mechanics we call a grand canonical ensemble a statistical ensemble in thermal equilibrium with a reservoir, with which it can exchange energy and particles. The grand canonical partition function, given the Hamiltonian operator $\hat{H}$ for such system, reads

$$\mathcal{Z} = \mathrm{Tr}\Big[e^{-\beta(\hat{H}-\mu\hat{N})}\Big], \tag{1.94}$$

where the chemical potential μ has been introduced as a parameter which couples to the particle number operator $\hat{N}$, which satisfies to $[\hat{H}, \hat{N}] = 0$. The latter can be used as a good argument to include the chemical potential inside the Quantum Chromodynamics partition function. Suppose to have the continuum action of a system of non interacting fermions in the Euclidean formulation,

$$S_F[\psi, \bar{\psi}] = \int_0^{\frac{1}{T}} d\tau \int d^3x\, \bar{\psi}^f(x)(\gamma_\mu \partial_\mu + M)\psi^f(x),$$

which we know to be invariant under global U(1) vector transformations,

$$\psi_f(x) \longrightarrow \psi'_f(x) = e^{i\alpha\mathbb{1}}\psi_f(x), \qquad \psi_f(x) \longrightarrow \bar{\psi}'_f(x) = \bar{\psi}_f(x)e^{-i\alpha\mathbb{1}}.$$

From the Noether's theorem [29], the corresponding conserved current is

$$J_\mu(x) = \bar{\psi}^f(x)\gamma_\mu\psi^f(x),$$

and the conserved quantity associated to this current is the so called *charge operator*,

$$\hat{N} = \int d^3x \bar{\psi}^f(x)\gamma_4\psi^f(x) = \int d^3x \psi^{\dagger\, f}(x)\psi^f(x),$$

whose expectation value on a specific eigenstate of the Hamiltonian returns the total charge, depending on the number of quarks and antiquarks. The next step consists in

comparing $\hat{N}$ to what is contained inside the partition function in equation (1.94). If one introduces the chemical potential through the product

$$-\frac{\mu\hat{N}}{T},$$

this will return, after making explicit $\hat{N}$, the QCD action contribution depending on the chemical potential,

$$-\frac{\mu}{T}\int d^3x\ \bar{\psi}^f(x)\gamma_4\psi^f(x) = -\int_0^{1/T} d\tau \int d^3x\ \bar{\psi}^f(x)\mu\gamma_4\psi^f(x) = S_\mu[\psi,\bar{\psi}]. \tag{1.95}$$

At this point, combining the contribution (1.95) to the actions in equation (1.91), the complete QCD partition function given in equation (1.90) becomes

$$\mathcal{Z}[T,\mu,V,M,g] = \int \mathcal{D}A \int \mathcal{D}\bar{\psi}\mathcal{D}\psi \exp\Big\{ - S_{QCD}[\psi,\bar{\psi},A]\Big\}, \tag{1.96}$$

where the complete QCD action reads

$$S_{QCD}[\psi,\bar{\psi},A] = S_F[\psi,\bar{\psi},A] + S_G[A] + S_\mu[\psi,\bar{\psi}].$$

Also, the quark number density can be computed using (1.96) as

$$n_q = \frac{1}{V}\langle\hat{N}\rangle = \frac{T}{V}\frac{\partial \ln \mathcal{Z}[T,\mu,V,M,g]}{\partial\mu},$$

as well as the corresponding baryon one. Using this result and a generic observable $\mathcal{O}$, its expectation value can be evaluated as follow

$$\langle\mathcal{O}\rangle = \frac{1}{Z}\int \mathcal{D}A \int \mathcal{D}\bar{\psi}\mathcal{D}\psi\mathcal{O} \exp\Big\{ - S_{QCD}[\psi,\bar{\psi},A]\Big\}. \tag{1.97}$$

Finally, the next step consists in translating $S_\mu[\psi,\bar{\psi}]$ to its lattice version. Taking into account the action in equation (1.95), a discretised version can be obtained as

$$S_\mu[\hat{\psi},\bar{\hat{\psi}}] = \sum_n \bar{\hat{\psi}}(n)\hat{\mu}\gamma_4\hat{\psi}(n),$$

where $\hat{\mu} = a\mu$ is an adimensional quantity which corresponds to the chemical potential on the lattice. Unfortunately, making use of this discretisation, the continuum limit would lead to a divergence in the renormalised free energy density, as shown in detail in [28] and in Chapter 12 of [11]. Furthermore, this problem is not related to doublers but is directly linked to the way the chemical potential has been introduced in the action: Indeed, as shown in equation (1.96), the chemical potential comes with the γ_4 matrix, which is the imaginary time component of the Dirac matrices in the Euclidean spacetime formalism. Using the arguments which lead to the introduction of the chemical potential in QED, one could consider an external abelian gauge field, such that

$$\bar{\psi}(x)\mu\gamma_4\psi(x) = -ig\bar{\psi}(x)\gamma_4\mu A_4^{\text{ext.}}(x)\psi(x), \tag{1.98}$$

where

$$A_4^{\text{ext.}}(x) = -i\frac{\mu}{g}. \tag{1.99}$$

The object in (1.98) can be embedded inside the QCD Lagrange equation and action and, following the prescriptions given in sections (1.3.3), (1.3.4) and (1.3.5), the discretised fermionic actions for both Wilson and staggered formulations become

$$\begin{aligned} S_F^W[\psi,\bar{\psi}] = -\frac{1}{2}\sum_n \Big\{ \sum_{i=1}^{3} \Big[\bar{\hat{\psi}}(n)(r-\gamma_i)U_i(n)\hat{\psi}(n+\hat{i}) + \bar{\hat{\psi}}(n+\hat{i})(r+\gamma_i)U_i^\dagger(n)\hat{\psi}(n)\Big] + \\ + \Big[e^{\hat{\mu}}\bar{\hat{\psi}}(n)(r-\gamma_4)U_4(n)\hat{\psi}(n+\hat{4}) + e^{-\hat{\mu}}\bar{\hat{\psi}}(n+\hat{4})(r+\gamma_4)U_4^\dagger(n)\hat{\psi}(n)\Big]\Big\} + \\ + (\hat{M}+4r)\sum_n \bar{\hat{\psi}}(n)\hat{\psi}(n), \end{aligned} \tag{1.100}$$

and

$$\begin{aligned} S_F^{\text{stagg.}}[\psi,\bar{\psi}] = \frac{1}{2}\sum_n \Big\{ \sum_{i=1}^{3} \eta_i(n)\Big[\bar{\chi}(n)U_i(n)\chi(n+\hat{i}) - \bar{\chi}(n)U_i^\dagger(n-\hat{i})\chi(n-\hat{i})\Big] + \\ + \eta_4(n)\Big[e^{\hat{\mu}}\bar{\chi}(n)U_4(n)\chi(n+\hat{4}) - e^{-\hat{\mu}}\bar{\chi}(n)U_4^\dagger(n-\hat{4})\chi(n-\hat{4})\Big]\Big\} + \\ + \hat{M}\sum_n \bar{\chi}(n)\chi(n), \end{aligned} \tag{1.101}$$

where the contributions along the spatial and temporal directions have been explicitly separated. The chemical potential is contained inside

$$e^{\hat{\mu}} = U_4^{\text{ext.}}(n) = e^{ig_0 A_4^{\text{ext.}}(x)}, \qquad e^{-\hat{\mu}} = U_4^{\dagger\,\text{ext.}}(n) = e^{-ig_0 A_4^{\text{ext.}}(x)}, \tag{1.102}$$

which come together with the gauge link in the time direction, $U_4(n)$ and $U_4^\dagger(n)$. One of the important consequences of including the chemical potential inside the partition function of QCD resides in the introduction of a new symmetry. As seen before, the charge operator $\hat{N}$ is directly linked to the net charge of a physical system as well as to the quark density. Under charge conjugation the eigenvalues of such operator flip their sign, and the whole QCD partition function in the continuum formulation would transform as

$$\Big[\int \mathcal{D}A \int \mathcal{D}\bar{\psi}\mathcal{D}\psi \exp\Big\{-S_F - S_G - S_\mu\Big\}\Big]^{\mathcal{C}} = \int \mathcal{D}A \int \mathcal{D}\bar{\psi}\mathcal{D}\psi \exp\Big\{-S_F - S_G + S_\mu\Big\}, \tag{1.103}$$

since the only effect characterises the S_μ contribution. In a more compact way, this transformation can be summarised as

$$\mathcal{Z}^{\mathcal{C}}(\mu_1,\cdots,\mu_f) = \mathcal{Z}(-\mu_1,\cdots,-\mu_f).$$

The same symmetry holds on the lattice as well, and a detailed discussion is given in [11] and [30]. The introduction of chemical potential in QCD carries some more issues: Indeed The Dirac operator, enhanced with such new parameter, nullify the possibility to perform simulations on the lattice. In Chapter 5 of [11], the γ_5-*hermiticity* is introduced as a symmetry for the Dirac operator

$$D^\dagger = \gamma_5 D \gamma_5, \tag{1.104}$$

which guatantees the eigenvalues of D to be either real or a pair of complex conjugated eigenvalues, which in turns guarantee the determinant of D to be real. The introduction

of a chemical potential in the theory produces, as a consequence, the breaking of the symmetry in (1.104), resulting in a complex determinant of the Dirac operator. In turns, this feature does not allow to perform simulations for $\mu \neq 0$ without precautions: Indeed, in the Markov chains production using Monte Carlo methods, the weights used to evaluate the expectation value of a generic observable $\mathcal{O}$ become either complex or negative in sign, which clearly exibit no physical meaning. This is known in literature as *sign problem* and different techniques, which can be found on many textbooks, have been developed to make it, at least, mild. In the next subsection we will present one of these techniques, the analytic continuation to imaginary chemical potentials, together with the effects it produces in numerical simulations.

1.6.3 The imaginary chemical potential

In the previous subsection a big limit concerning the introduction of a chemical potential in the theory has been presented when dealing with numerical simulations. Besides the others, in this subsection we will focus on a useful technique which allows to circumvent the sign problem by means of analytic continuation from real to imaginary chemical potentials,

$$\mu \longrightarrow i\mu_i, \tag{1.105}$$

for which the γ_5-hermiticity is again satisfied. The femionic actions in equations (1.100) and (1.101) can then be modified, accordingly, by performing the transformation

$$e^{\pm\hat{\mu}} \longrightarrow e^{\pm i\hat{\mu}_i},$$

and, consequently, also the QCD partition function will be modified. In equation (1.95), the dependence of the QCD action on the chemical potential has been introduced, in the continuum formulation, by taking into account the way μ/T couples to the number operator $\hat{N}$. Also, following the same prescription as for real chemical potentials on the lattice, the total contribution, assumed to have N_τ lattice sites, reads

$$e^{(\pm a\mu_i)^{N_\tau}} = e^{\pm\mu_i/T},$$

which is in agreement with the total contribution reported in equation (1.95). This represents a phase factor, and, in principle, it can be absorbed into the boundary conditions that can imposed on the fields along the time direction on the lattice[14]. Thus, taking into account the expectation value of a generic observable reported in equation (1.97), one can think about making explicit the dependence on the imaginary chemical potential by means of series expansion,

$$\langle\mathcal{O}\rangle(\mu_i) = \sum_k a_k \Big(\frac{\mu_i}{T}\Big)^k, \tag{1.106}$$

which holds in the parameter range $\mu_i/T < 1$. At any chance, it is worth to underline that the chemical potential, in the real world, stays always real and that the analytic continuation only represents a necessary a trick to circumvent the challenging sign problem. As a consequence, in order to correctly evaluate (1.106), a second analytic continuation must be performed when the series expansion is truncated, which allows to transport the results to the *real world*. The introduction of imaginary chemical potential is also responsible for a new symmetry of the QCD partition function,

$$Z\Big(\frac{\mu_i}{T}\Big) = Z\Big(\frac{\mu_i}{T} + i\frac{2\pi n}{N_c}\Big), \tag{1.107}$$

[14] A detailed explanation is given in Appendix C of [15].

which holds for a generic number of N_c colors, where $n \in \mathbb{Z}$. Such symmetry corresponds to a periodicity of the partition function in the interval $[0, 2\pi)$, which can therefore be separated into N_c equivalent sectors, corresponding to different critical chemical potential values,

$$\mu_{ic} = \frac{2\pi}{N_c}\Big(n + \frac{1}{2}\Big). \tag{1.108}$$

The difference between the N_c different sectors corresponds to different phases of the Polyakov loop: The translation in the μ_i/T value in (1.108) coincides with a center group Z_N rotation. This particular feature was presented first in 1986 by A. Robege and N. Weiss in [31] and will further be investigated in the next Chapter.

Chapter 2

The QCD phase diagram for different parameter settings

The introduction to Thermal Quantum Chromodynamics in the previous Chapter provides a series of tools which allows to investigate the thermodynamic aspects of QCD. It was 1964 when M. Gell-Mann [3] and G. Zweig [4] proposed the hadrons as bound states of fundamental particles, namely the quarks. From that moment on, much progress has been done both from the theoretical and experimental points of view, which led to the discovery of Quark-Gluon Plasma. In 1980 such classification first appeared in [32]: At that stage it was already clear that, due to the aymptotic freedom, at high temperatures and densities the ordinary nuclear matter does not consist in separated bound states, i.e. the hadrons, but rather in a plasma-like state of the hadrons constituents, thus a Quark-Gluon Plasma (QGP). The experimental evidences of this new state of matter were striclty connected to the progress in the quality and efficiency of the avaliable facilities. Since the beginning of the Seventies, the first experiments involving hadron collisions have been conducted at Lawrence Berkeley National Laboratory and at the Synchrophasotron of the Joint Institute for Nuclear Research in Dubna, even though, from the Eighties on, the CERN facilities allowed to reach the maximum energy in heavy ion collisions. The first experimental evidences of QGP were obtained and publicly announced in 2000 [33] after some astonishing research results in Geneva. After this important milestone, the investigation of the dense nuclear matter under extreme conditions has continued, involving relativistic energies both at LHC collider at CERN and the RHIC collider of the Brookheaven National Laboratories in New York, with different range of density guaranteed. [1]. In general, the changing nature of the state of the nuclear matter, depending on on the temperature and density, is a good example of phase transition. The investigation of such phenomenon is strictly related to lattice Quantum Chromodynamics: Indeed, although the properties connected to the asymptotic freedom in the deconfined QGP phase can be investigated by means of perturbative theory, the realisation of phase transitions depends, necessarily, on non-perturbative effects, which requires lattice simulations to be performed. Thanks to the latter, specific observables as, for instance, the order parameter of the considered phase transition can be measured and the results can further be analysed, taking into account suitable techniques.

Before deepening the details of the QCD phase diagram, we briefly introduce three of the

[1] A more detailed discussion about this chronological reconstruction of the events in the heavy ion collisions progress can be found in [34].

most important features which characterise it:

- Within the density and temperature region of the hadronic phase, the nuclear matter undergoes a liquid-gas phase transition at low temperatures and $\mu_B \approx 930\text{MeV}$, where μ_B is the baryon chemical potential. A gaesous phase characterises the lower μ_B sector, whereas for higher μ_B values a liquid phase takes places. Without going into further details, a nice introduction to the topic can be found in [35];

- Another interesting feature of QCD, which occurs at ultra-high densities and relatively low temperature, is given by the color superconductivity, 2SC, which is realised in the so called Color-Flavor Locked (CLF) phase. This state of matter consists in a degenerate liquid of quarks which spontaneously breaks the color gauge symmetry, due to the Cooper pairing [36] realised near the Fermi surface. The region between Quark-Gluon Plasma and the superconductive phase is still under debate, as the presence of a proper phase transition which separates the two states of matter [37] still requires investigation. More about this topic can be found in [35; 38; 39];

- Last, but not least, we can recall the chiral phase transition and briefly discuss about its realisation when density and temperature are varied. In the chiral limit fermions are massless particles, and in this limit the chiral symmetry is always realised in the continuum limit. When massive fermions are considered, the chiral symmetry is always explicitly broken. First simulations performed at the beginning of the Eighties by Kogut et all. [40] gave an interesting picture about the dependence of the chiral condensate on the temperature, which can be considered as the order parameter for the chiral phase transition. In the limit of massless quarks, for $N_f = 2$, they showed that the chiral symmetry is spontaneously broken at low temperature ($\langle\bar{\psi}\psi\rangle \neq 0$), whereas it is fully restored for higher temperatures ($\langle\bar{\psi}\psi\rangle \neq 0$). The investigation of the chiral phase transition in the chiral limit is provided, in detail, in the next sections and Chapters, when also different N_f values are considered;

In the following, we will focus on two main regimes depending on the *intensity* of the strong coupling, already mentioned in section 1.5, namely the weak coupling regime and the strong coupling one. In equation (1.65), the gauge coupling β has been introduced as an object which couples to the pure gauge action,

$$\beta(a) = \frac{6}{g_0(a)^2}, \tag{2.1}$$

assumed the physical number of colors $N_c = 3$. Depending on the values of the running coupling g_0 in the continuum formulation, two different regimes of QCD can be in principle investigated: The strong coupling regime, which corresponds to the range of large values of g_0 and the weak coupling regime, which is realised in the opposite scenario. Clearly, the value $\beta(a) = 0$ corresponds to the strong coupling limit, which is realised for $g_0 \longrightarrow \infty$.

2.1 The QCD phase diagram at weak coupling

A useful way to collect the different properties of Quantum Chromodynamics, depending on temperature and density (chemical potential), is given by the QCD phase diagram, of which an example is provided in figure (2.1). Along the orizontal axis we find the chemical potential μ_B, which accounts for the baryon density of the physical system, whereas along

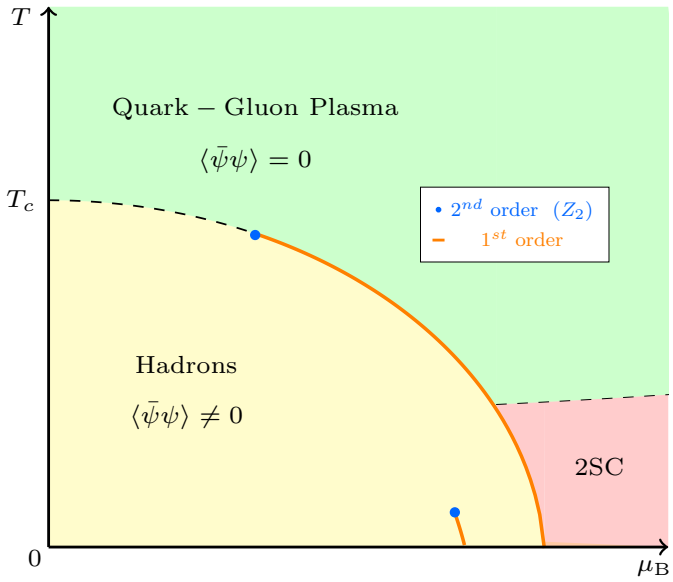

Figure 2.1: *The QCD phase diagram for $N_f = 2$, at the physical quark masses. The black-dashed line represents the analytic crossover.*

the vertical axis are the values of temperaure, T. In this diagram the different states of matter occupy different *regions*, whose boundaries consist in a true phase transition or simply an analytic crossover. Most of the times, research is still in progress and it is not yet possible to exclude more realisations in favour of a specific one. In the following a generic overview is presented and for more details on this topic, we refer, in particular, to [41] and [42].

2.1.1 The QCD phase diagram for $N_f = 2$

In figure (2.1) the QCD phase diagram for $N_f = 2$ is depicted, assuming the masses of the two light quarks to be degenerate and equal to the physical mass. In the region corresponding to lower densities, which belongs to the left area of the diagram, we can observe that the boundary between the QGP phase and the hadron one is marked by a black-dashed line, representing an analytic crossover, as confirmed by many studies throughout the years with $N_f = 2 + 1$ flavours, using different techniques and fermion actions [43] [44] [45] [46]. The crossover line intercepts the temperature axis at the critical temperature T_c, whose value, as shown in [46], corresponds to $T_c = (156.5 \pm 1.5)$MeV. Moving along the μ_B axis towards larger densities, for small temperature values, the liquid-gas phase transition is met, resulting in a first-order line which extents from $T = 0$ up to a critical point falling in $T \approx (16-18)$MeV [47]. Such critical point must be a second-order one, in the universality class of the Z_2 group, since a first-order line representing a two-phase coexistance cannot terminate in a first-order critical point. More argumentation about the nature of the univesality classes are in [48]. Going further ahead for higher densities, another first-order line enshrines the boundary between the hadron phase and the superconductivity and Quark-Gluon plasma regions. The existance of such first-order phase transition is based on different argumentations coming from results obtained using different models, as in [49], [50]. Again, the requirements for a first-order line to terminate

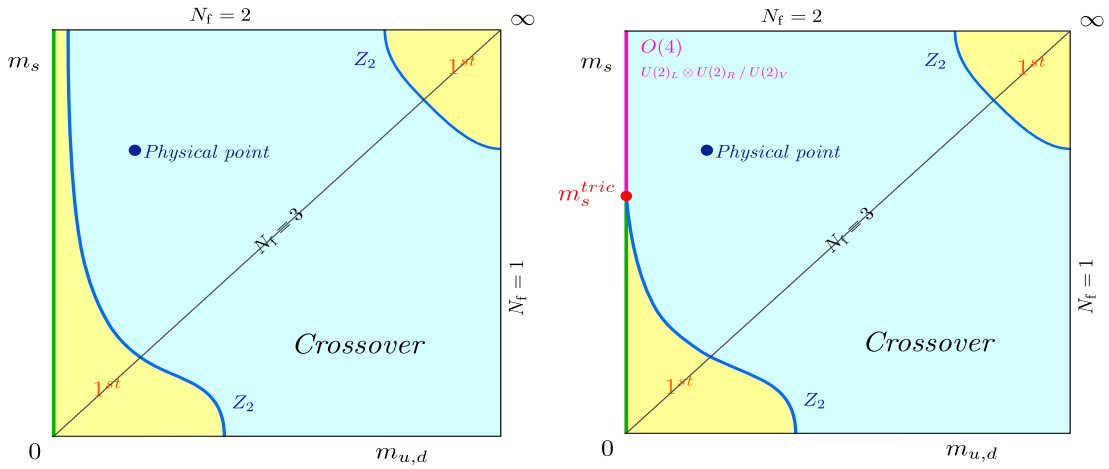

Figure 2.2: *Sketch of the Columbia plot. The differences in the left side of the plots are based on the ambiguity from [52] for the $N_f = 2$ chiral limit.*

into a second-order point in the universality class of the Z_2 group ensures the existance of a critical endpoint (CEP), where the first-order line meets the crossover one: At any chance, the exact location of this CEP is still under debate and strongly related to the extension of the crossover line. For ultra-high dense QCD, we find the aforementioned 2SC phase, which is still under examination, and in particular, as temperature is sufficiently raised to bring the system in the QGP phase, the observation a true phase transition is not necessary [51]. At this point, since much work is still in progress to better constrain the QCD phase diagram, it sounds correct to affirm that the diagram and the boundaries in figure (2.1) are constantly evolving and represent just a sketch of the possible QCD phase diagram for $N_f = 2$ degenerate quarks.

The situation is interestingly different as the $N_f = 2$ the chiral limit is included in discussion. In 1984, R.D. Pisarski and F. Wilczek provided in [8] a snapshot of the situation concerning the order of the chiral phase transition for $N_f = 2$ at $\mu_B = 0$ in that period. Indeed, if for $N_f \geq 3$ the order of the chiral phase transition was confirmed to be first, for two massless fermions the order turned out to depend on nonperturbative effects, as for instance the istantons, which rise up as temperature is varied. These effects have direct consequences on the realisation of the $U(1)_A$ anomalous symmetry, which is the responsible for the chiral phase transition in the $N_f = 2$ chiral limit to be either first or second-order. This *ambiguity* was depicted in 1990 in the so called *Columbia plot* [52], where the order of the chiral phase transition is provided for $N_f = 2 + 1$: The mass of the up and down quarks, assumed to be degenerate, are continuously varied between 0 and ∞, together with the mass of the strange quark, as shown in figure (2.2). The different regions correspond to different realisations of the chiral phase transition, being either a first-order, second-order phase transition or simply an analytic crossover. Along

the diagonal axis, which links the chiral limit in the left-bottom corner (also known as *light-masses corner*) to the *heavy-mass corner* in the top-right area of the plot, the $N_f = 3$ scenario is represented. The top border represents the $N_f = 2$ scenario, where m_{ud} are finite and $m_s = \infty$, whereas the $N_f = 1$ scenario is represented along the right border. The results from [8] are reported in figure (2.2):

- For $m_{ud} = 0$ and $m_s \neq 0$, the chiral phase transition is represented by a first-order triple line: Here, the chiral condensate can either be $\langle\bar{\psi}\psi\rangle = 0$ or $\langle\bar{\psi}\psi\rangle \neq 0$, the latter carrying a positive or negative sign, thus resulting in the coexistance of three different phases;

- The first-order region in the light-mass corner extents towards the $N_f = 2$ line differently as the mass of the strange quark m_s is varied. Indeed, in the plot to the left in figure (2.2) $N_f = 2$ belongs to the first-order region in the chiral limit, whereas in the plot to the right the second possible scenario is reported, where the first-order region shrinks down as m_s varies and collapses in the $N_f = 2$ chiral limit. The Z_2 boundary which separates the first-order chiral region from the crossover scales towards the chiral limit $m_{ud} = 0$ and terminates in a *tricritical point* m_s^{tric}, which corresponds to the point where the first-order triple line meets the second order one. The universality class for the second-order line is still under investigation, as it depends on the restoration of the $U(1)_A$ symmetry. At any chance, recent results contemplate a second-order phase transition in the 3D $O(4)$ universality class [53] [54] [55] [56] for $N_f = 2$, when the chiral and continuum limit are taken into account;

- A crossover region is collocated between the two first-order chiral regions which occupy the light and heavy-mass corners of the Columbia plot. The boundary between a first-order region and the crossover one is given by a second-order line in the 3D Ising universality class, namely a Z_2 critical line.

The intricated situation in the $N_f = 2$ chiral limit has been under debate for long time since, as already well known from the theory, it is not possible to perform simulations in the chiral limit. During the last fifteen years much work has been produced in order to unravel the $N_f = 2$ situation in the chiral limit, both using staggered [57], [58] and Wilson [59] fermions, which have confirmed the presence of a first-order region when simulations are performed on coarse lattices, with lattice temporal extent $N_\tau = 4$. In 2018 [57] a different idea has been proposed, which consists in promoting the parameter N_f, which is of course an integer parameter, to a non-integer one for numerical purposes. Indeed, the description of the first-order region in the light-mass corner by means of non-integer N_f values represented a valid alternative to extrapolate information about the order of the chiral phase transition for $N_f = 2$ in the chiral limit and about the tricritical scaling, expected in the proximity of the tricritical point for the Z_2 boundary. Thus, the non-integer N_f parameter can be used in place of the m_s parameter on the lattice to control the extrapolation, and in figure (2.3) are reported the two scenarios from (2.2), described by means of the number of flavours. The first results for $N_\tau = 4$, using unimproved staggered fermions, were presented in [57], showing consistancy with a tricritical scaling for $N_f \in [2.0, 2.2]$. A decise resolution to the $N_f = 2$ ambiguity arrived in 2021 [9], as an extension of the work [57] to larger N_f values and lattice temporal extents has been realised. The strategy used in [57] has been involved again and simulations have been realised for larger N_f values and more N_τ values, assumed the quarks to always be degenerate in masses. Simulations were performed for $N_\tau = \{4, 6, 8\}$ and, for any simulated N_f value, a critical mass value belonging to the Z_2 critical boundary could

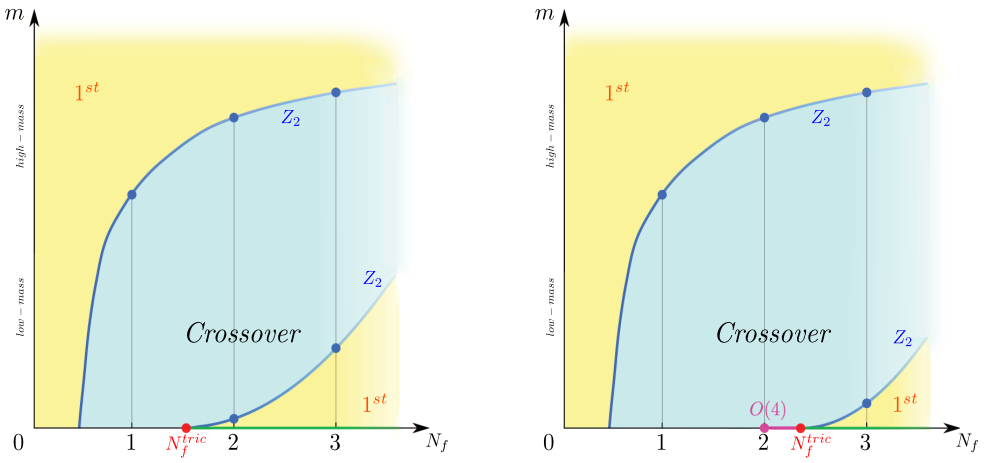

Figure 2.3: *The scenarios presented in* (2.2) *proposed in a different version, by using the* N_f *parameter as a non-integer parameter on the lattice. From [57].*

be obtained. As enough critical mass values are collected, this approach guaranteed to perform a continuum extrapolation to the chiral limit, hence to get information in the area of our interest, for every N_τ series of data. For $N_\tau = \{4, 6\}$ it is possible to appreciate a tricritical scaling of the Z_2 boundary in the proximity of the chiral region, suggesting the presence of a tricritical point in the chiral limit, where the second-order bonundary meets the first-order triple one. A generalisation of these results to $N_f \in [2, 7]$ is presented in figure (2.4), in the plot to the left, where we can see the first-order chiral region collapsing towards the $aT = N_\tau^{-1}$, due to the tricritical scaling of the Z_2 boundary. The existance of the tricritical point ensures that no first-order region survives when moving towards the chiral limit and, afterwards, to the continuum limit: As a consequence, this parameter region is characterised by a second-order chiral phase transition and the first-order region is relegated to a lattice artefact. This latest result is depicted in the plot to the right in figure (2.4). After this brief discussion, the phase diagram for $N_f = 2$ and massless up and down quarks can be represented as in figure (2.5). At zero density $\mu_B = 0$ the result just discussed is represented with a second-order point along the T-axis, whereas for non-zero density the situation will be clarified, being one of the aims of this research work. The separation between the hadron phase and the QGP and 2SC ones is trivially represented by a grey line at this stage, which represents the possibility to have different kind of realisations of the boundary.

2.1.2 The QCD phase diagram for $N_f = 3$

The $N_f = 3$ scenario involves, in addition to the two lightest quarks, also the strange quark. From results in [8], the order of the chiral phase transition for $N_f = 3$ was shown to always be first, independently on the realisation of the $U(1)_A$ symmetry. This was

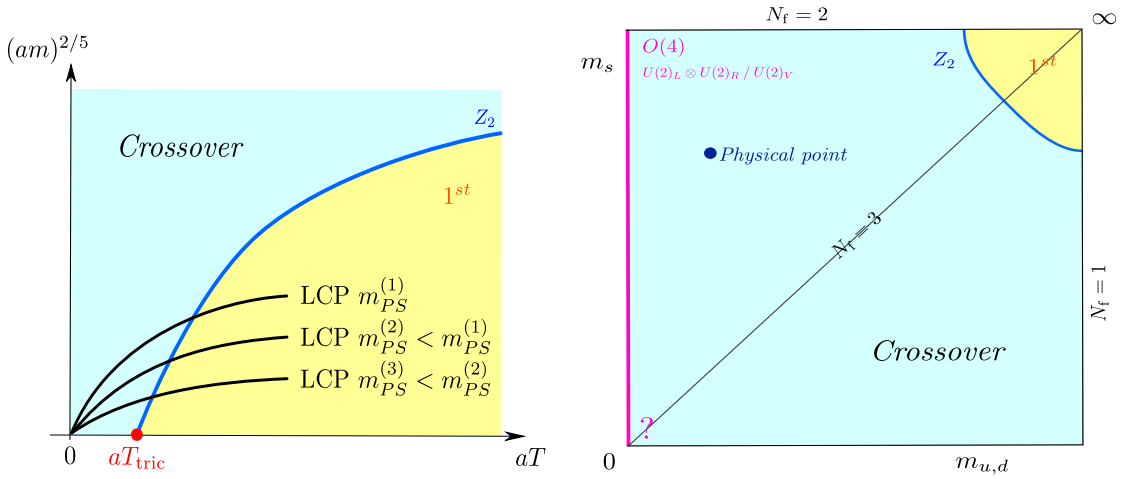

Figure 2.4: *Left: The extension of the first-order region, separated from the crossover one by the Z_2 critical line. The latter terminates in $aT^{\rm tric}$ along the orizontal axis. Right: Sketch of the Columbia Plot in the continuum limit. The chiral phase transition for $N_f = 2$ and $m_{ud} = 0$ is of second-order. From [9].*

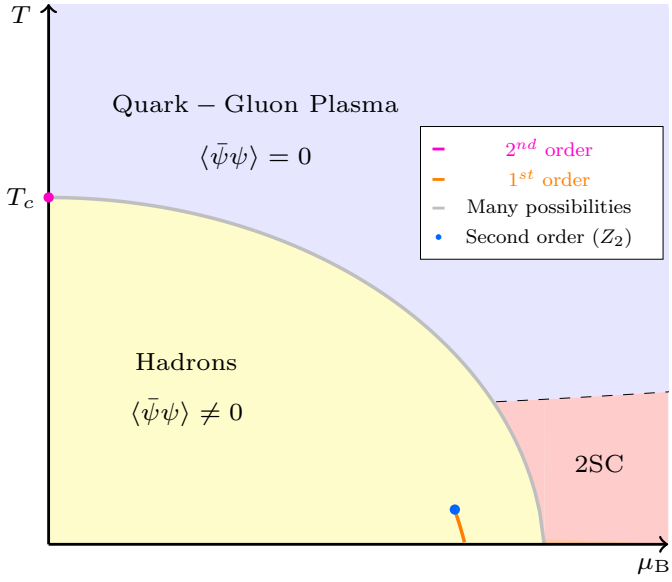

Figure 2.5: *The QCD phase diagram for $N_f = 2$, in the chiral limit. The black-dashed line represents the analytic crossover.*

confirmed by different works at the beginning of the current century, both using staggered [60; 61] and Wilson fermions [62; 63] for lattice temporal extent $N_\tau = 4$. Eventually, simulations on finer lattices provided different results when investigating the parameter region in the proximity of the chiral limit. Results using unimproved staggered fermions in [9], due to the behaviour of the Z_2 boundary near the chiral region, ensure compatibility of the chiral phase transition with a second-order one also for $N_f = 3$, in the continuum limit. In a recent work [64], where the authors made use of Highly Improved Staggered Quarks (HISQ), the investigation for $N_\tau = 8$ for $N_f = 3$ resulted in a second-order phase transition for pion masses $80\,\text{MeV} \leq m_\pi \leq 140$ MeV, whereas a first-order region for $N_\tau = 6$ has been detected only for larger N_f values [65]. Making use of Wilson action, it was shown in [9], by reanalysing data from previous works at $N_\tau = 12$ [66], $N_\tau = 10$ [67] and $N_\tau = \{4, 6, 8\}$ [68], the compatibility of $N_f = 3$ with a tricritical scaling of the Z_2 bundary as well as for staggered, then basically resulting in a second-order phase transition in the continuum limit. For a summary of the current results about the chiral critical point, for zero density and $N_f = 3$, we refer to Table 1 in [69]. Conceptually, the QCD phase diagram for $N_f = 3$ does not look much different from the ones in figure (2.1) and (2.5), at least for what it concerns the boundary between the hadron phase and the QGP one.

2.1.3 The QCD phase diagram with imaginary chemical potential

In section 1.6.3 of this work, the use of the imaginary chemical potential in lattice QCD was briefly introduced to get an idea of how the sign problem can be circumvented, when performing simulations at non-zero density. The QCD phase diagram has been deeply investigated when taking into account imaginary chemical potentials since the Eighties. As already mentioned in Chapter 1, the Roberge-Weiss periodicity [31], allows to extent the QCD phase diagram in different, equivalent, regions of μ/T values, providing an easy and direct extension of the Columbia plot by means of a *third axis*, namely the $(\mu/T)^2$ one. The positive side of the latter clearly refers to real values of chemical potential, whereas negative accounts for imaginary values.

The $N_f = 2$ scenario

The QCD phase diagram with non-zero chemical potential has been deeply investigated during the last twenty years. This has been done mainly by means of simulations at imaginary chemical potential, which entail an analytic continuation to real chemical potential values [70] [71] [72] when evaluating a specific observable. Results from simulations for $N_f = 2$, using staggered fermions and imaginary baryon chemical potential were presented in [72]. On a $8^3 \times 4$ lattice, assuming the two flavours to be degenerate in mass, the investigation for quark mass on the lattice of $am = 0.025$ showed compatibility with a first-order phase transition at the boundary between different, periodic, areas in the (T, μ_i) plane at the critical μ_{ic} values presented in equation (1.108). These phase transitions can be labelled as *Roberge-Weiss phase transition* and correspond to $Z(3)$ transitions, assumed the physical number of colors $N_c = 3$. Moreover, a continue phase transition was found to characterise the region $\mu_i/T < \pi/3$, separating the confined phase from the deconfined one. Further confirmation to this scenario were later provided in [73; 74]. For simulations performed in the light quark mass region, a first-order triple endpoint was found, corresponding to the point where three different first-order lines terminate: One corresponds to the separation between different $Z(3)$ sectors and the other two correspond to the link bewtween the neighboring endopoints, as shown in figure (2.6), with *dashed-lines*.

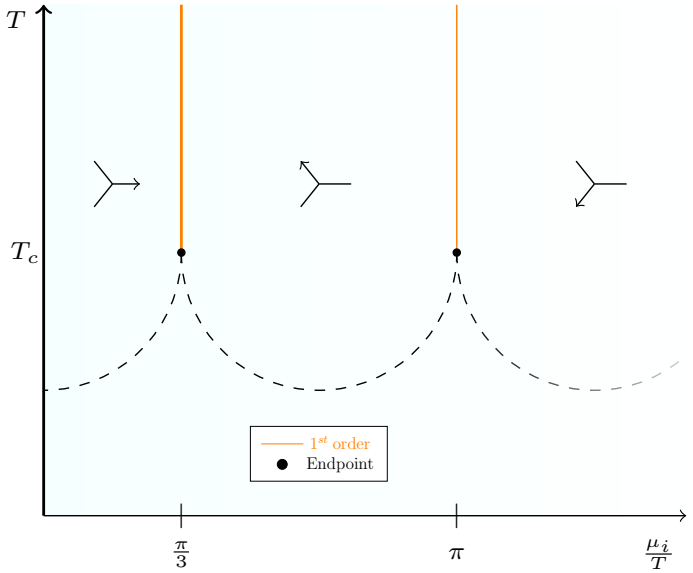

Figure 2.6: *The $(T, \mu_i/T)$ plane, with two first-order lines corresponding to the critical values of μ_i, separating the plane into three areas with different phases of the Polyakov Loop. The nature of the endpoints, as well as the nature of the dashed lines between the endpoints, depends on the number of flavours and quark masses.*

Varying the mass values, the same scenario is found in the heavy-mass region, whereas a different realisation of the endpoint characterises the mass region inbetween, resulting in a second-order phase transition. Thus, the phase diagram at the Roberge-Weiss chemical potential value, namely the Roberge-Weiss plane, for two degenerate flavours is separated into three areas, depending on the quark masses. Due to the nature of critical endpoints, the connection between the different areas is realised through tricritical mass boundaries. The values of the tricritical masses is highly dependent on the lattice cutoff: Investigations at finer lattices using $N_\tau = \{6, 8\}$ and unimproved Wilson fermions [75], and $N_\tau = 6$ with unimproved staggered fermions [76], provided a clear picture of this feature.

The $N_f = 2 + 1$ scenario

The investigation of the nature of the critical endpoints for $N_f = 2 + 1$ gives more contraints in the definition of the QCD phase diagram. In 2014, it was shown [77] the compatibility for on $N_\tau = 4$ lattices with a first-order phase transition in the chiral limit. In a more recent work from 2016 [78], simulations using $N_f = 2 + 1$ quark flavours and $N_\tau = \{4, 6\}$, resulted in a critical endpoint in the Z_2 universality class for a physical pion mass approximatively equal to 135 MeV, using stout improved staggered fermions. Confirmation to these results were provided in 2019 [79], for fixed strange quark mass and varying the light-quarks one in three different values, corresponding to pion masses of 100 Mev, 70 MeV and 50 MeV, showing the presence of a Z_2 endpoint. Also, in 2022 [80], by involving again improved staggered fermions, a second-order phase transition in the Z_2 universality class for pion masses in the range $40\,\text{MeV} \leq m_\pi \leq 130\,\text{MeV}$ was found. These results can be combined to the investigation of the chiral limit for $N_f = \{2, 3\}$ when using non-zero imaginary chemical potentials, as it will be discussed in the next Chapters.

The situation for $N_f = 3$ is not much different from what it has been observed for $N_f = 2$. Thanks to previous investigations [61; 81], simulations with staggered fermions for three degenerate quark flavours and $N_\tau = 4$ [82] confirmed the presence of two tricritical mass values on the Roberge-Weiss plane, separating the Z_2 region corresponding to *intermediate* masses from the first-order triple ones in the light and heavy-masses regimes. At this point, having in mind the main ingredients to characterise the QCD phase diagram, it is worth to collect and assemble the results from $N_f = \{2, (2+1), 3\}$ and $\mu_i \neq 0$ as for the Columbia plot. In figure (2.8) are reported the sketches of the extended Columbia plot, where the axis $(\mu/T)^2$ has been added, considering the. The two dimensional Columbia plot from the previous section corresponds to the plane $(\mu/T)^2 = 0$ and both the scenarios for $N_f = 2$ are reported, for ease of convenience. The $N_f = 3$ scenario is represented along the diagonal axis which connects the heavy and light-mass corners. Considering the two first-order regions and moving to $-(\mu/T)^2 \neq 0$ values, a general inflation can be observed when approaching the Roberge-Weiss plane [81; 83], and the Z_2 boundaries which delimit these two first-order regions extent as well towards the Roberge-Weiss plane by means of Z_2 surfaces. At the Roberge-Weiss critical value $(\mu/T)^2 = -(\pi/3)^2$, the first-order phase transition regions become first-order triple ones, due to a combination of a $Z(3)$ transformation and the explicit breaking of the chiral symmetry, where $\langle\bar{\psi}\psi\rangle \neq 0$ and carry both a positive or a negative sign. In this case, the $N_f = 2$ chiral limit is represented by a line of quadruple points, whereas the Z_2 boundaries become lines of tricritical masses, which separate the first-order triple regions from the Z_2 one, which here replaces the crossover from the Columbia plot.

2.1.4 The tricritical scaling

In the previous section we mentioned more than once the presence of a tricritical scaling region, referred to the behaviour of the Z_2 critical boundary. From the theory, assumed the quark masses to be a scaling field, the tricritical scaling region is where the quark mass field scales according to some specific tricritical exponents [84] and, in general, its identification can be a difficult task. In [9], an example the analysis of the tricritical scaling in the proximity of the chiral limit, when using different N_f values, is given. For each simulated N_τ, a set of critical quark masses belonging to the Z_2 boundary were computed, for different N_f values simulated, as shown in figure (2.7). The identification of the critical masses can be complicated when approaching the chiral limit: Indeed, being simulations here prohibited, one can think about simulating in the proximity of such limit, considering lower and lower bare quark masses on the lattice. But, as we will see in the next Chapters, this is not always a good strategy, since it can lead to problems related to the quality of the data to be produced. A good technique to gather information in the chiral phase transition in the chiral limit, as already mentioned in section 2.1.1, consists in performing *extrapolation* to the chiral limit for a specific scaling field. As in figure (2.7), using different N_f values for $N_\tau = \{4, 6\}$, it was possible to realise extrapolation which is compatible with a tricritical scaling, resulting in a specific N_f^{tric} value when the two extrapolation lines intersect the x-axis: This is the point where the first-order triple lines in the chiral limit meet the second-order ones, for different N_τ values. The extrapolation lines, for a specific N_τ value, are drawn according to equation

$$N_f^c(am(N_\tau), N_\tau) = N_f^{\text{tric}}(N_\tau) + \mathcal{A}_1(N_\tau)(am)^{2/5} + \mathcal{A}_2(N_\tau)(am)^{4/5} + \mathcal{O}((am)^{6/5}), \tag{2.2}$$

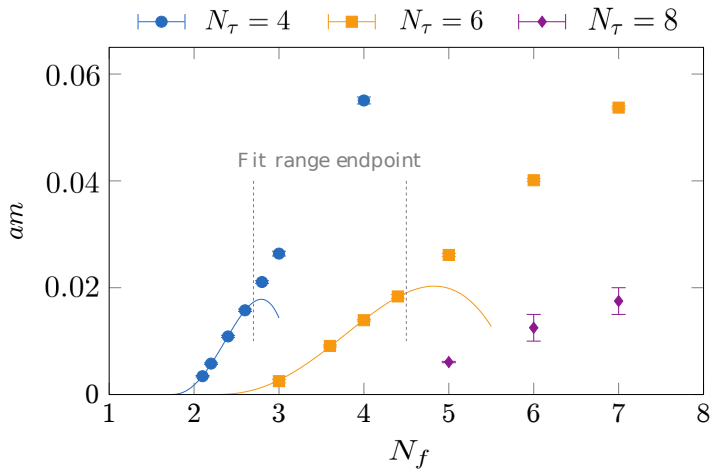

Figure 2.7: *The (am, N_f) plot, from [9]. The different points correspond to critical masses on the Z_2 boundary, for different lattice temporal extents.*

where am are the bare quark masses on the lattice, which scale according to the tipical tricritical scaling powers up to the next-to-leading order, whereas $\mathcal{A}_1(N_\tau)$ and $\mathcal{A}_2(N_\tau)$ are extrapolation parameters to be identified, depending on the lattice temporal extent. On the contrary, if one considers again the plot to the right in figure (2.2), the scaling field to be used in order to investigate the tricritical scaling would be the strange quark mass. Analogously to equation (2.2), in the proximity of the $N_f = 2$ chiral limit, the scaling would be described by

$$m_s(m_{ud})^c = m_s^{\text{tric}} + \mathcal{A}m_{ud}^{2/5} + \mathcal{O}((am)^{4/5}), \tag{2.3}$$

where clearly the tricritical point for $m_{ud} = 0$ is given by m_s^{tric}. A tricritical scaling is also observed for the Z_2 boundary as the Roberge-Weiss plane is approache, as the values of the chemical potential are sufficiently close to the Roberge-Weiss one. But, as the investigation of this area of the 3D Columbia plot does not belong to the topic of interest of this dissertation, we will not add more details about.

2.2 The QCD phase diagram at strong coupling

The investigation of the QCD phase diagram by means of strong coupling techniques applied to the theory has been estensively performed throughout the last forty years. As discussed in the previous Chapter, the presence of the sign problem when using a non-zero chemical potential on the lattice becomes a serious impediment to simulations, although a series of techniques have been developed, resulting successful in the $(\mu_B/T) \lesssim 1$ region of the phase diagram. Using strong coupling expansions in the theory provides useful tools to make the sign problem, at least, milder and results in further elements to constrain the QCD phase diagram in the cold, dense region. The investigation of the strong coupling regime and strong coupling limit, that for ease of notation will be indicated from now on,

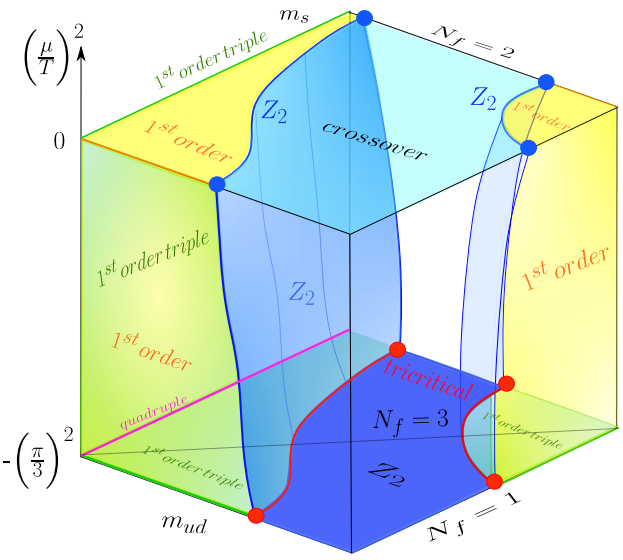

(a)

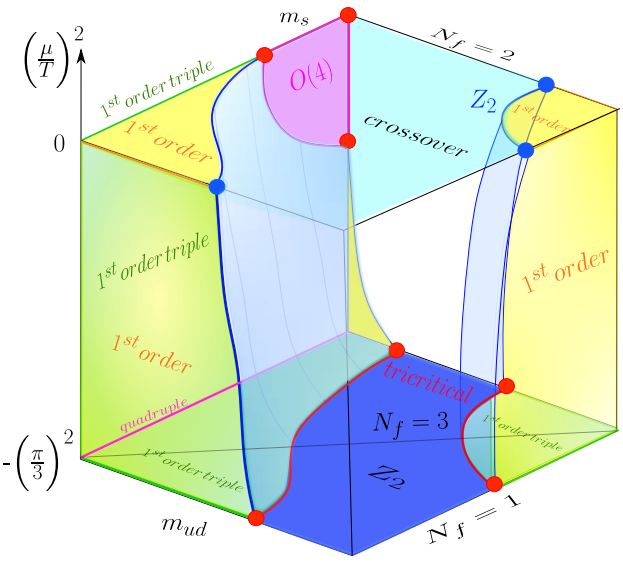

(b)

Figure 2.8: *Schematic representation of the 3D Columbia plot for $N_\tau = 4$, when using both the scenarios for the $N_f = 2$ chiral limit. The red points represent tricritical points whereas the blue points refer to Z_2 points. Inspired by figures 2.12 ans 2.13 of [15] and [72].*

respectively, as SCR and SCL, has been realised both making use of mean field theory and Monte Carlo methods. It has developed together with the investigation of the weak coupling regime, whose results define constraints in the $\mu_B/T \lesssim 1$ region [2]. In this section, we will briefly discuss the chronology of the strongly coupled QCD techniques and how the QCD phase diagram in the SCL has been structured up to these days.

2.2.1 Mean field techniques in strongly coupled QCD

The employement of analytic methods based on the computation of effective Lagrangians [85; 86] for different number of colors brought, in 1985 [87], to some interesting results about the nature of the chiral phase transition in the SCL at finite density and $N_f = 1$. These results consist in a second-order chiral phase transition for SU(N = 2), whereas the order was found to be first for SU(N $\geq$ 3), the latter with critical baryon chemical potential $\mu_c \simeq 290$ Mev. In 1986 [88] a detailed analysis was proposed for the chiral phase transition, deriving an effective potential and studying its dependence on β, as the number of colors and the quark masses were varied, for $N_f = 1$. In particular, in the massless SU(3) case a first-order phase transition was found for $\beta \gtrsim 0.4$ [3] and a second-order one for lower β values. Confirmations arrived when also considering corrections of the order of $1/g^2$ to the strong coupling expansion of the free energy for $SU(3)$, as well as $1/d$ expansion [4]. In this scenario, for $N_\tau = 4$ and $d = 3$, at zero density [89], a second-order chiral phase transition was found, corresponding to a critical temperature of $T_c = 220$MeV for $\beta = 0$, whereas a first-order one was found for lower temperature values, with some specific critical baryon chemical potential values, μ_c. For $\beta = \{2, 3, 5\}$, the critical temperature boundary between the first and the second-order phase transition was found to stay approximatively stable around $T_c = 220$MeV, whereas the corresponding μ_c values became larger as β was made larger. Also, the nature of the phase transition was found to be dependent on number of flavours [90], both in the SCL and SCR, at zero density and finite temperature. On the contrary, no dependence on N_f was shown at zero temperature. A more detailed description of the QCD phase diagram at strong coupling was proposed in 2004 [91], for $N_c = 3$ and $N_f = 4$ and finite baryon chemical potential, using staggered fermions: In the chiral limit, a second-order phase transition was found for higher temperature values whereas a first-order one characterises the lower temperature region, as the baryon chemical potential is varied. Furthermore, the two lines, which describe the two different phase transitions, meet in a tricritical point. When involving non-zero masses, the second-order line is reduced to an analytic crossover, whereas the first-order one is still found, although for higher values of μ_B. This surviving line terminates in a critical endpoint, whose nature can only be second-order. A more recent work from 2009 [92] showed how the position of the tricritical point in the (T, μ_B) plane varies for $N_f = 1$ staggered fermions, when $\beta = \{0, 3, 4.5, 6\}$, always given in lattice units. As a result, the tricritical point has been found in the SCL up to $\beta = 3$ and coincides with lower positions in the plane as β grows. For $\beta \geq 4.5$, the first-order line does not terminate in the second-order one, namely a critical endpoint appears, which is not a tricritical point. In general, the extension of the second-order region becomes shrinker

[2] Just to give an idea of the tipical β values in such regime, it is worth to report again the work [9], where simulations where performed for $4.73 \lesssim \beta(a) \lesssim 5.24$, corresponding to a weak coupling regime

[3] Here, the β values are reported in lattice units. We will omitt the explicit dependence on the lattice cutoff, but it is understood when the values refers to lattice simulations.

[4] Here d denotes the space dimension.

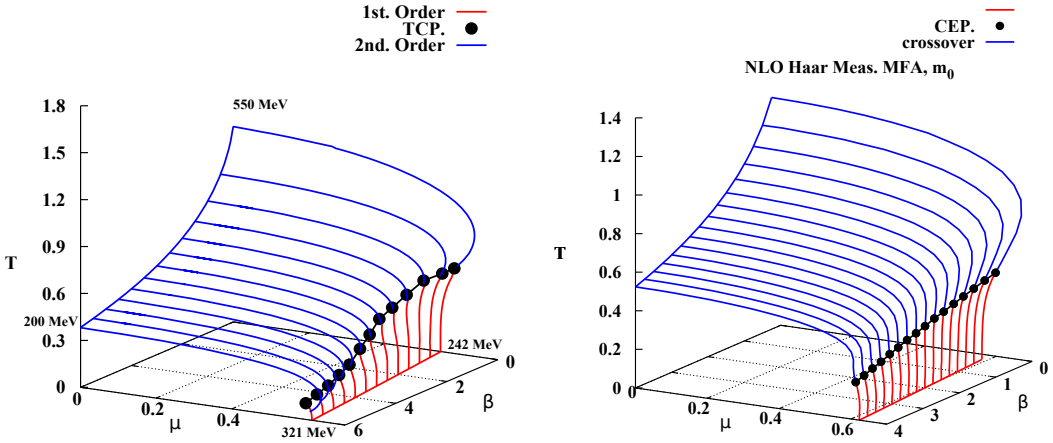

Figure 2.9: *The QCD phase diagram in the SCR from mean field approximation. On the left, the investigation on the tricritical point position in the diagram using the Haar measure mean field approximation; on the right, the results about the critical endpoint involving the Weiss mean field approximation. In both the cases, $\mathcal{O}(\beta)$ corrections have been considered. From [94].*

as moving towards the continuum limit $\beta \longrightarrow \infty$ [5]. The investigation of the critical end point and the tricritical point in the phase diagram has been persued also throughout the last decade. In particular, the study of the chiral phase transition when including $\mathcal{O}(1/g^4)$ correction terms and leading order Polyakov terms in theory [93] led to confirmation of the behaviour of the two points of interest [94]. Indeed, the critical endpoint was found for lower values of temperature as the beta values considered were made larger, and the same behaviour was found for the tricritical point, namely both the second-order and the crossover regions become more dominant as moving from zero to finite β values.

2.2.2 Monte Carlo techniques at strong coupling

The nowaday knowledge about the QCD phase diagram at strong coupling has also received major contributions from the development of suitable Monte Carlo methods, applied to QCD, in such regime. Two pioneering works about this topic were published in 1984 [95] by P. Rossi and U. Wolff and 1985 [96] by U. Wolff. Here, the authors showed that, for finite lattice volumes and number of colors, the partition function of QCD in the SCL, when using staggered fermions, can be made equivalent to the one of a *monomer-dimer system* [97] in statistical mechanics, where the degrees of freedom are given by monomer, dimers and baryon-antibaryon loops. This is realised as the integration over the gauge links is performed first, leaving the theory with only color singlets, namely the hadrons. Indeed, given a lattice with a certain number of sites, one has for $SU(N)$ that:

- *Monomers* represent the fermionic degrees of freedom which come in the partition

[5] It is here worth to recall that working with $N_f = 1$ species of staggered fermions means to work with $N_f = 4$ degenerate quarks in the continuum limit.

function as a mass-like term, and occupy the lattice sites in a number from 0 to N;

- *Dimers* represent a combination of fermionic degrees of freedom, which realises the meson contribution to the theory. They live along the links between different lattice sites in a number from 0 to N;
- *Baryonic* and *Antibaryonic loops* represent, respectively, the contribution coming from baryons and antibarions to the theory and are represented by closed loops on the lattice. These are isolated objects, namely if a lattice site is occupied by one of such loops, then no other object can be found there.

This representation allowed to determine some of the most important features of the chiral phase transition in the SCL and SCR by means of Monte Carlo simulations. First results from simulations performed for SU(2) and SU(4) gauge groups [98], on coarse lattices, arrived in 1987. The lack of resuts for SU(3) was ascribable to the nature of the weights of the baryon loop, since they turned to be positive only for even values of the gauge group dimension N, permitting Monte Carlo simulations to be performed only in these cases. The outcome of this work provided a first idea of the phase diagram based on numerical methods, identifying for SU(4) a first-order chiral phase transition in the dense and cold region whereas a second-order one appeared in the opposite region of parameteres. The outcome for SU(2) was more complicated: In particular, when varying the baryon chemical potential at low temperatures, three different regions are identified, depending on the values assumed by the baryon condensate, separated by second-order boundaries. These results, both for SU(2) and SU(4), were obtained by making use of bare quark masses values close to the chiral limit, and showed a good agreement with the results from mean field theory studies. A resolution to the challenge provided by the sign of the weights carried by baryon loops was proposed in [99]. Simulations for SU(3), $N_f = 4$ and $N_\tau = 4$ in the SCL were provided for non-zero baryon chemical potential, given the *Monomer-Dimer-Polymer* (MDP) representation for the partition function of such system, which also makes the sign problem milder. A first-order chiral phase transition was found, corresponding to a critical chemical potential value on the lattice $a\mu_c = (0.69 \pm 0.015)$ for bare quarks mass $am = 0.1$, whereas the extrapolation to the chiral limit resulted in $a\mu_c = (0.63 \pm 0.02)$. A further investigation [100] for $SU(3)$, by means of one single species of staggered fermions, confirmed the second-order phase transition to be described by the same universality class as the three dimensional $O(2)$ group, in agreement with the early findings by [8]. In more recent times, the QCD phase diagram in the strong coupling limit has been deeper constrained [101] from direct simulations in the chiral limit. For $\mu = 0$, the location of the critical temperature value where the second-order phase transition takes place was determined for $N_\tau = \{2, 4, 6\}$, showing a discrepacy with the mean field results due to the better accuracy of the methods involved in the latter. For $\mu \neq 0$, the second-order line was found to terminate into a tricritical point at $(aT, a\mu) = (0.94(7), 0.33(3))$. In the latter, an anisotropy parameter was introduced in the theory, which allows to perform simulations for continuous values of temperatures or times [102]. An interesting development was introduced in [103], where gauge corrections up to the order $\mathcal{O}(\beta)$ were included in the determination of the partition function. This technique allowed to constrain the QCD phase diagram also for $\beta \neq 0$ values in the proximity of the SCL by performing simulations for $\beta = \{0.5, 1.0, 1.5\}$, and the results are shown in figure (2.10). The second-order line becomes less dependent on μ as the values of β grow, namely when moving towards the weak coupling regime and, thus, towards the continuum. Furthermore, the position of the tricritical point was found to stay stable at different coupling values, whereas the nuclear critical endpoint

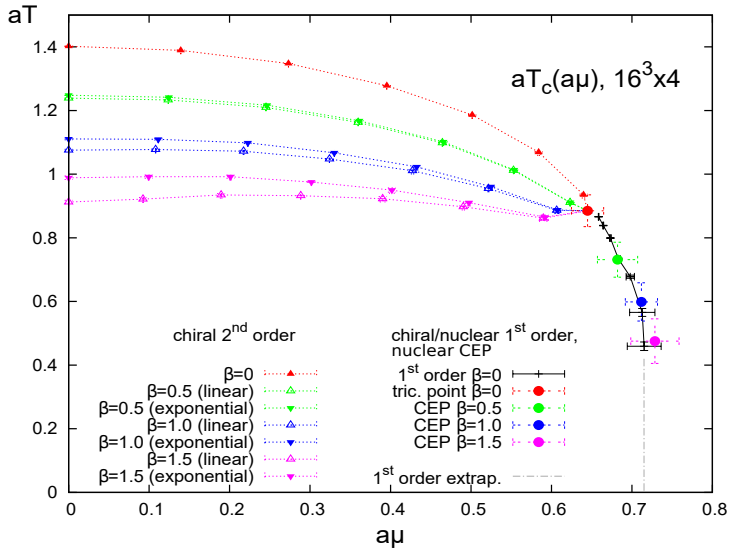

Figure 2.10: *Representation of the QCD phase diagram in the* $(aT, a\mu)$ *plot, from Monte Carlo simulations performed for* $N_\tau = 4$, $N_\sigma = 16$ *and SU(3) in the chiral limit. The extension of the first-order and second-order lines is shown for different* β *values. Figure from [103].*

(CEP) moves to lower temperature values as β is larger. Thus, the effects of adding $\mathcal{O}(\beta)$ correction to the partition function result in a split between the CEP and the tricritical point, which do coincide only in the SCL, as shown more in detail in figure (2.11). Here, the second-order surface moves to lower values of temperature as β becomes larger, since larger β values correspond to finer lattices, resulting in a lower lattice critical temperature values. Recent results [104], obtained by making use of the so called *dual representation* [105] for staggered fermions and the aforementioned lattice anisotropy, showed good agreement with the mean field results [94], confirming that the first-order critical line has no dependence on the values of β, differently from the second-order one.

2.3 Outline of this work

So far in this Chapter we have retraced the history of the Quantum Chromodynamics phase diagram from the Eighties up to these days, both in the weak and the strong coupling regimes, included the strong coupling limit. Naturally, many are the open questions related to this topic aimed to further constrain the picture we have described so far, resulting in a fervent research activity from many different research groups, and that is also the reason why we clearly pointed out that the structure of the QCD phase diagram, for different parameters setup, is in a constant evolution. This thesis is devoted to present some contributions to the study of the chiral phase transition in the weak and strong coupling regimes by making use of Monte Carlo methods, and consists of two different projects, which will be shorty introduced in the next lines of this section.

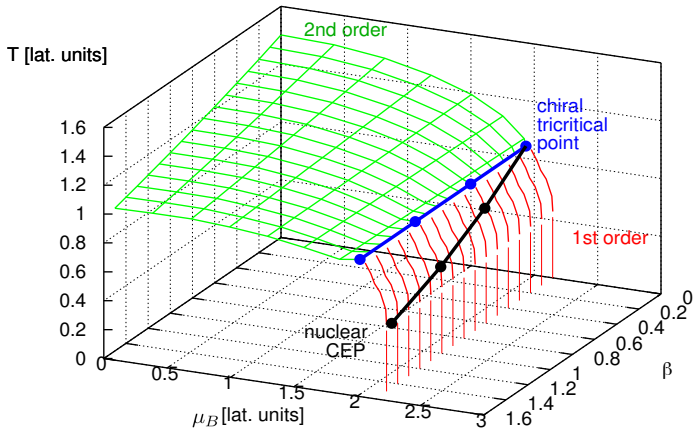

Figure 2.11: *Representation of the results from [103] in the SCL and SCR, from Monte Carlo simulations. The third axis provides the explicit dependence of the chiral phase transition on β. Figure from [106].*

2.3.1 The chiral phase transition at non-zero imaginary baryon chemical potential for different numbers of quark flavours

In figure (2.8), focusing on the description about the light-mass corner, it has been pointed out the behaviour of the the first-order region, laying on the Columbia plot, which undergoes inflation when moving to non-zero values of the baryon chemical potential, as the value of $(\mu/T)^2$ approaches the Roberge-Weiss one. The boundary, realised in the Columbia plot by a Z_2 critical line of masses, becomes a Z_2 critical surface as moving towards the Roberge-Weiss plane, where the first-order region is converted into a first-order triple region whereas the Z_2 surface terminates into a line of tricritical mass points. Also, some recent results from [9] have been reported, where the investigation of the chiral phase transition at zero density was performed by means of Monte Carlo simulations for lattice temporal extents $N_\tau = \{4, 6, 8\}$ and non-integer N_f values. This strategy, as described in the previous section, allowed to observe the tricritical scaling of the Z_2 boundary in the proximity of the chiral limit for different lattice temporal extents, and allowed to constrain the order of the chiral phase transition for $N_f = 2$, in the continuum and chiral limit. One of the two projects which build up this work is based on the same strategy involved in [9], applied to a non-zero imaginary baryon chemical potential scenario. The main idea is to investigate the extension of the first-order region in the *light corner* by means of numerical simulations involving a non-zero μ_i value and, at least for $N_\tau = 4$ lattices, the first-order chiral region is expected to inflate, as shown in figure (2.8). The value of the imaginary chemical potential involved differs from the Roberge-Weiss one: This detail ensures to investigate a Z_2 boundary between a first-order chiral region and a crossover one. Besides this feature, by the end of this project we expect to gather information concerning the order of the chiral phase transition for $N_f = 2$, in the continuum limit, as non-zero density is involved. Indeed, if a tricritical scaling region can be found also at $\mu_i \neq 0$, for different lattice temporal extents, then a discussion about the dependence of the order of the chiral phase transition on the values of μ_i can be done. This project is the outcome of a joint cooperation of the author of this thesis and his collegues Reinhold Kaiser and Dr. Michael Fromm, supervised by Prof. Dr. Owe Philipsen.

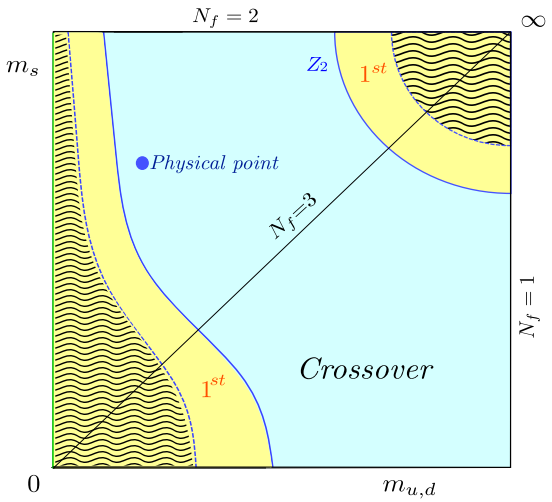

Figure 2.12: *Schematic representation of a section of the 3D Columbia plot in figure* (2.8). *For a generic* $-(\pi/3)^2 < (\mu_i/T)^2 < 0$, *the first-order chiral regions are represented in yellow and compared to the extension at* $\mu_i = 0$ *in the Columbia plot, distinguished by a wavy pattern.*

2.3.2 The chiral phase transition from strong to weak coupling

The second project is devoted to the investigation of the order of the chiral phase transition in the strong coupling regime, at zero density. Based on the results in the weak coupling regime from [9], the extension of the first-order chiral region in the (am, N_f) plane, as reported in figure (2.7), strongly depends on the temporal extent used during simulations, namely on the lattice cutoff, as it becomes shrinker for larger N_τ values. For fixed N_f, it is then possible to schematically reproduce this result in the $(am/aT, aT)$ plane, where $aT = 1/N_\tau$: Involving the results for $N_\tau = \{4, 6, 8\}$, a monotonic behaviour of the Z_2 boundary line can be appreciated, as in figure (2.13), with a tricritical scaling in the proximity of the chiral region, when using N_f as scaling parameter. At this point, moving to the strong coupling regime means to perform simulations on the coarsest possible lattice, namely when using $N_\tau = 2$. This can be easily shown by taking into account equation (2.1) and, recalling that $g_0(a)$ scales on the lattice according to the spacing a. Thus, for fixed temperature T, one observes that $N_\tau = 1/aT$:

- Assumes smaller values as a becomes larger, thus for larger $g_0(a)$ values;
- Vice versa, assumes larger values as a becomes smaller, thus for smaller $g_0(a)$ values.

The aim of this project resides in the interest of constraining the order of the chiral phase transition in the strong coupling regime, by investigating the critical Z_2 boundary. This will be done for two numbers of flavour, $N_f = 4$ and $N_f = 8$ and the results will be compared to the studies in literature presented as references to the previous section. Based on the latter, we expect to identify a small critical mass belonging to the Z_2 critical line for $N_f = 8$ when compared to the critical mass identified for $N_\tau = 4$, whereas for $N_f = 4$ we expect to detect a more ambiguous scenario, which will be better discussed

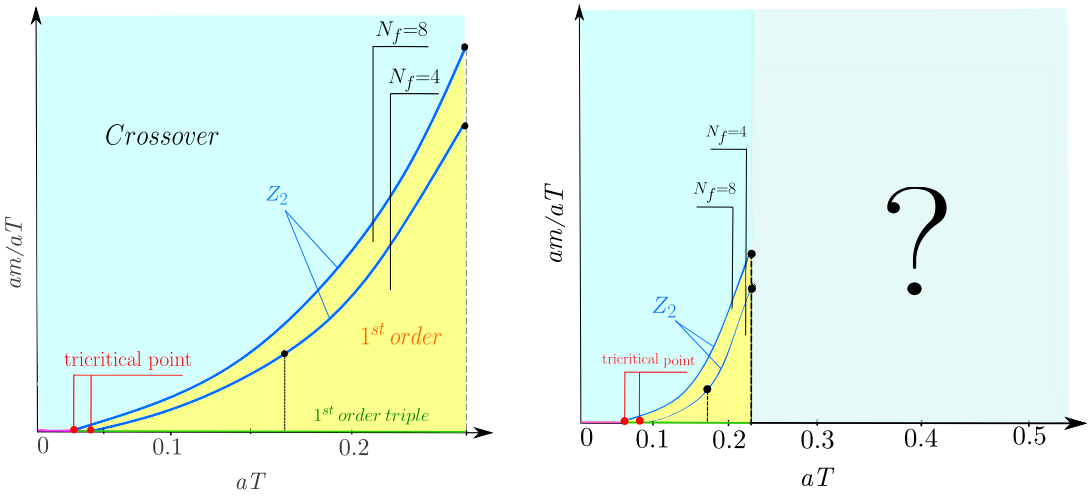

Figure 2.13: *Left: The extension of the first-order chiral region in the weak coupling regime in the* $(am/aT, aT)$ *plane, for* $N_f = \{4, 8\}$ *and* $N_\tau = \{4, 6, 8\}$ *[9]. The black dots along the* Z_2 *boundary represents the corresponding critical masses computed by means of Monte Carlo techniques. Right: What does the extension of the first-order chiral region to larger* aT *values (lower* N_τ*) look like?*

in the last Chapter of this work. This difference is due to the reduced extension of the first-order region for $N_f = 4$ when compared to $N_f = 8$, from the results shown in the weak coupling regime: In general, we expect to observe a non-monotonic behaviour of the Z_2 boundary when moving to larger aT values in figure (2.13), namely a maximum is expected inbetween $aT = 0.25$ and $aT = 0.50$ (corresponding to $N_\tau = 4$ and $N_\tau = 2$, respectively), followed by a negative slope of the same line. As also reported in [53], the second-order chiral phase transition expected in the chiral limit for $N_f = 2$ is well described by means of the 3D $O(2)$ spin model universality class, when the lattice cutoff stay finite, which is the case of the strong coupling regime. Thus, the investigation of the order of the chiral phase transition, at least for $N_f = 4$, will involve a comparison between finite-size scalings based on the Z_2 and the $O(2)$ universality classes. This project has been autonomously developed by the author, under the constant supervision of the supervisor Prof. Dr. Owe Philipsen.

Chapter 3

Lattice simulations and analysis tools

The core of this work consists in performing Monte Carlo simulations on the lattice, applied to Quantum Chromodynamics, both in the weak and strong coupling regimes, in order to produce a suitable amount of data, necessary to investigate our fields of interests. In this Chapter the necessary algorithms will be introduced, mostly taking as a reference Chapter 16 of [10], Chapters 4 and 8 of [11], and [107; 108]. The strategy involved will be discussed in details, together with the analysis tool used to extrapolate the results. Also, in the last section of this Chapter we will briefly recall the code used to perform simulations, together with the software used to handle simulations on the clusters and realise data analysis.

3.1 Monte Carlo methods

In Chapter 1, the QCD partition function has been introduced when a generic number of flavours N_f is considered in the theory, and this object, as already mentioned, is essential when the expectation value of a generic observable $\mathcal{O}$ is to be evaluated. After integrating out the fermionic degrees of freedom inside the partition function, the latter will only depend on the gauge fields, to which we will refer here as U and, based on this prescription, it reads

$$\mathcal{Z}[U, N_f] = \int \mathcal{D}[U](\det D[U])^{N_f} e^{-S_g[U]}, \tag{3.1}$$

where $S_g[U]$ is the pure gauge action as reported in equation (1.13), which comes inside the Boltzmann factor $\exp\{-S_g[U]\}$, whereas $(\det D[U])^{N_f}$ represents the remnat of the fermionic contribution to $\mathcal{Z}[U, N_f]$. The evaluation of this object through Monte Carlo simulations is a highly prohibitive process: The dimension of the integration space can be extremely huge, making, in fact, impossible to directly use it in simulations without a proper simplification work on its form [1], and one way to solve this challenging point consists in resorting to the so called *importance sampling*. Making use of the partition function given in equation (3.1), the evaluation of the expectation value of a generic observable $\mathcal{O}$ reads

$$\langle \mathcal{O} \rangle [U] = \frac{1}{\mathcal{Z}[U, N_f]} \int \mathcal{D}U \mathcal{O}[U](\det D[U])^{N_f} e^{-S_g[U]}, \tag{3.2}$$

[1] An example of this problem is given in Chapter 4 of [11] for a 4D Ising spin model.

where the terms can be rearranged such that

$$\langle \mathcal{O} \rangle = \int \mathcal{D}U P[U] \mathcal{O}[U], \tag{3.3}$$

after the definition of

$$P[U] = \frac{1}{\mathcal{Z}[U, N_f]} \, e^{-S_g[U]} (\det D[U])^{N_f}. \tag{3.4}$$

The interpretation of $P[U]$ relies on statistical mechanics principles: Indeed, this can be understood as a probability distribution, according to which the gauge fields U are distributed, while the femionic determinant $(\det D[U])^{N_f}$ inside $P[U]$ represents a weight factor, whose values must be non-negative and real in order to validate this interpretation. At this point, one can suppose to sample the range of values that the gauge fields can assume by determining a generic number N of possible entries, such that

$$\langle \mathcal{O} \rangle [U] = \frac{1}{N} \lim_{N \to \infty} \sum_{n=1}^{N} \mathcal{O}[U_n], \tag{3.5}$$

where U_n are the values of the gauge fields sampled according to the probability distribution in equation (3.4) [2]. Due to the presence of the Boltzmann factor in (3.1), the contributions to $\langle \mathcal{O} \rangle [U]$ will highly depend on the values assumed by $S_g[U]$ and consequently some weights will acquire more *importance* when compared to other ones: This is the essence of the importance sampling. In order to collect the gauge field configurations U_n, following the probability distribution $P[U]$, one can build up stochastic chains of configurations by assuming a random configuration as the initial one and building up, step by step, a sequence which will tend to the distribution $P[U]$ at the equilibrium. The sequences are ordered by the index n, which corresponds to the *computer time* at which a specific configuration has been computed. The chains of configurations are named *Markov chains* and the subsequent steps are the *Monte Carlo steps*, which realise the update of the values of the gauge configurations. A generic update from the configuration $U_{n-1} \equiv U$ to the configuration $U_n \equiv U'$ is subjected to a transition probability, which only depends on the value of the two subsequent configurations and does not accunt for the index n in the chain. For more details about this point, we refer to [11], while here we avoid adding more information.

When dealing with the Dirac operator on the lattice, a general technique which can be used consists in the even-odd preconditioning [109]. The matrix representing $D[U]$ can be defined through a different *organisation* of the lattice sites, depending on the nature of the indices they are labelled with. Indeed, one can imagine to use a multi-index vector to identify one single site, but, when $D[U]$ is to be evaluated, the process can result to be complicated and poorly efficient in time. Then, the indices can be recombined such that the lattice sites can be separated depending on the overall index they carry and, restricting for ease to notation to a two-dimensional lattice, one obtains

$$D[U] = \begin{bmatrix} D_{ee} & D_{eo} \\ \\ D_{oe} & D_{oo} \end{bmatrix}, \tag{3.6}$$

[2] The U_n samples are also known as gauge field configurations.

where e and o refers, respectively, to *even* and *odd* lattice site indices. Taking into account a two dimensional volume, the new indices are obtained according to the following prescription:

- $(-1)^{nx+ny} = +1 \longrightarrow$ even,
- $(-1)^{nx+ny} = -1 \longrightarrow$ odd,

where nx and ny are the indices referred to the $n{-}th$ site. In this way, the Dirac operator is represented by a four-block matrix, which simplifies the computation process during simulations. In general, Monte Carlo algorithms can be applied to different scenarios, including different fermions discretisations on the lattice. In this work, staggered unimproved fermions have been used in both the projects and the algorithm involved to compute Markov chains is the Rational Hybrid Monte Carlo algorithm (RHMC), which will be briefly discussed in the next sections.

3.1.1 The Rational Hybrid Monte Carlo algorithm

In Chapter 1 and in Appendix A it has been shown that, when using the staggered formulation to discretise the fermionic action for one-flavour fermions, the continuum limit results in four degenerate quark flavours (tastes), as a remnant of the doubling problem. At any chance, in order to get rid of this degeneration in the continuum limit, a useful technique consists in applying the so called *rooting*. Considering the partition function in equation (3.1), one takes the fourth-root of the determinant such that

$$\mathcal{Z}[U, N_f] = \int \mathcal{D}[U](\det D[U])^{\frac{N_f}{4}} e^{-S_g[U]}, \tag{3.7}$$

which is legitimate since in the continuum limit the four degenerate fermions are represented by $D \otimes \mathbb{1}$, where D is a one-taste Dirac operator. In this way, as explained in [110], one obtains that

$$\det(D \otimes \mathbb{1}) = (\det D)^4,$$

thus taking the fourth-root allows to obtain again $(\det D)$. Although this technique turned out to enhance the process of data collection during simulations and to avoid the undesired degeneration in tastes in the continuum limit, it still presents some problematics related to validity of its application. In particular, most is referred to the non-locality of the theory once the rooting technique is used and if it really represents a good strategy to take the fourth-root of the fermion determinant before applying the continuum limit, namely for a lattice spacing $a \longrightarrow 0$. For more details we still refer to [110], whereas here we mostly focus on the description of the algorithms contained inside the RHMC, showing how they are involved in data production.

In the next sections we will give an introduction to the main ingredients that characterise the RHMC algorithm, namely, in the order of discussion, the pseudofermion fields and the gauge fields and gauge momenta fields. Also, the methods involved in the update of such objects during the Markov chain production will be discussed.

The pseudofermion field

The application of Monte Carlo techniques to pure gauge theory was already understood at the beginning of the Eighties. In 1981 [111], an extension to a theory including fermionic

degrees of freedom was proposed and, still today, it represents a peculiar feature of Monte Carlo simulations. After integrating out the fermionic degrees of freedom from the partition function, the computation of the fermion determinant when evaluating a generic observable can become extremely complicated: The introduction of the *pseudofermion fields*, χ and $\chi^\dagger$, allows to treat this object analytically by means of a bosonic Gaussian integral,

$$\alpha \det D[U] = \int \mathcal{D}\chi \mathcal{D}\chi^\dagger \exp\Big(-\chi^\dagger D^{-1}[U]\chi\Big), \tag{3.8}$$

where the pseudofermion fields are full-fledged boson fields, whereas α is a constant. The basic constraint that must hold for equation (3.8) to be valid and to guarantee a convergence of the integral consists in requiring $D[U]^{-1}$ to be positive-defined [107]. One way to fullfill such statement comes from a simple mathematical observation,

$$\alpha \det\big(D^2[U]\big) = \alpha \det\Big(D[U]D^\dagger[U]\Big) = \int \mathcal{D}\chi \mathcal{D}\chi^\dagger \exp\Big(-\chi^\dagger (D[U]D^\dagger[U])^{-1}\chi\Big), \tag{3.9}$$

that, as it will shown in the next lines, will be strictly connected to the pseudofermion field generation for a Monte Carlo step. Combining equations (3.9) and (3.7), one obtains[3]

$$\mathcal{Z}[U, N_f] = \int \mathcal{D}[U] e^{(-\chi^\dagger (D[U]D^\dagger[U])^{-1}\chi)^{N_f/4}} e^{-S_g[U]}, \tag{3.10}$$

and, introducing the field

$$R = (D[U]D^\dagger[U])^{-N_f/8}\chi, \tag{3.11}$$

equation (3.9) can be rewritten as

$$\det\big(D^2[U]\big) \propto \int \mathcal{D}\chi \mathcal{D}\chi^\dagger \exp\Big(-R^\dagger R\Big). \tag{3.12}$$

The latter represents a Gaussian distribution: This ensures the R field to be generated throughout the Markov chain production from a Gaussian heat bath, and, to further simplify the process, the entire evaluation on the lattice can be made by restricting either to the even or odd block of $D[U]$ shown in equation (3.6). But how can the pseudofermion fields be evaluated during Monte Carlo simulations?

Suppose to have a generic Hermitian matrix A, which can be diagonalised through the unitary transformation

$$A = UBU^{-1},$$

where U is a unitary matrix whereas B is a diagonal matrix. By letting a function act on the matrix A, one obtains

$$f(A) = f(UBU^{-1}) = Uf(B)U^{-1},$$

and the latter, as shown in detail in section 3.1.3 of [15], can be expanded by means of a *rational approximation*. Indeed, after the application of a partial fraction expansion, the function $f(A)$ can be written as

$$f(A) \approx \mathbb{1} a_0 + \sum_{j=1}^{N} \frac{a_j}{A + bj},$$

[3]The constant α does not provide a difference in physical terms, thus it has not been reported.

where a_0, a_j and b_j are coefficients to be evaluated[4].

At this point, since the nature of the R, $R^\dagger$ fields is already known, one can take advantage of the rational approximation technique to evaluate the pseudofermion fields at each Monte Carlo step. Considering equation (3.11), this can be inverted in order to extract the field χ as

$$\chi = (D[U]D^\dagger[U])^{N_f/8}R, \tag{3.13}$$

and making use of the rational approximation this can be approximated to

$$\chi \approx \Big(\mathbb{1}a_0 + \sum_{j=1}^{N} \frac{a_j}{A+bj}\Big)R. \tag{3.14}$$

The first term is easy to be computed since it represents the multiplication of the scalar coefficient a_0 to the vector R, whereas the second one can be computed by means of the Remez algorithm [112], which consents to extrapolate the optimal coeffients in the approximation according to the Chebyshev theorem. In reality, it is sufficient to apply the Remez algorithm only to compute the coefficients at the end of the first Monte Carlo step[5], whereas the rest of the update is realised through the application of a solver based on the Multi-shift Conjugate Gradient method [113].

The gauge fields and the gauge momenta fields

The update of the gauge fields during a Markov chain production can be performed by making use of the Molecular Dynamics algorithm. In order to evaluate the gauge fields at each Monte Carlo step, it becomes necessary to introduce in the theory a new arbitrary field, the *gauge momenta field*, which acts as the conjugated field to the gauge one. This can be easily done by taking into account the Hamilton theory of a classical system, which allows to define the needed equations of motion. The first step to perform consists in defining a suitable Hamiltonian for our physical system,

$$\mathcal{H} = \frac{6}{g_0^2}\sum_n \sum_{\mu<\nu}\Big[\mathbb{1} - \frac{1}{3}\,\mathrm{Re}(\mathrm{Tr}\Pi_{\mu\nu}(n))\Big] + \Big[\chi^\dagger (DD^\dagger)^{N_f/4}\chi\Big] + \frac{1}{4}\sum_{\mu,n}\sum_B [H_\mu^B(n)H_\mu^B(n)], \tag{3.15}$$

where the term containing the pseudofermion fields is still restricted to the even or to the odd part of the Dirac operator, while the gauge momenta fields are contained in the third term in (3.15), where

$$H_\mu(n) = \sum_{B=1}^{8} H_\mu^B(n)\frac{\lambda^B}{2},$$

being $H_\mu^B(n)$ eight real numbers, and they are elements of the $SU(3)$ gauge group, namely traceless Hermitian matrices. In equation (3.15), these fields have been introduced analogously to the way it is done in classical theory. Indeed, considering that a trace over the color space has been performed in the third term of equation (3.15), the values of the gauge momenta fields can be generated throughout the building up of the Markov chain according to the probability distribution

$$p(x) = \frac{1}{(4\pi)^{1/2}}\exp\Big(\frac{-x^2}{4}\Big),$$

[4]This approximation holds in a specific interval of eigenvalues of the matrix A.

[5]This point is exaustively discussed in section 3.1.3 of [15].

which resembles the way the pseudofermions fields gets updated by means of a Gaussian heat bath. At this point, it is still to be defined the way the gauge fields can be updated during Monte Carlo lattice simulations. Following [114], one can consider again the Hamiltonian equation in (3.15) and define the equations of motion for the gauge links $U_\mu(n)$ and the gauge momenta fields $H_\mu(n)$ as

$$\dot{U}_\mu(n) = \frac{\partial \mathcal{H}}{\partial H_\mu(n)}, \tag{3.16}$$

$$\dot{H}_\mu(n) = -\frac{\partial \mathcal{H}}{\partial U_\mu(n)}, \tag{3.17}$$

where the evolution is assumed with respect to a fictional time scale τ, conciding with the simulation time. Before working on the latter, one can observe that the gauge momenta fields are conjugated to the gauge fields $A^C_\mu(n)$, contained inside the definition of $U_\mu(n)$. Then, starting from equation (3.16), the equation of motion for one of the eight values of the gauge fields in color space reads

$$\dot{A}^C_\mu(n) = \frac{\partial \mathcal{H}}{\partial H^C_\mu(n)} = \frac{1}{2} H^C_\mu(n). \tag{3.18}$$

With this results, one can explicitly evaluate the time derivative in equation (3.16) as

$$\begin{aligned}\dot{U}_\mu(n) = \frac{dU_\mu(n)}{d\tau} &= \frac{d}{dt}\Big[\exp\Big(ig_0 a \sum_{C=1}^{8} A^C_\mu(n)\frac{\lambda^C}{2}\Big)\Big] \\ &= ig_0 a \sum_{C=1}^{8} \dot{A}^C_\mu(n)\frac{\lambda^C}{2} U_\mu(n) = ig_0 a \sum_{C=1}^{8} \frac{1}{2} H^C_\mu(n)\frac{\lambda^C}{2} U_\mu(n),\end{aligned}$$

which after some algebra can be written as

$$\dot{U}_\mu(n) = iH_\mu(n)U_\mu(n). \tag{3.19}$$

We can now proceed to obtain the analytic form of equation (3.17) by requiring the Hamiltonian (3.15) to be a constant of the motion, namely

$$\frac{d\mathcal{H}}{d\tau} = 0,$$

which consists in the sum of three different time derivatives to be studied separately. Here we will not repeat all the steps: A very detailed analysis can be found in section 3.1.5 of [15], where the final form of the equation of motion for the gauge momenta fields is obtained step by step.

The system of equations (3.16) and (3.17) allows to evolve the gauge fields and gauge momenta fields for the whole duration of a Markov chain production. At the completion of each Monte Carlo step, the Molecular Dynamics algorithm returns a new gauge configuration $U'_\mu(n)$ and the Hamiltonian $\mathcal{H}$ in (3.15) will be updated to a new value, $\mathcal{H}'$. The latter is crucial, since the acceptance or the rejection of the new configuration will depend on it:

- If $\mathcal{H}' \leq \mathcal{H}$, then the new configuration will be accepted;
- If $\mathcal{H}' > \mathcal{H}$, then the new configuration will be accepted according to the probability $p = \exp(\mathcal{H} - \mathcal{H}')$.

This procedure is the essence of the *Metropolis algorithm*, conceived in 1953 by Metropolis et all. [115], which provides an acceptance test to ensure the gauge configuration heavily affected by numeric errors to be rejected. In general, when the $\mathcal{H}'$ differs considerably from $\mathcal{H}$, then the weight of the numerical error can be substantial and the best strategy consists in rejecting the configuration. Thus, $\mathcal{H}' = \mathcal{H}$ and a new Monte Carlo step can be produced. The realisation of a Molecular Dynamics trajectory requires a suitable integrator to solve equations (3.16) and (3.17). The class of integrators which will be involved in this work is presented in details in Appendix B and a furhter discussion will be provided in the next Chapter.

3.1.2 Multiple pseudofermion fields

Performing Monte Carlo simulations in presence of fermion fields requires to find a good balance between the values assumed by the different simulation parameters needed, in order to contain the computational costs. In section 3.1.1 we showed how the fermion determinant can be treated once a pseudofermion field gets introduced in the theory. At any chance, the evaluation of the fermionic force, following the application of the heat bath algorithm, could be distorted by the effects of stochastic fluctuations when only one pseudofermion field is involved [116]. Then, a possible strategy to enhance the quality of simulations consists in introducing in the theory n pseudofermion fields, which allow to redefine the fermion determinant in (3.8) as

$$\det D^2[U] = [\det D^2[U]^{1/n}]^n \propto \prod_{i=1}^{n} \int \mathcal{D}\chi \mathcal{D}\chi^\dagger \exp\Big(-\chi_i^\dagger (D[U]D^\dagger[U])^{-1}\chi_i\Big), \tag{3.20}$$

and the same procedure as in 3.1.1 can be repeated, where the R vector appearing in the heat bath algorithm will now be promoted to a field R_i, with $i = 1, \cdots, n$. The introduction of this strategy provides, besides the reduction of stochastic fluctuations, a reduction of the total numerical cost of a Markov chain production when low quark masses are involved.

3.2 Simulations and analysis tools

In this section we will discuss about the strategy followed in order to persue the aim of both the projects introduced at the end of the previous Chapter. Both requires a large amount of numerical simulations to be performed, in order to produce a suitable number of Markov chains, by means of the RHMC algorithm presented in the previous section. The data produced through simulations are needed to evaluate an observable, namely the order parameter of the chiral phase transition, which will be analysed by means of suitable analysis, described in the following.

3.2.1 The parameter setup

In figures (3.1) and (3.2) is reported, schematically, the parameter setup used to perform simulations both in the weak and strong coupling regimes. This corresponds to a four-dimensional space $(N_f, N_\tau, am, \beta(a))$, where N_f corresponds to the number of quark flavours, N_τ and N_σ are, respectively, the lattice temporal extent and the lattice spatial extent, the latter giving the spatial volume on the lattice as N_σ^3, whereas am represents quark masses on lattice for which simulations are performed, being a the lattice cutoff. The procedure needed to produce data can be summarised as follow:

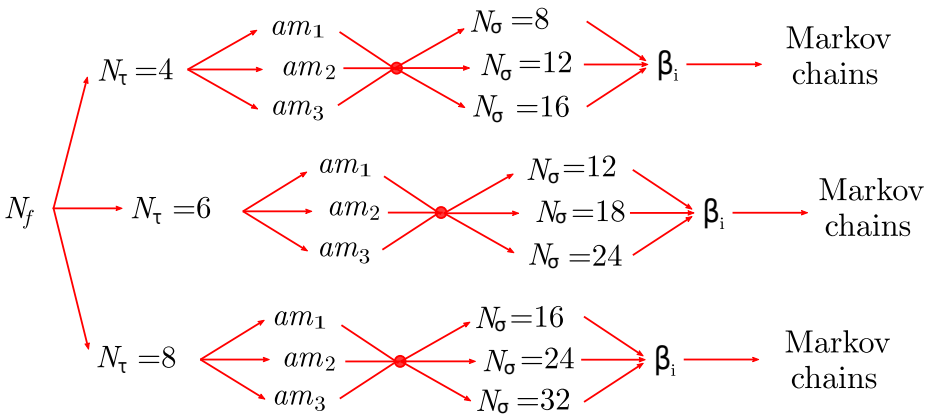

Figure 3.1: *Schematic workflow used to realise the investigation at non-zero imaginary baryon chemical potential.*

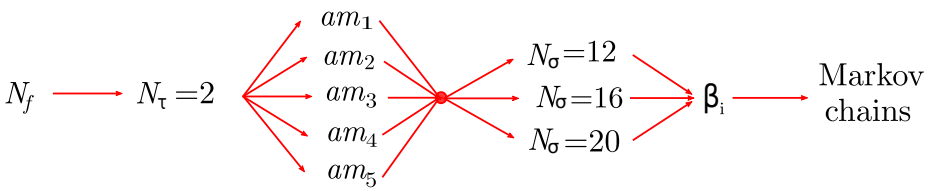

Figure 3.2: *Schematic workflow used to realise the investigation in the strong coupling regime, at zero baryon chemical potential.*

- The number of quark flavours N_f has to be set, and its numerical value can be either integer or non-integer, depending on the aim of the project.

- For any fixed N_f value, different lattice temporal extents are to be set, in order to produce simulations at different lattice cutoffs, in agreement with what has been said in section 1.6.1. Indeed, if temperature is a fixed parameter, one observes from the relations
$$\beta(a) = \frac{2N_c}{g_0^2(a)}, \qquad\qquad N_\tau = \frac{1}{aT},$$
that the variation of the lattice cutoff a through $g_0(a)$ produces a variation of $\beta(a)$ and N_τ. As a result, lower N_τ values correpond to coarser lattices with larger cutoffs, and, vice versa, finer lattices are realised when larger N_τ values are involved.

- As already mentioned, the aim of this work resides in computing some critical quark masses values which belong to the Z_2 critical boundary between the first-order region and the crossover one we want to constrain. This can be achieved by setting, for any fixed N_τ value, different lattice quark masses am to be simulated and, for any fixed am value, simulations are performed for different lattice spatial extents, N_σ, namely three different aspect ratios N_σ/N_τ are to be used. This last point will make possible the realisation of a finite-size scaling when analysing data.

- The strategy is complete once, for any fixed N_σ value, a set of different $\beta(a)$ values is defined. As a general rule, at least two values are needed and, as we will show, many times three or four are necessary. For any $\beta(a)$ value in the chosen set, a set of Markov chains is produced by means of the RHMC algorithm, following some specific instructions.

3.2.2 The numerical strategy

The production process of Markov chains consists of two different steps: The thermalisation phase, which in turn consists of two separated stages, and the chain production phase. In the following paragaphs the structure of Monte Carlo simulations will be defined for our purposes and these fundamental steps will be discussed.

Thermalisation phase

As shown in equation (3.3), the evaluation of a generic observable by means of Monte Carlo simulations is performed according to a probability distribution, $P[U]$, to which a Markov chain must tend after a series of updates. Schematically, one could show that starting from an arbitrary initial configuration U_0, whose probability distribution reads $P^0[U]$, one obtains after a series of updates
$$P^0[U] \longrightarrow P^1[U] \longrightarrow \cdots \longrightarrow P[U], \tag{3.21}$$
where $P[U]$ coincides with the equilibrium distribution, which is reached after a subsequential application of a transition matrix. Considering (3.21), the initial configurations in a Markov chain are not produced according to the correct probability distribution and a good strategy requires those ones not to count towards the total average of configurations. Thus, a *thermalisation* process is needed in order to let the system evolve towards the desired equilibrium distribution before the Markov chain production takes place. Suppose to have fixed in the parameter setup, in the order, N_f, N_τ, am and a

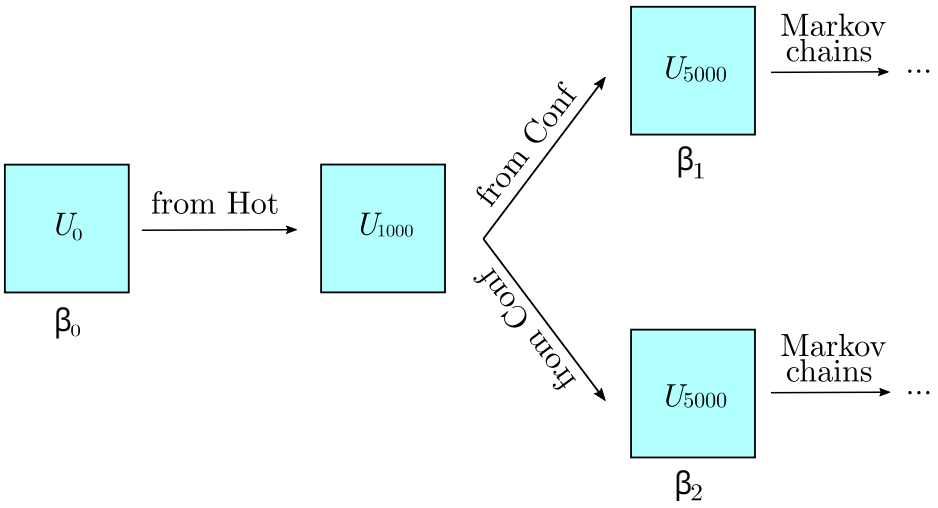

Figure 3.3: *The thermalisation phase.*

suitable spatial extent N_σ. A $\beta(a)$ value is then chosen and a *thermalisation from Hot* is lauched, namely a a series of Monte Carlo steps are realised by using as a starting point a random gauge configuration [11], which in figure (3.3) is indicated as U_0. The total number of trajectories required for this stage is one thousand, which represents, on average, a good number according to the analysis of the computed observables in this phase: Indeed, if the equilibrium is still to be reached, the values of a generic observable are expected to fluctuate at each Monte Carlo step, whereas fluctuations are expected to tend to zero at the equilibrium. The last configuration produced during this phase reads U_{1000}, and it is saved as it will be used as a starting point for the next step. The thermalisation process continues by fixing at least two $\beta(a)$ values and for any of them a *thermalisation from Conf* (namely from configuration) is launched. The goal of such stage consists in four thousand trajectories to be realised, and the final configuration U_{5000} is saved.

Markov chains

After the thermalisation process, the physical system we want to investigate will be at the equilibrium. The gauge configuration U_{5000}, saved at the end of the thermalisation from Conf processes, will be used as the new starting point for the Markov chain production. Our stategy, which will be explained in detail in the following sections, requires four Markov chains to be produced for each $\beta(a)$ value, labelled with four different *seeds*. The latter consists of an integer number of four digits and will be assigned randomly, as it does not play any role in the physics of the investigation. A suitable number of trajectories will be produced for each chain, according to a protocol finalised to maximise the quality and reliability of the produced data.

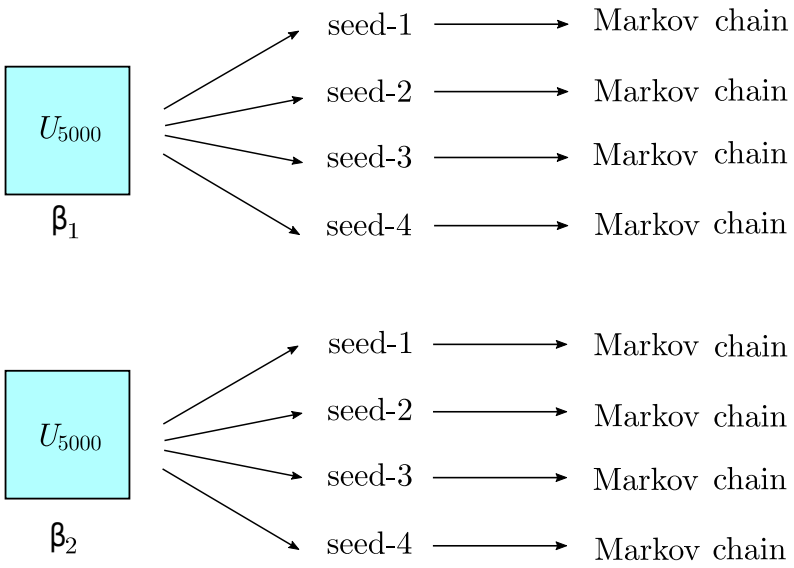

Figure 3.4: *Scheme of the Markov chains production, as a continuation of figure* (3.3).

3.2.3 Investigating the chiral phase transition

The investigation of the extension of the first-order chiral region in favour of the crossover region in the QCD phase diagram goes through the definition, computation and analysis of the order parameter of the chiral phase transition, namely the chiral condensate $\langle\bar{\psi}(x)\psi(x)\rangle$. From the theoretical point of view, the latter has already been introduced in Chapter 1: In the chiral limit, it vanishes when the chiral symmetry is realised, whereas nonzero values are assumed as the symmetry gets broken. At any chance, numerical simulations cannot be performed in the chiral limit, thus nonzero values of am must be used. As an aftermath of this numerical requirement, the chiral symmetry we want to investigate will always be broken and the chiral condensate must be handled more carefully, distinguishing two different scenarios:

- $\langle\bar{\psi}(x)\psi(x)\rangle$ is a **true** order parameter only in the chiral limit;
- $\langle\bar{\psi}(x)\psi(x)\rangle$ is an **approximate** order parameter when away from the chiral limit.

Even in the second scenario the chiral condensate still provides information about the order of the chiral phase transition, at least when the values of the masses for which simulations are produced are not extremely large, resulting thus meaningful to compute this observable during the Markov chain production for our aim. Using staggered fermions, the chiral consensate on the lattice can be obtained. A detailed discussion is given in section 3.4.1 of [15], and here just the relevant steps are proposed. The chiral condensate on the lattice is defined as

$$N_\sigma^3 N_\tau \langle\bar{\psi}\psi\rangle = \frac{\partial}{\partial \hat{M}} \log \mathcal{Z}, \tag{3.22}$$

being N_σ and N_τ the spatial and temporal lattice extents. Taking into account the partition function considered in equation (3.7) and recalling that the determinant in (3.7)

is equivalent to

$$\det D[U] = \exp(\mathrm{Tr}(\log D[U])),$$

equation (3.22) becomes

$$N_\sigma^3 N_\tau \langle \bar{\psi}\psi \rangle = \frac{1}{\mathcal{Z}} \frac{\partial}{\partial \hat{M}} \int \mathcal{D}[U] (e)^{\frac{N_f}{4} \mathrm{Tr}(\log D[U])} e^{-S_g[U]} = \frac{1}{4} \langle \mathrm{Tr} \Big(D^{-1}[U] \frac{\partial}{\partial \hat{M}} D[U] \Big) \rangle, \tag{3.23}$$

where the expectation value is computed according to the importance sampling procedure already discussed. Resorting to the noise sources techniques, a series of n sources can be involved with the properties

$$\langle \eta_i \rangle_n = 0, \qquad \langle \eta_i^\dagger \eta_j \rangle = \frac{1}{n} \sum_{i=1}^{n} \eta_i^\dagger \eta_j = \delta_{ij},$$

and the trace of the Dirac operator in equation (3.23) can be computed. Using the even-odd preconditioning one obtains after some algebra, for a specific gauge configuration,

$$\bar{\psi}\psi = \frac{N_f}{N_\sigma^3 N_\tau n} \sum_{i=1}^{n} \Big[\Big(\eta_e^n \Big)^\dagger \zeta_e^n + \Big(\eta_o^n \Big)^\dagger \zeta_o^n \Big], \tag{3.24}$$

where

$$\begin{aligned} \zeta_e^n &= (\hat{M}^2 - D_{eo} D_{oe})^{-1} (\hat{M} \eta_e^n - D_{eo} \eta_o^n) \\ \zeta_o^n &= \frac{1}{\hat{M}} \Big(\eta_o^n - D_{oe} \zeta_e^n \Big). \end{aligned} \tag{3.25}$$

But how can the chiral phase transition be investigated?

Analysis of an observable

The evaluation of the chiral condensate is performed at every Monte Carlo step, as well as the other observables. Naturally, it may seems more efficient to compute the observables just for some steps, depending on the value of the integrated autocorrelation time τ_{int}. Unfortunately, since the latter is only evaluated during the analysis process, it is not known beforehand and thus it is necessary to compute a number of values of an observable coinciding with the number of Monte Carlo steps and collect them as a time series. At the end of the analysis process, these values will contribute to the computation of the expectation value of the observable, together with the associated statistical error. In this subsection, we will mainly refer to Chapter 4 of [11] and to [117; 118].

Considering a series of N correlated measurements[6] of a generic observable $\mathcal{O}_i[U_i] = \{\mathcal{O}_0, \mathcal{O}_1, \cdots, \mathcal{O}_n\}$, an unbiased estimator for the expectation value is represented by

$$\langle \mathcal{O} \rangle = \bar{\mathcal{O}} + \sigma_c, \tag{3.26}$$

which consists of the mean value of the observable,

$$\bar{\mathcal{O}} = \frac{1}{N} \sum_i \mathcal{O}_i,$$

[6] Here, the measured values are also defined *events*.

plus the associated variance

$$\sigma_c^2 = \tau_{int}\sigma_u^2,$$

where the index c refers to *correlated values* wheras u to *uncorrelated values*. At this point, since data are necessarily correlated, one way to remove the correlation consists in organising the different values through a histogram, whose dimension of bins, l, depends on the value of the integrated autocorrelation time, $l = 2\tau_{int}$. The total number of independent (uncorrelated) events can be obtained by

$$N_u = \frac{N_c}{l},$$

and, the value of the observable is replaced by the value of (3.26) inside the considered bin[7]. At this point, when trying to work with more complicated functions of the generic observable $\mathcal{O}$, some problematics may rise up: Indeed, when dealing with non-linear functions of $\mathcal{O}$, a biased estimator is obtained [117] and the associated variance cannot be obtained by using the prescription given for an unbiased estimator. Then, a different strategy has to be involved and a suitable one consists in using the *jackknife method* [11; 119]. Suppose to have a function of the previous set of values of our generic observable, $f(\mathcal{O}_i)$. The jackknife estimator is defined as $f^J = f(\mathcal{O}^J)$, whose mean value reads

$$\bar{f}(\mathcal{O}^J) = \frac{1}{N}\sum_{i=1}^{n} f_i^J, \tag{3.27}$$

and the variables $\mathcal{O}^J$ are defined as

$$\mathcal{O}^J = \frac{1}{N-1}\sum_{k\neq 0}\mathcal{O}_k. \tag{3.28}$$

Finally, the error on $\bar{f}^J$ is obtained as

$$\sigma^2(\bar{f}(\mathcal{O}^J)) = \frac{N-1}{N}\sum_{i=1}^{n}(f_i^J - \bar{f}^J)^2, \tag{3.29}$$

which, naturally, is reduced to the unbiased case error in case the function $f(\mathcal{O}_i)$ is not affected by bias problems.

The standardised moments

Once the (approximate) order parameter is evaluated, its analysis provides information in order to locate the chiral phase transition and to characterise its order. In the following, we will show how to deal with these two further steps, by taking into account the theory reported in the previous section. Locating the chiral phase transition means to identify a critical mass value am_c belonging to the Z_2 critical boundary, and a corresponding pseudo-critical $\beta_{pc}(a)$ value [8]. From figure (3.1), once the lattice temporal extent is fixed, our strategy requires to set at least three values of quark masses on the lattice, $am_{i,i=1,2,3}$. For each am_i value, three spatial volumes are set and simulations are performed for some specific $\beta(a)$ values: The result consists in the computation of the histogram of the

[7] This procedure goes under the name of *binning*.

[8] The adjective *pseudo* refers to the nature of this parameter. Indeed, as simulations are performed on different lattice volumes for a specific am value, $\beta_{pc}(a)$ will still depend on the particular N_σ value. In the next sections we will see how to obtain the proper critical $\beta(a)_c$.

sampled distribution of the chiral condensate, according to (3.3), assuming $\langle\mathcal{O}\rangle = \langle\bar{\psi}\psi\rangle$. The shape of the histograms varies, depending on the chiral phase which is sampled for a specific $\beta(a)$ value: In particular, in the proximity of $\beta(a) = \beta_{pc}(a)$, the histogram shows a two-peaks shape since the physical system is sensitive to both the chirally restored and broken phases and, in principle, a perfect symmetry is realised when $\beta(a) = \beta_{pc}(a)$. Essentially, large lattice gauge coupling values, namely higher T values, allow to sample the restored phase whereas the broken one can be investigated for lower values. As already pointed out, the set of $\beta(a)$ values is finite and, in general, between two and four values are sufficient to our aim. This is a natural limit imposed from numerical reasons: In fact, the number of processes which can be launched in the frame of numerical simulations always depends on the hardware system and technology, like for instance the number of available GPUs. Then, locating the pseudo-critical gauge coupling becomes non-trivial and requires some methods to be applied. From the theory of probability [120], the features of the shape of a generic distribution function $f(x)$ can be explored by means of the so called *moments*

$$m_n = \int_{-\infty}^{\infty} x^n f(x) dx, \tag{3.30}$$

and *central moments*

$$\mu_n = \int_{-\infty}^{\infty} (x - m_1)^n f(x) dx, \tag{3.31}$$

where n refers to the order of the moments. From the latter, another quantity involved in this kind of analysis are the *cumulants*: These can be defined by taking into account the generating function at time t of the standardised moments,

$$M_X(t) = \int_{-\infty}^{\infty} e^{tx} f(x) dx,$$

from which, defining the cumulant generating function as

$$K_X(t) = \log M_X(t),$$

the cumulants are obtained as

$$k_n = K_X^n(t = 0).$$

Looking closer to these definitions, it is obviuos that m_1 corresponds to the mean value of the function $f(x)$ whereas μ_2 corresponds to its variance. From the two definitions, the *standardised moments* can be derived as

$$B_n = \frac{\mu_n}{(\mu_2)^{n/2}}, \qquad n \geq 3, \tag{3.32}$$

which reads as the n-th central moment normalised to the n-th power of the variance. Making the latter more explicit, one obtains, for $\langle\mathcal{O}\rangle = \langle\bar{\psi}\psi\rangle$,

$$B_n(\mathcal{O}) = \frac{\langle (O - \langle\mathcal{O}\rangle)^n \rangle}{\langle (O - \langle\mathcal{O}\rangle)^2 \rangle^{n/2}}$$

The third standardised moment is called *skewness* and provides an estimation of the asymmetry of the distribution function with respect to its mean. In case of a symmetric shape of the distribution function, the value of the skewness equals zero. Thus, since for $\beta(a) = \beta_{pc}(a)$ the order parameter exibits a symmetric distribution shape, then a useful

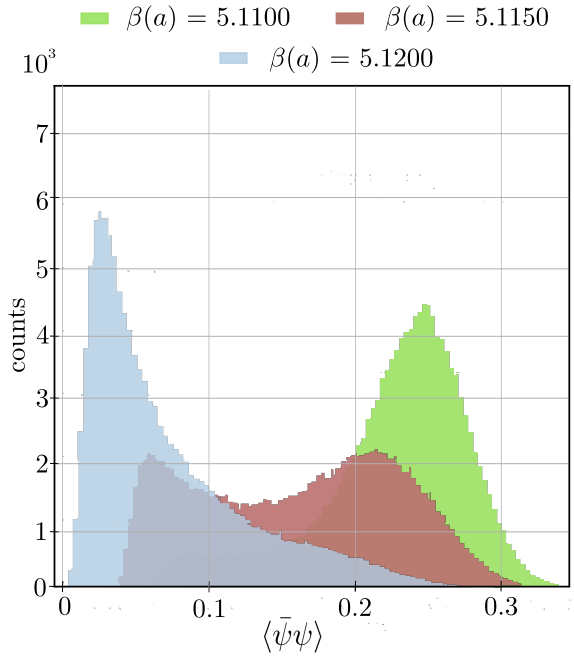

Figure 3.5: *Histograms of* $\langle\bar{\psi}\psi\rangle$ *corresponding to the parameter setup* $am = 0.0020$, $N_\tau = 8$, $N_\sigma = 16$, $\mu_i = 0.81\pi T/3$, *for three gauge coupling values,* $\beta(a) = \{5.110, 5.115, 5.120\}$.

condition to locate the chiral phase transition reads $B_3(\beta_{pc}(a)) = 0$ [9]. On the contrary, non-zero values of $B_3(\beta(a))$ correspond to an asymmetric shape of the distribution of the order parameter: In this particular scenario, B_3 assumes positive values in case of a right-tailed function, whereas a negative sign highlights the presence of a left tail. An example of the histograms of $\langle\bar{\psi}\psi\rangle$ for a specific parameter setup when three different $\beta(a)$ values are involved is given in figure (3.5), where the difference between the three histograms is appreciable: The chirally broken phase is characterised by a positive skewness and is sampled by means of the largest $\beta(a)$ wheras a negative skewness value marks the histrogram corresponding to the sampling of the chirally restored phase, which happens for the lowest, simulated $\beta(a)$ value. In the middle, a double-peaked histogram provides the sampling of the region in the proximity of the chiral phase transition. Ideally, if an infinite set of $\beta(a)$ values could be used, then a continuous transformation of one histogram corresponding to $\beta(a)_{\text{min}}$ into the $\beta(a)_{\text{max}}$ one could be observed. The fourth standardised moment is the *kurtosis*, directly connected to the *Binder cumulant* [121], and provides a measure of the "tailedness" of the probability distribution and which is indicated as B_4. Compared to a typical Gaussian distribution, the latter could exibit a particular peaked shape, whose extension and thickness of both the tails can be evaluated, contributing to different values of B_4. These values depend on the kind of distribution as well as on the universality group and some of the most useful values, evaluated in the infinite volume limit, are reported in table (3.1), and, as one can observe, they vary discontinuously, from one scenario to another one. In particular, the values that will be useful to realise our projects are the 3D Ising Z_2 one, $B_4(\infty) = 1.604(1)$, the one corresponding to the 3D $O(2)$ universality class, $B_4(\infty) = 1.2491(39)$ [124], and the crossover one, $B_4(\infty) = 3$, the

[9] Note that the opposite is not true in general. Asymmetric distributions with $B_3 = 0$ are possible, due to the compensation of the asymmetries.

	Crossover	First-order triple	Tricritical	3D Ising (Z_2)	$O(2)$
$B_4(V=\infty)$	3	3/2	2	1.604(1)	1.2491(39)
ν	-	-	-	0.6301(4)	0.7076(4)
y	-	-	-	0.8948(13)	1.0863(29)

Table 3.1: *In the first raw are reported the values of the kurtosis for different scenarios, in the infinite volume limit. In the second and third raws are the values of the corresponding critical exponents, used to realise the finite-size scaling. Values from [122], [123] and [124].*

latter corresponding to a Gaussian distribution of the order parameter. The evaluation of the kurtosis as a function of the lattice gauge coupling results useful both to identify the value of $\beta_{pc}(a)$ and the order of the chiral phase transition we are studying. Indeed, the point $B_4(\beta(a) = \beta_{pc}(a))$ corresponds to the global minimimum of the kurtosis, which in turn coincides with the point where the condition $B_3(\beta_{pc}(a)) = 0$ is satisfied. At any chance, since the number of gauge coupling values to be simulated is finite, locating the real $\beta_{pc}(a)$ value could sound particularly challenging: In fact, guessing the candidate-to-be $\beta(a) = \beta_{pc}(a)$ would rather sound like a lottery game than real physics. Moreover, simulations on the lattice are always performed at finite volumes: In this context, the values assumed by B_4 vary continuosly between the ones reported in table (3.1), and pretenting to use large volumes (corresponding to aspect ratio larger than three) can lead to extremely high numerical costs, which de facto renders simulations impossible.

The Ferrenberg-Swendsen reweighting

In order to circumvent these problematics, one has to resort to a method that allows to "fill" the segments of $\beta(a)$ values between the ones in the chosen parameter setup by reconstucting a set of new, fictitious points, and then identify the corresponding skewness and kurtosis values. A useful technique is the Ferrenberg-Swendsen *reweighting* [125; 126], which allows to obtain new data in a specific β range, made possible by the linearity of the gauge action in the $\beta(a)$ variable. This method, applied to the multiple histograms obtained for different $\beta(a)$ value, is based on the idea that the gauge coupling values used to perform simulations must be separated by a suitable $\Delta\beta$ gap, such that the different gauge actions computed in the different samplings do overlap [127]. This requirement is necessary in order to first, allow the reweighting to be performed and second, to guarantee a higher reliability of the reweighting's results. With this technique, we are able to locate the pseudo-critical $\beta_{pc}(a)$ value as well as the corresponding $B_4(\beta_{pc}(a))$ value: The latter will be the only meaningful kurtosis value, since it provides information about the order of the chiral phase transition, namely for gauge coupling values different from the pseudo-critical one the kurtosis value are not of physical interest. At this point, following the schemes in figures (3.1) and (3.2), we obtain one $\beta_{pc}(a)$ value and its corresponding $B_4(\beta_{pc}(a))$ value for any fixed lattice volume, which leads to a set of data corresponding to different quark masses. On this data set, more analysis has to be performed to obtain a critical mass value on the Z_2 boundaries. In order to persue this aim, one can start by first removing the dependence on the spatial extents N_σ of the results and then, elaborate a stategy which allows to compute a critical mass value, as it will be shown in

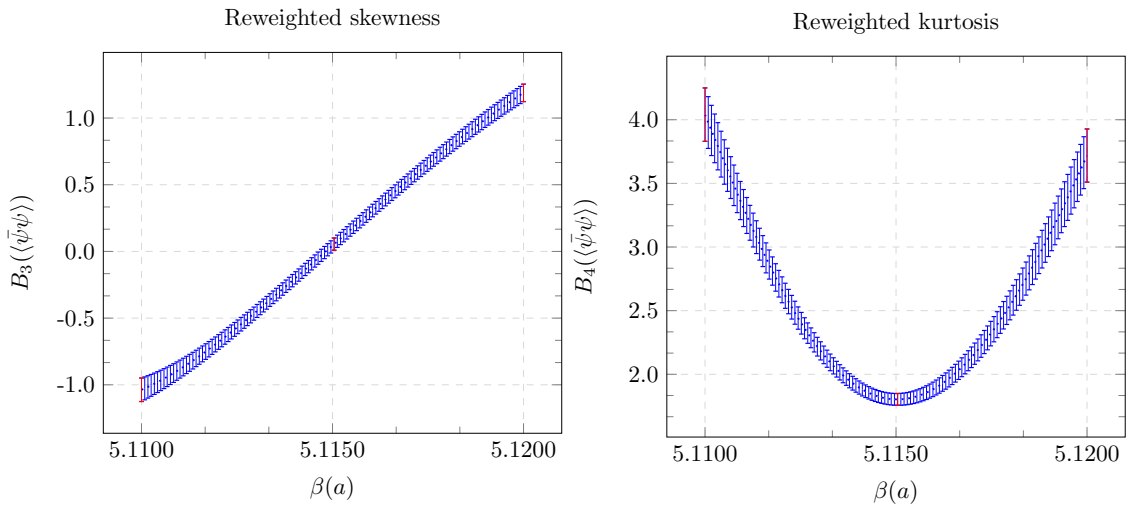

Figure 3.6: *Example of reweighting applied to the skewness (left) and kurtosis (right) of the chiral condensate, for the parameter setup* $am = 0.0020$, $N_\tau = 8$, $N_\sigma = 16$, $\mu_i = 0.81\pi T/3$. *The number of* $\beta(a)$ *values used is 120: in red are the simulated ones whereas in blue are the resulting ones from the reweighting process.*

the following subsection. Before continuing, it is worth to remark one important point. In subsection 3.2.3 we briefly discussed about the importance of using the jackknife method when analysing observables, whose data come from simulations. When involving the multiple histograms method, the jackknife method can still be applied, assuming the generic observable to be now dependent on $\beta(a)$ as $\mathcal{O}(\beta(a))$. For more details, we refer again to [127].

The finite-size scaling

As breafly mentioned, the investigation of the order of the chiral phase transition by means of the values of the kurtosis of the chiral condensate is strictly related to the concept of universality class. These are characterised by a set of critical parameters which describe the behaviour of some specific quantities as a function of temperature in the proximity of the phase transition, and such parameters are almost totally independent on the specific model. Thus, studying more complicated physical systems can be done by taking into account simpler models, which belong to the same universality class of the system of our interest. According to this statement, it is then possible to study the boundary between the first-order chiral region on the lattice and the crossover region by looking for a Z_2 point (mass), which represents a second-order phase transition in the universality class of a 3D Ising model. The values the kurtosis assumes in such scenario is well known, as already reported in table (3.1), as well as some of the critical parameters, which will be employed in the next lines. Consider again figure (3.1) and suppose to have fixed N_f, N_τ. For any fixed am and N_σ value, is it basically possible to proceed as it has been explained in the previous paragraph up to the identification of a pseudo-critical $\beta_{pc}(a)$ by means of the reweighting method, giving a specific kurtosis value $B_4(\beta_{pc}(a))$ associated. These data provide information we need in order to identify a critical am_c value, to which a critical $\beta_c(a)$ value will be associated. At this point, using the fact that for finite volumes the kurtosis values vary continuously and considering that far from the phase transition the partition function of a physical system is an analytic function of the physical parameters,

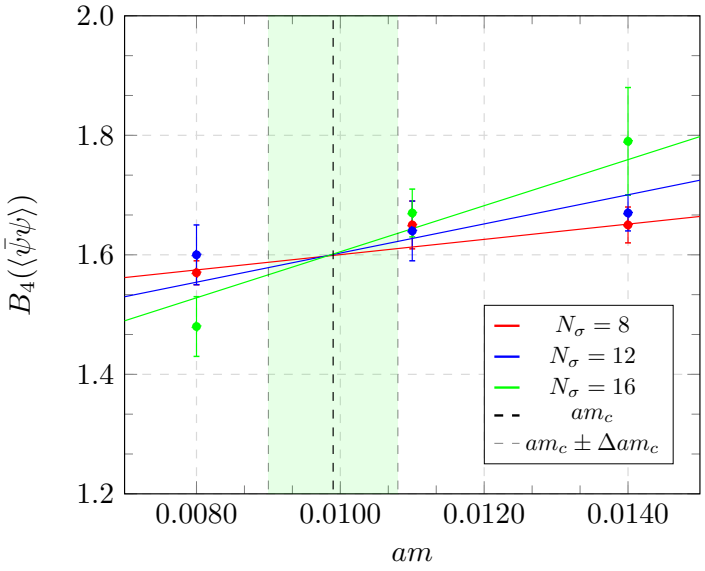

Figure 3.7: *Finite-size scaling applied to the results for the parameter setup* $N_f = 2.2$, $N_\tau = 4$, $am = \{0.0080, 0, 0110, 0.0140\}$, $N_\sigma = \{8, 12, 16\}$. *Along the vertical axis are the values of the kurtosis whereas along the orizontal axis are the values of the simulated quark masses. The critical mass* am_c*=0.0099(9) identifies a point belonging to the* Z_2 *boundary. For this fit, a reduced chi-squared* $\chi^2_{ndf} = 0.638$ *and* $Q = 61.9\%$ *have been obtained.*

the kurtosis can suitably be expandend around $\beta_{pc}(a)$ as follow[10]

$$B_4(\beta_{pc}(a), am, N_\sigma) \approx B_4(N_\sigma = \infty) + c(am - am_c)N_\sigma^{\frac{1}{\nu}}, \tag{3.33}$$

where $(am - am_c)$ is the scaling variable. The latter can be further modified by including a subleading finite volume correction term [128]

$$B_4(\beta_{pc}(a), am, N_\sigma) \approx \Big(B_4(N_\sigma = \infty) + c(am - am_c)N_\sigma^{\frac{1}{\nu}}\Big)\Big(1 + bN_\sigma^{-y}\Big), \tag{3.34}$$

where the y parameter is reported in table (3.1). By fitting equation (3.34) to the kurtosis values obtained from the reweighting, the result consists of a joint fit, with as many fitting lines as simulated volumes. Since we are interested in locating the Z_2 boundary, then we set $B_4(\infty) = 1.604$, $\nu = 0.6301$ and $y = 0.8948$ in (3.34) and the value of am_c can consequently be extracted. An example of such procedure is reported in figure (3.7) for a specific parameter setup, where three quark masses have been involved[11]. In general, the simulated points for $am < am_c$ lay in the first-order chiral region whereas the values for $am > am_c$ sample the crossover region. It is important, with reference to the quality of the fit, to take into account two objects: the reduced chi-squared χ^2_{ndf} [12]and the Q parameter. The former is defined as the ratio between the chi-squared χ^2 and the number of degrees of freedom for the specific parameter setup and a value χ^2_{ndf} around one corresponds to a

[10]This can be obtained by taking into account the renormalisation group theory [122].
[11]In case of a fit performed according to equation (3.33), the three lines would have met as $am = am_c$.
[12]Naturally, *ndf* is the acronym for *number of degrees of freedom*.

good fit quality [13]. The latter is defined as [119]

$$Q = \frac{1}{2^{m/2}\Gamma(m/2)} \int_{\chi^2/2}^{\infty} x^{(m/2)-1} e^{-x} dx, \qquad m = \chi^2_{ndf} \tag{3.35}$$

where $\Gamma(m/2)$ is the Euler gamma function, and, given a specific χ^2 for a specific data set, it represents the probability that a different one could occur with a larger χ^2 value, assumed the same probability distribution for both the data set. The optimal value corresponds to $Q = 50\%$, whereas a value of $Q \approx 100\%$ would result in a high probability for a greater χ^2 to happen for a different data set. Once this prescription is applied to all the N_f values for which simulations have been realised, it will be possible to obtain a set of critical mass points belonging to the different critical boundaries, for any N_τ value.

The finite-size effects

Working on finite lattice volumes is of course a necessity when performing lattice simulations. For some parameter setup, finite-size effects can be considered as a source of error affecting the quality of data and, in particular, rendering useless the results coming from reweighting. Much about this topic can be found in textbooks ad [11; 127], but for a detailed discussion, even more related to the aim of this work, we refer to section IV of [57]. Suppose to perform simulations for a generic parameter setup, using two gauge coupling values such that the restored and broken phases are correctly sampled. For sufficiently large $\Delta\beta$ no tunneling between the two phases happens, then two distinct histograms are observed with Gaussian distribution, which do not overlap and whose corresponding skewness values, according to section 3.2.3, equals zero. As soon as the gap between the chosen $\beta(a)$ values to perform simulations becomes smaller, the probability to realise tunneling between the two different phases becomes larger: This results in a non-zero skewness value associated to the corresponding chiral condensate's distributions, since right or left tails appear in the two histograms. In any case, a very important constraint related to the bare quark masses is that simulations cannot be performed directly in the chiral limit. This imposes that the chiral condensate never vanishes, when even small am values are involved and as a consequence for sufficiently small N_σ values, finite-size effects become prominent. Consider, as an example, the scenario reported in figure (3.8). The bare quark mass involved in this case is $am = 0.0030$, which is a relatively small one considered the lattice temporal extent $N_\tau = 6$. As one can see, there are two $\beta(a)$ values for which simulations have been performed, when using a lattice spatial extent $N_\sigma = 12$, corresponding to an aspect ratio of two. A big difference in the shape of the two corresponding histograms of $\bar{\psi}\psi$ can be noticed: In particular, $\beta(a) = 5.2150$ samples the chirally broken phase whereas $\beta(a) = 5.2350$ samples the chirally restored one, and for the latter a long right-tailed histogram is reported, with a distinct narrow peak when compared to the other histogram. This shape is the evidence of finite-size effects affecting the physics and corresponds to a pure lattice artefact. Indeed, the reason why this happens resides in the accumulation of data points in the proximity of the narrow peak, since in principle a symmetric tail would extend to the left of the peak. But, since a non-zero mass has been involved, there is no chance the histogram could extend any further towards the origin of the axis. Then, the results of the reweighted skewness and kurtosis are highly compromised and do not represent a physical and reliable situation. This scenario tends to happen more often when the combination of small bare quark

[13] In general, $\chi^2_{ndf} > 1$ indicates, from the defintion of χ^2, that some points are not hit by the fitting line whereas $\chi^2_{ndf} < 1$ highlights a possible overestimation of the errorbars.

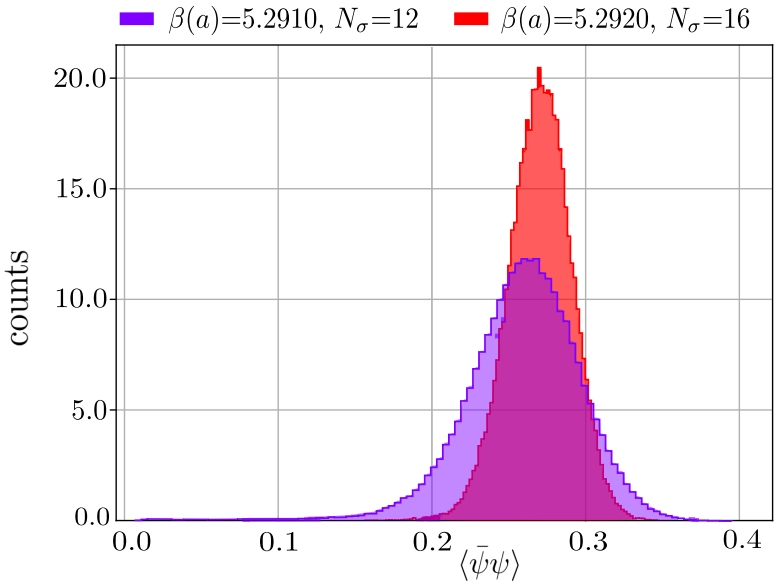

Figure 3.8: *Histograms of* $\langle\bar{\psi}\psi\rangle$ *for the parameter setup* $N_f = 1.9$, $\mu_i = 0.81\pi T/3$, $am = 0.0020$, $N_\tau = 4$, *corresponding to two different lattice spatial extents and* $\beta(a)$ *values.*

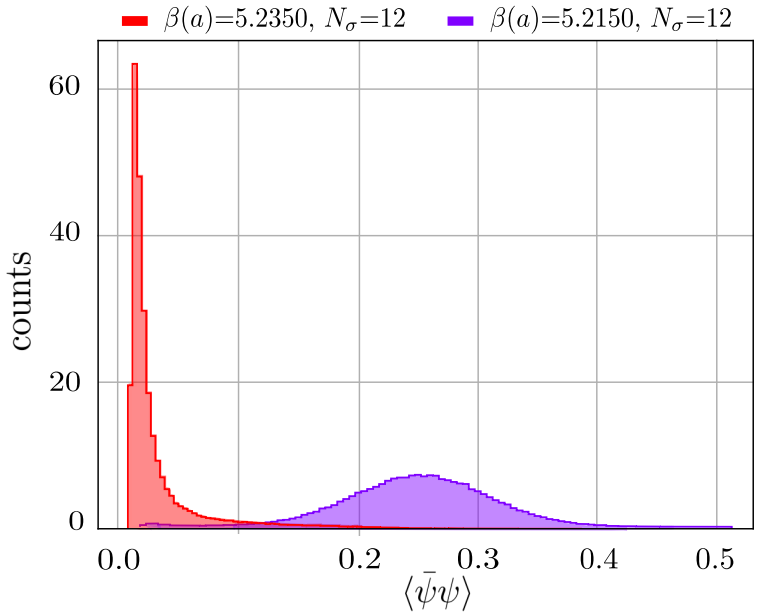

Figure 3.9: *Histograms of* $\langle\bar{\psi}\psi\rangle$ *for the parameter setup* $N_f = 3.0$, $\mu_i = 0.81\pi T/3$, $am = 0.0030$, $N_\tau = 6$, $N_\sigma = 12$ *and two different* $\beta(a)$ *values.*

masses and small lattice volumes is realised. As a further example, let's consider figure (3.9) where we can appreciate a difference in the shape of two different histograms corresponding to two different, but close, $\beta(a)$ values, being $\Delta\beta = 0.001$, and two different lattice spatial extents, $N_\sigma = 12$ and $N_\sigma = 16$. The rest of the parameters is identical. The histogram corresponding to the smallest volume exibits a smoothed peak with a wider extension in terms of values whereas, moving to the largest volume, we see how the histogram becomes more peaked and the overall results in a thinner shape: This is the basic reason why finite-size effects occur the less when larger volumes are involved. A clear explanation to the finite-size effect realisation comes from the perturbation theory, thanks to the Gell-Mann-Oakes-Renner (GMOR) relation [129],

$$m_\pi^2 = \frac{m_u + m_d}{f_\pi^2} |\langle 0|\bar{u}u|0\rangle|, \tag{3.36}$$

which connects the pion mass to the masses of the up and down quarks by means of the pion decay constant f_π and the vacum energy term $|\langle 0|\bar{u}u|0\rangle|$. As the magnitude of the finite-size effects scales as an exponential function of

$$-m_\pi N_\sigma, \tag{3.37}$$

and the only way their impact can be made vanishing resides in working in a lattice region where $m_\pi N_\sigma \gg 1$, namely the lattice spatial extent must be asymptotically equivalent to the factor f_π. Thus, when small quarks masses are involved in simulations the relation (3.37) suggest the volume the lattice spatial extent to become larger.

3.2.4 Further details

Before moving further, it is necessary to spend some words on the scheme in figure (3.4). In figure (3.5), we reported an example of three different histograms corresponding to three different simulated $\beta(a)$ values for a specific parameter setup. Then, in figure (3.7), a finite-size scaling procedure has been shown for a different parameter setup, where the points in the plot correspond, for different simulated masses and lattice volumes, to different kurtosis values: The latter, are associated to a specific $\beta_{pc}(a)$ value, extracted as shown in figure (3.6). In reality, in section 3.2.2 it has been mentioned that our strategy requires four Markov chains to be produced, using four different *seeds*, which act as different labels. These values are not just labels, but rather correspond to the seed which initialise the pseudo-random numbers generator (PNRG) algorithm, which is needed in the application of the RHMC algorithm. Then, in order to make the procedure clear, it is fundamental to explain how the two things are connected. Focusing on the analysis methods already discussed in this Chapter, two procedures can be realised concerning the four different chains:

- They can be analysed as *single chains*, namely individual productions: The chiral condesate is analysed separately and four values of skewness and kurtosis are obtained for a specific parameter setup;
- Data obtained from the four different chains can be *merged* in one single chain. This allows to extract the $\beta_{pc}(a)$ as in figure (3.6) and provide a corresponding value of kurtosis. The total amount of statistics of the merged chain is given as the sum of the four single amounts [14].

[14] The total number of trajectories produced in the four single chains does not vary with the seed.

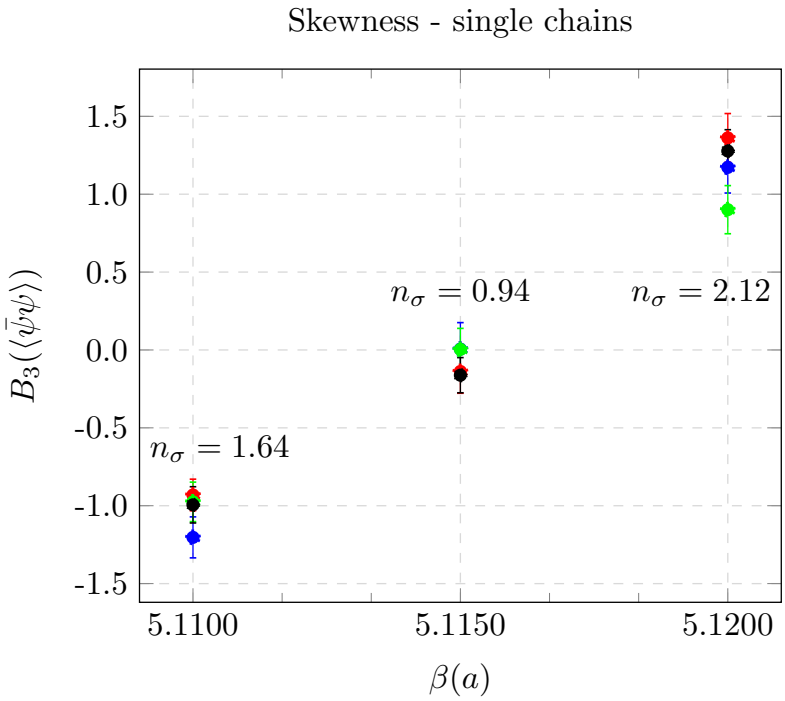

Figure 3.10: *Skewness values from the single chain analysis, for the parameter setup* $am = 0.0020$*,* $N_\tau = 8$ *and* $\beta(a) = \{5.1100, 5.1150, 5.1200\}$*. The* n_σ *parameter takes into account the deviation between the highest and lowest skewness values for a specific* $\beta(a)$*, in units of standard deviation. [9].*

The first procedure can be further deepen considering another point. Suppose to submit a certain number of simulations, for different $\beta(a)$ values and seeds and suppose to perform, regularly, a complete data analysis thoughout the chains production. Since, simulations cannot be run indefinitely in time, a good criterion to determine a valid total amount of statistics is needed, thus a *goal* must be indicated as the total number of molecular dynamics trajectories to be performed. In our case, the plan includes two rules, based on some of the features we have discussed in the previous subsections, to be simultaneously fullfilled:

- As shown in the example in figure (3.10), for each quartet of chains we obtain four values of skewness. After a certain amount of trajectories, since the investigated physics is the same for any chosen seed, ideally we expect the four Markov chains to eventually tend to the same chiral condensate's mean value, as well as to the same skewness and kurtosis values associated. Then, taking into account the highest and the lowest values of skewness and kurtosis in the four chains, we require them to be compatible within three standard deviations, which we indicate as $n_\sigma(B_3) = 3$.

- Since we are interested in locating the chiral phase transition through the study of the Z_2 critical boundary, the lowest and largest simulated $\beta(a)$ values need to sample, respectively, the fist-order and the crossover regions. Thus, we require the quartets of skewness value not to be compatible with $B_3 = 0$ within their errorbars.

The second point is to be treated carefully: As previously mentioned, it is fundamental the overlap between the histograms of gauge actions corresponding to different $\beta(a)$ values to take place, in order to realise the reweighting and identify the $\beta_{pc}(a)$ values. Hence, using

two $\beta(a)$ values can be problematic in some cases, mainly for larger N_σ values, where the tunneling probability between broken phase and restored phase is suppressed. Indeed using a too large $\Delta\beta$ could make impossible a trustable reweighting to be performed, whereas, on the contrary, a too small gap could not ensure to correctly sample the two different chiral regions. As a consequence, in many cases using more than two $\beta(a)$ values guarantees a higher data analysis quality. In general, when the two rules reported above are fullfilled, one can consider to stop the data collection and validate the results coming from its analysis. One more interesting point is represented by the number of independent events for each of the four Markov chain, for each $\beta(a)$, according to the integrated autocorrelation time. As shown in subsection 3.2.3, the number of independent events with respect to the total number of events collected depends on the value of τ_{int}, on which, in turn, also the binsize of the bins in the histograms depends. In general, having the number of independent events above thirty can be considered as the third rule, together with the already discussed ones, to determine when the amount of statistics is sufficient.

3.3 Software

Performing simulations requires, in general, high-performance machines, equipped with Central Processing Units (CPUs) and Graphics Processing Unit (GPUs), which are usually collocated in clusters of supercomputers. So far we have discussed about the generalities of the Monte Carlo method we will adoperate to achieve the results of in this thesis work and also the general strategy we follow when producing the different Markov chains during the simulations' production. Thus, as a conclusion to this Chapter, this section will be dedicated to a synthetic introduction to the software which contains the instructions to realise and complete simulations, as well as to submit, handle and manage the different jobs on the clusters, and, finally, to synchronise data from the clusters on the local machines and, locally, analyse them.

3.3.1 The CL^{2}QCD code

The first software to be presented is the CL^{2}QCD code, which is a publicly available software previously released in its version 1.0 [130] and currently available also in the upgraded version 1.1 [131], entirely written in C++. It has been developed throughout the last decade [132] [133] [134] [135], based on the open standard OpenCL [15], and it is planned to both work on CPUs and GPUs. This code allows to perform lattice QCD simulations using Monte Carlo methods, as it includes the basic algorithms needed, among the others the HMC and RHMC ones with more algorithms contained inside them, and its structure consists of four different communicating areas:

- **physics**, which contains the main ingredients concerning the measurement of observables during simulations. Indeed, here the gauge fields, gauge momenta fields and fermionic fields are defined, together with the aforementioned algorithms. Also, the physical observables are here defined, as for instance the chiral condensate for staggered fermions, which is the one we will need to measure in this thesis work;

- **meta**, which stores the values simulation parameters assumed in input and contains instructions to save configurations and PRNG states as output files during simulations;

[15] https://www.khronos.org/opencl/

- **hardware**, devoted to handle the code on the suitable devices which host simulations on the different clusters [16], and the parameters referred to such devices are initialised at runtime. Furthermore, in this area the memory management is realised;

- **OpenCl kernels**, which allows to compile the OpenCl code at runtime.

For more information, we refer to the cited references. In this work, simulations have always been performed by means of the RHMC algorithm applied to unimproved staggered fermions. The strong coupling regime project has fully been developed by means of the supercomputers of the Goethe-HLR cluster [17], whereas the non-zero imaginary baryon chemical potential project has been completed on the HCP cluster VIRGO [18] from the GSI [19] research facility. Furthermore, some tests about the minimum norm integrators have been performed on the former L-CSC cluster [136], also from the GSI research facility.

3.3.2 BaHaMAS

BaHaMAS [137] is the acronym for *Bash Handler to Monitor and Administrate Simulations* and consists of a series of Bash scripts which consent to handle simulations to be performed by means of the CL^{2}QCD code on a specific cluster, where the *slurm* scheduler [20] is provided. As a first step, BaHaMAS requires some elements to be idicated in its setup in order to correctly work, like the name of the executable we need to run in CL^{2}QCD as well as some suitable paths. Then, the entire tool is based on the preliminary definition on the cluster of a specific file, namely the *betas* file, where a set of indispensable simulation parameters is stored. Here are set the $\beta(a)$ values, together with the corresponding seeds needed to initialise the PRNG algorithm, the number of integration steps to perform the Molecular Dynamics step (when using two time scales, two values are to be set), the goal, namely the total number of Monte Carlo steps to be performed and the approximate time needed to produce one trajectory [21]. Also, if the flag *rlast* is indicated for a specific seed, then simulations can always be resumed from the last gauge configuration saved. In its functionalities, BaHaMAS can be run with different possible options, in order to generate an input file, where the parameters corresponding to the flow shown in figures (3.1) and (3.2) (except the $\beta(a)$ values) are stored. These parameters are directly read from the path where the *betas* file is located, since it is defined according to a definite template of folders and subfolders. At this point, a corresponding job file is created accordingly and then submitted to the available devices. Depending on what kind of simulations are to be performed, BaHaMAS allows to use the options *thermalize* and *new-chain*, together with more options which serves, for instance, to specify how often gauge configurations and PRNG states must be saved and if an observable is to be measured. Once the chain production begins, this can be kept under control by means of the option *simulation-status*: This provides some indicators as, for instance, the acceptance rate, the average plaquette values over one thousand trajectories, the time needed to produce the last trajectory and the average time per trajectory over the total number of trajectories already completed

[16] In our case, simulations are always performed on GPUs.
[17] https://csc.uni-frankfurt.de
[18] https://hpc.gsi.de/virgo
[19] https://www.gsi.de
[20] https://slurm.schedmd.com/
[21] This provides information to the scheduler in order to optimise the management of the queues on the clusters, given the total number of trajectories to be performed.

and many others, which gives the possibility to gradually supervise the quality of the simulations. Another option is *job-status* and gives an overview of all the jobs submitted to the cluster partition indicated in the BaHaMAS setup[22], returning the list of the running and pending jobs in a specific partition for any user. Lastly, BaHaMAS also provides a *database*, where information about all the simulations performed is available and can suitably be filtered. More about BaHaMAS can also be found in section 3.5 of [15].

3.3.3 PLASMA

After having briefly discussed about the software we need to produce data on clusters, the next step consists in presenting another numerical tool that is largely used in our working group in order to analyse data. The name of this tool is PLASMA[23], which is the acronym for *Python Library for Automatic Simulations Management and Analysis*, and it consists of a set of scripts, written in python, which contain the instructions needed to complete the analysis of the measured observables. The software has some options available which allow to first synchronise data from remote, namely from the cluster where simulations are realised, and then to start the analysis process. Recalling the methods discussed in section 3.2.3, which will be used throughout this thesis work, PLASMA allows to analyse data by means of the jackknife method through the option *analyseWithJackknife* and also to perform the analysis of the single Markov chains, corresponding to different seeds, by means of the option *analyzeSingleChains*. Then, the histograms of the chiral condensate, as well as the gauge action, τ_{int}, skweness and kurtosis values will be computed and this will give a first overview of the results obtained. Furthermore, the reweighting process can entirely be done through PLASMA and, by means of suitable options, it is possible to set the $\Delta\beta$ in which the reweighting has to take place, identifying a minimum and maximum $\beta(a)$ value. Once this is set, also the number of points to be created can be chosen.

3.3.4 The python fitting GUI

This tool has been developed by Reinhold Kaiser, member of the Philipsen's group and presented in his master's thesis [24], and allows to perform the finite-size scaling presented in section 3.2.3 as shown in figure (3.7) by means of a series of scripts written in python and providing a graphical user inteface (GUI). In particular, for any simulated quark mass value, this tool takes in input the kurtosis values corresponding to different N_σ values from a single file where these are stored and then, depending on the critical parameters used, the fit can be performed. Besides the graphic, also the quality of the fit can be investigated by means of the Q parameter and the χ^2_{ndf}, which are evaluated at the end of any fit.

[22] In our case it coincides with the GPU partition always.

[23] PLASMA is contained in https://gitlab.itp.uni-frankfurt.de/lattice-qcd/plasma as it has not been released yet.

[24] It can be found at https://itp.uni-frankfurt.de/philipsen/theses/kaiser_ma.pdf.

Chapter 4

Results

In this final Chapter, the analysis and the results concerning the different investigations already introduced in section 2.3 will be presented, together with conclusions which can be drawn downstream the discussion. Before going in the details of the two main topics, a preliminary step has been made concerning the implementation of the fourth-order minimum norm integrator 4MN, both in one and two-time scales, in the CL^{2}QCD code, and its performances have been compared to the ones of the second-order minimum norm integrator 2MN, with two-time scales. Both the integrators and their structures have been reported in Appendix B, where many references are reported to support. This step represented the earliest stage and the starting point of this dissertation, as the decision on which integrator was to be involved in the Molecular Dynamics steps for the other two topics was definitely based on it.

4.1 A comparison between the 2MN and 4MN integrators

At the end of any produced Molecular Dynamics step (or, equivalently, trajectory), the variation in energy of the physical system is measured according to the Hamiltionan $\mathcal{H}$. As shown in equations (B.3) and (B.4), the integration error produced by means of symplectic integrators is of order $\mathcal{O}(\Delta t^3)$ for the 2MN integrator and $\mathcal{O}(\Delta t^5)$ for the 4MN one. In general, as shown in section 3 of [138], the variation in energy is proportional to the discretised time steps,

$$\Delta\mathcal{H} \sim \Delta t^n, \tag{4.1}$$

where n represents the order of the integrator and Δt is obtained as the ratio between the interval in which the integration is performed and the number of integration steps used. Furthermore, using the prescription in [139] for the expectation value of the energy variation,

$$\langle\Delta\mathcal{H}\rangle \sim \frac{1}{2}\langle\Delta\mathcal{H}^2\rangle, \tag{4.2}$$

the dependence of $\Delta\mathcal{H}$ on the lattice volume V can be investigated for multiple MD trajectories. Indeed, for large enough volumes [1], one expects $\langle\Delta\mathcal{H}\rangle$ to vary linearly with V, or slower, and, assuming the time intervals to be sufficiently small, one obtains

$$\langle\Delta\mathcal{H}^2\rangle \approx C_n V \Delta t^{2n} \longrightarrow \langle\Delta\mathcal{H}^2\rangle^{\frac{1}{2}} \approx \tilde{C_n} V^{\frac{1}{2}} \Delta t^n, \tag{4.3}$$

[1] Here, *large enough* refers to the comparison with the correlation length. We refer to [138] for more details.

where C_n and $\tilde{C_n}$ are generic coefficients depending on the order of the integrator. In section 3.1.1, the Metropolis algorithm has been presented concerning the acceptance of a gauge configuration at each Molecular Dynamics step. At the end of each Markov chain, a probability acceptance rate can be defined as an average over the total number of Monte Carlo steps, and, depending on the order n of the integrator involved, an optimal acceptance probability [140] rate is obtained. Assuming again to work with sufficiently large volumes, the acceptance rate is described by means of the Gauss error function [138]

$$\langle P_{\text{acc}} \rangle = \text{erfc}\Big(\frac{1}{2}\Delta\mathcal{H}^{\frac{1}{2}}\Big), \tag{4.4}$$

which can be replaced by an easier alternative equation [140] as follow

$$\langle P_{\text{acc}} \rangle = \exp\Big(-\frac{2}{\sqrt{\pi}}\langle\frac{1}{8}\Delta\mathcal{H}^{\frac{1}{2}}\rangle\Big). \tag{4.5}$$

Assuming the efficience of the integrator to depend on the time interval Δt, one can define the efficiency function [140]

$$E(\Delta t) = \langle P_{\text{acc}} \rangle(\Delta t) \times \Delta t, \tag{4.6}$$

which provides information on the speed of the algorithm inside the integrators, and from equation (4.6) the optimal acceptance rate can be obtained as

$$P_{\text{opt}} = \max\Big\{E(\Delta t)\Big\}, \tag{4.7}$$

which can be redefined by taking into account equations (4.3) and (4.5) as

$$P_{\text{opt}} = e^{-\frac{1}{n}}, \tag{4.8}$$

being n the order of the integrator. Thus, for the 2MN integrator it reads $P_{\text{opt}} \approx 61\%$, whereas for the 4MN integrator it is $P_{\text{opt}} \approx 78\%$.

The implementation of the 2MN integrator in the CL^{2}QCD code was already provided in the first version released, both in one and two-time scales, in the position-like version [2]. On the contrary, the 4MN integrator has been implemented at the beginning of this thesis work, in the velocity-like position, to which we refer as 4MN5FV [3]. Then, in order to study the performances of the latter, a series of tests have been produced and followed by a direct comparison to the performances of the 2MN integrator, with two-time scales [4]. The analysis is performed by means of Monte Carlo simulations and unimproved staggered fermions, thus involving the RHMC algorithm, using an already existing gauge configuration as starting point. To the aim of this stage of the work, it was sufficient to perform 500 Molecular Dynamics trajectories for each simulated setup, which includes:

[2] We refer to Appendix B for more details about the nomenclature.

[3] The reason why the velocity version is preferred in this work to the position one is based on the results shown in [141]: Indeed, the 4MN5FP integrator shows a deviation from the Δt^4 asymptotic line at small $\sqrt{\langle\Delta\mathcal{H}^2\rangle}$ values, which makes it more unattractive since it can negatively affect the quality of data production.

[4] The comparison only includes the 2MN integrator with two-time scales, which has been the mostly involved one in the research group.

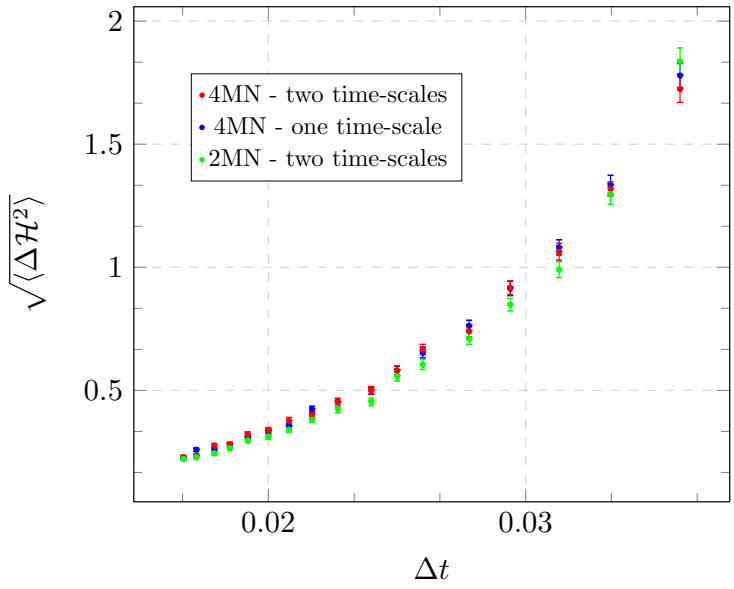

Figure 4.1: *Plot of* $\sqrt{\langle \Delta \mathcal{H}^2 \rangle}$ *as a function of the discretised time intervals* Δt *for the 4MN integrator in one and two-time scales and the 2MN integrator in two-time scales.*

- $N_f = 5$, which is the number of degenerate quark flavours,
- $am = 0.900$, which is the mass of the degenerate quarks on the lattice, which represents a relatively large mass, ensuring to work in a region sufficiently far from the chiral limit,
- $N_\tau = 4$, $N_\sigma = 12$,
- $\Delta t = \tau/n$, where τ represents the time interval in which a MD trajectory is performed and is set to $\tau = 1$, whereas n is the number of integration steps involved [5].

Simulations have been performed for $\beta(a) = 4.0$ and zero density, namely $\mu = 0$. In the current investigation, the number of integration steps when involving two-time scales is given for the *gauge update* as $n_0 = 2$, whereas the *fermionic update* is based on different n_1 integration steps[6]. At the end of each produced Markov chain the average energy variation at each step is evaluated as $\sqrt{\langle \Delta \mathcal{H}^2 \rangle}$, with an associated error $\sigma(\sqrt{\langle \Delta \mathcal{H}^2 \rangle})$. The latter can be obtained by propagating the uncertainty on $\langle \Delta \mathcal{H}^2 \rangle$, which is given as

$$\sigma(\langle \Delta \mathcal{H}^2 \rangle) = \frac{1}{\sqrt{N}} \sqrt{\frac{1}{N-1} \sum_{i=1}^{N} (\Delta H_i^2 - \bar{\mu})^2}, \tag{4.9}$$

where N is the number of trajectories performed whereas $\bar{\mu}$ reads

$$\bar{\mu} = \frac{1}{N} \sum_{i=1}^{N} \Delta \mathcal{H}_i^2.$$

[5] For more details about these definitions we refer to Appendix B, where also the difference between one and two-time scales is well explained.

[6] Again, for the nomenclature we refer to Appendix B

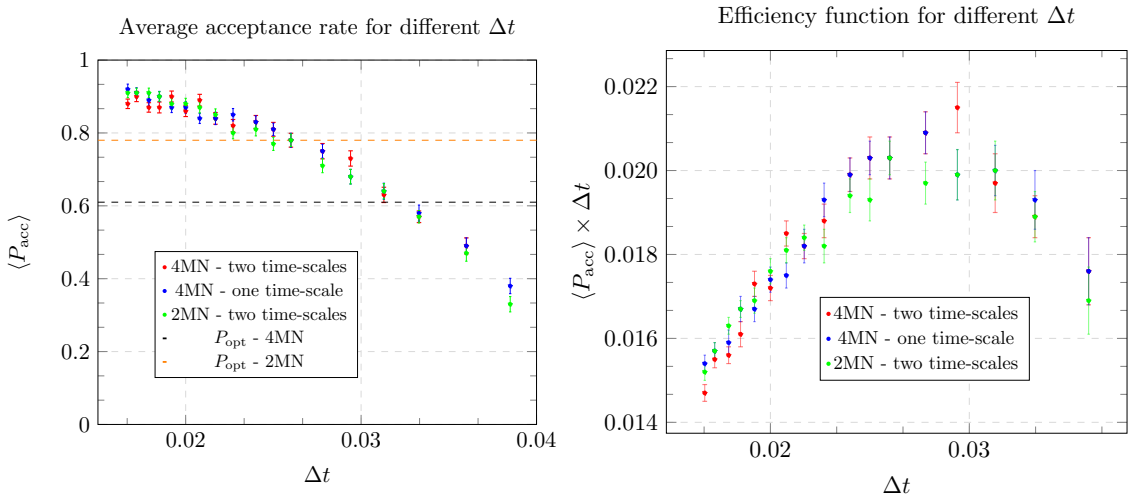

Figure 4.2: *Left: Plot of* $\langle P_{\rm acc}\rangle$ *as a function of the discretised time intervals* Δt *for the 4MN integrator in one and two-time scales and the 2MN integrator in two-time scales. Right: Evaluation of the efficiency of the integrators by means of* $\langle P_{\rm acc}\rangle \times \Delta t$ for different Δt values.

In order to evaluate $\sqrt{\langle \Delta\mathcal{H}^2\rangle}$ for different integrators, a scan in Δt is realised by varying the number of integration steps for the fermionic update in a suitable range. In figure (4.1) is reported the plot of $\sqrt{\langle \Delta\mathcal{H}^2\rangle}$ evaluated at different time intervals, when using the 4MN integrators in one and two-time scales and the 2MN integrator with two-time scale. This was performed by varying n_1 in the range $[24 : 60]$, resulting in $\Delta t \in [0.0167 : 0.0360]$. For any simulated setup, the average acceptance rate is also evaluated and reported in the plot to the left in figure (4.2), where the optimal acceptance rate has been indicated for both the integrators. Larger Δt values correspond to lower values of acceptance probability, which tends to $P_{\rm acc} \approx 90\%$ for smaller time intervals. In the plot to the right in figure (4.2) is represented the evaluation of the efficiency function $\langle P_{\rm acc}\rangle \times \Delta t$ for the three integrators, as Δt varies. Since the investigation is made for a finite number of fermionic integration steps, it is not possible to identify a corresponding maximum value of the function but rather a family of points which belong to a plateau: For the the three different scenarios, the latter corresponds to Δt values in the range $[0.25 : 0.31]$. At this point we analysed in more detail the results in figure (4.1) by taking into account equation (4.3). For the 4MN integrators we expect to observe the asymptotic behaviour $\sqrt{\langle \Delta\mathcal{H}^2\rangle} \approx \Delta t^4$, at least for sufficiently small Δt values. As reported in both the plots in figure (4.3), this seems to be a difficult task to be realised: Indeed, the expected behaviour only takes place for a few points as $\sqrt{\langle \Delta\mathcal{H}^2\rangle} \longrightarrow 0.1$ and locally in the proximity of $\Delta t_{\rm opt}$, but the overall trend seems to be better described when higher powers of Δt are involved. As well explained in section 3 of [138], after involving Creutz's equality, $\langle \Delta\mathcal{H}\rangle$ can be expanded into *cumulants* as

$$\langle \Delta\mathcal{H}\rangle = \frac{1}{2}\langle(\Delta\mathcal{H} - \langle \Delta\mathcal{H}\rangle)^2\rangle + \text{higher order cumulants}, \tag{4.10}$$

where the higher order cumulants correspond to higher powers of Δt. The realisation of (4.3) requires the contributions coming from the higher order cumulants to vanish, for large enough volumes tending to infinity. This can be obtained by varying Δt such that

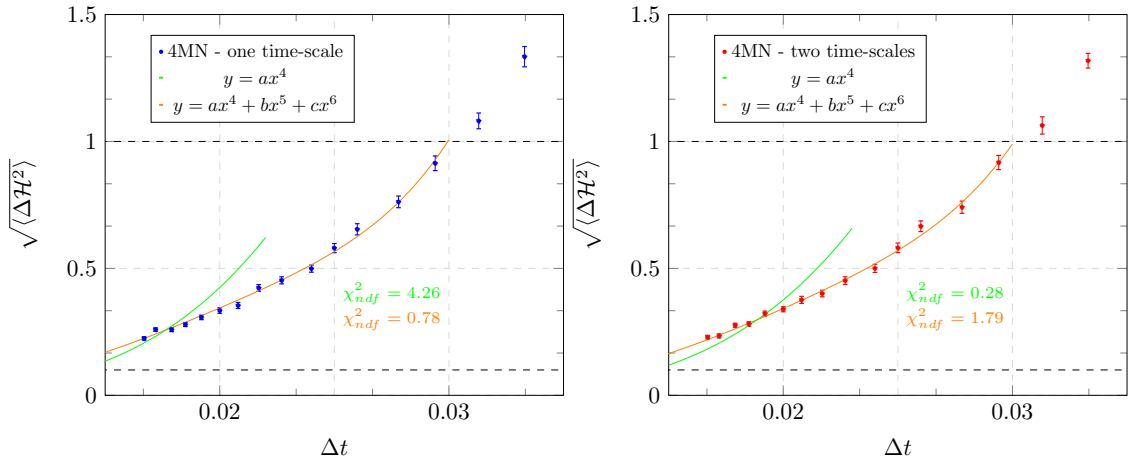

Figure 4.3: *Fits of $\sqrt{\langle \Delta\mathcal{H}^2 \rangle}$ as a function of Δt for the 4MN integrator in one-time scale (left) and the 4MN integrator in two-time scales (right).*

the error associated to $\langle \Delta\mathcal{H} \rangle$ is kept fixed, which in our case results in a hard statement to be fullfilled: Indeed, simulations are performed on a large lattice volume which is still a finite volume and the uncertainity associated to $\langle \Delta\mathcal{H} \rangle$ varies at each simulated setup. For the lowest Δt values, this variation becomes, eventually, negligible, which is the region where the investigation of the behaviour in (4.3) is more reasonable, for $\Delta t \lesssim 0.018$. For the 2MN integrator we expect to observe $\sqrt{\langle \Delta\mathcal{H}^2 \rangle} \approx \Delta t^2$, at least for sufficiently small Δt values. The sceanario reported in the plot to the left in figure (4.4) represents a completely different picture, when compared to the results in figure (4.3). In this case, the statement in equation (4.3) is realised for $\Delta t \lesssim 0.024$, which is a rather larger threeshold when compared to the previous results. Thus, for the 2MN integrator the role played by higher order cumulants appears to be *more negligible*, as confirmed by the reduced χ^2 value of the fit in figure (4.4). It is also worth to explain why in figures (4.4) and (4.3) the region corresponding to $0.1 \leq \sqrt{\langle \Delta\mathcal{H}^2 \rangle} \leq 1$ is delimited. As from figure (4.2), the *region* of acceptance probability where the current investigation results more logical is the one approximatively corresponding to the optimal one, namely $55\% \leq \langle P_{\text{acc}} \rangle \leq 90\%$, which corresponds to the delimitation drawn in figures (4.4) and (4.3). Finally, another parameter to take into account in this investigation is the average time needed to produce a Molecular Dynamics update in the Markov chains production. We refer to this parameter as $\tilde{t}$ and the results concerning its evaluation are reported the plot to the right in figure (4.4), for the three integrators. The 4MN integrator, in both the time-scale versions, requires an amount of time to solve the Molecular Dynamics integration which is approximatively equivalent to twice the time needed by the 2MN integrator. The difference in time grows as $\Delta t \longrightarrow 0.01$: In the proximity of the optimal Δt value the results show $\tilde{t} = 28.5s$ for the 4MN with two-time scales, $\tilde{t} = 25.5s$ for the 4MN integrator with one-time scale whereas for the 2MN integrator we obtain $\tilde{t} = 8.7s$, and in general this difference grows as Δt assumes smaller values. The results of this analysis lead to a possible conclusion about the comparison between the two integrators. As shown in detail in Appendix B, the 4MN integrator in both the time-scales versions ensures error terms in the integration of the order $\mathcal{O}(\Delta t^5)$, which makes it more attractive to be used with respect to the 2MN integrators, whose integration error is of magnitude

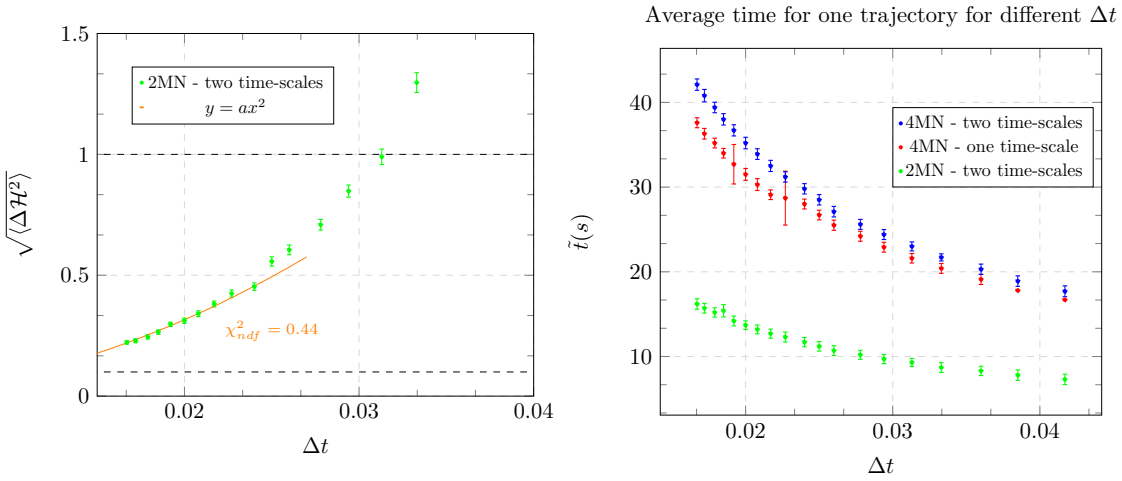

Figure 4.4: *Left: Fit of* $\sqrt{\langle \Delta \mathcal{H}^2 \rangle}$ *as a function of* Δt *for the 2MN integrator in two-time scales. Right : The average time needed to produce one single Monte Carlo step for different* Δt *values.*

$\mathcal{O}(\Delta t^3)$. Nevertheless, the 4MN integrator shows, in our implementation, some weak spots:

- The asymptotic behaviour expected for the variation in energy during a Markov chain production is equivalent to Δt^4 for extremely low Δt values, resulting in a huge influence from higher comulants even in the optimal acceptance probability region;
- The errors associated to $\sqrt{\langle \Delta \mathcal{H}^2 \rangle}$ are compatible for the same parameter setup. On average, the relative error evaluated as

$$\bar{\sigma_r}(\sqrt{\langle \Delta \mathcal{H}^2 \rangle}) = \sum_{i=1}^{N} \frac{\sigma_r^i(\sqrt{\langle \Delta \mathcal{H}^2 \rangle})}{N},$$

  is approximatively equal to 3% for the three integrators, where N is the number of parameter setups.
- The time needed to produce one MD trajectory is considerably higher when involving the 4MN integrators. Since the set of simulations involved in the topics which will be discussed in the next sections often include highly consuming ones, it sounds particularly prohibitive to involve the 4MN integrators.

In conclusion, being the unfavorable factors predominant with respect to the favorable ones, we opted for perfoming the next investigations by means of the 2MN integrator, with two-time scales.

4.2 The chiral phase transition at non-zero imaginary baryon chemical potential for different numbers of quark flavours

The project concerning the investigation of the extension of the first-order region in the light corner of the three-dimensional Columbia plot has been introduced in section 2.3.1,

as a natural continuation of the study on the chiral phase transition with non-integer numbers of quark flavours at zero density [9]. Besides the analysis methods, in Chapter 3 a general idea of the numerical strategy involved has been presented and summarised in figure (3.1). The use of a non-zero imaginary baryon chemical potential results in moving downwards from the Columbia plot, at $(\mu/T)^2 = 0$, to the Roberge-Weiss plane, at $(\mu/T)^2 = -(\pi/3)^2$, in the 3D Columbia plot, represented in figure (2.8) for $N_\tau = 4$, where inflation for the first-order chiral region in the light-mass corner is observed. Since we are interested in characterising this feature by means of Monte Carlo simulations, a good strategy resides in using an imaginary baryon chemical potential whose value is sufficiently higher than zero and sufficiently lower than the Roberge-Weiss [7] one. The reason for this choice consists in the necessity to compare our results with the ones from [9]: Indeed, in the RW plane the first-order chiral phase transition region becomes a first-order triple region and the Z_2 critical boundary is replaced by a tricritical line of masses, beyond which a Z_2 region can be found. Thu,s simulations in this parameter region would make difficult a direct comparison to the results in [9]. The imaginary baryon chemical potential value used in this project reads $\mu_i = 0.81\pi T/3$, namely the investigation is performed for a density approximatively equal to the 80% of the Roberge-Weiss one. Furthermore, the main conclusion in [9] consists in the order of the chiral phase transition in the continuum limit and chiral limit for $N_f \in [2, 7]$, which is second-order one. This result was obtained from the analysis of the tricritical scaling of the Z_2 boundary, performing extrapolation to the chiral limit for the different N_τ values for which the critical masses belonging to the Z_2 boundary have been computed. In this project, we will involve the same numerical strategy as in [9] and the parameter setups for which simulations have been performed is reported in table (4.1), where the number of degenerate quark masses for which data have been produced is indicated. For more details about the latter, we refer to Appendix C, where the results of the analysis have been reported for each parameter setup in details.

$N_\tau = 4$			$N_\tau = 6$			$N_\tau = 8$		
N_f	Nr. am values	N_σ	N_f	Nr. am values	N_σ	N_f	Nr. am values	N_σ
1.9	3	8-12-16	3.0	3	12-18-24	4.0	5	16-24
2.0	3	8-12-16	3.3	4	12-18-24	4.5	3	16-24-32
2.1	3	8-12-16	3.6	3	12-18-24			
2.2	3	8-12-16	4.0	3	12-18-24			
3.6	4	8-12-16	4.5	3	12-18-24			
4.0	4	8-12-16						
4.5	3	8-12-16						

Table 4.1: *The parameter setup used to perform simulations at* $\mu_i = 0.81\pi T/3$.

[7] In some cases we will use, for convenience, the acronym RW.

4.2.1 The extrapolation to the chiral limit in the (am, N_f) plane

Following the prescription in section 3.2.2, the study of the Z_2 boundary can be realised for any lattice cutoff (equivalently, for any lattice temporal extent) once a set of critical masses is computed, by means of the finite-size scaling procedure. These values are

N_f	N_τ	$am_{\min}$	$am_{\max}$	am_c	Δam_c	ndf	χ^2_{ndf}	Q	β_c	$\Delta\beta_c$
1.9	4	0.0020	0.0060	0.0036	0.0006	5	0.71	60.1%	5.3011	0.0011
2.0	4	0.0040	0.0120	0.0052	0.0007	6	0.77	59.2%	5.2873	0.0016
2.1	4	0.0060	0.0130	0.0080	0.0009	6	0.50	80.8%	5.2753	0.0026
2.2	4	0.0080	0.0140	0.0099	0.0008	7	0.74	72.4%	5.2629	0.0017
3.6	4	0.0370	0.0520	0.0459	0.0008	10	1.31	28.1%	5.1248	0.0015
4.0	4	0.0500	0.0650	0.0562	0.0007	10	1.31	21.6%	5.0925	0.0013
4.5	4	0.0650	0.0750	0.0684	0.0009	7	2.68	0.89%	5.0544	0.0022
3.0	6	0.0010	0.0030	0.0017	0.0005	5	0.25	90.1%	5.2276	0.0020
3.3	6	0.0030	0.0075	0.0042	0.0002	9	0.51	86.4%	5.1869	0.0008
3.6	6	0.0050	0.0100	0.0066	0.0005	6	0.59	73.2%	5.1481	0.0016
4.0	6	0.0075	0.0125	0.0107	0.0003	6	0.58	74.6%	5.1012	0.0012
4.5	6	0.0100	0.0180	0.0157	0.0005	6	0.56	76.2%	5.0441	0.0018
4.0	8	0.0010	0.0030	0.0013	0.0005	5	0.29	91.8%	5.1099	0.0035
4.5	8	0.0020	0.0040	0.0027	0.0009	3	0.57	63.3%	5.0339	0.0069

Table 4.2: *Results for the critical masses am_c belonging to the Z_2 critical boundary, their associated error, the critical $\beta(a)$ values corresponding to the am_c ones and the associated error for each simulated parameter setup.*

collected in the third column in table (4.2), where in the fourth column the corresponding error Δam_c has been reported, obtained from the finite-size scaling performed according to equations (3.33) and (3.34). In table (4.2) are also reported the minimum and maximum am values for which simulations have been realised, for fixed N_f and N_τ values, as well as the fitting parameters from the finite-size scaling, as the number of degrees of freedom *ndf*, the reduced chi squared χ^2_{ndf} and the Q parameter for the quality of the fit, introduced in equation (3.35). These results are represented in the (am, N_f) plane in figure (4.5), together with other points which are not reported in table (4.2), produced from the collaboration with other members of the research group [8]. The plot to the left represents the critical masses on the Z_2 boundaries for $N_\tau = 4$, $N_\tau = 6$ and $N_\tau = 8$, which separate the first-order chiral region that lays below from the crossover which lays above, for $\mu_i = 0.81\pi T/3$. Along the N_f-axis, a first-order triple line extends for $am = 0$, in correspondence to the first-order chiral region for non-zero bare quark masses. the plot to the right represents a comparison to the results obtained from the $\mu_i = 0$ investigation,

[8] Here we refer to all the points corresponding to $N_f = 6.0$, $N_f = 5.5$, $N_f = 5.0$ and $N_f = 2.3$.

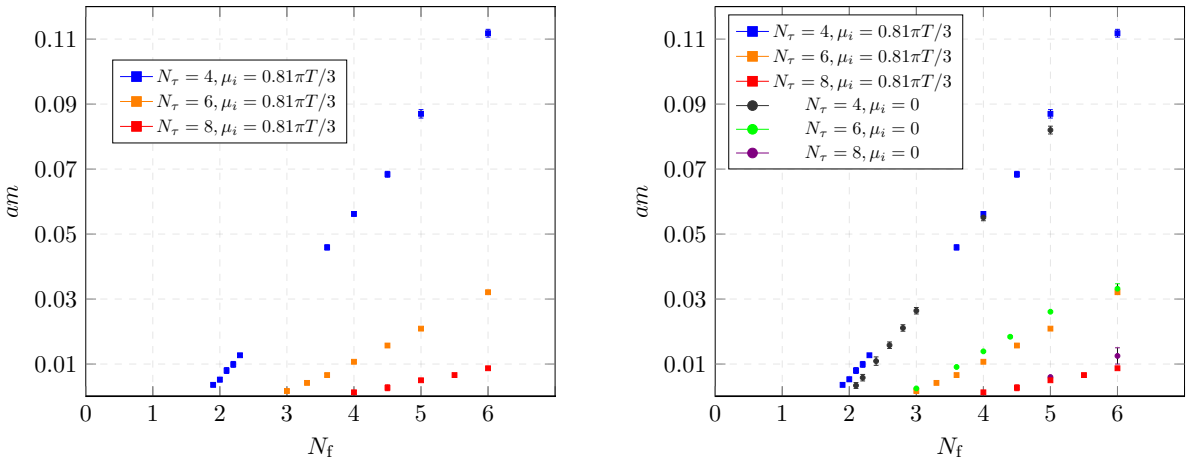

Figure 4.5: *Left: The critical masses belonging to the Z_2 boundary represented in the (am, N_f) plane for simulations peformed at $\mu_i = 0.81\pi T/3$. Right: Comparison between the results at $\mu_i = 0.81\pi T/3$ and $\mu_i = 0$ from [9].*

which provides an interesting result: Indeed, in the proximity of the chiral limit for $N_\tau = 4$ (namely for $N_f \in [1.9, 2.6]$), the critical masses corresponding to the zero density investigation assume lower values than the ones at non-zero density, which is the expected scenario, as reported in figure (2.8). For $N_\tau = 6$ and $N_\tau = 8$ the scenario in figure (4.5) is the opposite: For smaller lattice cutoffs, the critical masses from the zero density investigation are generally larger than the ones from the non-zero density investigation. As we are interested in the characterisation of the chiral phase transition in the chiral limit, extrapolation to the chiral limit is involved, to the aim of locating a corresponding tricritical $N_f^{\rm tric}$ point along the N_f-axis for the three lattice temporal extents. As already introduced in section 2.1.4, if a tricritical point exists for some specific $N_f^{\rm tric}$ value, then the critical masses scale in the proximity of the chiral limit as a tricritical scaling field. In equation (2.2), the function describing the tricritical scaling when N_f is involved as a scaling field has been reported. In the (am, N_f) plane, the scaling variable which can be used to investigate the tricritical scaling is the bare quark mass am and a suitable equation to describe such behaviour in the proximity of the chiral limit is obtained by inverting the polynomial equation in (2.2), which for ease of convenience we recall here,

$$N_f^c(am(N_\tau), N_\tau) = N_f^{\rm tric}(N_\tau) + a(N_\tau)(am)^{2/5} + b(N_\tau)(am)^{4/5} + \mathcal{O}((am)^{6/5}), \quad (4.11)$$

where N_f is given without error and the only variable provided with error is am. Let's explicitly derive the inverse of the latter for the zero density case. The first step consists in rewriting equation (2.2) as

$$N_f^c(am(N_\tau), N_\tau) - N_f^{\rm tric}(N_\tau) = a(N_\tau)(am)^{2/5} + b(N_\tau)(am)^{4/5} + \mathcal{O}((am)^{6/5}), \quad (4.12)$$

and, defining the variables [9]

$$N_f^c - N_f^{\rm tric} = y, \qquad am = x, \quad (4.13)$$

[9] To simplify the notation we avoid to report the dependencies of N_f, $N_f^{\rm tric}$ and am, which are understood.

the polynomial (4.12) reads

$$y = a(x)^{2/5} + b(x)^{4/5} + \cdots , \tag{4.14}$$

whereas the inverse polynomial we want to derive is given in the form

$$x^{2/5} = Ay + By^2 + \cdots . \tag{4.15}$$

At this point, one can substitute equation (4.15) in the polynomial (4.14),

$$y = aAy + aBy^2 + A^2by^2 + 2ABby^3 + B^2by^4 + \cdots ,$$

and, considering just the linear and quadratic terms in y, the corresponding coefficients can be obtained,

$$A = a^{-1}, \qquad\qquad B = -ba^{-3}.$$

From the latter, equation (4.15) becomes

$$x^{2/5} = a^{-1}y - ba^{-3}y^2 + \cdots ,$$

and, recalling the original variables,

$$(am)^{2/5} = C(N_f^c - N_f^{\text{tric}}) + D(N_f^c - N_f^{\text{tric}})^2 + \cdots ,$$

where $C = a^{-1}$ and $D = -ba^{-3}$. Since our interest is to study the scaling of am as a function of $(N_f^c(am(N_\tau), N_\tau) - N_f^{\text{tric}}(N_\tau))$, the polynomial we need reads

$$am = \Big[C(N_f^c - N_f^{\text{tric}}) + D(N_f^c - N_f^{\text{tric}})^2 + \cdots\Big]^{5/2}, \tag{4.16}$$

which can be expanded by means of a Puiseux series for $N_f^c \approx N_f^{\text{tric}}$. This can be done by simplyfing the notation again resorting to the substitutions in (4.13),

$$am = [Cy + Dy^2 + \cdots]^{5/2} = y^{5/2}[C + Dy + \cdots]^{5/2}, \tag{4.17}$$

and expanding the term in square brackets around $y = 0$ one obtains

$$[C + Dy + \cdots]^{5/2} \approx \frac{5}{2}C^{3/2}D + \frac{15}{4}C^{1/2}D^2y + \cdots .$$

The latter can be substituted in equation (4.17),

$$am = \frac{5}{2}C^{3/2}Dy^{5/2} + \frac{15}{4}C^{1/2}D^2y^{7/5} + \cdots ,$$

which becomes, after making again the variable y explicit and suitably redefining the coefficients,

$$\begin{aligned} am(N_\tau, N_f) = {} & \mathcal{A}_1(N_\tau)(N_f - N_f^{\text{tric}})^{5/2} + \\ & \mathcal{A}_2(N_\tau)(N_f - N_f^{\text{tric}})^{7/2} + \mathcal{O}(N_f - N_f^{\text{tric}})^{9/2}), \end{aligned} \tag{4.18}$$

where $\mathcal{A}_1$, $\mathcal{A}_2$ are parameters to be identified in the extrapolation. This procedure can be repeated when a non-zero imaginary baryon chemical potential is included in the theory, with the parameters in equation (4.18) that will also depend on it. In this case, the

N_τ	N_f^{tric}	$\mathcal{B}_1$	$\mathcal{B}_2$	χ^2_{ndf}	N_f^{min}	N_f^{max}
4	1.45(9)	0.0339(189)	-0.0176(182)	0.0003	1.9	2.3
6	2.24(7)	0.0046(7)	-0.0011(3)	0.0002	3.0	4.5
8	2.81(17)	0.0011(3)	-0.0002(1)	0.0002	4.0	6.0

Table 4.3: *Results of the extrapolation to the chiral limit.*

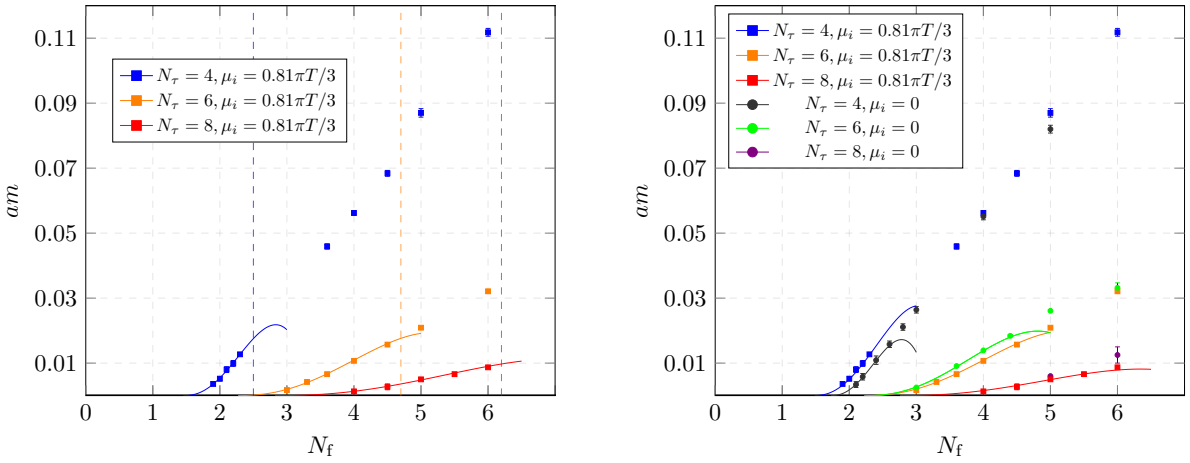

Figure 4.6: *Left: Representation of the extrapolation to the chiral limit for simulations performed at* $\mu_i = 0.81\pi T/3$*, according to equation* (4.19)*. Right: Comparison with the extrapolation to the chiral limit for results obtained at* $\mu_i = 0$ *[9].*

extrapolation can be performed by means of

$$\begin{aligned} am(N_\tau, N_f, \mu_i) = \mathcal{B}_1(N_\tau, \mu_i)(N_f - N_f^{\text{tric}})^{5/2} + \\ \mathcal{B}_2(N_\tau, \mu_i)(N_f - N_f^{\text{tric}})^{7/2} + \mathcal{O}(N_f - N_f^{\text{tric}})^{9/2}), \end{aligned} \tag{4.19}$$

where again $\mathcal{B}_1$, $\mathcal{B}_2$ are parameters, now depending on μ_i. The results of extrapolation to the chiral limit are reported in table (4.3), where N_f^{tric}, the parameters $\mathcal{B}_1$ and $\mathcal{B}_2$, the χ^2_{ndf} and the range of N_f values involved, are indicated for each N_τ value. The N_f^{tric} values from the $\mu_i = 0$ investigation can be compared to the ones in table (4.3): At zero density, the extrapolation to the chiral limit has been realised for $N_\tau = 4$ and $N_\tau = 6$, resulting, respectively, in $N_f^{\text{tric}}(N_\tau = 4) = 1.719(24)$ and $N_f^{\text{tric}}(N_\tau = 6) = 2.23(8)$. Compared to the results obtained in this work, the value for $N_\tau = 6$ shows compatibility within errorbars, meaning that the gap between the critical masses vanishes as the chiral limit is approached, whereas the value for $N_\tau = 4$ is definitely lower at non-zero density. Thus, the first-order triple line along the N_f-axis meets a second-order line at N_f^{tric}. The results of the extrapolation to the chiral limit in the (am, N_f) plane are reported in figure (4.6): In the plot to the left is represented the scenario for non-zero density, whereas

the comparison to the zero density results is given in the plot to the right. The vertical dashed-lines represent, approximatively, the N_f value for which, proceeding towards the chiral limit, it is reasonable to investigate the tricritical scaling.

4.2.2 The extrapolation to the chiral limit in the $(\beta(a)/(am)^{2/5})$ plane

The analysis of the results proceeds to the investigation of the critical $\beta_c(a)$ values associated to the critical masses on the Z_2 boundary. In section 3.2.3, the Ferrenberg-Swendsen reweighting has been introduced as a tool to obtain the pseudo-critical $\beta_{pc}(a)$ value to be associated to a specific parameter setup, which locates the chiral phase transition by means of $B_3(\beta_{pc}(a)) = 0$ for any N_τ, am and N_σ values. We stress again that this is the reason why we refer to these values as *pseudo-critical*: Indeed, they are not associated to the critical masses on the Z_2 boundaries and they still depend on the different quark masses on the lattice for which simulations are produced, as well as on the lattice spatial extents. Then, what is a good strategy to identify the $\beta_c(a)$ values to be associated to the critical masses in the (am, aT) plane, for fixed N_f? Given a specific parameter setup, at least three lattice spatial extents have been used, in order to realise the finite-size scaling: The largest ones, corresponding to the aspect ratio $(N_\sigma/N_\tau) = 4$, are the ones *closer* to the continuum limit [10], which means they represent a good source of data from which reliable values of $\beta_c(a)$ can be obtained. Taking into account only the results in this scenario, we consider the $\beta_{pc}(a)$ values corresponding to each bare quark mass involved in our numerical strategy, and the desired $\beta_c(a)$ value can be obtained by means of interpolation, realised according to the linear function

$$\beta_c(a) = \mathcal{C}_1 + \mathcal{C}_2(am - am_c), \tag{4.20}$$

where $\mathcal{C}_1$ and $\mathcal{C}_2$ are parameters to be identified and am_c are the critical masses in table (4.2). An example of such procedure is reported in figure (4.7), where the interpolation is represented. The dashed-black line identifies the am_c of the corresponding parameter setup whereas the gray lines delimit the values $am_c \pm \Delta am_c$, where $\beta_c(a)$ is given by the intersection between the interpolation function in red and the black-dashed line. The values obtained for each parameter setup are also reported in table (4.2), together with the errors $\Delta\beta_c(a)$, obtained by a more scrupulous analysis of the interpolation plot. Indeed, the dashed lines corresponding to $am_c \pm \Delta am_c$ also hit the intepolation function, thus, since the parameters $\mathcal{C}_1$ and $\mathcal{C}_2$ are known as well as am_c, it is sufficient to evaluate equation (4.20) for $am = am_c \pm \Delta am_c$, which provides the values reported in the last column to the right in table (4.2). Repeating this procedure for all the parameter setups, a further investigation on the $\beta_c(a)$ values can be made by means of extrapolation to the chiral limit. In figure (4.8) the values of the critical gauge coupling on the lattice are represented in the $(\beta(a), (am)^{2/5})$ plane, where the independent variable represents the bare quark mass scaled according to the tricritical scaling power, for $N_\tau = \{4, 6, 8\}$. In the proximity of the chiral limit, considering again an extrapolation process, the behaviour of the $\beta_c(a)$ points as $(am)^{2/5}$ varies is well described for $\mu_i = 0$ by [9]

$$\beta_c(am, N_f(N_\tau), N_\tau) = \beta^{\text{tric}}(N_\tau) + \mathcal{F}_1(N_\tau)(am^{2/5}) + \mathcal{F}_2(N_\tau)(am^{4/5}) + \mathcal{O}((am^{6/5})), \tag{4.21}$$

which contains the dependencies on the mass field $(am)^{2/5}$ up to the next-to-leading order, being $\mathcal{F}_1$ and $\mathcal{F}_2$ the tipical parameters of the extrapolation to be identified. When

[10] Of course, simulations are always performed at finite lattice spatial and temporal extents. The statement here, qualified by the adjective *closer*, is meant to stress that the lattice becomes finer as N_σ becomes larger, for fixed N_τ values.

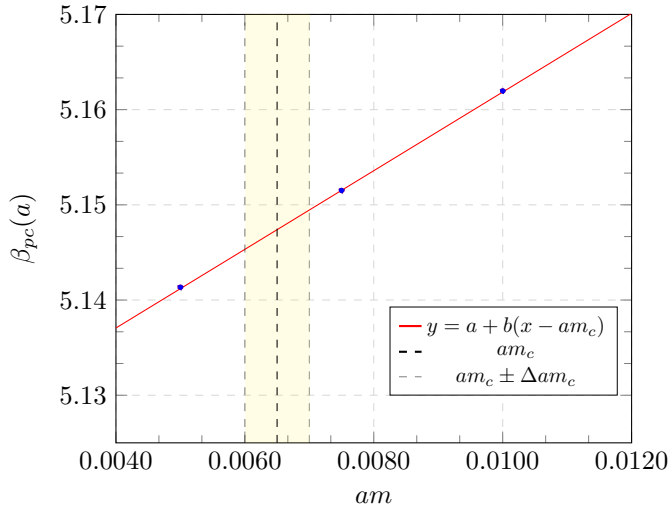

Figure 4.7: *Example of interpolation realised to obtain the* $\beta_c(a)$ *for the parameter setup* $N_f = 3.6$, $N_\tau = 6$.

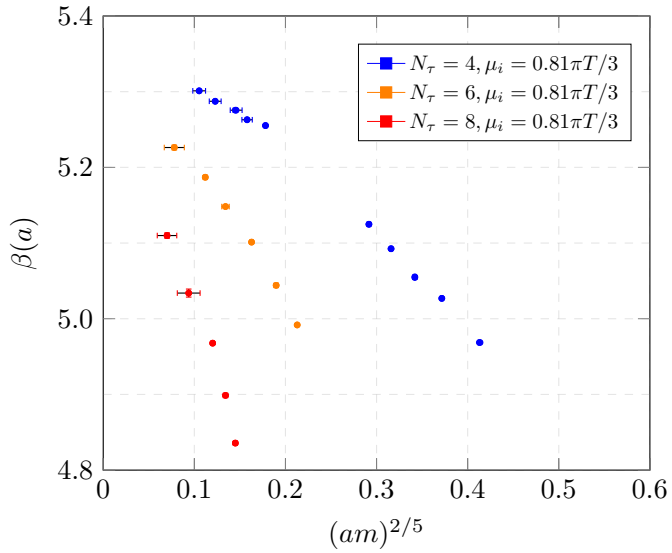

Figure 4.8: *The* $\beta_c(a)$ *values as a function of the mass field* $(am)^{2/5}$ *for* $N_\tau = \{4, 6, 8\}$.

N_τ	LO + NLO extrapolation						
	$\beta(a)^{\text{tric}}$	$\Delta\beta(a)^{\text{tric}}$	$\mathcal{F}_1$	$\Delta\mathcal{F}_1$	$\mathcal{F}_2$	$\Delta\mathcal{F}_2$	χ^2_{ndf}
4	5.3115	0.0156	0.1697	0.1653	-2.7737	0.4057	1.43
6	5.2462	0.0325	0.3245	0.4801	-7.5831	1.6870	0.64
8	5.0770	0.1264	2.3718	2.6290	-27.4582	12.9998	0.55

Table 4.4: *Results of the extrapolation to the chiral limit for $N_\tau = \{4, 6, 8\}$, taking into account the $\beta_c(a)$ values in figure* (4.8)*, using equation* (4.21).

non-zero imaginary baryon chemical potentials are involved, equation (4.21) becomes

$$\begin{aligned}\beta_c(am, N_f(N_\tau), N_\tau, \mu_i) =& \beta^{\text{tric}}(N_\tau, \mu_i) + \mathcal{F}_1(N_\tau, \mu_i)(am^{2/5}) + \\ & \mathcal{F}_2(N_\tau, \mu_i)(am^{4/5}) + \mathcal{O}((am^{6/5})),\end{aligned} \tag{4.22}$$

and the results of the application of equation (4.22) to the points in the plot in figure (4.8) are reported in the plot to the left in figure (4.9), whereas the details on β^{tric}, as well as on the extrapolation parameters, have been reported in table (4.4). Observing the extrapolation lines for $N_\tau = \{4, 6, 8\}$, an unexpected change in slope for $(am)^{2/5} \lesssim 0.008$ is shown, which is milder for $N_\tau = 4$. Furthermore, from data in table (4.4), one

NLO etrapolation					
N_τ	$\beta(a)^{\text{tric}}$	$\Delta\beta(a)^{\text{tric}}$	$\mathcal{G}$	$\Delta\mathcal{G}$	χ^2_{ndf}
4	5.3277	0.0027	-2.3689	0.0632	1.33
6	5.2681	0.0038	-6.4544	0.1513	0.54
8	5.1970	0.0212	-16.2212	1.3970	0.55

Table 4.5: *Results of the extrapolation to the chiral limit for $N_\tau = \{4, 6, 8\}$, taking into account the $\beta_c(a)$ values in figure* (4.8)*, using only the quadratic term (next-to-leading term) in equation* (4.21).

notices that the parameters which couples to the leading order term in equation (4.22) are affected by an extemely large uncertainity, for each N_τ value, de facto rendering the $\mathcal{F}_1$ overestimated. Thus, the values of β^{tric} obtained are not reliable and further work is to be done. Considering again equation (4.22) and removing the linear term in $(am)^{2/5}$,

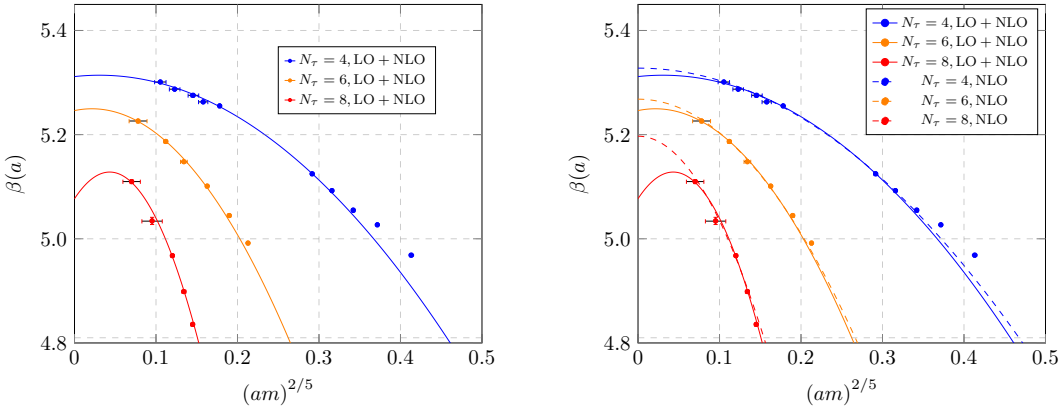

Figure 4.9: *Left: Representation of the extrapolation to the chiral limit for simulations performed at* $\mu_i = 0.81\pi T/3$*, on the* $(\beta(a), (am)^{2/5})$ *plane, using leading and nex-to-leading orders in* $(am)^{2/5}$*. Right: Comparison to the extrapolation performed by means of the only next-to-leading term in* $(am)^{2/5}$*.*

the extrapolation function reads

$$\beta_c(am, N_f(N_\tau, \mu_i), N_\tau) = \beta^{\text{tric}}(N_\tau, \mu_i) + \mathcal{G}(N_\tau, \mu_i)(am^{4/5}) + \mathcal{O}((am^{6/5})), \tag{4.23}$$

which contains only a quadratic dependence on the scaled mass field, where $\mathcal{G}$ is the extrapolation parameter to be evaluated. The outcome of the application of equation (4.23) to the points in figure (4.8) can be read in table (4.5), and a comparison to the previously obtained results by means of (4.22) si reported in the plot to the right in figure (4.9), using dashed lines. Comparing table (4.4) to table (4.5), the values of β^{tric} differ, resulting in larger values from the extrapolation performed by means of equation (4.23). The corresponding extrapolation lines do not show a change in slope as previously happened and the error on β^{tric} are considerably lower than the previous ones, for each N_τ value. Thus, from this last analysis we can conclude that the results of our investigation do not belong to the linear-scaling region of masses $(am)^{2/5}$ and a dependence on the leading-order term in equation (4.22) would, presumably, become predominant for larger temporal extents, $N_\tau \gtrsim 10$.

4.2.3 The extrapolation to the chiral limit in the $((am)^{2/5}, aT)$ plane

The last part of this analysis consists in translating the results in the (am, N_f) plane to the $((am)^{2/5}, aT)$ plane and studying the tricritical scaling of the critical masses performing extrapolation to the chiral limit again. In table (4.6) are reported the values of the critical masses according to the power describing a tricritical scaling, $(am)^{2/5}$, considering only the physical values of N_f, namely $N_f = 4.0$, $N_f = 5.0$ and $N_f = 6.0$, for the three different N_τ values. The location of the tricritical aT point in the chiral limit is realised, for zero density and a specific N_τ value, according to equation [9]

$$aT(am, N_f) = aT_{\text{tric}} + \mathcal{D}_1(N_f)(am)^{2/5} + \mathcal{D}_2(N_f)(am)^{4/5} + \mathcal{O}(am^{6/5}), \tag{4.24}$$

which can be adapted to the non-zero density case by accounting for new parameters that, differently from $\mathcal{D}_1$ and $\mathcal{D}_2$, will also depend on μ_i,

$$aT(am, N_f, \mu_i) = aT_{\text{tric}} + \mathcal{E}_1(N_f, \mu_i)(am)^{2/5} + \mathcal{E}_2(N_f, \mu_i)(am)^{4/5} + \mathcal{O}(am^{6/5}), \tag{4.25}$$

N_f	N_τ	aT	$(am_c)^{2/5}$	$\Delta(am_c)^{2/5}$
4.0	4	0.250	0.3159	0.0016
4.0	6	$0.1\overline{66}$	0.1628	0.0018
4.0	8	0.125	0.0701	0.0107
5.0	4	0.250	0.3765	0.0023
5.0	6	$0.1\overline{66}$	0.2128	0.0012
5.0	8	0.125	0.1204	0.0004
6.0	4	0.250	0.41262	0.00012
6.0	6	$0.1\overline{66}$	0.25163	0.00003
6.0	8	0.125	0.14851	0.00001

Table 4.6: *The critical masses assumed as a tricritical scaling field, with corresponding errors. Results for different N_τ (aT) values, for $N_f = 4.0$, $N_f = 5.0$ and $N_f = 6.0$.*

N_f	aT_{tric}	$\mathcal{E}_1$	$\mathcal{E}_2$
4.0	0.0967	3.281	-3.507
5.0	0.0766	2.9877	-2.498
6.0	0.0748	3.9217	-4.823

Table 4.7: *Results of the extrapolation in equation* (4.25)*, applied to the points in the plot to the left in figure* (4.10)*.*

with $\mathcal{E}_1$ and $\mathcal{E}_2$ to be identified [11]. In figure (4.10), the scaled critical masses in the $((am)^{2/5}, aT)$ plane obtained from the values in (4.1) are reported whereas a direct comparison to the results at $N_f = 5.0$, $N_f = 6.0$ and $N_f = 7.0$ for $\mu_i = 0$ from [9] is shown in the plot to the right. The results of the application of equations (4.24) and (4.25) to these points is reported in figure (4.11), where the extrapolation lines to the chiral limit are represented. A first-order chiral region extends below these extrapolation lines, a crossover region above and again a first-order triple line extends below these curves, for $am = 0$.

[11] Equations (4.24) and (4.25) are also obtained by inverting the polynomial equation in (2.2).

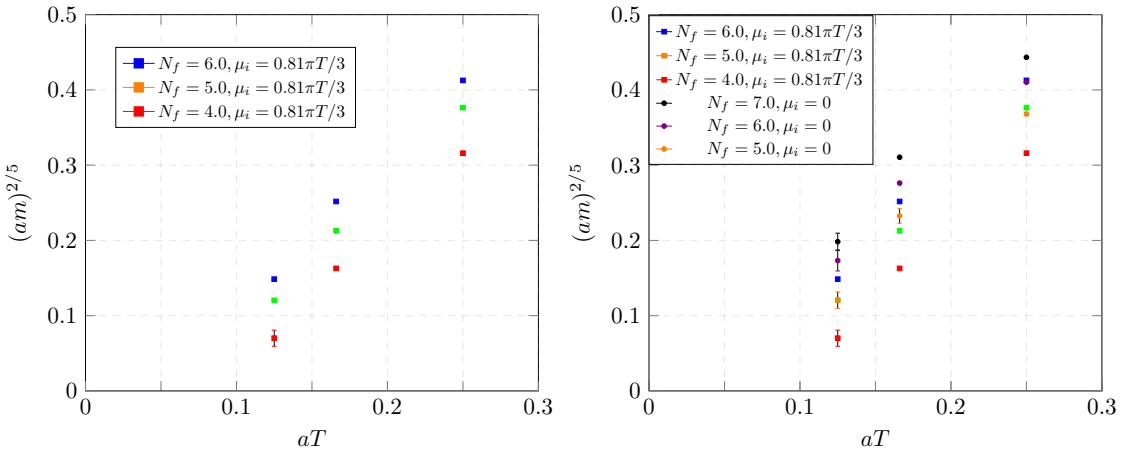

Figure 4.10: *Left: Representation of the critical masses in Table* (4.10) *for three* N_f *values in the* $((am)^{2/5}, aT)$ *plane for* $\mu_i = 0.81\pi T/3$. *Right: Comparison to the results obtained at* $\mu_i = 0$ *[9].*

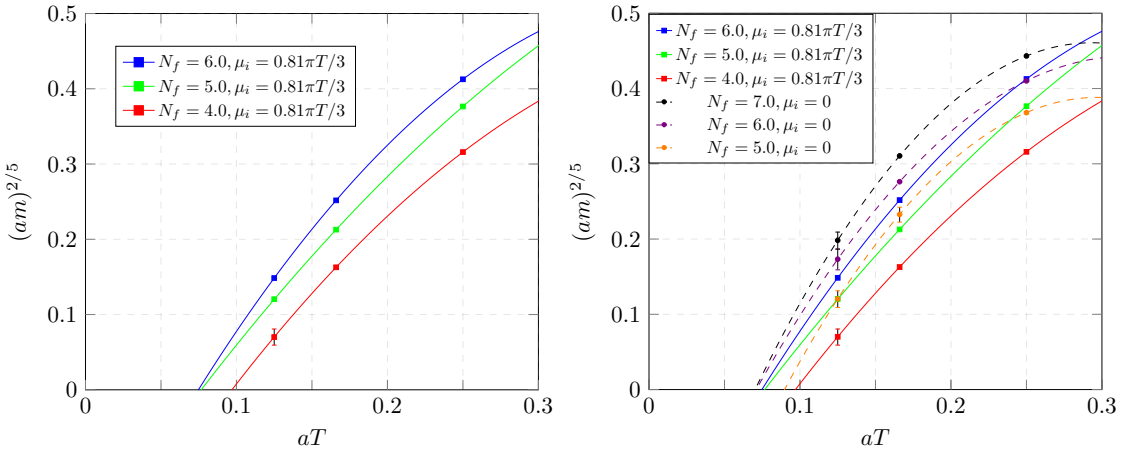

Figure 4.11: *Left: Representation of the extrapolation to the chiral limit in the* $((am)^{2/5}, aT)$ *plane for* $\mu_i = 0.81\pi T/3$. *Right: Comparison to the extrapolation at* $\mu_i = 0$ *[9], represented by means of dashed lines.*

Comparing the results of the two analysis, the behaviour for $\mu_i = 0.81\pi T/3$ shows compatibility with a tricritical scaling, thus with the presence of aT_{tric} along the aT axis, as for the the zero density investigation. The overall results can be generalised once more in a plot as the one reported to the left in figure (2.4), for a generic N_f value: The range of validity of such representation for $\mu_i = 0.81\pi T/3$ coincides with the range $N_f \in [2, 6]$ and the results of the extrapolation by means of (4.25) are given in table (4.7) [12]. Before drawing conclusions about this section, a further comment can be formulated when studying the behaviour of the critical masses as a function of the inverse of the lattice temporal extent. In principle, when fixing some N_f values as in figure (4.10) there is no guarantee a tricritical scaling can be obtained in the proximity of the chiral limit, and, as a consequence, a first-order phase transition could extend towards the continuum limit. In order to further check the validity of the results obtained, a good strategy consists in studying the behaviour of the critical masses by means of a polynomial function, derived from a Taylor expansion of $am_c(N_\tau, N_f, \mu_i)$ around $aT = 0$, namely for $N_\tau \longrightarrow \infty$,

$$am_c(N_\tau, N_f, \mu_i) = \mathcal{P}_1(N_f, \mu_i)aT + \mathcal{P}_2(N_f, \mu_i)(aT)^2 + \mathcal{P}_3(N_f, \mu_i)(aT)^3 + \cdots , \quad (4.26)$$

where the value $am_c(N_\tau) = 0$ as $N_\tau \longrightarrow \infty$. An example of this investigation is reported in

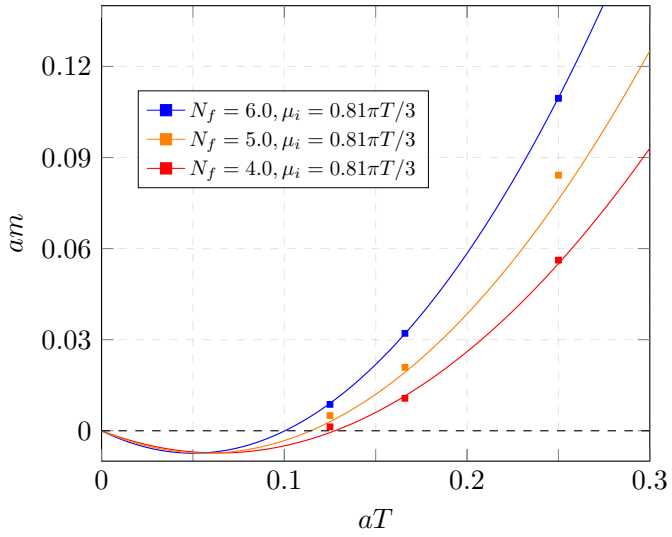

Figure 4.12: *Example of the scaling of the critical masses for three N_f values in the (am, aT) plane for $\mu_i = 0.81\pi T/3$ according to equation (4.26), when involving the linear and quadratic terms in aT.*

figure (4.12) for $N_f = \{4, 5, 6\}$. Although for $N_f = 6$ the behaviour may be well described by equation (4.26), the same does not apply to $N_f = 4$ and $N_f = 5$. Indeed, comparing figure (4.12) to the plot to the left in figure (4.11), the incompatibility of the results with equation (4.26) becomes evident, in favour of the tricritical scaling. Furthermore, the results in figure (4.12) show compatibility with negative lattice masses, which do not represent a physical scenario. In table (4.8) are reported the details of the parameters of the fit, according to equation (4.26), when using the combinations of linear and quadratic

[12] No error is displayed for the paramaters, since the numbers of parameters and critical mass points conincides.

N_f	$\mathcal{P}_1$	$\mathcal{P}_2$	$\mathcal{P}_3$	χ^2_{ndf}
4.0	-	-0.6500(599)	6.2105(0.2780)	2.34
	-0.2294(321)	1.7982(0.1773)	-	22.82
5.0	-	-0.257(22)	2.347(0.137)	49.05
	-0.2569(220)		-	23.72
6.0	-	-0.172(315)	7.75(1.48)	52.21
	-0.294(5)	2.931(28)	-	0.49

Table 4.8: *Results of the fit according to equation* (4.26)*, for different parameter setups.*

terms or quadratic and cubic terms. The values of the χ^2_{ndf} suggest a good quality only in one scenario, whereas, in general, they are large to give credence to these fits, and this statement is sufficient to validate the results according to the tricritical scaling of am_c as a function of aT.

4.2.4 Conclusions

At this point, enough results have been collected to draw conclusions out of this project. The main points of the analysis can be summariesed as follow:

- Extrapolation to the chiral limit in the (am, N_f) plane for $\mu_i = 0.81\pi T/3$ shows compatibility of the Z_2 boundary for $N_\tau = \{4, 6, 8\}$ with a tricritical scaling, for sufficiently small degenerate quark masses on the lattice. From a direct comparison to the results obtained for $\mu_i = 0$ in [9], the first-order chiral region for $\mu_i = 0.81\pi T/3$ and $N_\tau = 4$ extends to larger values of Z_2 critical masses when compared to the zero density results. The opposite applies for $N_\tau = \{6, 8\}$. The results of the extrapolation confirm N_f^{tric} to be smaller for $N_\tau = 4$ at non-zero density whereas for $N_\tau = 6$ the values at different densities are compatible within error bars.

- The tricritical scaling has been observed in the $(\beta(a), (am)^{2/5})$ plane for $\mu_i = 0.81\pi T/3$. The results showed a predominant quadratic dependence on the scaled mass field $(am)^{2/5}$ when the extrapolation to the chiral limit is performed, providing different $\beta(a)^{\text{tric}}$ values for $N_\tau = \{4, 6, 8\}$.

- The translation of the results to the $((am)^{2/5}, aT)$ plane for $\mu_i = 0.81\pi T/3$ confirmed the presence of aT^{tric} points along the x-axis for $N_f = \{4.0, 5.0, 6.0\}$. Compared to the results from $\mu_i = 0$, the same behaviour is observed.

The interpretation of this outcome, based on simulations performed with unimproved staggered fermions, leads to the classification of the first-order chiral region as a lattice artifact, with no correspondence in the continuum limit. In principle, to draw this conclusion some precautions need to be used: The discretisation involved for the fermionic action explicitly breaks the chiral symmetry also in the chiral limit, which means that reasonable results could be obtained by performing, in the order, the continuum limit

and the chiral limit. Nevertheless, the power of numerical strategy involved in this work consists in the possibility to gather information in the chiral limit by a direct observation of the results in the $((am)^{2/5}, aT)$ plane, in figures (4.24) and (4.25): If a tricritical scaling is observed for a specific N_f value and aT_{tric} is identified, then moving towards the continuum limit ($a \longrightarrow 0$, namely the origin of the axis of the plot) along the first-order triple line a tricritical point is to be trepassed. Beyond the latter, only a second-order line extends. This is the same statement concerning the fate of the first-order chiral region on the Columbia plot [9], removing the ambiguity on the order of the chiral phase transition for $N_f = 2$, in the continuum limit.

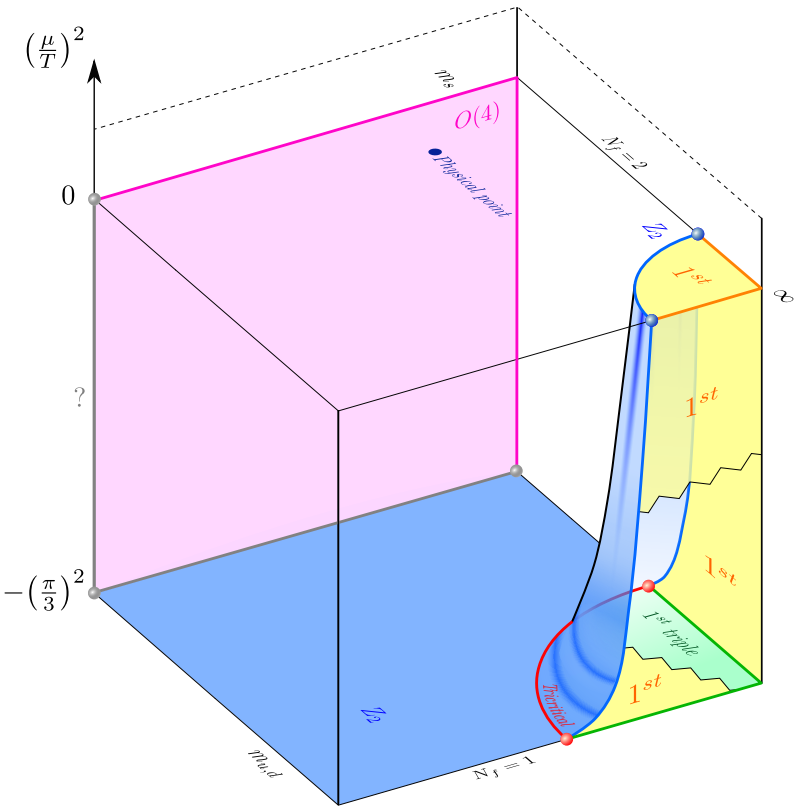

Figure 4.13: *Representation of the 3D Columbia plot. For $N_f = 2$, a second-order chiral phase transition is given for any value of μ_i, in the continuum limit and chiral limit. Picture of Dr. Alessandro Sciarra.*

As a general conclusion, no dependence of the order of the chiral phase transition on the imaginary baryon chemical potential has been detected from our results: In the 3D Columbia plot reported in figure (4.13) this is represented, in the continuum limit, by means of a second-order chiral surface extending from the Columbia plot ($\mu_i = 0$) downwards to the Roberge-Weiss plane ($\mu_i = \pi T/3$)(which is excluded from this analysis) as the imaginary baryon chemical potential is varied, for $N_f = 2$. Thus, our results are in good agreement with more works in literature, as [64; 65; 80], where HISQ have been involved in the numerical strategy.

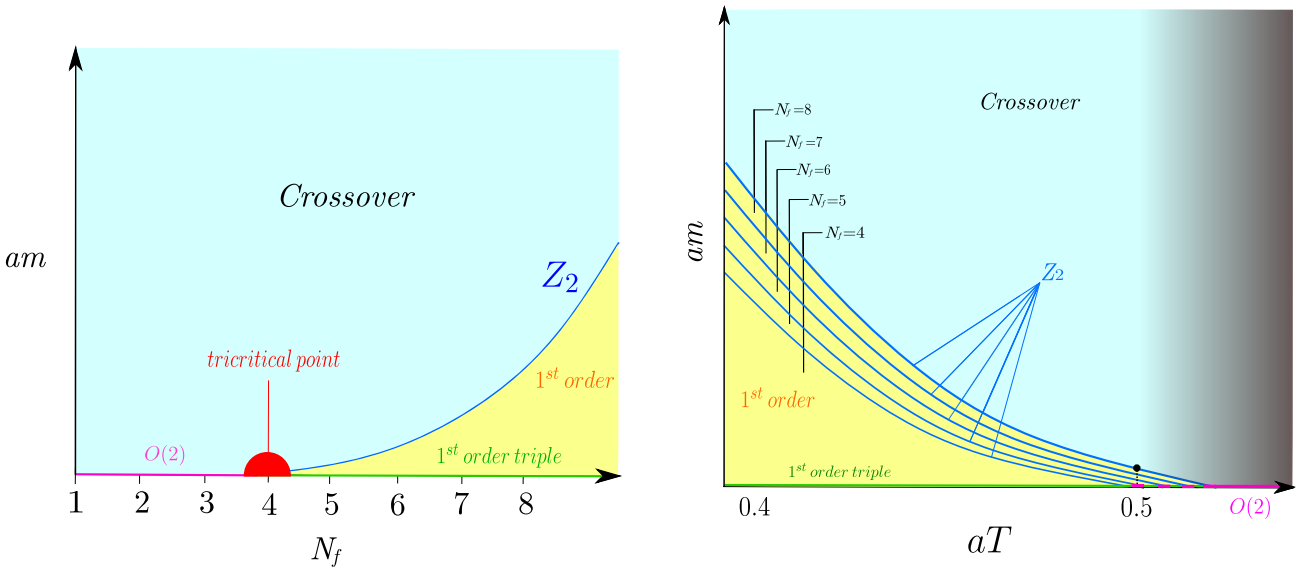

Figure 4.14: *Left: The extension of the first-order chiral region in the* (am, N_f) *plane for* $N_\tau = 2$*: The red semicircle in the proximity of* $N_f = 4$ *in the chiral limit represents the location of the tricritical point, which is difficult to locate based on our results. Right: Representation of the first-order chiral region for different* N_f *values in the strong coupling regime: The gray gradient beyond* $aT = 0.5$ *represents an area where no information coming from simulations is given.*

4.3 The chiral phase transition from strong to weak coupling

In Chapter 2, a discussion on the QCD phase diagram at strong coupling has been presented, where the methodology and techniques involved have been introduced in details. In section 2.3.2, in particular, an introduction to the aim of the project developed in this section was given: Using the same numerical strategy involved in the project discussed in section 4.2, the extension of the first-order chiral region in the strong coupling regime has been investigated on a coarse lattice, whose temporal extent reads $N_\tau = 2$, for $\mu_i = 0$. In the weak coupling regime it was shown how the extension of the first-order chiral region grows when moving from a finer lattice ($N_\tau = 8$) to a coarser one ($N_\tau = 4$). Based on the literature presented in section 2.3.2, a non-monotonic behaviour of the Z_2 boundary is expected, namely the slope of the latter changes after a global maximum for $0.25 < aT < 0.50$ takes place, resulting in a shrinking of the first-order region for $N_\tau = 2$. As schematically represented in the plot to the left in figure (4.14), the scaling of the Z_2 boundary in the proximity of the chiral limit is compatible with a tricritical scaling. Along the N_f-axis in the (am, N_f) plane and along the aT axis in the (am, aT) plane, a first-order triple line is given, since the axis coincides with the lattice chiral limit, $am = 0$. Thus, the tricritical point represents the meeting point between the first-order triple line and a second-order line, extending in correspondence to the crossover region, in the chiral limit. Nevertheless, the study of the Z_2 boundary, using the numerical strategy reported

in figure (3.2), results in a challeging task for numerical purposes: The extension of the first-order region for $am \neq 0$ is limited to the region of lattice quark masses in the proximity of the chiral limit and the time-consuming Markov chains production, together with finite-size effects for the smaller lattice spatial extents, impact negatively on the quality of data production. In the following, the results of the study for $N_f = 8$ and $N_f = 4$ are discussed.

4.3.1 The investigation for $N_f = 8$

The first parameter setup to be investigated in the strong coupling regime corresponds to $N_f = 8$, $N_\tau = 2$ and a set of quark masses on the lattice is defined. The choice of $N_f = 8$ represents a good starting point: Indeed, the extension of the first-order chiral region for $aT = 0.5$ is wider when compared to lower N_f values, thus locating a critical mass on the Z_2 boundary is a more feasible task. Furthermore, it represents the upper boundary in terms of N_f values for which a chiral phase transition takes place, at finite temperature: This statement relies on the presence of the *conformal window* of N_f values [142] [143] [144], whose conformal N_f^* point is expected in the range $9 \leq N_f^* \leq 12$. As

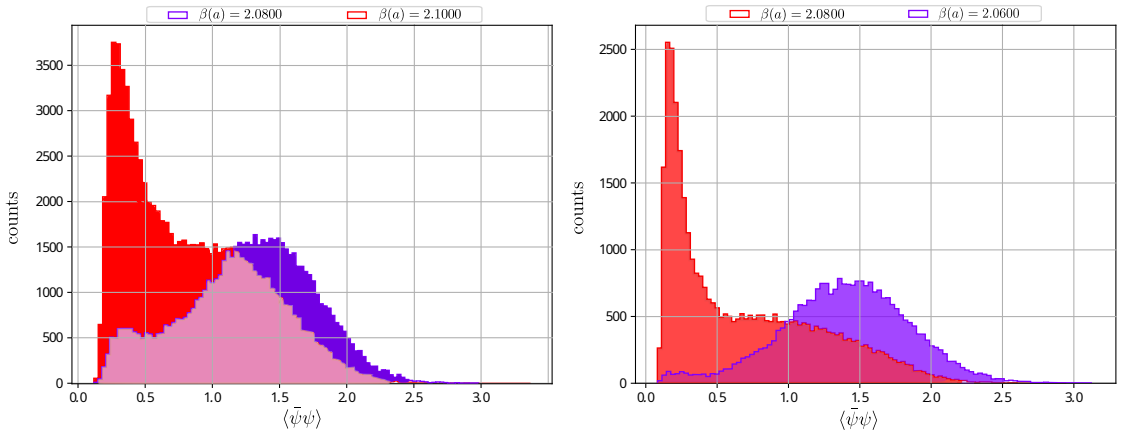

Figure 4.15: *The histograms of $\langle\bar{\psi}\psi\rangle$ corresponding to two $\beta(a)$ values for the parameter setups $N_f = 8$, $\mu_i = 0$, $am = 0.0020$, $N_\tau = 2$, $N_\sigma = 10$ (left) and $N_f = 8$, $\mu_i = 0$, $am = 0.0010$, $N_\tau = 2$, $N_\sigma = 12$ (right).*

the critical mass belonging to the Z_2 boundary is expected to be small, a scan has been produced for the set $am = \{0.0010, 0.0015, 0.0020, 0.0025, 0.0035\}$, as reported in the analysis results in Appendix C. For these masses, the first attempts to produce Markov chains and evaluate the sampled distribution of the chiral condensate proved unsuccessful: Using $N_\sigma/N_\tau = \{3, 4, 5\}$ resulted in clear finite-size effects[13] as shown in two examples in figure (4.15), and the analysis and reweighting procedure applied to these results provide unreliable values of skewness and kurtosis and, consequently, unreliable values of $\beta_{pc}(a)$. This means that the physical system requires larger aspect ratios to be involved, namely $N_\sigma/N_\tau = \{6, 8, 10\}$: If this adjustment in the numerical strategy allows to remove or make the finite-size effects milder, on the other hand the time needed to produce one step in the Markov chains production grows dramatically for some parameter setup, mainly for the lowest am values and largest volume considered. As a consequence, a certain inbalance between the total statistics accumulated for the minimum and maximum value

[13] The topic has been discussed in section 3.2.3.

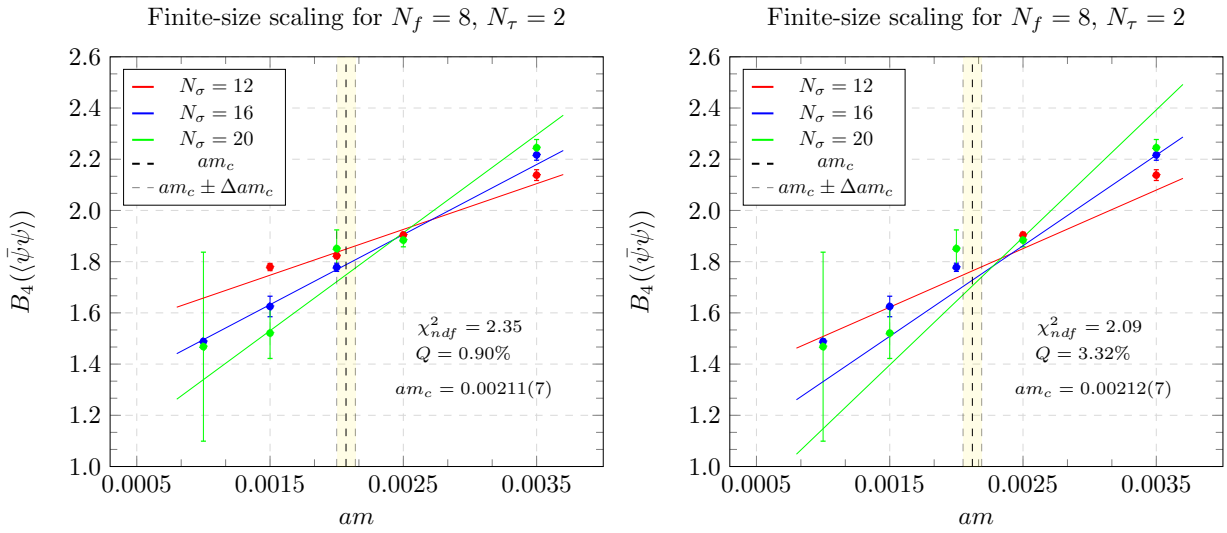

Figure 4.16: *Left: The results of the finite-size scaling for $N_f = 8$ when using $N_\sigma = 12$, $N_\sigma = 16$, $N_\sigma = 20$, looking for a Z_2 boundary. Right: The finite-size scaling performed after excluding the points corresponding to $am = \{0.0015, 0.0020\}$, for $N_\sigma = 12$.*

of masses used for simulations can be observed [14]. Following the methodology presented in Chapter 3, the investigation of the Z_2 boundary is performed and the results of the finite-size scaling, using equation (3.34), is shown in figure (4.16). The plot to the left represents the finite-size scaling performed taking into account the three aspect ratios $N_\sigma/N_\tau = \{6, 8, 10\}$. The critical mass identified in this scenario reads $am_c = 0.00211(7)$, even though the quality of the fit, based on the values of χ^2_{ndf} and Q, is not sufficiently good to completely rely on the outcome. The reason of this situation depends on two characteristics shown in the plot:

- The lower amount of statistics for lower masses and higher volumes results in larger error bars on the value of B_4;
- The points corresponding to $N_\sigma = 12$ may already be affected by finite-size effects, even though in a mild form. This can be detected from the behaviour of the points corresponding to $am = \{0.0015, 0.0020\}$, $N_\sigma = 12$, which shows a light upwards shift when compared to the other points for the same lattice spatial extent .

Then, giving credence to the last statement, the $N_\sigma = 12$ points for $am = 0.0015$ and $am = 0.0020$ are excluded from the fit and the result of the finite-size scaling is shown in the plot to the right of figure (4.16). Although the fit still lacks in quality, a lowering of the χ^2_{ndf} and a growth in Q can be appreciated. Continuing on this path, the finite-size scaling is repeated after removing all the points for $N_\sigma = 12$: In the plot in figure (4.17) the results are shown, where a marked increase in value for Q is observed and improvement in the quality is noticeable in the lower χ^2_{ndf} value, with a corresponding critical mass $am_c = 0.00236(13)$. At any chance, the values of the critical masses obtained in the tree different scenarios are compatible within errorbars when also the $N_\sigma = 12$ points are

[14] As an example, for $am = 0.0010$, $N_\sigma = 20$ and $\beta(a) = 2.0800$ the total amount of trajectories reads 12k, whereas for $am = 0.0035$, $N_\sigma = 12$ and $\beta(a) = 2.1400$ it reads 240k.

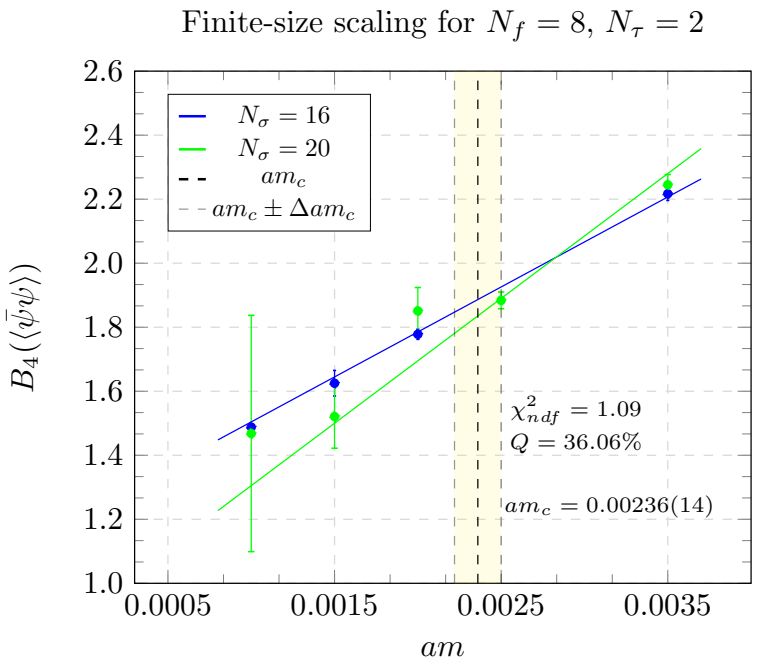

Figure 4.17: *The results of the finite-size scaling for* $N_f = 8$ *when using* $N_\sigma = 16$ *and* $N_\sigma = 20$.

am_c	Δam_c	Nr. of degrees of freedom	χ^2_{ndf}	Q
0.00211	0.00007	10	2.35	0.90%
0.00212	0.00007	8	2.09	3.32%
0.00236	0.00013	6	1.09	36.06%

Table 4.9: *Summary of the results of the finite-size scaling for* $N_f = 8$, $N_\tau = 2$.

included and the gap with the critical mass in the scenario in figure (4.17) is extremely small. The results obtained in this section have been summarised in in table (4.9). Using the same strategy as in section 4.2.1 it is possible to associate a critical $\beta_c(a)$ value to the critical masses found, which reads 5.0355(1). Since for this purpose we only rely on the results for the largest volume, which coincides with $N_\sigma = 20$, and since the set of results for $N_\sigma = 20$ has always been taken into account in its entirety to realise the finite-size scaling, no difference will be shown between the different scenarios reported in table (4.9) in terms of $\beta_c(a)$.

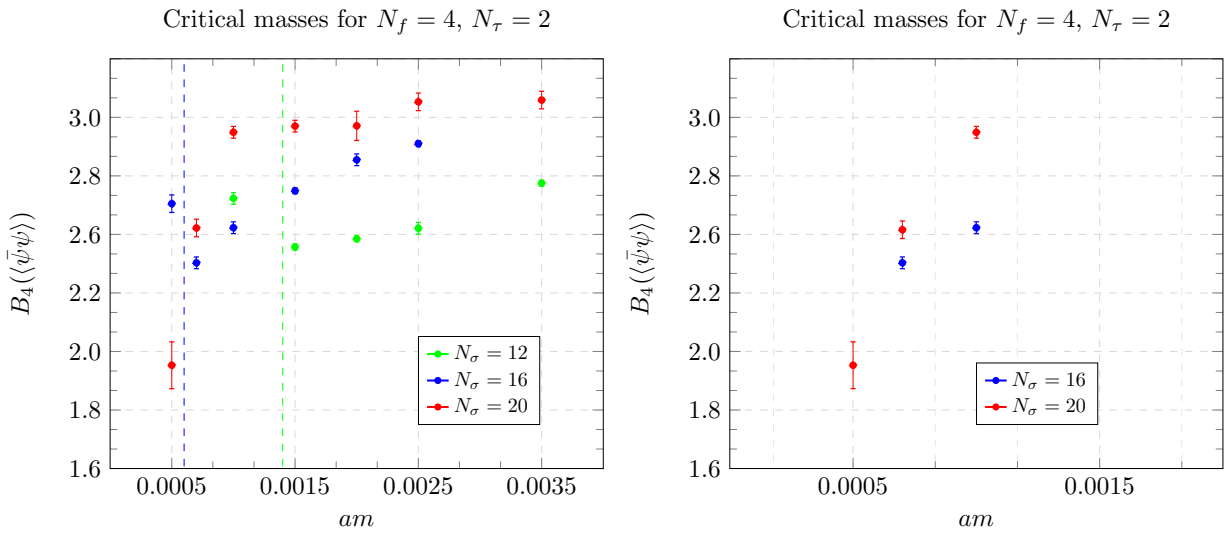

Figure 4.18: *Left: Results of the investigation for $N_f = 4$. Right: Shrinkage of the region of interest.*

4.3.2 The investigation for $N_f = 4$

Similarly to the investigation for $N_f = 8$, we now present the analysis and results concerning the investigation for $N_f = 4$, $N_\tau = 2$. At the beginning of this section we illustrated a potential challenging situation for $N_f = 4$, due to the extemely reduced extension of the first-order chiral region in the proximity of $aT = 0.5$. Furthermore, confirmation on this point arrives from the results for $N_f = 8$, where we located the Z_2 boundary for $am \approx 0.0022$, which is a relatively small value, sufficiently close to the chiral limit. The numerical strategy adopted in this case consists in first using the same quark masses as for $N_f = 8$. The results obtained for the corresponding kurtosis values are reported in figure (4.18), which includes results for $0.0005 \leq am \leq 0.0035$ for $N_\sigma = \{12, 16, 20\}$, where the dashed-vertical lines represent the limit, for specific N_σ value, beyond which, moving from larger to smaller am values, the impact of the finite-size effects are not negligible. The reason why $am \leq 0.0010$ have been considered, in addition to the am values involved for the $N_f = 8$ investigation is a consequence derived from the observation of the kurtosis values corresponding to $0.0010 < am \leq 0.0035$, which can be summarised as follow:

- Results for $N_\sigma = 12$ provide kurtosis values $2.5 \lesssim B_4(\langle\bar{\psi}\psi\rangle) \lesssim 2.8$, which show compatibility with crossover, in absence of a proper scaling behaviour. Furthermore, for $am = 0.0010$ the corresponding kurtosis value is larger than the one obtained for $am = 0.0015$: This result, together with the analysis of the corresponding histograms for the chiral condensate, reveal the influence of the finite-size effect for $am = 0.0010$ to be predominant and, consequently, the entire set of results for $N_\sigma = 12$ cannot be used for any finite-size scaling purpose;

- The same discussion applies to the results for $N_\sigma = 16$. In this case the kurtosis values show a more marked scaling behaviour for $0.0007 \leq am \lesssim 0.0020$, although still belonging to the range $B_4(\langle\bar{\psi}\psi\rangle) \in [2.3 : 2.9]$, related to the crossover region. The value corresponding to $am = 0.0005$ is to be excluded a priori, due to the

dominant finite-size effects, which results in a corresponding kurtosis value larger than the one observed for $am = 0.0007$;

- The scenario for $N_\sigma = 20$ is different: For $0.0010 \lesssim am \lesssim 0.0035$ the kurtosis values are definitely showing compatibility with crossover, since they fluctuate in the proximity of $B_4(\langle\bar{\psi}\psi\rangle) = 3$. For $am \lesssim 0.0010$ a scaling is observed and no finite-size effects have been detected even for the lowest mass $am = 0.0005$.

After this examination, we proceed to analyse data for $am = \{0.0005, 0.0007, 0.0010\}$ and $N_\sigma = \{16, 20\}$, performing a finite-size scaling, in order to locate a critical mass am_c and check whether the behaviour observed is compatible with a Z_2 scaling (and thus, identifying am_c belonging to the Z_2 critical boundary) or a $O(2)$ scaling [15], whose critical exponents are reported in table (3.1), as well as the $B_4(V = \infty)$ value.

The results of the application of (3.34) have been reported in figures (4.19) and (4.20), as well as in tables (4.10) and (4.11). Different scenarios have been explored by varying the number of am points to consider in the finite-size scaling for $N_\sigma = 16$. In figure (4.19a), is reported the finite-size scaling when all the points in the scaling region of interest are taken into account, when investigating the $O(2)$ scaling: As a result, the critical mass identified assumes a negative value, which is not compatible with positive values of am within error bars. Furthermore, the quality of the fit results poor, with a huge χ^2_{ndf} value. Looking closer to the results for $N_\sigma = 16$, two further statements can be discussed:

- The point corresponding to $N_\sigma = 16$, $am = 0.0007$ may already be affected by finite-size effects, in a mild form;

- The point corresponding to $N_\sigma = 16$, $am = 0.0010$ may be still sufficiently far from the scaling region of interest.

Then, in figure (4.19b) the finite-size scaling has been performed when considering the first hypothesis, resulting in a considerably lower χ^2_{ndf}, but still not indicating enough quality. Moreover, the resulting am_c value is again negative, within its errorbars, which makes this outcome not physically acceptable. The last attempt, based on the second hypothesis, is shown in figure (4.19c). Although the quality of the fit is still poor, the result for the critical mass is given by a positive am_c value, which is not compatible with $am = 0$ within errorbars. The same procedure is repeated for the investigation of a Z_2 scaling. In figure (4.20a), the finite-size scaling, when all the points in the region of interest are involved, is reported, showing again a huge value of χ^2_{ndf} and a negative critical mass, which stays negative within its error bars. A better scenario is shown in figure (4.20b): The exclusion of the point corresponding to $N_\sigma = 16$, $am = 0.0007$ produces the identification of a positive critical mass value, which stays positive within error bars, and a certain enhancement in the quality of the fit. A positive mass is also found when $N_\sigma = 16$, $am = 0.0010$ is the excluded point, as in figure (4.20c). At any chance, the overall scenario is, as expected, extremely intricated: The amount of data collected in this project is partially sufficient to investigate the two possible scalings for low masses, but the proximity of the latter to the chiral limit prevents to improve the quality of the results in a reasonable computational time. Furthermore, the interference of the finite-size effects appears to be drastic and larger lattice spatial extents should, in principle, be involved. The outcome of the analysis based on our simulations shows the impossibility to favour a Z_2 or a $O(2)$ scaling and the kurtosis values obtained for the different am values are sensitive to changes in amount of trajectories produced, mainly for the lowest masses in the two different N_σ sets.

[15] This is based on the discussion in section 2.2. In particular we refer to [53].

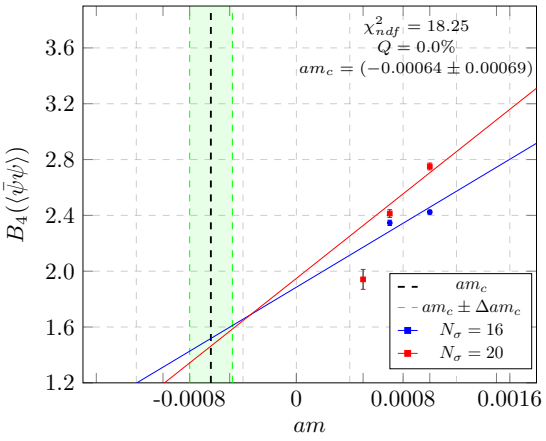

(a)

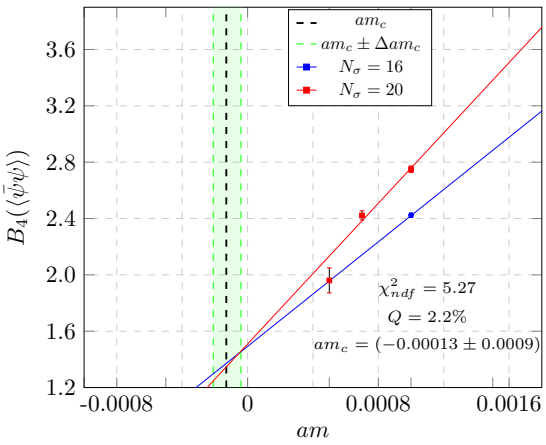

(b)

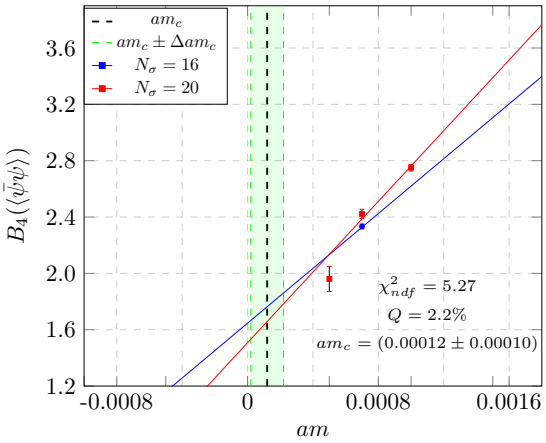

(c)

Figure 4.19: *Representation of the $O(2)$ scaling applied to the $N_f = 4$, $N_\tau = 2$ results. In* (4.19a) *all the points shown in the plot to the right in figure* (4.18) *have been considered. In* (4.19b) *the point corresponding to $N_\sigma = 0.0016$, $am = 0.0007$ has been excluded. In* (4.19c) *the point corresponding to $N_\sigma = 0.0016$, $am = 0.0010$ has been excluded.*

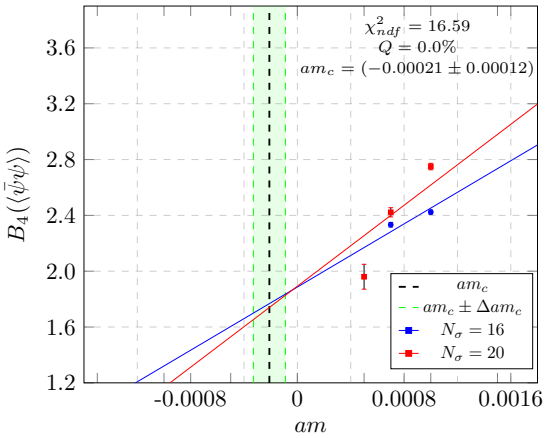

(a)

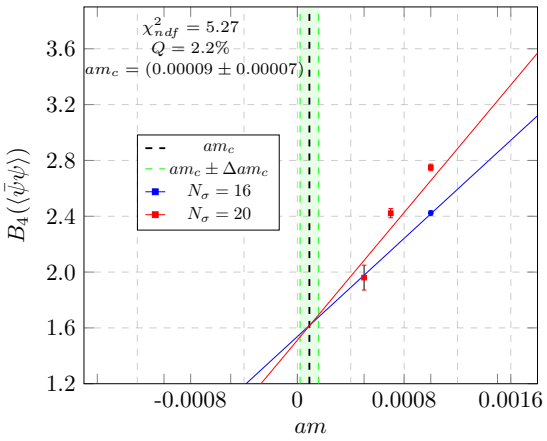

(b)

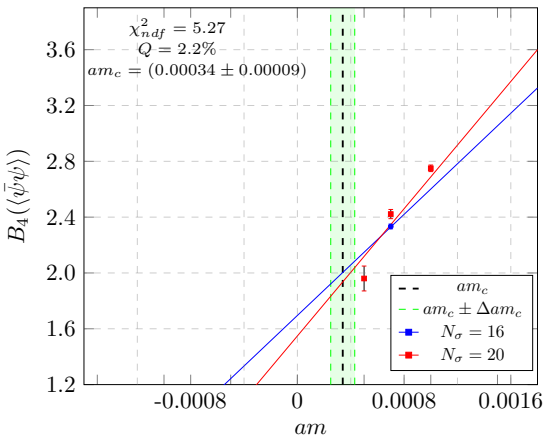

(c)

Figure 4.20: *Representation of the Z_2 scaling applied to the $N_f = 4$, $N_\tau = 2$ results. In* (4.20a) *all the points shown in the plot to the right in figure* (4.18) *have been considered. In* (4.20b) *the point corresponding to $N_\sigma = 0.0016$, $am = 0.0007$ has been excluded. In* (4.20c) *the point corresponding to $N_\sigma = 0.0016$, $am = 0.0010$ has been excluded.*

$O(2)$ scaling												
	N_σ					Fit parameters						
	16		20			c	b	am_c	Δam_c	ndf	χ^2_{ndf}	Q
am	0.0007	0.0010	0.0005	0.0007	0.0010							
	✓	✓	✓	✓	✓	9.4(1.0)	4.4(6)	-0.00064	0.00016	2	18.25	0.0%
	✗	✓	✓	✓	✓	16.8(1.8)	2.0(7)	-0.00013	0.00009	1	5.27	2.2%
	✓	✗	✓	✓	✓	13.7(1.1)	8.4(1.0)	0.00012	0.00010	1	5.27	2.2%

Table 4.10: *Summary of the results of the finite-size scaling for $N_f = 4$, $N_\tau = 2$, when investigating the $O(2)$ scaling. A tick mark suggests that the corresponding am value has been included in the scaling.*

Z_2 scaling												
	N_σ					Fit parameters						
	16		20			c	b	am_c	Δam_c	ndf	χ^2_{ndf}	Q
am	0.0007	0.0010	0.0005	0.0007	0.0010							
	✓	✓	✓	✓	✓	6.3(6)	1.23(27)	-0.00021	0.00012	2	16.59	0.0%
	✗	✓	✓	✓	✓	10.7(1.1)	0.1(3)	0.00009	0.00007	1	5.27	2.2%
	✓	✗	✓	✓	✓	8.9(7)	3.0(5)	0.00034	0.00009	1	5.27	2.2%

Table 4.11: *Summary of the results of the finite-size scaling for $N_f = 4$, $N_\tau = 2$, when investigating the Z_2 scaling. A tick mark suggests that the corresponding am value has been included in the scaling.*

4.3.3 Conclusions

The results obtained in this section have been schematically depicted in figure (4.21). As pointed out in the introduction to this section, a global maximum is expected in the aT region which separates the weak coupling regime ($4.7 \lesssim \beta(a) \lesssim 5.4$) from the strong coupling regime $2.0 \lesssim \beta(a) \lesssim 3.5$, due to the change in the slope of the Z_2 boundary. The conclusions, following the analysis presented in this section, are summarised in the following:

- The scenario for $N_f = 8$, $N_\tau = 2$ clearly shows the presence of a Z_2 boundary, which separates the first-order chiral phase transition (below) from the crossover region (above). The extension of the former is limited to the area in the proximity of the chiral limit, as the critical mass belonging to the Z_2 critical line reads $am \approx 0.0020$. The amount of statistics accumulated for the different bare quark masses involved in simulation is not homogeneous and tends to decrease as the smallest am values are considered. The reason of this inbalance resides in the time needed to produce single steps in the Markov chains, which is generally large due to the combination of large aspect ratios and small masses. The necessity of using large aspect ratios, as $N_\sigma/N_\tau = 10$, is the aftermath of the dominance of finite size-effects in many parameter setups, when lower lattice spatial extents are considered;

- The results for $N_f = 4$ do not show a first-order chiral region. The values of bare quark masses for which simulations have been performed and for which a scaling is visible belong to the region $am \leq 0.0010$ and, identically to the case of $N_f = 8$, the time-consuming processes render the data production extremely complex. A comparison between the Z_2 and $O(2)$ scaling is been presented: A validation of the former would lead to the identification of a Z_2 boundary and thus, to the identification of a first-order chiral region, whereas the validation of the latter would highlight the presence of a second-order chiral phase transition, in the chiral limit, in the $O(2)$ universality class. Unfortunately, the results did not provide a unique solution sufficiently strong to favour one of the two scenarios: In principle, a critical Z_2 mass could characterise the region of am values close to $am = 0$, but am_c would be extremely small to be detectable with our strategy. Equivalently, the $N_\tau = 2$ scanario could already be described, in the chiral limit, by a $O(2)$ scaling, showing a second-order chiral phase transition. To unravel this mosaic, a different approach should be involved, from the numerical point of view. Based on the fit parameters, it also worth to remark that the whole analysis for $N_f = 4$ lacks in quality and more work is needed to draw more complete and valid conclusions about.

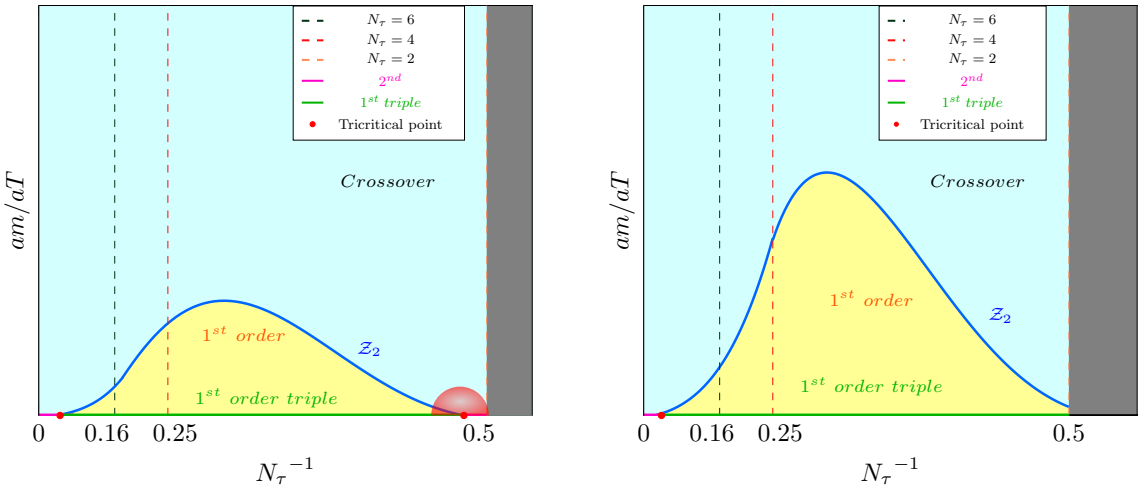

Figure 4.21: *Schematic representation of the extension of the first-order chiral region from the weak to the strong coupling regime, as aT varies, for $N_f = 4$ (left) and $N_f = 8$ (right). The gray gradient represents the lack of information from simulations beyond $aT = 0.5$ and the red semicircle for the $N_f = 4$ scenario along the aT axis represents the location of the tricritical point, which stays unknown from our results.*

4.4 General conclusions

In this final section a general summary of this work is presented. The first sections of Chapter 1 are devoted to the introduction to Quantum Chromodynamics on the lattice, starting from the Lagrangian and action of QCD in the continuum formulation, showing how they can be regularised on the lattice. Also, a focus on the chiral symmetry is provided in a dedicated section and in the last sections temperature and baryon chemical potential are introduced in the theory. A summary of the basic steps that led to the phase

diagram of QCD as we know it today was provided in Chapter 2, both in the weak and the strong coupling regimes, highlighting the different methodologies involved from the Eighties on. The two pillars of this dissertation, introduced in the last sections of Chapter 2, rely on the production of lattice simulations using unimproved staggered fermions, resorting to the Rational Hybrid Monte Carlo (RHMC) algorithm. The latter has been introduced in Chapter 3, where also the numerical strategy involved in this work has been discussed, together with the analysis methods which allow to gather information on the order of the chiral phase transition for different parameter setups. Also, the numerical code used to produce data, together with the analysis software, has been introduced. The techniques involved to locate a chiral phase transition and to obtain its order have been explained, with specific examples. In Chapter 4, the results concerning the aforementioned analysis have been presented, together with an in-depth study of the performances of the fourth-order minimum norm integrator, with one and two-time scales, when compared to those of the second-order minimun norm integrator, with one-time scale. Both the integrators belong to the class of symplectic integrators, and represent an essential element for the Markov chain production in the frame of Monte Carlo simulations, in particular for the Molecular Dynamics algorithm contained inside the RHMC one. A separate discussion has been made for the investigation of the first-order chiral region in the extended Columbia plot, when using a non-zero imaginary baryon chemical potential, and in the strong coupling regime, at zero density, and the results obtained have been compared to the ones in literature. For the former, the general conclusion based the extrapolation to the chiral limit suggests that the order of the chiral phase transition in the chiral limit and continuum limit does not depend on the value of the chemical potential involved, and compatibility with a second-order chiral phase transition is observed. Indeed, this is true for $N_f \in [2:6]$ and this statement relies on the comparison to the outcome of the investigation of the extension of the first-order chiral region in the extended Columbia plot, when using a zero chemical potential. Thus, confimation to the nature of the first-order chiral phase transition being a lattice artifact were obtained. A further analysis could include more results in the frame of different values of non-zero imaginary baryon chemical potentials, aiming to characterise the dependence of specific observables on the chemical potential. The results from the study of the Z_2 boundary in the strong coupling regime resulted in a more ambiguous scenario. The investigation provided for $N_f = 8$ led to the identification of a critical mass on the Z_2 critical boundary, thus a first-order chiral region survives in such regime, although its extension is limited to the mass region in the proximity of the chiral limit. The scenario for $N_f = 4$ does not allow to draw a clear conclusion: After realising the finite-size scaling for different parameter setups, the probability to observe a Z_2 scaling is compatible with the one to observe a $O(2)$ scaling, and a better constraint requires more statistics to be collected. As the bare quark masses involved in the numerical setup are relatively close to the chiral limit, collecting statistics resulted in time-consuming simulations and, in some cases, in the predominance of finite-size effects, thus a different numerical strategy should be adopted to improve the amount of data. At any chance, the investigation provided in the strong coupling regime, as it is realised on a coarse lattice, does not provide information on the chiral phase transition in the continuum limit.

Appendix A

The staggered formulation

This Appendix is devoted to provide some more details about the staggered formulation for fermions on the lattice. It is mostly based on [10], [11], as well as on the thesis work [15] and is aimed to show the correct continuum limit starting from the discretised staggered fermion action, as well as the correct derivation of the continuum fermion propagator.

A.1 The continuum limit of the staggered fermion action

Let's consider the staggered fermion action obtained in Chapter 1,

$$S_F^{\text{stagg.}}[\psi,\bar{\psi}] = \frac{1}{2}\sum_{\mu,n}\eta_\mu(n)\Big[\bar{\chi}(n)\chi(n+\hat{\mu}) - \bar{\chi}(n)\chi(n-\hat{\mu})\Big] + \hat{M}\sum_n \bar{\chi}(n)\chi(n). \quad \text{(A.1)}$$

Suppose to have a hypercube located on a four dimensional lattice of unitary spacing with one of its vertices, which corresponds to a lattice site, labelled by the quadruplet $2N = (2n_1, 2n_2, 2n_3, 2n_4)$, as shown in figure (1.4). Using this as the *origin* of the considered hypercube, the other sites coincinding with the other vertices of the same hypercube will be identified through the four vector $r = 2N + \rho$, where the four components of ρ assume values 0 or 1. For instance, assuming the origin of the hypercube to be $\mathbf{O} = (0,0,0)$ in three dimension, the first neighbour $\mathbf{P}$ along the x-axis can be reached realising the translation $\mathbf{P} = \mathbf{O} + (\pm 1, 0, 0)$. As a consequence, the fermion fields on the sixteen different sites of the same hypercube can be described by one single field as

$$\chi(N) = \chi(2N+\rho). \quad \text{(A.2)}$$

Before using this prescription in equation (A.1), one observes that moving along the different μ directions on the lattice it is not guaranteed to stay inside the same hypercube. Indeed, considering $\chi(2N+\rho\pm\hat{\mu})$, two realisations can take place:

- If $\rho+\hat{\mu}$ is a *ρ-like* four vector, then
  - The site located at $2N+\rho+\hat{\mu}$ belongs to the hypecube of orgin $2N$ and the corresponding field can be labelled as $\chi(2N+\rho+\hat{\mu}) = \chi_{\rho+\hat{\mu}}(N)$;
- If $\rho+\hat{\mu}$ is not a *ρ-like* four vector, then
  - The site located at $2N+\rho+\hat{\mu}$ does not belong to the hypecube of orgin $2N$, but the one located at $2N+\rho-\hat{\mu}$ does. Then, the corresponding field becomes $\chi(2N+\rho+\hat{\mu}) = \chi_{\rho-\hat{\mu}}(N+\hat{\mu})$.

Taking into account the two scenarios, the fermionic fields on a hypercube will receive both the contributions from $\rho-$like and not $\rho-$like four vectors. Then,

$$\begin{aligned}\chi(2N+\rho+\hat{\mu}) &= \sum_{\rho'}[\delta_{\rho+\hat{\mu},\rho'}\chi_{\rho'}(N)+\delta_{\rho-\hat{\mu},\rho'}\chi_{\rho'}(N+\hat{\mu})],\\ \chi(2N+\rho-\hat{\mu}) &= \sum_{\rho'}[\delta_{\rho-\hat{\mu},\rho'}\chi_{\rho'}(N)+\delta_{\rho+\hat{\mu},\rho'}\chi_{\rho'}(N-\hat{\mu})]\end{aligned} \tag{A.3}$$

and the forward, backward and symmetric derivatives can be obtained as

$$\begin{aligned}&\hat{\partial^F_\mu}\chi(N) = \chi(N+\hat{\mu})-\chi(N),\\ &\hat{\partial^B_\mu}\chi(N) = \chi(N)-\chi(N-\hat{\mu}),\\ &\hat{\partial}_\mu = \frac{1}{2}(\hat{\partial^F_\mu}+\hat{\partial^B_\mu}),\\ &\hat{\Box}\mu = \hat{\partial^F_\mu}-\hat{\partial^B_\mu}.\end{aligned} \tag{A.4}$$

Recalling equation (1.50) and using equations (A.3), (A.4), the staggered action reads

$$\begin{aligned}S_F^{\text{stagg.}}[\psi,\bar{\psi}] &= \frac{1}{2}\sum_{\mu,n}\eta_\mu(n)\Big[\bar{\chi}(n)\chi(n+\hat{\mu})-\bar{\chi}(n)\chi(n-\hat{\mu})\Big]+\hat{M}\sum_n\bar{\chi}(n)\chi(n)\\ &= \sum_N\sum_{\rho,\rho'}\sum_\mu\frac{1}{2}\eta_\mu(\rho)\bar{\chi}(N)[(\delta_{\rho+\hat{\mu},\rho'}+\delta_{\rho-\hat{\mu},\rho'})\hat{\partial}_\mu+(\delta_{\rho-\hat{\mu},\rho'}-\delta_{\rho+\hat{\mu},\rho'})\hat{\Box}_\mu]\\ &+\hat{M}\sum_N\sum_\rho\bar{\chi}_\rho(N)\chi_\rho(N)\\ &= \sum_N\sum_{\rho,rho'}\frac{1}{2}\hat{\chi}_\rho(N)\Big[\Big(\sum_\mu\Gamma^\mu_{\rho\rho'}\hat{\partial}_\mu+\frac{1}{2}\Gamma^{5\mu}_{\rho\rho'}\hat{\Box}_\mu\Big)+2\hat{M}\delta_{\rho\rho'}\Big]\chi_{\rho'}(N),\end{aligned} \tag{A.5}$$

where $\Gamma^\mu_{\rho\rho'}$ and $\Gamma^{5\mu}_{\rho\rho'}$ are 16×16 matrices satisfying to the algebra

$$\begin{aligned}&\{\Gamma^\mu,\Gamma^{5\nu}\}=0,\\ &\{\Gamma^{5\mu},\Gamma^{5\nu}\}=-2\delta_{\mu\nu}\mathbb{1}_{16\times16},\end{aligned} \tag{A.6}$$

as, respectively, $\gamma_\mu\otimes\mathbb{1}$ and $\gamma_5\otimes\gamma_\mu\gamma_5$ do. This suggest that a unitary transformation that connects the latter to the $\Gamma^\mu,\Gamma^{5\mu}$ matrices introduced before exists. Focusing on $\gamma_\mu\otimes\mathbb{1}$ and $\gamma_5\otimes\gamma_\mu\gamma_5$, the matrices to the left of the product symbol can be understood as to act on the four dimensional Dirac space, whereas the ones to the right of the symbol as to operate on the four dimensional taste space. This statement is important in order to link the action in (A.5) to its version in the continuum limit: Assuming the unitary transformation

$$\gamma_\mu\otimes\mathbb{1} = U^\dagger\Gamma^\mu U, \tag{A.7}$$

one observes that the product $(\gamma_\mu\otimes\mathbb{1})\partial_\mu$ is directly connected to the product $\gamma_\mu\partial_\mu$ in equation (1.52), since the fermion fields $\psi^f_\alpha(x)$ carry both Dirac and taste indices. Then, the next step is to connect the $\chi(N)$ fields to the $\psi^f_\alpha(x)$ fields and this can be done analogously to equation (1.44). Indeed, one defines the transformations

$$\begin{aligned}\hat{\psi}_{\alpha\beta}(N) &= \mathcal{N}\sum_\rho U_{\alpha\beta,\rho}\chi_\rho(N),\\ \bar{\hat{\psi}}_{\alpha\beta}(N) &= \mathcal{N}\sum_\rho\bar{\chi}_\rho(N)U^\dagger_{\alpha\beta,\rho},\end{aligned} \tag{A.8}$$

where N is a normalization constant, and, focusing on the unitary transformations, these are defined as

$$U_{\alpha\beta,\rho} = \frac{1}{2}(T_\rho)_{\alpha\beta}. \tag{A.9}$$

In the latter, $T_\rho = \gamma_1^{\rho_1}\gamma_2^{\rho_2}\gamma_3^{\rho_3}\gamma_4^{\rho_4}$ is equivalent to the operator $T(n)$ in equation (1.45), whereas ρ is the vector that spans over the sixteen sites of the hypercube and $\alpha, \beta = 1, 2, 3, 4$. Thus, the unitary transformation (A.9) is realised by means of a 16×16 matrix. At this point the transformations (A.8) can be inverted by taking into account the ortogonality identity $\mathrm{Tr}(T_\rho^\dagger T'_\rho) = 4\delta_{\rho\rho'}$, as well as the unitarity of the U matrices. The result reads

$$\begin{aligned} \chi_\rho(N) &= \frac{1}{\mathcal{N}} \sum_{\alpha,\beta} U^\dagger_{\rho,\alpha\beta} \hat{\psi}_{\alpha\beta}(N), \\ \bar{\chi}_\rho(N) &= \frac{1}{\mathcal{N}} \sum_{\alpha,\beta} \bar{\hat{\psi}}_{\alpha\beta}(N) U_{\alpha\beta,\rho}, \end{aligned} \tag{A.10}$$

and, replacing the latter in equation (A.5), one obtains

$$\begin{aligned} S_F^{\text{stagg.}}[\psi, \bar{\psi}] = \frac{1}{2\mathcal{N}} \sum_N \sum_{\alpha,\beta} \sum_{\alpha',\beta'} \bar{\hat{\psi}}_{\alpha\beta}(N) \Big\{ \sum_\mu \Big[\Lambda^\mu_{\alpha\beta,\alpha'\beta'} \hat{\partial}_\mu + \frac{1}{2} \Lambda^{5\mu}_{\alpha\beta,\alpha'\beta'} \hat{\Box}_\mu \Big] + \\ + 2\hat{M}\delta_{\alpha\alpha'}\delta_{\beta\beta'} \Big\} \hat{\psi}_{\alpha'\beta'}(N), \end{aligned} \tag{A.11}$$

where the 16×16 matrices $\Lambda^\mu_{\alpha\beta,\alpha'\beta'}$ and $\Lambda^{5\mu}_{\alpha\beta,\alpha'\beta'}$ are related to the γ_μ ones through

$$\begin{aligned} \Lambda^\mu_{\alpha\beta,\alpha'\beta'} &= \sum_{\rho,\rho'} U_{\alpha\beta,\rho} \Gamma^\mu_{\rho\rho'} U^\dagger_{\rho',\alpha'\beta'} = (\gamma_\mu)_{\alpha\alpha'}\delta_{\beta\beta'}, \\ \Lambda^{5\mu}_{\alpha\beta,\alpha'\beta'} &= \sum_{\rho,\rho'} U_{\alpha\beta,\rho} \Gamma^{5\mu}_{\rho\rho'} U^\dagger_{\rho',\alpha'\beta'} (\gamma_5)_{\alpha\alpha'} (t_\mu t_5)_{\beta\beta'}, \end{aligned}$$

being $t_\mu = \gamma_\mu^*$, $t_5 = \gamma_5$. Using the same prescription used for the Γ^μ and $\Gamma^{5\mu}$ matrices, it comes straightforward to observe that the following replacement holds

$$\begin{aligned} \Lambda^\mu &= \gamma_\mu \otimes \mathbb{1}, \\ \Lambda^{5\mu} &= \gamma_5 \otimes t_\mu t_5. \end{aligned}$$

Now it is possible to replace the dimensional objects in the action (A.11),

$$\begin{aligned} S_F^{\text{stagg.}}[\psi, \bar{\psi}] = \sum_x \sum_\rho \sum_\mu a^4 \bar{\psi} \Big[(\gamma_\mu \otimes \mathbb{1}) \partial_\mu + \frac{1}{2} a (\gamma_5 \otimes t_\mu t_5) \Box_\mu \Big] + \\ + 2M \sum_x \bar{\psi}(x) \mathbb{1} \otimes \mathbb{1} \psi(x), \end{aligned} \tag{A.12}$$

where $\mathcal{N} = 1/\sqrt{2}$ and the lattice spacing a corresponds to twice the original lattice spacing. Applying the continuum limit, one obtains

$$\lim_{a \longrightarrow 0} S_F^{\text{stagg.}}[\psi, \bar{\psi}] = \sum_f \int d^4x \; \bar{\psi}^f(x) \Big[\sum_\mu \gamma_\mu \partial_\mu + M' \Big] \psi^f(x), \tag{A.13}$$

where $M' = 2M$, due to the dependence of $\hat{M}$ on the lattice cutoff, which in the staggered formulation becomes twice the original extension. This action describes a system of four

non-interacting, degenerate Dirac fermions in the taste space.

Before proceeding to the fermion propagator, one observes that the term proportional to the Laplace operator in equation (A.12) is similar to the $mass-like$ term which rose up in equation (1.39), which is the responsible for the explicit breaking of the chiral symmetry even in the chiral limit $M \longrightarrow 0$. Also, when using the staggered formulation this object breaks explicitly the chiral symmetry but, differently from the Wilson formulation, a $U(1) \times U(1)$ remnant of such symmetry survives. Its generator is $(\gamma_5 \otimes \gamma_5)$ and the symmetry is realised by transforming the fermion fields by means of

$$U = e^{i\theta(\gamma_5 \otimes \gamma_5)}, \tag{A.14}$$

which makes the action in (A.12) invariant in the chiral limit.

A.2 The fermion propagator

The next step consists in studying the two point function in the staggered formulation and check whether the fermion propagator in the continuum limit can be obtained. Consider again the hypercube on the lattice that has been used in the previous section. In the momentum space, the fields $\chi_\rho(N)$ and $\bar{\chi}_\rho$ become

$$\begin{aligned} \chi_\rho(N) &= \int_{-\pi}^{\pi} \frac{d^4\hat{p}}{(2\pi)^4} \tilde{\chi}_\rho(\hat{p}) e^{i\hat{p}\cdot N}, \\ \hat{\chi}_\rho(N) &= \int_{-\pi}^{\pi} \frac{d^4\hat{p}}{(2\pi)^4} \tilde{\chi}_\rho(\hat{p}) e^{i\hat{p}\cdot N}, \end{aligned} \tag{A.15}$$

and the fermion action in equation (A.5) can be translated in the momentum space as

$$S_F^{\text{stagg.}}[\psi, \bar{\hat{\psi}}] = \sum_{\rho,\rho'} \int \frac{d^4\hat{p}}{(2\pi)^4} \bar{\tilde{\chi}}_\rho(\hat{p}) K_{\rho\rho'}(\hat{p}) \tilde{\chi}_{\rho'}(\hat{p}). \tag{A.16}$$

The matrix between the femion fields in the integral can be made explicit,

$$\begin{aligned} K_{\rho\rho'}(\hat{p}) &= \sum_\mu i\Gamma^\mu_{\rho\rho'} \sin\left(\frac{\hat{p}_\mu}{2}\right) + M\delta_{\rho\rho'} \\ &= \sum_\mu i\eta_\mu(\rho) e^{i\hat{p}\cdot(\rho-\rho')/2} [\delta_{\rho+\hat{\mu},\rho'} + \delta_{\rho-\hat{\mu},\rho'}] \sin\left(\frac{\hat{p}_\mu}{2}\right) + M\delta_{\rho\rho'}, \end{aligned} \tag{A.17}$$

and, using the commutation rules in equation (A.6), the propagator in the lattice momentum space becomes

$$K^{-1}(\hat{p}) = \frac{-i\sum_\mu \Gamma^\mu(\hat{p}) \sin\frac{\hat{p}_\mu}{2} + \hat{M}}{\sum_\mu \sin^2\frac{\hat{p}_\mu}{2} + \hat{M}^2}. \tag{A.18}$$

At this point, one can translate these objects to the lattice coordinate space. Using the results from equations (A.17) and (A.18), the two points function reads

$$\langle \chi_\rho(N) \bar{\chi}_{\rho'}(N) \rangle = \int_{-\pi}^{\pi} \frac{d^4\hat{p}}{(2\pi)^4} K^{-1}_{\rho\rho'}(\hat{p}) e^{i\hat{p}\cdot(N-N')}, \tag{A.19}$$

which is connected to the femion propagator in the *Dirac* $\otimes$ *taste* space by means of

$$\langle \hat{\psi}^{f}_{\alpha}(N)\bar{\hat{\psi}}^{f'}_{\alpha'}(N)\rangle = \frac{1}{2}\sum_{\rho,\rho'} U_{\alpha f,\rho}\langle \chi_{\rho}(N)\bar{\chi}_{\rho'}(N)\rangle U^{\dagger}_{\alpha' f',\rho'}, \tag{A.20}$$

where the U matrices are the ones defined in equation (A.8). One way to evaluate the propagator (A.20) consists in making explicit the action (A.12) in the momentum space and then, computing the inverse of the matrix which lays between the fermion fields. In order to persue this results, the following Fourier transformations are needed:

$$\begin{aligned} \psi(Na) &= \int_{-\pi}^{\pi} \frac{d^4p}{(2\pi)^4}\tilde{\psi}(p)e^{ip\cdot Na}, \\ \bar{\psi}(Na) &= \int_{-\pi}^{\pi} \frac{d^4p}{(2\pi)^4}\bar{\tilde{\psi}}(p)e^{ip\cdot Na} \end{aligned} \tag{A.21}$$

and, recalling that

$$\sum_{N} a^4 e^{i(p-p')\cdot Na} = (2\pi)^4\delta^{(4)}_{P}(p-p'), \tag{A.22}$$

with P labelling the periodicity of the δ function, the action in equation (A.16) becomes

$$\begin{aligned} S_F^{\text{stagg.}}[\tilde{\psi},\bar{\tilde{\psi}}] = \int_{-\pi/a}^{\pi/a} \frac{d^4p}{(2\pi)^4}\bar{\tilde{\psi}}(p)\Big\{ \sum_{\mu} i\Big[\big(\gamma_\mu\otimes\mathbb{1}\big)\frac{1}{a}\sin(p_\mu a) + \\ + \frac{1}{a}\Big(1-\cos(p_\mu a)\Big)\gamma_5\otimes t_\mu t_5\Big] + M\Big\}\tilde{\psi}(p). \end{aligned} \tag{A.23}$$

As we are interested in the fermion propagator in the continuum limit, the matrix contained in the curly brackets which must be inverted. After some algebra the result reads

$$K^{-1}(p) = \sum_{\mu} \frac{\Big[-i(\gamma_\mu\otimes\mathbb{1})\frac{1}{a}\sin(p_\mu a) + \frac{2}{a}\sin^2(p_\mu a/2)\gamma_5\otimes t_\mu t_5\Big] + M(\mathbb{1}\otimes\mathbb{1})}{\sum_\mu \frac{4}{a^2}\sin^2(p_\mu a/2) + M^2}, \tag{A.24}$$

and, performing the continuum limit, the fermon propagator is obtained,

$$\lim_{a\longrightarrow 0} K^{-1}(p) = \frac{-i\sum_\mu -i(\gamma_\mu\otimes\mathbb{1})\cdot p_\mu + M(\mathbb{1}\otimes\mathbb{1})}{p^2+M^2}, \tag{A.25}$$

which is the correct one. This result is guaranteed by the presence of a factor 2 inside the argument of the sinusoidal function in the denominator of equation (A.24), which reduces the extension of the Brillouin Zone up to the half of the dimension of the Brillouin Zone in figure (1.2).

Appendix B

The minimum norm integrators

Producing simulations by means of the RHMC algorithm requires the Molecular Dynamics steps to be performed by means of suitable algorithms on the lattice. An interesting class of integrators which turns to be useful to this aim is represented by the *minimum norm integrators*, which will be discussed in this Appendix. The integrator to which we are interested must guarantee two peculiar features:

- It must be symplectic, hence the $2-$form $dp \wedge dq$ in the phase space must be conserved,
- It must be reversible in time,

which are the fundamentals of the so called *detailed balance*, which will be extensively debated in the following. As previously mentioned, the time evolution of the equations of motion (3.16) and (3.17) takes place in a specific time interval τ. The latter can be separated into identical time intervals in a number depending on the number of integration time steps to be used, with size Δt. A class of integrators satisfying to the detailed balance is the one of the symplectic integrators, [145; 146], and here we will mainly focus on two of them, the *second-order* and *fourth-order minimum norm integrators*, respectively indicated with the acronyms 2MN and 4MN.

B.1 The symplectic integrators

This class of integrators can be structured following a recursive scheme, presented in [141], which defines a time evolution scheme based on a given Hamiltonian, which in its most generic formulation reads

$$e^{\Delta t(T+V)} = \prod_{j=1}^{k} e^{(c_j \Delta t\ T)} e^{(d_j \Delta t\ V)} + \mathcal{O}(\Delta t^{n+1}), \tag{B.1}$$

assumed Δt to be sufficiently small. In this scheme, the first exponential operator realises the time evolution with respect to the position-like operators and the second one realises the time evolution for the momentum-like operators. The coefficients c_j and d_j are real numbers: They satisfy to the following conditions

$$\sum_{j=1}^{k} c_i = 1, \qquad\qquad \sum_{j=1}^{k} d_i = 1, \tag{B.2}$$

and, depending on the value of k, different relations must hold between the different coefficients to make the integrator symplectic and time-reversible. Depending on the structure of (B.1), one could have two different versions of a specific integrator: We refer to *velocity-like* versions when the the first exponential operator in (B.1) depends on the V operator, whereas in case it depends on the T operator, then we refer to *position-like* versions. The reason why such integrators are called minimum norm integrators is now explained. Considering again equation (B.1) for orders $n = 2$ and $n = 4$, the approximation error reads, respectively,

$$\mathcal{O}(\Delta t^3) = \alpha[T,[V,T]] + \beta[V,[V,T]], \tag{B.3}$$

$$\begin{aligned}\mathcal{O}(\Delta t^5) = \gamma[T,[T,[T,[T,V]]]] + \delta[T,[T,[V,[T,V]]]] \\ + \epsilon[V,[T,[T,[T,V]]]] + \zeta[V,[V,[T,[T,V]]]],\end{aligned} \tag{B.4}$$

where the coefficients in front of the commutators are functions of the coefficients c_j and d_j. At this point, a strategy to constraint the approximation errors consists in minimising the norm of the coefficients which come with the commutators inside (B.3) and (B.4),

$$f(\alpha,\beta) = \min(\sqrt{\alpha^2+\beta^2}), \tag{B.5}$$

$$f(\gamma,\delta,\epsilon,\zeta) = \min(\sqrt{\gamma^2+\delta^2+\epsilon^2+\zeta^2}). \tag{B.6}$$

from which the definition of minimum norm integrators is derived.

In [147] and, later, in [148; 149] a different kind of integrator for the molecular dynamics equation was proposed: In order to reduce the discretisation errors, the authors presented an improvement of the Leapfrog integration scheme by involving multiple time scales, differently from what has been presented so far. In the following, we will:

- Report the 2MN integrator both in one and two-time scales,
- Report the 4MN integrator in one-time scales,
- Build up the 4MN integrator with two-time scales and use it to perform some tests with our code [1].

B.2 The 2MN integrator

The second-order minimimum norm integrator in its position-like version [145; 146] is given as

$$I_{2MN}(\Delta t,\lambda) = e^{\lambda\Delta t T} e^{\frac{\Delta t}{2}V} e^{(1-2\lambda)\Delta t T} e^{\frac{\Delta t}{2}V} e^{\lambda\Delta t T}, \tag{B.7}$$

where the sum of the coefficients which come with Δt in the exponential operators equals one, and two force calculations per step are realised. In order to obtain a two-time scales version of (B.7), two different numbers of integration steps must be introduced, thus two different intervals of integration. The basic idea is to take into account again the Hamiltonian in (3.15) and consider to evolve the pure gauge term and the gauge momenta one according to a one-time scale integrator and the pseudofermion term according to a

[1] See Chapter 3.

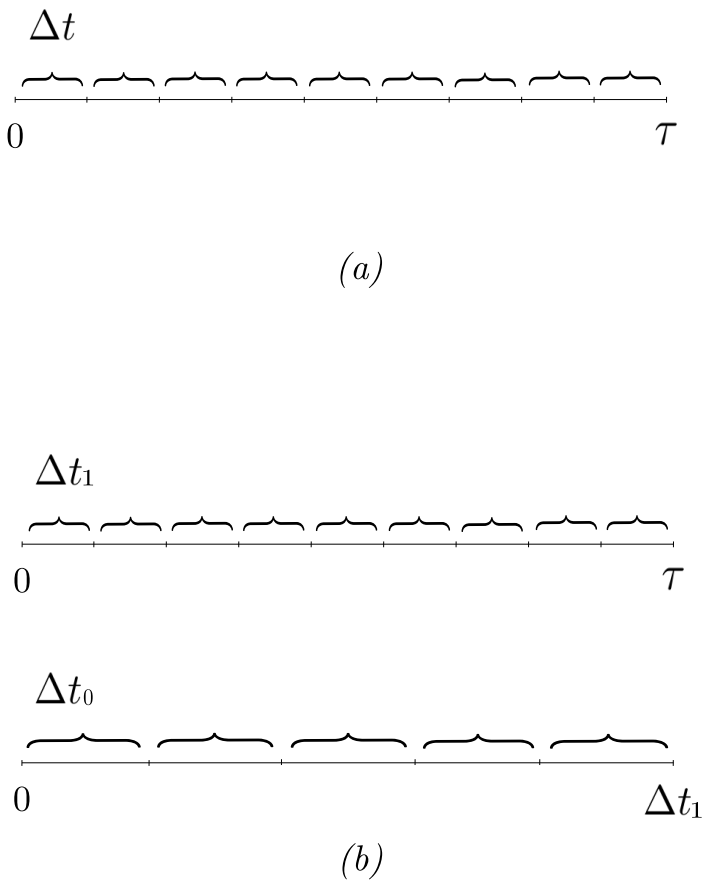

Figure B.1: *In (a) is the representation of one-time scales for Molecular Dynamics trajectories. The integration time τ has been divided into nine intervals of step size Δt. In (b) is the representation of a two-time scales method to perform the integration. The time interval τ is still divided as in (a), but now we refer to intervals of size Δt_1. Each one of the latter is further divided into five interval, whose size corresponds to Δt_0.*

different one-time scale integrator. Hence, one can think about redefining the T operator inside (B.7) as

$$T = T_1 + T_2,$$

where now T_1 refers to the update of the gauge momenta fields whereas T_2 accounts for the update of the pseudofermion fields. With this prescription,

$$e^{\Delta t(T+V)} = e^{\Delta t(T_1+T_2+V)} \equiv e^{\Delta t(T_2+W)}, \tag{B.8}$$

where the W operator is defined as

$$W \equiv V + T_1,$$

and the 2MN integrator will read

$$I_{2MN}(\Delta t, \lambda)_{2ts} = e^{\lambda \Delta t T_2} e^{\frac{\Delta t}{2} W} e^{(1-2\lambda)\Delta t T_2} e^{\frac{\Delta t}{2} W} e^{\lambda \Delta t T_2}. \tag{B.9}$$

The latter can be written in more details by making explicit the dependence on the two-time scales: All the time intervals Δt can be promoted to Δt_1 and, rewriting the terms depending on the operator W as

$$e^{\frac{\Delta t_1}{2} W} = \left[e^{\frac{\Delta t_1}{2n_0} W} \right]^{n_0},$$

one can define the time scale [149]

$$\Delta t_0 = \frac{\Delta t_1}{2n_0}, \tag{B.10}$$

where n_0 is the number of integration steps needed to perform the update according to the time scale Δt_0. Thus, the 2MN integrator with two-time scales can be written as

$$I_{2MN}(\Delta t_1, \Delta t_2, \lambda)_{2ts} = e^{\lambda \Delta t_1 T_2} \left[e^{\Delta t_0 W} \right]^{n_0} e^{(1-2\lambda)\Delta t_1 T_2} \left[e^{\Delta t_0 W} \right]^{n_0} e^{\lambda \Delta t_1 T_2}, \tag{B.11}$$

where now the terms containing the W operator are themselves 2MN integrators in the form of (B.7).

B.3 The 4MN integrator

One can now repeat the same procedure as in the previous subsection for the fourth-order minimum norm integrator. Let's just consider the 4MN integrator in its velocity-like version, which for one-time scale reads

$$\begin{aligned} I_{4MN}(\Delta t, \lambda, \mu, \theta, \rho) =& e^{\theta \Delta t V} e^{\rho \Delta t T} e^{\lambda \Delta t V} e^{\mu \Delta t T} e^{1-2(\lambda+\theta)\frac{\Delta t}{2} V} e^{1-2(\mu+\rho)\frac{\Delta t}{2} T} \times \\ & \times e^{1-2(\lambda+\theta)\frac{\Delta t}{2} V} e^{\mu \Delta t T} e^{\lambda \Delta t V} e^{\rho \Delta t T} e^{\theta \Delta t V}, \end{aligned} \tag{B.12}$$

where again the four coefficients which come with Δt in the exponential functions equal one when summed and five force calculations are realised. The strategy to obtain the two-time scales version of (B.12) consists in redefining again the operator T as a sum of two contributions and making explicit the dependence on the number of integration steps n_0. What makes things more complicated is the number of parameters which now appears in the integrator, which requires a bit more attention to be paid. Proceeding as

in the previous case, one obtains the $W \equiv T_1 + V$ operator, promotes the time intervals to Δt_1 and

$$
\begin{aligned}
e^{\theta \Delta t_1 W} &= \left[e^{\frac{\theta}{n_0} \Delta t_1 W} \right]^{n_0} \longrightarrow \Delta t_{0,A} = \frac{\Delta t_1}{n_0} \theta, \\
e^{\lambda \Delta t_1 W} &= \left[e^{\frac{\lambda}{n_0} \Delta t_1 W} \right]^{n_0} \longrightarrow \Delta t_{0,B} = \frac{\Delta t_1}{n_0} \lambda, \\
e^{1-2(\theta+\lambda) \Delta t_1 W} &= \left[e^{\frac{1-2(\theta+\lambda)}{n_0} \Delta t_1 W} \right]^{n_0} \longrightarrow \Delta t_{0,C} = \frac{\Delta t_1}{n_0} 1 - 2(\theta + \lambda).
\end{aligned}
\tag{B.13}
$$

These objects can be replaced inside (B.12) and, following the same scheme as for (B.9), the two-time scales version reads

$$
\begin{aligned}
I_{4MN}(\Delta t, \lambda, \mu, \theta, \rho)_{2ts} = & \Big[e^{\theta \Delta t_{0,A} V} e^{\rho \Delta t_{0,A} T_1} e^{\lambda \Delta t_{0,A} V} e^{\mu \Delta t_{0,A} T_1} e^{1-2(\lambda+\theta) \frac{\Delta t_{0,A}}{2} V} e^{1-2(\mu+\rho) \frac{\Delta t_{0,A}}{2} T_1} \times \\
& \times e^{1-2(\lambda+\theta) \frac{\Delta t_{0,A}}{2} V} e^{\mu \Delta t_{0,A} T_1} e^{\lambda \Delta t_{0,A} V} e^{\rho \Delta t_{0,A} T_1} e^{\theta \Delta t_{0,A} V} \Big]^{n_0} e^{\rho \Delta t_1 T_2} \times \\
& \Big[e^{\theta \Delta t_{0,B} V} e^{\rho \Delta t_{0,B} T_1} e^{\lambda \Delta t_{0,B} V} e^{\mu \Delta t_{0,B} T_1} e^{1-2(\lambda+\theta) \frac{\Delta t_{0,B}}{2} V} e^{1-2(\mu+\rho) \frac{\Delta t_{0,B}}{2} T_1} \times \\
& \times e^{1-2(\lambda+\theta) \frac{\Delta t_{0,B}}{2} V} e^{\mu \Delta t_{0,B} T_1} e^{\lambda \Delta t_{0,B} V} e^{\rho \Delta t_{0,B} T_1} e^{\theta \Delta t_{0,B} V} \Big]^{n_0} e^{\mu \Delta t_1 T_2} \times \\
& \Big[e^{\theta \Delta t_{0,C} V} e^{\rho \Delta t_{0,C} T_1} e^{\lambda \Delta t_{0,C} V} e^{\mu \Delta t_{0,C} T_1} e^{1-2(\lambda+\theta) \frac{\Delta t_{0,C}}{2} V} e^{1-2(\mu+\rho) \frac{\Delta t_{0,C}}{2} T_1} \times \\
& \times e^{1-2(\lambda+\theta) \frac{\Delta t_{0,C}}{2} V} e^{\mu \Delta t_{0,C} T_1} e^{\lambda \Delta t_{0,C} V} e^{\rho \Delta t_{0,C} T_1} e^{\theta \Delta t_{0,C} V} \Big]^{n_0} e^{(1-2(\mu+\rho)) \frac{\Delta t_1}{2} T_2} \dots ,
\end{aligned}
\tag{B.14}
$$

which has been properly truncated for ease of notation. It is worth to stress again that every product of exponentials inside the brakets consist of a one-time scale 4MN integrator, repeated n_0 times. The values of the parameters λ, θ, ρ, μ are choosen in order to fullfill the requirements in (B.5) and (B.6) and can be consulted in [146].

Appendix C

Tables of data

In this Appendix we report the results for any simulated parameter setup, including the number of quark flavours N_f, the lattice temporal extents N_τ, the bare quark masses on the lattice am, the lattice spatial extents N_σ, the number of $\beta(a)$ values involved in the investigation, the investigated $\beta(a)$ range and the total amount of statistics accumulated. In the frame of the multiple histogram method and multiple Markov chains production, for each $\beta(a)$ we decided to also include in the tables the number of Markov chains whose skewness values are compatible with $B_3 = 0$ ($n_c(B_3 \approx 0)$), and the compatibility in terms of standard deviations between the two Markov chains whose skewness values are the most distant ($n_\sigma^{\max}(B_3)$).

C.1 The chiral phase transition at non-zero imaginary baryon chemical potential

C.1.1 $N_\tau = 4$

N_f	N_τ	am	N_s	$\beta(a)$ range	$\beta(a)$ values	Statistics	$n_c(B_3 \approx 0)$	$n_\sigma^{\max}(B_3)$
1.9	4	0.0020	8	5.2900 - 5.3000	2	400k	0	2.33
			12	5.2910 - 5.2990	2	400k	0	1.43
			16	5.2920 - 5.3020	3	325k	0	2.65
1.9	4	0.0040	8	5.2960 - 5.3060	2	400k	0	2.81
			12	5.2970 - 5.3050	2	400k	0	2.16
			16	5.2980 - 5.3040	2	350k	0	2.43
1.9	4	0.0060	8	5.3020 - 5.3120	2	400k	0	1.64
			12	5.3030 - 5.3100	2	400k	0	1.73
			16	5.3040 - 5.3090	2	400k	0	2.67

N_f	N_τ	am	N_s	$\beta(a)$ range	$\beta(a)$ values	Statistics	$n_c(B_3 \approx 0)$	$n_\sigma^{\max}(B_3)$
2.0	4	0.0040	8	5.2800 - 5.2900	2	400k	0	2.87
			12	5.2800 - 5.2900	4	800k	0	1.86
			16	5.2840 - 5.2880	2	400k	0	1.88
2.0	4	0.0080	8	5.2900 - 5.3000	2	400k	0	2.82
			12	5.2850 - 5.2950	2	400k	0	3.64
			16	5.2900 - 5.2960	2	400k	0	2.21
2.0	4	0.0120	8	5.2900 - 5.3100	3	600k	0	2.24
			12	5.2970 - 5.3060	2	400k	0	3.49
			16	5.2970 - 5.3040	4	800k	0	1.42
2.1	4	0.0060	8	5.2640 - 5.2740	2	400k	0	2.24
			12	5.2650 - 5.2810	3	600k	0	2.57
			16	5.2660 - 5.2760	3	600k	0	4.66
2.1	4	0.0100	8	5.2750 - 5.2850	2	400k	0	4.02
			12	5.2760 - 5.2840	2	400k	0	2.12
			16	5.2770 - 5.2830	2	400k	0	2.98
2.1	4	0.0130	8	5.2820 - 5.2920	2	400k	0	1.66
			12	5.2830 - 5.2910	2	400k	0	1.04
			16	5.2840 - 5.2900	2	400k	0	1.84
2.2	4	0.0080	8	5.2500 - 5.2700	3	600k	0	1.71
			12	5.2500 - 5.2600	2	400k	0	2.76
			16	5.2530 - 5.2650	3	600k	0	1.36
2.2	4	0.0110	8	5.2600 - 5.2730	2	400k	0	3.46
			12	5.2580 - 5.2670	2	400k	0	2.42
			16	5.2610 - 5.2710	3	600k	0	1.96
2.2	4	0.0140	8	5.2670 - 5.2770	2	400k	0	3.17
			12	5.2640 - 5.2740	2	400k	0	2.52
			16	5.2650 - 5.2720	2	400k	0	1.71

N_f	N_τ	am	N_s	$\beta(a)$ range	$\beta(a)$ values	Statistics	$n_c(B_3 \approx 0)$	$n_\sigma^{\max}(B_3)$
3.6	4	0.0370	8	5.1050 - 5.1100	2	400k	0	3.13
			12	5.1040 - 5.1100	2	400k	0	5.15
			16	5.1070 - 5.1110	2	400k	0	2.08
3.6	4	0.0420	8	5.1150 - 5.1200	2	400k	0	2.55
			12	5.1170 - 5.1210	2	400k	0	1.81
			16	5.1170 - 5.1210	2	400k	1	2.09
3.6	4	0.0470	8	5.1250 - 5.1300	2	400k	0	2.22
			12	5.1250 - 5.1290	2	400k	0	1.40
			16	5.1250 - 5.1280	2	400k	0	1.76
3.6	4	0.0520	8	5.1300 - 5.1400	2	400k	0	2.67
			12	5.1300 - 5.1400	2	400k	0	1.87
			16	5.1350 - 5.1400	2	400k	0	0.88
4.0	4	0.0500	8	5.0720 - 5.0820	2	400k	0	2.06
			12	5.0750 - 5.0850	3	600k	0	3.76
			16	5.0760 - 5.0820	4	800k	0	1.42
4.0	4	0.0550	8	5.0850 - 5.0950	2	400k	0	2.68
			12	5.0850 - 5.0950	3	400k	0	3.21
			16	5.0880 - 5.0930	3	600k	0	4.74
4.0	4	0.0600	8	5.0950 - 5.1050	2	400k	0	1.55
			12	5.0950 - 5.1050	3	600k	0	4.50
			16	5.0980 - 5.1020	3	600k	0	3.74
4.0	4	0.0650	8	5.1070 - 5.1130	2	400k	0	3.25
			12	5.1070 - 5.1130	2	400k	0	4.09
			16	5.1070 - 5.1130	2	400k	0	3.58

N_f	N_τ	am	N_s	$\beta(a)$ range	$\beta(a)$ values	Statistics	$n_c(B_3 \approx 0)$	$n_\sigma^{\max}(B_3)$
4.5	4	0.0650	8	5.0400 - 5.0500	2	400k	0	2.57
			12	5.0450 - 5.0500	2	400k	0	2.42
			16	5.0460 - 5.0490	2	400k	1	2.94
4.5	4	0.0700	8	5.0530 - 5.0630	3	600k	0	3.02
			12	5.0530 - 5.0630	3	600k	0	3.92
			16	5.0520 - 5.0600	3	600k	0	2.14
4.5	4	0.0750	8	5.0630 - 5.0730	3	600k	0	2.77
			12	5.0630 - 5.0730	3	600k	0	2.91
			16	5.0640 - 5.0700	3	600k	0	3.56

C.1.2 $N_\tau = 6$

N_f	N_τ	am	N_s	$\beta(a)$ range	$\beta(a)$ values	Statistics	$n_c(B_3 \approx 0)$	$n_\sigma^{\max}(B_3)$
3.0	6	0.0010	12	5.2150 - 5.2350	3	360k	0	3.06
			18	5.2200 - 5.2300	3	320k	0	2.02
3.0	6	0.0020	12	5.2250 - 5.2350	2	240k	0	2.41
			18	5.2250 - 5.2350	3	330k	0	2.62
			24	5.2240 - 5.2320	3	235k	1	3.29
3.0	6	0.0030	12	5.2300 - 5.2400	2	240k	0	2.72
			18	5.2300 - 5.2350	2	240k	0	2.88
			24	5.2300 - 5.2340	2	240k	1	2.35

N_f	N_τ	am	N_s	$\beta(a)$ range	$\beta(a)$ values	Statistics	$n_c(B_3 \approx 0)$	$n_\sigma^{\max}(B_3)$
3.3	6	0.0030	12	5.1750 - 5.1850	2	240k	0	1.98
			18	5.1800 - 5.1850	2	260k	0	3.90
			24	5.1800 - 5.1830	3	325k	0	1.36
3.3	6	0.0045	12	5.1800 - 5.1900	2	320k	0	1.98
			18	5.1850 - 5.1900	2	240k	0	1.01
			24	5.1850 - 5.1900	3	340k	0	2.08
3.3	6	0.0060	12	5.1900 - 5.2000	2	400k	0	1.09
			18	5.1900 - 5.2000	3	560k	0	3.22
			24	5.1930 - 5.1960	2	320k	0	1.57
3.3	6	0.0075	12	5.1950 - 5.2050	2	400k	0	2.81
			18	5.2000 - 5.2050	2	400k	0	1.73
			24	5.2000 - 5.2080	3	600k	0	1.79
3.6	6	0.0050	12	5.1380 - 5.1420	2	400k	0	2.22
			18	5.1390 - 5.1440	2	400k	1	4.17
			24	5.1390 - 5.1420	3	460k	1	3.84
3.6	6	0.0075	12	5.1500 - 5.1600	2	400k	0	2.17
			18	5.1500 - 5.1600	3	600k	0	2.08
			24	5.1500 - 5.1550	2	520k	0	0.98
3.6	6	0.0100	12	5.1600 - 5.1700	2	400k	0	1.95
			18	5.1600 - 5.1700	2	400k	0	3.59
			24	5.1580 - 5.1660	3	600k	0	1.52

N_f	N_τ	am	N_s	$\beta(a)$ range	$\beta(a)$ values	Statistics	$n_c(B_3 \approx 0)$	$n_\sigma^{\max}(B_3)$
4.0	6	0.0075	12	5.0870 - 5.0940	2	400k	1	2.32
			18	5.0870 - 5.0940	3	600k	0	4.32
			24	5.0870 - 5.0900	3	550k	0	2.92
4.0	6	0.0100	12	5.0960 - 5.1020	2	400k	0	3.21
			18	5.0960 - 5.1020	3	600k	0	3.30
			24	5.0960 - 5.1020	4	600k	0	2.96
4.0	6	0.0125	12	5.1020 - 5.1140	2	400k	0	1.30
			18	5.1020 - 5.1140	4	800k	0	1.96
			24	5.1080 - 5.1140	2	400k	0	1.75
4.5	6	0.0100	12	5.0180 - 5.0220	2	400k	0	2.61
			18	5.0180 - 5.0260	3	520k	1	2.90
			24	5.0205 - 5.0240	6	720k	0	2.93
4.5	6	0.0140	12	5.0330 - 5.0430	2	400k	0	1.57
			18	5.0330 - 5.0420	3	600k	0	5.31
			24	5.0380 - 5.0420	2	400k	1	2.67
4.5	6	0.0180	12	5.0520 - 5.0570	2	400k	0	3.25
			18	5.0500 - 5.0580	3	600k	0	2.29
			24	5.0520 - 5.0550	2	400k	0	2.63

C.1.3 $N_\tau = 8$

N_f	N_τ	am	N_s	$\beta(a)$ range	$\beta(a)$ values	Statistics	$n_c(B_3 \approx 0)$	$n_\sigma^{\max}(B_3)$
4.0	8	0.0010	16	5.1040 - 5.1100	2	175k	0	2.74
4.0	8	0.0015	16	5.1050 - 5.1140	2	200k	0	2.46
4.0	8	0.0020	16	5.1100 - 5.1200	3	360k	0	2.12
	8							
	8	0.0020	24	5.1130 - 5.1170	2	20k	4	2.22
4.0	8	0.0025	16	5.1150 - 5.1260	2	400k	0	2.33
	8	0.0025	24	5.1160 - 5.1210	2	220k	0	1.87
4.0	8	0.0030	16	5.1180 - 5.1240	2	400k	0	1.39
	8	0.0030	24	5.1200 - 5.1240	2	240k	0	1.64
4.5	8	0.0020	16	5.0200 - 5.0350	2	350k	1	2.34
4.5	8	0.0030	16	5.0350 - 5.0400	2	400k	1	3.08
	8	0.0030	24	5.0320 - 5.0380	2	240k	0	1.41
	8		16	5.0350 - 5.0450	2	320k	1	1.74
4.5	8	0.0040	24	5.0400 - 5.0450	2	240k	1	2.65
	8		32	5.0400 - 5.0450	2	200k	1	2.63

C.2 The chiral phase transition from strong to weak coupling

N_f	N_τ	am	N_s	$\beta(a)$ range	$\beta(a)$ values	Statistics	$n_c(B_3 \approx 0)$	$n_\sigma^{\max}(B_3)$
4.0	2	0.0005	20	3.5000 - 3.5500	2	60k	0	1.25
4.0	2	0.0007	16	3.5100 - 3.5300	2	200k	0	3.83
	2	0.0007	20	3.5100 - 3.5300	2	85k	0	2.23
4.0	2	0.0010	16	3.4600 - 3.5000	2	240k	0	2.53
	2			3.5100 - 3.5300	3	290k	0	1.56
	2		20	3.5100 - 3.5300	2	150k	3	2.54
4.0	2	0.0015	12	3.5000 - 3.5200	2	240k	0	2.50
	2		16	3.5200 - 3.5400	2	240k	0	2.28
	2		20	3.5100 - 3.5400	2	95k	2	2.35
4.0	2	0.0020	12	3.5100 - 3.5300	2	240k	0	2.91
	2		16	3.5100 - 3.5500	2	240k	0	2.48
	2		20	3.5100 - 3.5500	2	165k	0	1.04
4.0	2	0.0025	12	3.5250 - 3.5500	4	480k	0	1.67
	2		16	3.5300 - 3.5500	2	240k	0	1.17
	2		20	3.5300 - 3.5500	2	240k	0	1.60
4.0	2	0.0035	12	3.5000 - 3.5700	6	690k	0	2.08
	2							
	2	0.0035	20	3.5200 - 3.5600	2	220k	3	2.89

N_f	N_τ	am	N_s	$\beta(a)$ range	$\beta(a)$ values	Statistics	$n_c(B_3 \approx 0)$	$n_\sigma^{\max}(B_3)$
	2	0.0010	16	2.0800 - 2.0900	2	160k	0	1.80
8.0								
	2	0.0010	20	2.0800 - 2.1000	2	40k	0	1.40
	2	0.0015	16	2.0800 - 2.1000	3	230k	3	1.71
8.0								
	2	0.0015	20	2.0800 - 2.0900	2	85k	0	1.12
	2		12	2.0800 - 2.1000	2	360k	0	2.54
8.0	2	0.0020	16	2.0800 - 2.1000	2	320k	0	1.43
	2		20	2.0900 - 2.1000	2	115k	2	2.65
	2	0.0025	12	2.0900 - 2.1100	3	420k	0	1.94
8.0								
	2	0.0025	20	2.0900 - 2.1100	2	180k	0	2.14
	2		12	2.1100 - 2.1400	2	240k	0	1.89
8.0	2	0.0035	16	2.1100 - 2.1300	2	240k	0	5.58
	2		20	2.1100 - 2.1300	2	200k	0	3.08

Bibliography

[1] Y. Ne'eman. Derivation of strong interactions from a gauge invariance. *Nuclear Physics*, 26(2):222–229, 1961. ISSN 0029-5582. doi: https://doi.org/10.1016/0029-5582(61)90134-1. URL https://www.sciencedirect.com/science/article/pii/0029558261901341. (Cited on page X.)

[2] Murray Gell-Mann. Symmetries of baryons and mesons. *Phys. Rev.*, 125:1067–1084, Feb 1962. doi: 10.1103/PhysRev.125.1067. URL https://link.aps.org/doi/10.1103/PhysRev.125.1067. (Cited on page X.)

[3] Murray Gell-Mann. A Schematic Model of Baryons and Mesons. *Phys. Lett.*, 8:214–215, 1964. doi: 10.1016/S0031-9163(64)92001-3. (Cited on pages X and 35.)

[4] G. Zweig. *An SU(3) model for strong interaction symmetry and its breaking. Version 2*, pages 22–101. 2 1964. (Cited on pages X and 35.)

[5] David J. Gross and Frank Wilczek. Ultraviolet behavior of non-abelian gauge theories. *Phys. Rev. Lett.*, 30:1343–1346, Jun 1973. doi: 10.1103/PhysRevLett.30.1343. URL https://link.aps.org/doi/10.1103/PhysRevLett.30.1343. (Cited on pages X and 5.)

[6] H. David Politzer. Reliable perturbative results for strong interactions? *Phys. Rev. Lett.*, 30:1346–1349, Jun 1973. doi: 10.1103/PhysRevLett.30.1346. URL https://link.aps.org/doi/10.1103/PhysRevLett.30.1346. (Cited on pages X and 5.)

[7] Kenneth G. Wilson. Confinement of quarks. *Phys. Rev. D*, 10:2445–2459, Oct 1974. doi: 10.1103/PhysRevD.10.2445. URL https://link.aps.org/doi/10.1103/PhysRevD.10.2445. (Cited on pages XI and 5.)

[8] Robert D. Pisarski and Frank Wilczek. Remarks on the chiral phase transition in chromodynamics. *Phys. Rev. D*, 29:338–341, Jan 1984. doi: 10.1103/PhysRevD.29.338. URL https://link.aps.org/doi/10.1103/PhysRevD.29.338. (Cited on pages XI, 38, 39, 40, and 49.)

[9] Francesca Cuteri, Owe Philipsen, and Alessandro Sciarra. On the order of the qcd chiral phase transition for different numbers of quark flavours. *Journal of High Energy Physics*, 2021, 11 2021. doi: 10.1007/JHEP11(2021)141. (Cited on pages XI, XII, XIII, 39, 41, 42, 44, 45, 47, 51, 52, 53, 76, 87, 89, 91, 92, 95, 96, 97, 99, and 100.)

[10] Heinz J. Rothe. *Lattice Gauge Theories : An Introduction (Fourth Edition)*, volume 43. World Scientific Publishing Company, 2012. ISBN 978-981-4365-87-1, 978-981-4365-85-7. doi: 10.1142/8229. (Cited on pages 1, 11, 28, 55, and 113.)

[11] Christof Gattringer and Christian B. Lang. *Quantum chromodynamics on the lattice*, volume 788. Springer, Berlin, 2010. ISBN 978-3-642-01849-7, 978-3-642-01850-3. doi: 10.1007/978-3-642-01850-3. (Cited on pages 1, 12, 20, 29, 30, 31, 55, 56, 64, 66, 67, 73, and 113.)

[12] Thomas DeGrand and Carleton E. Detar. *Lattice methods for quantum chromodynamics*. 2006. (Cited on page 1.)

[13] Joseph I. Kapusta. *Finite Temperature Field Theory*. Cambridge Monographs on Mathematical Physics. Cambridge University Press, Cambridge, 1989. ISBN 978-0-521-35155-3. (Cited on pages 1, 26, and 28.)

[14] Franz Mandl and Graham Shaw. *QUANTUM FIELD THEORY*. 1985. (Cited on pages 1 and 23.)

[15] Alessandro Sciarra. *The QCD phase diagram at purely imaginary chemical potential from the lattice*. PhD thesis, Goethe U., Frankfurt (main), 2016. (Cited on pages 1, 32, 46, 58, 59, 60, 65, 79, and 113.)

[16] G. C. Wick. Properties of bethe-salpeter wave functions. *Phys. Rev.*, 96:1124–1134, Nov 1954. doi: 10.1103/PhysRev.96.1124. URL `https://link.aps.org/doi/10.1103/PhysRev.96.1124`. (Cited on page 2.)

[17] K.G. Wilson. The origins of lattice gauge theory. *Nuclear Physics B - Proceedings Supplements*, 140:3–19, 2005. ISSN 0920-5632. doi: https://doi.org/10.1016/j.nuclphysbps.2004.11.271. URL `https://www.sciencedirect.com/science/article/pii/S0920563204007650`. LATTICE 2004. (Cited on page 5.)

[18] H.B. Nielsen and M. Ninomiya. A no-go theorem for regularizing chiral fermions. *Physics Letters B*, 105(2):219–223, 1981. ISSN 0370-2693. doi: https://doi.org/10.1016/0370-2693(81)91026-1. URL `https://www.sciencedirect.com/science/article/pii/0370269381910261`. (Cited on page 11.)

[19] Stephen L. Adler. Axial-vector vertex in spinor electrodynamics. *Phys. Rev.*, 177:2426–2438, Jan 1969. doi: 10.1103/PhysRev.177.2426. URL `https://link.aps.org/doi/10.1103/PhysRev.177.2426`. (Cited on pages 11 and 22.)

[20] J. S. Bell and R. Jackiw. A PCAC puzzle: $\pi^0 \to \gamma\gamma$ in the σ model. *Nuovo Cim. A*, 60:47–61, 1969. doi: 10.1007/BF02823296. (Cited on pages 11 and 22.)

[21] Luuk H. Karsten and Jan Smith. Lattice fermions: Species doubling, chiral invariance and the triangle anomaly. *Nuclear Physics B*, 183(1):103–140, 1981. ISSN 0550-3213. doi: https://doi.org/10.1016/0550-3213(81)90549-6. URL `https://www.sciencedirect.com/science/article/pii/0550321381905496`. (Cited on page 11.)

[22] Kenneth G. Wilson. Quarks and Strings on a Lattice. In *13th International School of Subnuclear Physics: New Phenomena in Subnuclear Physics*, 11 1975. (Cited on page 11.)

[23] John Kogut and Leonard Susskind. Hamiltonian formulation of wilson's lattice gauge theories. *Phys. Rev. D*, 11:395–408, Jan 1975. doi: 10.1103/PhysRevD.11.395. URL `https://link.aps.org/doi/10.1103/PhysRevD.11.395`. (Cited on page 12.)

[24] R. L. Workman and Others. Review of Particle Physics. *PTEP*, 2022:083C01, 2022. doi: 10.1093/ptep/ptac097. (Cited on pages 22 and 23.)

[25] Yoichiro Nambu. Quasi-particles and gauge invariance in the theory of superconductivity. *Phys. Rev.*, 117:648–663, Feb 1960. doi: 10.1103/PhysRev.117.648. URL `https://link.aps.org/doi/10.1103/PhysRev.117.648`. (Cited on page 23.)

[26] J. Goldstone. Field Theories with Superconductor Solutions. *Nuovo Cim.*, 19:154–164, 1961. doi: 10.1007/BF02812722. (Cited on page 23.)

[27] Gert Aarts. Introductory lectures on lattice QCD at nonzero baryon number. *J. Phys. Conf. Ser.*, 706(2):022004, 2016. doi: 10.1088/1742-6596/706/2/022004. (Cited on page 29.)

[28] P. Hasenfratz and F. Karsch. Chemical potential on the lattice. *Physics Letters B*, 125(4):308–310, 1983. ISSN 0370-2693. doi: https://doi.org/10.1016/0370-2693(83)91290-X. URL `https://www.sciencedirect.com/science/article/pii/037026938391290X`. (Cited on pages 29 and 30.)

[29] E. Noether. Invariante variationsprobleme. *Nachrichten von der Gesellschaft der Wissenschaften zu Göttingen, Mathematisch-Physikalische Klasse*, 1918:235–257, 1918. URL http://eudml.org/doc/59024. (Cited on page 29.)

[30] Katsumi Itoh, Mitsuhiro Kato, Michika Murata, Hideyuki Sawanaka, and Hiroto So. Genuine Symmetry of a Staggered Fermion. *Progress of Theoretical Physics*, 114(3):631–641, 09 2005. ISSN 0033-068X. doi: 10.1143/PTP.114.631. URL https://doi.org/10.1143/PTP.114.631. (Cited on page 31.)

[31] André Roberge and Nathan Weiss. Gauge theories with imaginary chemical potential and the phases of QCD. *Nuclear Physics B*, 275(4):734–745, 1986. ISSN 0550-3213. doi: https://doi.org/10.1016/0550-3213(86)90582-1. URL https://www.sciencedirect.com/science/article/pii/0550321386905821. (Cited on pages 33 and 42.)

[32] Edward V. Shuryak. Quantum chromodynamics and the theory of superdense matter. *Physics Reports*, 61(2):71–158, 1980. ISSN 0370-1573. doi: https://doi.org/10.1016/0370-1573(80)90105-2. URL https://www.sciencedirect.com/science/article/pii/0370157380901052. (Cited on page 35.)

[33] Ulrich Heinz and Maurice Jacob. Evidence for a new state of matter: An assessment of the results from the cern lead beam programme, 2000. URL https://arxiv.org/abs/nucl-th/0002042. (Cited on page 35.)

[34] Marek Gazdzicki, Mark Gorenstein, and Peter Seyboth. Brief history of the search for critical structures in heavy-ion collisions. *Acta Phys. Polon. B*, 51:1033, 2020. doi: 10.5506/APhysPolB.51.1033. (Cited on page 35.)

[35] Dirk H. Rischke. The Quark gluon plasma in equilibrium. *Prog. Part. Nucl. Phys.*, 52:197–296, 2004. doi: 10.1016/j.ppnp.2003.09.002. (Cited on page 36.)

[36] Leon N. Cooper. Bound electron pairs in a degenerate fermi gas. *Phys. Rev.*, 104:1189–1190, Nov 1956. doi: 10.1103/PhysRev.104.1189. URL https://link.aps.org/doi/10.1103/PhysRev.104.1189. (Cited on page 36.)

[37] Simon Hands. The phase diagram of qcd. *Contemporary Physics*, 42(4):209–225, 2001. doi: 10.1080/00107510110063843. URL https://doi.org/10.1080/00107510110063843. (Cited on page 36.)

[38] Mark G. Alford, Andreas Schmitt, Krishna Rajagopal, and Thomas Schaefer. Color superconductivity in dense quark matter. *Rev. Mod. Phys.*, 80:1455–1515, Nov 2008. doi: 10.1103/RevModPhys.80.1455. URL https://link.aps.org/doi/10.1103/RevModPhys.80.1455. (Cited on page 36.)

[39] Kenji Fukushima and Tetsuo Hatsuda. The phase diagram of dense qcd. *Reports on Progress in Physics*, 74(1):014001, dec 2010. doi: 10.1088/0034-4885/74/1/014001. URL https://dx.doi.org/10.1088/0034-4885/74/1/014001. (Cited on page 36.)

[40] J. Kogut, M. Stone, H. W. Wyld, W. R. Gibbs, J. Shigemitsu, Stephen H. Shenker, and D. K. Sinclair. Deconfinement and chiral symmetry restoration at finite temperatures in su(2) and su(3) gauge theories. *Phys. Rev. Lett.*, 50:393–396, Feb 1983. doi: 10.1103/PhysRevLett.50.393. URL https://link.aps.org/doi/10.1103/PhysRevLett.50.393. (Cited on page 36.)

[41] Jana N. Guenther. Overview of the QCD phase diagram: Recent progress from the lattice. *Eur. Phys. J. A*, 57(4):136, 2021. doi: 10.1140/epja/s10050-021-00354-6. (Cited on page 37.)

[42] Anirban Lahiri. Aspects of finite temperature QCD towards the chiral limit. *PoS*, LATTICE2021:003, 2022. doi: 10.22323/1.396.0003. (Cited on page 37.)

[43] Y. Aoki, G. Endrodi, Z. Fodor, S. D. Katz, and K. K. Szabo. The Order of the quantum chromodynamics transition predicted by the standard model of particle physics. *Nature*, 443:675–678, 2006. doi: 10.1038/nature05120. (Cited on page 37.)

[44] Szabolcs Borsanyi, Zoltán Fodor, Christian Hoelbling, Sandor Katz, Stefan Krieg, Claudia Ratti, and Kalman Szabo. Is there still any tc mystery in lattice qcd? results with physical masses in the continuum limit iii. *Journ. of High Energy. Phys.*, 09, 05 2010. doi: 10.1007/JHEP09(2010)073. (Cited on page 37.)

[45] A. Bazavov, Tanmoy Bhattacharya, C. DeTar, H.-T. Ding, Steven Gottlieb, Rajan Gupta, P. Hegde, U. M. Heller, F. Karsch, E. Laermann, L. Levkova, Swagato Mukherjee, P. Petreczky, C. Schmidt, C. Schroeder, R. A. Soltz, W. Soeldner, R. Sugar, M. Wagner, and P. Vranas. Equation of state in $(2+1)$-flavor qcd. *Phys. Rev. D*, 90:094503, Nov 2014. doi: 10.1103/PhysRevD.90.094503. URL `https://link.aps.org/doi/10.1103/PhysRevD.90.094503`. (Cited on page 37.)

[46] A. Bazavov, H.-T. Ding, P. Hegde, O. Kaczmarek, F. Karsch, N. Karthik, E. Laermann, Anirban Lahiri, R. Larsen, S.-T. Li, Swagato Mukherjee, H. Ohno, P. Petreczky, H. Sandmeyer, C. Schmidt, S. Sharma, and P. Steinbrecher. Chiral crossover in qcd at zero and non-zero chemical potentials. *Physics Letters B*, 795:15–21, 2019. ISSN 0370-2693. doi: https://doi.org/10.1016/j.physletb.2019.05.013. URL `https://www.sciencedirect.com/science/article/pii/S0370269319303223`. (Cited on page 37.)

[47] B. Borderie and J.D. Frankland. Liquid–gas phase transition in nuclei. *Progress in Particle and Nuclear Physics*, 105:82–138, 2019. ISSN 0146-6410. doi: https://doi.org/10.1016/j.ppnp.2018.12.002. URL `https://www.sciencedirect.com/science/article/pii/S0146641018301030`. (Cited on page 37.)

[48] Jürgen Berges and Krishna Rajagopal. Color superconductivity and chiral symmetry restoration at non-zero baryon density and temperature. *Nuclear Physics B*, 538(1):215–232, 1999. ISSN 0550-3213. doi: https://doi.org/10.1016/S0550-3213(98)00620-8. URL `https://www.sciencedirect.com/science/article/pii/S0550321398006208`. (Cited on page 37.)

[49] Mikhail A. Stephanov. QCD phase diagram and the critical point. *Prog. Theor. Phys. Suppl.*, 153:139–156, 2004. doi: 10.1142/S0217751X05027965. (Cited on page 37.)

[50] Asakawa Masayuki and Yazaki Koichi. Chiral restoration at finite density and temperature. *Nuclear Physics A*, 504(4):668–684, 1989. ISSN 0375-9474. doi: https://doi.org/10.1016/0375-9474(89)90002-X. URL `https://www.sciencedirect.com/science/article/pii/037594748990002X`. (Cited on page 37.)

[51] Mark G. Alford. Color superconducting quark matter. *Ann. Rev. Nucl. Part. Sci.*, 51:131–160, 2001. doi: 10.1146/annurev.nucl.51.101701.132449. (Cited on page 38.)

[52] Frank R. Brown, Frank P. Butler, Hong Chen, Norman H. Christ, Zhihua Dong, Wendy Schaffer, Leo I. Unger, and Alessandro Vaccarino. On the existence of a phase transition for qcd with three light quarks. *Phys. Rev. Lett.*, 65:2491–2494, Nov 1990. doi: 10.1103/PhysRevLett.65.2491. URL `https://link.aps.org/doi/10.1103/PhysRevLett.65.2491`. (Cited on page 38.)

[53] Heng-Tong Ding and Prasad Hegde. Chiral phase transition of N_f=2+1 and 3 QCD at vanishing baryon chemical potential. *PoS*, LATTICE2015:161, 2016. doi: 10.22323/1.251.0161. (Cited on pages 39, 53, and 106.)

[54] Jens Braun, Marc Leonhardt, Jan M. Pawlowski, and Daniel Rosenblüh. Chiral and effective $u(1)_\mathrm{a}$ symmetry restoration in qcd, 2020. URL `https://arxiv.org/abs/2012.06231`. (Cited on page 39.)

[55] Andrea Pelissetto and Ettore Vicari. Relevance of the axial anomaly at the finite-temperature chiral transition in qcd. *Phys. Rev. D*, 88:105018, Nov 2013. doi: 10.1103/PhysRevD.88.105018. URL https://link.aps.org/doi/10.1103/PhysRevD.88.105018. (Cited on page 39.)

[56] Jens Braun, Wei-jie Fu, Jan M. Pawlowski, Fabian Rennecke, Daniel Rosenblueh, and Shi Yin. Chiral susceptibility in $(2+1)$-flavor qcd. *Phys. Rev. D*, 102:056010, Sep 2020. doi: 10.1103/PhysRevD.102.056010. URL https://link.aps.org/doi/10.1103/PhysRevD.102.056010. (Cited on page 39.)

[57] Francesca Cuteri, Owe Philipsen, and Alessandro Sciarra. Qcd chiral phase transition from noninteger numbers of flavors. *Phys. Rev. D*, 97:114511, Jun 2018. doi: 10.1103/PhysRevD.97.114511. URL https://link.aps.org/doi/10.1103/PhysRevD.97.114511. (Cited on pages 39, 40, and 73.)

[58] Claudio Bonati, Philippe de Forcrand, Massimo D'Elia, Owe Philipsen, and Francesco Sanfilippo. Chiral phase transition in two-flavor qcd from an imaginary chemical potential. *Phys. Rev. D*, 90:074030, Oct 2014. doi: 10.1103/PhysRevD.90.074030. URL https://link.aps.org/doi/10.1103/PhysRevD.90.074030. (Cited on page 39.)

[59] Owe Philipsen and Christopher Pinke. $N_f = 2$ qcd chiral phase transition with wilson fermions at zero and imaginary chemical potential. *Phys. Rev. D*, 93:114507, Jun 2016. doi: 10.1103/PhysRevD.93.114507. URL https://link.aps.org/doi/10.1103/PhysRevD.93.114507. (Cited on page 39.)

[60] Christian Schmidt, F. Karsch, and E. Laermann. The chiral critical point in 3-flavour qcd. *Nuclear Physics B - Proceedings Supplements*, 520:423–425, 07 2001. doi: 10.1016/S0920-5632(01)01734-0. (Cited on page 42.)

[61] Philippe de Forcrand and Owe Philipsen. The QCD phase diagram for three degenerate flavors and small baryon density. *Nucl. Phys. B*, 673:170–186, 2003. doi: 10.1016/j.nuclphysb.2003.09.005. (Cited on pages 42 and 44.)

[62] Y. Iwasaki, K. Kanaya, S. Kaya, S. Sakai, and T. Yoshié. Finite temperature transitions in lattice qcd with wilson quarks: Chiral transitions and the influence of the strange quark. *Phys. Rev. D*, 54:7010–7031, Dec 1996. doi: 10.1103/PhysRevD.54.7010. URL https://link.aps.org/doi/10.1103/PhysRevD.54.7010. (Cited on page 42.)

[63] Xiao-Yong Jin, Yoshinobu Kuramashi, Yoshifumi Nakamura, Shinji Takeda, and Akira Ukawa. Critical endpoint of the finite temperature phase transition for three flavor qcd. *Phys. Rev. D*, 91:014508, Jan 2015. doi: 10.1103/PhysRevD.91.014508. URL https://link.aps.org/doi/10.1103/PhysRevD.91.014508. (Cited on page 42.)

[64] Lorenzo Dini, Prasad Hegde, Frithjof Karsch, Anirban Lahiri, Christian Schmidt, and Sipaz Sharma. Chiral phase transition in three-flavor qcd from lattice qcd. *Phys. Rev. D*, 105:034510, Feb 2022. doi: 10.1103/PhysRevD.105.034510. URL https://link.aps.org/doi/10.1103/PhysRevD.105.034510. (Cited on pages 42 and 100.)

[65] Frithjof Karsch, Anirban Lahiri, Marius Neumann, and Christian Schmidt. A machine learning approach to the classification of phase transitions in many flavor QCD. *PoS*, LATTICE2022:027, 2023. doi: 10.22323/1.430.0027. (Cited on pages 42 and 100.)

[66] Xiao-Yong Jin, Yoshinobu Kuramashi, Yoshifumi Nakamura, Shinji Takeda, and Akira Ukawa. Critical endpoint of the finite temperature phase transition for three flavor qcd. *Phys. Rev. D*, 91:014508, Jan 2015. doi: 10.1103/PhysRevD.91.014508. URL https://link.aps.org/doi/10.1103/PhysRevD.91.014508. (Cited on page 42.)

[67] Xiao-Yong Jin, Yoshinobu Kuramashi, Yoshifumi Nakamura, Shinji Takeda, and Akira Ukawa. Critical point phase transition for finite temperature 3-flavor qcd with nonperturbatively O(a) improved wilson fermions at $N_{\rm t} = 10$. *Phys. Rev. D*, 96:034523, Aug 2017. doi: 10.1103/PhysRevD.96.034523. URL `https://link.aps.org/doi/10.1103/PhysRevD.96.034523`. (Cited on page 42.)

[68] Yoshinobu Kuramashi, Yoshifumi Nakamura, Hiroshi Ohno, and Shinji Takeda. Nature of the phase transition for finite temperature $n_f = 3$ QCD with nonperturbatively $o(a)$ improved wilson fermions at $n_t = 12$. *Phys. Rev. D*, 101:054509, Mar 2020. doi: 10.1103/PhysRevD.101.054509. URL `https://link.aps.org/doi/10.1103/PhysRevD.101.054509`. (Cited on page 42.)

[69] Owe Philipsen. Lattice Constraints on the QCD Chiral Phase Transition at Finite Temperature and Baryon Density. *Symmetry*, 13(11):2079, 2021. doi: 10.3390/sym13112079. (Cited on page 42.)

[70] P. Giudice and A. Papa. Real and imaginary chemical potential in two color QCD. *Phys. Rev. D*, 69:094509, 2004. doi: 10.1103/PhysRevD.69.094509. (Cited on page 42.)

[71] Massimo D'Elia and Maria-Paola Lombardo. Finite density QCD via imaginary chemical potential. *Phys. Rev. D*, 67:014505, 2003. doi: 10.1103/PhysRevD.67.014505. (Cited on page 42.)

[72] Philippe de Forcrand and Owe Philipsen. The qcd phase diagram for small densities from imaginary chemical potential. *Nuclear Physics B*, 642(1):290–306, 2002. ISSN 0550-3213. doi: https://doi.org/10.1016/S0550-3213(02)00626-0. URL `https://www.sciencedirect.com/science/article/pii/S0550321302006260`. (Cited on pages 42 and 46.)

[73] Massimo D'Elia and Francesco Sanfilippo. The Order of the Roberge-Weiss endpoint (finite size transition) in QCD. *Phys. Rev. D*, 80:111501, 2009. doi: 10.1103/PhysRevD.80.111501. (Cited on page 42.)

[74] Claudio Bonati, Guido Cossu, Massimo D'Elia, and Francesco Sanfilippo. The Roberge-Weiss endpoint in $N_f = 2$ QCD. *Phys. Rev. D*, 83:054505, 2011. doi: 10.1103/PhysRevD.83.054505. (Cited on page 42.)

[75] Christopher Czaban, Francesca Cuteri, Owe Philipsen, Christopher Pinke, and Alessandro Sciarra. Roberge-weiss transition in $n_f = 2$ QCD with wilson fermions and $n_\tau = 6$. *Phys. Rev. D*, 93:054507, Mar 2016. doi: 10.1103/PhysRevD.93.054507. URL `https://link.aps.org/doi/10.1103/PhysRevD.93.054507`. (Cited on page 43.)

[76] Owe Philipsen and Alessandro Sciarra. Finite Size and Cut-Off Effects on the Roberge-Weiss Transition in $N_{\rm f} = 2$ QCD with Staggered Fermions. *Phys. Rev. D*, 101(1):014502, 2020. doi: 10.1103/PhysRevD.101.014502. (Cited on page 43.)

[77] Claudio Bonati, Philippe de Forcrand, Massimo D'Elia, Owe Philipsen, and Francesco Sanfilippo. Chiral phase transition in two-flavor QCD from an imaginary chemical potential. *Phys. Rev. D*, 90(7):074030, 2014. doi: 10.1103/PhysRevD.90.074030. (Cited on page 43.)

[78] Claudio Bonati, Massimo D'Elia, Marco Mariti, Michele Mesiti, Francesco Negro, and Francesco Sanfilippo. Roberge-weiss endpoint at the physical point of $N_f = 2 + 1$ QCD. *Phys. Rev. D*, 93:074504, Apr 2016. doi: 10.1103/PhysRevD.93.074504. URL `https://link.aps.org/doi/10.1103/PhysRevD.93.074504`. (Cited on page 43.)

[79] Claudio Bonati, Enrico Calore, Massimo D'Elia, Michele Mesiti, Francesco Negro, Francesco Sanfilippo, Sebastiano Fabio Schifano, Giorgio Silvi, and Raffaele Tripiccione. Roberge-weiss endpoint and chiral symmetry restoration in $N_f = 2 + 1$ qcd. *Phys. Rev. D*, 99:014502, Jan 2019. doi: 10.1103/PhysRevD.99.014502. URL `https://link.aps.org/doi/10.1103/PhysRevD.99.014502`. (Cited on page 43.)

[80] F. Cuteri, J. Goswami, F. Karsch, Anirban Lahiri, M. Neumann, O. Philipsen, Christian Schmidt, and A. Sciarra. Toward the chiral phase transition in the Roberge-Weiss plane. *Phys. Rev. D*, 106(1):014510, 2022. doi: 10.1103/PhysRevD.106.014510. (Cited on pages 43 and 100.)

[81] Philippe de Forcrand and Owe Philipsen. The Chiral critical point of $N_f = 3$ QCD at finite density to the order $(\mu/T)^4$. *JHEP*, 11:012, 2008. doi: 10.1088/1126-6708/2008/11/012. (Cited on page 44.)

[82] Philippe de Forcrand and Owe Philipsen. Constraining the qcd phase diagram by tricritical lines at imaginary chemical potential. *Phys. Rev. Lett.*, 105:152001, Oct 2010. doi: 10.1103/PhysRevLett.105.152001. URL `https://link.aps.org/doi/10.1103/PhysRevLett.105.152001`. (Cited on page 44.)

[83] Seyong Kim, Ph. de Forcrand, S. Kratochvila, and T. Takaishi. The 3-state Potts model as a heavy quark finite density laboratory. *PoS*, LAT2005:166, 2006. doi: 10.22323/1.020.0166. (Cited on page 44.)

[84] Ian D Lawrie and Stéphane Sarbach. Theory of tricritical points. *Phase transitions and critical phenomena*, 9:1–161, 1984. (Cited on page 44.)

[85] N. Kawamoto and J. Smit. Effective lagrangian and dynamical symmetry breaking in strongly coupled lattice qcd. *Nuclear Physics B*, 192(1):100–124, 1981. ISSN 0550-3213. doi: https://doi.org/10.1016/0550-3213(81)90196-6. URL `https://www.sciencedirect.com/science/article/pii/0550321381901966`. (Cited on page 47.)

[86] Jaap Hoek, Noboru Kawamoto, and Jan Smit. Baryons in the effective lagrangian of strongly coupled lattice qcd. *Nuclear Physics B*, 199(3):495–522, 1982. ISSN 0550-3213. doi: https://doi.org/10.1016/0550-3213(82)90357-1. URL `https://www.sciencedirect.com/science/article/pii/0550321382903571`. (Cited on page 47.)

[87] P.H. Damgaard, D. Hochberg, and N. Kawamoto. Effective lagrangian analysis of the chiral phase transition at finite density. *Physics Letters B*, 158(3):239–244, 1985. ISSN 0370-2693. doi: https://doi.org/10.1016/0370-2693(85)90964-5. URL `https://www.sciencedirect.com/science/article/pii/0370269385909645`. (Cited on page 47.)

[88] P.H. Damgaard, N. Kawamoto, and K. Shigemoto. Strong coupling analysis of the chiral phase transition at finite temperature. *Nuclear Physics B*, 264:1–28, 1986. ISSN 0550-3213. doi: https://doi.org/10.1016/0550-3213(86)90470-0. URL `https://www.sciencedirect.com/science/article/pii/0550321386904700`. (Cited on page 47.)

[89] Neven Bilic, Kresimir Demeterfi, and Bengt Petersson. Strong coupling analysis of the chiral phase transition at finite chemical potential and finite temperature. *Nucl. Phys. B*, 377:651–665, 1992. doi: 10.1016/0550-3213(92)90305-U. (Cited on page 47.)

[90] Neven Bilic, Frithjof Karsch, and Krzysztof Redlich. Flavor dependence of the chiral phase transition in strong coupling QCD. *Phys. Rev. D*, 45:3228–3236, 1992. doi: 10.1103/PhysRevD.45.3228. (Cited on page 47.)

[91] Yusuke Nishida. Phase structures of strong coupling lattice qcd with finite baryon and isospin density. *Phys. Rev. D*, 69:094501, May 2004. doi: 10.1103/PhysRevD.69.094501. URL `https://link.aps.org/doi/10.1103/PhysRevD.69.094501`. (Cited on page 47.)

[92] Kohtaroh Miura, Takashi Z. Nakano, Akira Ohnishi, and Noboru Kawamoto. Phase diagram evolution at finite coupling in strong coupling lattice QCD. *Phys. Rev. D*, 80:074034, 2009. doi: 10.1103/PhysRevD.80.074034. (Cited on page 47.)

[93] Takashi Z. Nakano, Kohtaroh Miura, and Akira Ohnishi. Chiral and deconfinement transitions in strong coupling lattice qcd with finite coupling and polyakov loop effects. *Phys. Rev. D*, 83:016014, Jan 2011. doi: 10.1103/PhysRevD.83.016014. URL https://link.aps.org/doi/10.1103/PhysRevD.83.016014. (Cited on page 48.)

[94] Kohtaroh Miura, Noboru Kawamoto, Takashi Z. Nakano, and Akira Ohnishi. Polyakov loop effects on the phase diagram in strong-coupling lattice qcd. *Phys. Rev. D*, 95:114505, Jun 2017. doi: 10.1103/PhysRevD.95.114505. URL https://link.aps.org/doi/10.1103/PhysRevD.95.114505. (Cited on pages 48 and 50.)

[95] Pietro Rossi and Ulli Wolff. Lattice qcd with fermions at strong coupling: A dimer system. *Nuclear Physics B*, 248(1):105–122, 1984. ISSN 0550-3213. doi: https://doi.org/10.1016/0550-3213(84)90589-3. URL https://www.sciencedirect.com/science/article/pii/0550321384905893. (Cited on page 48.)

[96] Ulli Wolff. Baryons in lattice qcd at strong coupling. *Physics Letters B*, 153(1):92–96, 1985. ISSN 0370-2693. doi: https://doi.org/10.1016/0370-2693(85)91448-0. URL https://www.sciencedirect.com/science/article/pii/0370269385914480. (Cited on page 48.)

[97] Stuart Samuel. The Use of Anticommuting Integrals in Statistical Mechanics. 3. *J. Math. Phys.*, 21:2820, 1980. doi: 10.1063/1.524406. (Cited on page 48.)

[98] Elbio Dagotto, Adriana Moreo, and Ulli Wolff. Lattice su(n) ocd at finite temperature and density in the strong coupling limit. *Physics Letters B*, 186(3):395–400, 1987. ISSN 0370-2693. doi: https://doi.org/10.1016/0370-2693(87)90315-7. URL https://www.sciencedirect.com/science/article/pii/0370269387903157. (Cited on page 49.)

[99] F. Karsch and K. H. Mutter. STRONG COUPLING QCD AT FINITE BARYON NUMBER DENSITY. *Nucl. Phys. B*, 313:541–559, 1989. doi: 10.1016/0550-3213(89)90396-9. (Cited on page 49.)

[100] G. Boyd, J. Fingberg, F. Karsch, L. Kärkkäinen, and B. Peterson. Critical exponents of the chiral transition in strong coupling qcd. *Nuclear Physics B*, 376(1):199–217, 1992. ISSN 0550-3213. doi: https://doi.org/10.1016/0550-3213(92)90074-L. URL https://www.sciencedirect.com/science/article/pii/055032139290074L. (Cited on page 49.)

[101] Ph. de Forcrand and M. Fromm. Nuclear physics from lattice qcd at strong coupling. *Phys. Rev. Lett.*, 104:112005, Mar 2010. doi: 10.1103/PhysRevLett.104.112005. URL https://link.aps.org/doi/10.1103/PhysRevLett.104.112005. (Cited on page 49.)

[102] Wolfgang Unger and Philippe de Forcrand. Continuous Time Monte Carlo for Lattice QCD in the Strong Coupling Limit. *PoS*, LATTICE2011:218, 2011. doi: 10.22323/1.139.0218. (Cited on page 49.)

[103] Philippe de Forcrand, Jens Langelage, Owe Philipsen, and Wolfgang Unger. Lattice QCD Phase Diagram In and Away from the Strong Coupling Limit. *Phys. Rev. Lett.*, 113(15): 152002, 2014. doi: 10.1103/PhysRevLett.113.152002. (Cited on pages 49, 50, and 51.)

[104] Jangho Kim, Marc Klegrewe, and Wolfgang Unger. Gauge Corrections to Strong Coupling LQCD on Anisotropic Lattices. *PoS*, LATTICE2019:210, 2020. doi: 10.22323/1.363.0210. (Cited on page 50.)

[105] Giuseppe Gagliardi and Wolfgang Unger. New dual representation for staggered lattice QCD. *Phys. Rev. D*, 101(3):034509, 2020. doi: 10.1103/PhysRevD.101.034509. (Cited on page 50.)

[106] Philippe de Forcrand, Owe Philipsen, and Wolfgang Unger. QCD phase diagram from the lattice at strong coupling. *PoS*, CPOD2014:073, 2015. doi: 10.22323/1.217.0073. (Cited on page 51.)

[107] A. D. Kennedy. Algorithms for dynamical fermions. 7 2006. (Cited on pages 55 and 58.)

[108] M. A. Clark. The Rational Hybrid Monte Carlo Algorithm. *PoS*, LAT2006:004, 2006. doi: 10.22323/1.032.0004. (Cited on page 55.)

[109] Thomas A. Degrand and Pietro Rossi. Conditioning techniques for dynamical fermions. *Computer Physics Communications*, 60(2):211–214, 1990. ISSN 0010-4655. doi: https://doi.org/10.1016/0010-4655(90)90006-M. URL `https://www.sciencedirect.com/science/article/pii/001046559090006M`. (Cited on page 56.)

[110] Stephen R. Sharpe. Rooted staggered fermions: Good, bad or ugly? *PoS*, LAT2006:022, 2006. doi: 10.22323/1.032.0022. (Cited on page 57.)

[111] F. Fucito, E. Marinari, G. Parisi, and C. Rebbi. A proposal for monte carlo simulations of fermionic systems. *Nuclear Physics B*, 180(3):369–377, 1981. ISSN 0550-3213. doi: https://doi.org/10.1016/0550-3213(81)90055-9. URL `https://www.sciencedirect.com/science/article/pii/0550321381900559`. (Cited on page 57.)

[112] Evgeniĭ Remez. *General computational methods of Chebyshev approximation: The problems with linear real parameters.* (Cited on page 59.)

[113] Beat Jegerlehner. Krylov space solvers for shifted linear systems. 12 1996. (Cited on page 59.)

[114] Steven Gottlieb, W. Liu, D. Toussaint, R. L. Renken, and R. L. Sugar. Hybrid-molecular-dynamics algorithms for the numerical simulation of quantum chromodynamics. *Phys. Rev. D*, 35:2531–2542, Apr 1987. doi: 10.1103/PhysRevD.35.2531. URL `https://link.aps.org/doi/10.1103/PhysRevD.35.2531`. (Cited on page 60.)

[115] N. Metropolis, A. W. Rosenbluth, M. N. Rosenbluth, A. H. Teller, and E. Teller. Equation of state calculations by fast computing machines. *J. Chem. Phys.*, 21:1087–1092, 1953. doi: 10.1063/1.1699114. (Cited on page 61.)

[116] M. A. Clark and A. D. Kennedy. Accelerating dynamical fermion computations using the rational hybrid Monte Carlo (RHMC) algorithm with multiple pseudofermion fields. *Phys. Rev. Lett.*, 98:051601, 2007. doi: 10.1103/PhysRevLett.98.051601. (Cited on page 61.)

[117] Bernd A. Berg. Introduction to Markov chain Monte Carlo simulations and their statistical analysis. 10 2004. (Cited on pages 66 and 67.)

[118] Ulli Wolff. Monte Carlo errors with less errors. *Comput. Phys. Commun.*, 156:143–153, 2004. doi: 10.1016/S0010-4655(03)00467-3. [Erratum: Comput.Phys.Commun. 176, 383 (2007)]. (Cited on page 66.)

[119] Peter Young. Everything you wanted to know about data analysis and fitting but were afraid to ask. *arXiv preprint arXiv:1210.3781*, 2012. (Cited on pages 67 and 73.)

[120] A. Papoulis and S.U. Pillai. *Probability, Random Variables, and Stochastic Processes.* McGraw-Hill series in electrical engineering: Communications and signal processing. Tata McGraw-Hill, 2002. ISBN 9780070486584. URL `https://books.google.it/books?id=g6eUoWOlcQMC`. (Cited on page 68.)

[121] K. Binder. Finite size scaling analysis of ising model block distribution functions. In John L. CARDY, editor, *Finite-Size Scaling*, volume 2 of *Current Physics–Sources and Comments*, pages 79–100. Elsevier, 1988. doi: https://doi.org/10.1016/B978-0-444-87109-1.50012-1. URL `https://www.sciencedirect.com/science/article/pii/B9780444871091500121`. (Cited on page 69.)

[122] Andrea Pelissetto and Ettore Vicari. Critical phenomena and renormalization group theory. *Phys. Rept.*, 368:549–727, 2002. doi: 10.1016/S0370-1573(02)00219-3. (Cited on pages 70 and 72.)

[123] HWJ Blote, Erik Luijten, and Jouke R Heringa. Ising universality in three dimensions: a monte carlo study. *Journal of Physics A: Mathematical and General*, 28(22):6289, 1995. (Cited on page 70.)

[124] Paul Springer and Bertram Klein. O(2)-scaling in finite and infinite volume. *Eur. Phys. J. C*, 75(10):468, 2015. doi: 10.1140/epjc/s10052-015-3667-3. (Cited on pages 69 and 70.)

[125] Alan M. Ferrenberg and Robert H. Swendsen. New monte carlo technique for studying phase transitions. *Phys. Rev. Lett.*, 61:2635–2638, Dec 1988. doi: 10.1103/PhysRevLett.61.2635. URL `https://link.aps.org/doi/10.1103/PhysRevLett.61.2635`. (Cited on page 70.)

[126] Alan M. Ferrenberg and Robert H. Swendsen. Optimized monte carlo data analysis. *Phys. Rev. Lett.*, 63:1195–1198, Sep 1989. doi: 10.1103/PhysRevLett.63.1195. URL `https://link.aps.org/doi/10.1103/PhysRevLett.63.1195`. (Cited on page 70.)

[127] M.E.J. Newman and G.T. Barkema. *Monte Carlo Methods in Statistical Physics*. Clarendon Press, 1999. ISBN 9780198517962. URL `https://books.google.it/books?id=KKL2nQEACAAJ`. (Cited on pages 70, 71, and 73.)

[128] Shinji Takeda, Xiao-Yong Jin, Yoshinobu Kuramashi, Yoshifumi Nakamura, and Akira Ukawa. Update on Nf=3 finite temperature QCD phase structure with Wilson-Clover fermion action. *PoS*, LATTICE2016:384, 2017. doi: 10.22323/1.256.0384. (Cited on page 72.)

[129] Murray Gell-Mann, R. J. Oakes, and B. Renner. Behavior of current divergences under $su_3 \times su_3$. *Phys. Rev.*, 175:2195–2199, Nov 1968. doi: 10.1103/PhysRev.175.2195. URL `https://link.aps.org/doi/10.1103/PhysRev.175.2195`. (Cited on page 75.)

[130] Christopher Pinke, Matthias Bach, Alessandro Sciarra, Francesca Cuteri, Lars Zeidlewicz, Christian Schäfer, Tim Breitenfelder, Christopher Czaban, Stefano Lottini, and Paul Frederik Depta. Cl2qcd, September 2018. URL `https://doi.org/10.5281/zenodo.5121895`. (Cited on page 77.)

[131] Alessandro* Sciarra, Christopher Pinke, Matthias Bach, Francesca Cuteri, Lars Zeidlewicz, Christian Schäfer, Tim Breitenfelder, Christopher Czaban, Stefano Lottini, and Paul Frederik Depta. Cl2qcd, February 2021. URL `https://doi.org/10.5281/zenodo.5121917`. (Cited on page 77.)

[132] Owe Philipsen, Christopher Pinke, Christian Schafer, Lars Zeidlewicz, and Matthias Bach. LatticeQCD using OpenCL. *PoS*, LATTICE2011:044, 2011. doi: 10.22323/1.139.0044. (Cited on page 77.)

[133] Matthias Bach, Volker Lindenstruth, Owe Philipsen, and Christopher Pinke. Lattice QCD based on OpenCL. *Comput. Phys. Commun.*, 184:2042–2052, 2013. doi: 10.1016/j.cpc.2013.03.020. (Cited on page 77.)

[134] Matthias Bach, Volker Lindenstruth, Christopher Pinke, and Owe Philipsen. Twisted-Mass Lattice QCD using OpenCL. *PoS*, LATTICE2013:032, 2014. doi: 10.22323/1.187.0032. (Cited on page 77.)

[135] Owe Philipsen, Christopher Pinke, Alessandro Sciarra, and Matthias Bach. CL^2QCD - Lattice QCD based on OpenCL. *PoS*, LATTICE2014:038, 2014. doi: 10.22323/1.214.0038. (Cited on page 77.)

[136] David Rohr, Matthias Bach, Gvozden Nešković, Volker Lindenstruth, Christopher Pinke, and Owe Philipsen. Lattice-csc: Optimizing and building an efficient supercomputer for lattice-qcd and to achieve first place in green500. pages 179–196, 07 2015. ISBN 978-3-319-20118-4. doi: 10.1007/978-3-319-20119-1_14. (Cited on page 78.)

[137] Alessandro Sciarra. Bahamas, February 2021. URL https://doi.org/10.5281/zenodo.4577425. (Cited on page 78.)

[138] Sourendu Gupta, A. Irbäc, F. Karsch, and B. Petersson. The acceptance probability in the hybrid monte carlo method. *Physics Letters B*, 242(3):437–443, 1990. ISSN 0370-2693. doi: https://doi.org/10.1016/0370-2693(90)91790-I. URL https://www.sciencedirect.com/science/article/pii/037026939091790I. (Cited on pages 81, 82, and 84.)

[139] Michael Creutz. Global monte carlo algorithms for many-fermion systems. *Phys. Rev. D*, 38:1228–1238, Aug 1988. doi: 10.1103/PhysRevD.38.1228. URL https://link.aps.org/doi/10.1103/PhysRevD.38.1228. (Cited on page 81.)

[140] Tetsuya Takaishi. Choice of integrator in the hybrid monte carlo algorithm. *Computer Physics Communications*, 133(1):6–17, 2000. ISSN 0010-4655. doi: https://doi.org/10.1016/S0010-4655(00)00161-2. URL https://www.sciencedirect.com/science/article/pii/S0010465500001612. (Cited on page 82.)

[141] Tetsuya Takaishi and Philippe de Forcrand. Testing and tuning new symplectic integrators for hybrid Monte Carlo algorithm in lattice QCD. *Phys. Rev. E*, 73:036706, 2006. doi: 10.1103/PhysRevE.73.036706. (Cited on pages 82 and 119.)

[142] Thomas DeGrand. Lattice tests of beyond Standard Model dynamics. *Rev. Mod. Phys.*, 88:015001, 2016. doi: 10.1103/RevModPhys.88.015001. (Cited on page 102.)

[143] Daniel Nogradi and Agostino Patella. Strong dynamics, composite Higgs and the conformal window. *Int. J. Mod. Phys. A*, 31(22):1643003, 2016. doi: 10.1142/S0217751X1643003X. (Cited on page 102.)

[144] Benjamin Svetitsky. Looking behind the Standard Model with lattice gauge theory. *EPJ Web Conf.*, 175:01017, 2018. doi: 10.1051/epjconf/201817501017. (Cited on page 102.)

[145] IP Omelyan, IM Mryglod, and Reinhard Folk. Optimized verlet-like algorithms for molecular dynamics simulations. *Physical Review E*, 65(5):056706, 2002. (Cited on pages 119 and 120.)

[146] I.P. Omelyan, I.M. Mryglod, and R. Folk. Symplectic analytically integrable decomposition algorithms: classification, derivation, and application to molecular dynamics, quantum and celestial mechanics simulations. *Computer Physics Communications*, 151(3):272–314, 2003. ISSN 0010-4655. doi: https://doi.org/10.1016/S0010-4655(02)00754-3. URL https://www.sciencedirect.com/science/article/pii/S0010465502007543. (Cited on pages 119, 120, and 123.)

[147] J.C. Sexton and D.H. Weingarten. Hamiltonian evolution for the hybrid monte carlo algorithm. *Nuclear Physics B*, 380(3):665–677, 1992. ISSN 0550-3213. doi: https://doi.org/10.1016/0550-3213(92)90263-B. URL https://www.sciencedirect.com/science/article/pii/055032139290263B. (Cited on page 120.)

[148] Mike J. Peardon and James Sexton. Multiple molecular dynamics time scales in hybrid Monte Carlo fermion simulations. *Nucl. Phys. B Proc. Suppl.*, 119:985–987, 2003. doi: 10.1016/S0920-5632(03)01738-9. (Cited on page 120.)

[149] C. Urbach, K. Jansen, A. Shindler, and U. Wenger. HMC algorithm with multiple time scale integration and mass preconditioning. *Comput. Phys. Commun.*, 174:87–98, 2006. doi: 10.1016/j.cpc.2005.08.006. (Cited on pages 120 and 122.)